

Politecnico di Bari

Repository Istituzionale dei Prodotti della Ricerca del Politecnico di Bari

Design of optical links for integrated terrestrial and non-terrestrial networks

This is a PhD Thesis

Original Citation:
Design of optical links for integrated terrestrial and non-terrestrial networks / Cantore, C.. - ELETTRONICO. - (2026).

Availability:
This version is available at http://hdl.handle.net/11589/308441 since: 2026-10-14

Published version
DOI:

Publisher: Politecnico di Bari

Terms of use:

(Article begins on next page)

25 October 2026

Politecnico di Bari

Department of Electrical and Information Engineering
ELECTRICAL AND INFORMATION ENGINEERING
Ph.D. Program
SSD: IINF-02/A–ELECTROMAGNETIC FIELDS

Final Dissertation

Design of Optical Links for Integrated Terrestrial and Non-Terrestrial Networks

---

by
Carla Cantore

Supervisors:

Prof. Antonella D'Orazio

Prof. Giovanni Magno

Dr. Ilaria Marasco

Coordinator of Ph.D. Program:
Prof. Nicola Giaquinto

Course n°38, 01/04/2023-30/06/2026

Politecnico di Bari

Department of Electrical and Information Engineering
ELECTRICAL AND INFORMATION ENGINEERING
Ph.D. Program
SSD: IINF-02/A –ELECTROMAGNETIC FIELDS

Final Dissertation

Design of Optical Links for Integrated Terrestrial and Non-Terrestrial Networks

---

by
Carla Cantore

Referees:

Prof. Marco Donald Migliore

Dr. Vincenzo Schena

Supervisors:

Prof. Antonella D'Orazio

Prof. Giovanni Magno

Dr. Ilaria Marasco

Coordinator of Ph.D Program:
Prof. Nicola Giaquinto

Course n°38, 01/04/2023-30/06/2026

In loving memory of Marco Grande

I should've asked you questions
I should've asked you how to be

And if I didn't know better
I'd think you were talking to me now
If I didn't know better
I'd think you were still around

What died didn't stay dead
You're alive, so alive

Acknowledgements

When it comes to the end of a journey that significantly shaped your life in so many ways, it's never easy to find the right words. I am thankful for all the great opportunities that this PhD brought me and for all the special people I got to meet during the journey, but the thing I am most grateful for is that I had the chance to get to know and work along with Prof. Marco Grande.

Marco, you have been more than a professor and a supervisor to me. You were and always will be the kind of person I would like to become. You are the smartest, most brilliant, dedicated scientist I have ever met. You were coming up with new ideas every second and sharing them with everyone. The passion you had for research was tangible, but the integrity, honesty, kindness, and care for others you always had really made the difference. The love, support, and trust you constantly showed for us, your students, made us feel part of a group. I chose to pursue this PhD program because of the passion you conveyed to me, and the only year I had the honor to work by your side gave me the strength and motivation to finish it. Even now, you are shaping my future. I would not only have done a PhD, but I would also not have my job at ESA without you. Many times during my days I'd like to talk to you, ask for your wise advice. It has never been and never will be easy to cope with the idea that this is not possible. But I hope that, wherever you are, you are proud of the legacy you built, of the values you taught us, of what we have been able to build since then. And while the "ottimo lavoro" words you used to have for me are all I would need to hear now, I hope to have been, for one time, "smart enough".

I would like to thank Prof. Antonella D'Orazio for taking the role of my supervisor during such a difficult time, for trusting me, and for giving me many

opportunities of growth during these years. You always took care of making me feel part of the nPEG family, thank you.

Thanks to my other two supervisors, Ilaria and Giovanni, for all the memories we have built. Poliba will always feel like a second home to me.

A heartfelt thanks goes to Prof. Ernesto Ciaramella and Dr. Giulio Cossu, as well as to Luca and Sujit, for the chance they gave me to work in such a stimulating lab and for their constant support. The invaluable technical guidance I received from Prof. Ciaramella and Giulio has been essential for me to grow in this field.

A huge thanks goes to Gionni, Francisca, and Davide. Nothing would have been the same without you and, even if I am not the kind of person who frequently expresses her feelings, now I can say that you will always have a special place in my heart.

Gionni, we have known each other for a long time. You are always so kind and polite to everyone but, now that I know your evil side, I feel like this is a real friendship. Jokes aside, you have the kindest soul, you are always there to help, and have a nice word for everyone. But you can also switch off microphones and steal pieces of cake, which all together make you the funniest, smartest, and kindest friend one could have.

Francesca, since the days you were coming in the lab, taking your dielectric constant measurements, and going straight away without speaking a word to us, I knew that you were the coolest girl. And indeed, you are always there, bringing a ray of sun in our lives. I really admire your brightness, sincerity, and integrity, but also your dedication to work and capability to enjoy life at the same time. I feel like you are always taking the best from every situation and opportunity you have, while taking care of making others feel involved.

Davide, I don't think I will find the right words. You were the first person I met in this group, even before starting the PhD. I was forced to work with you, but this is another thing I will forever be thankful for (grazie Marco). With you it has always been easy to be myself, to not care about always being perfect, and to express my real feelings. I know I can complain with you whenever I need to and that you will listen but will also motivate me to do my best. You usually do this by going against all my thoughts, but in some strange way it works. We shared every important moment together in these last three years, both the good and the

bad, even if always in different parts of the world. Along the path, I saw you going from the initial desperation to even more desperation and finally becoming smart enough. I don't know if I could have make it without your friendship, but I am glad that I didn't need to know.

I really hope that les bandits will always find a way to reach each other, to meet wherever in the world it will be, and to laugh together while writing limericks on ChatGPT.

Thanks to Ajmal, you have been there from the beginning. I really appreciate the passion you put in your job and the kindness you show with everyone. I will always remember the coffee and cornetto and the biryani lunches together with the others in Bari.

A big thanks to the people I met during my period at ESA. To Angelo, for all the interesting technical discussions but, first of all, for being a friend. To TEC-SEC, for always making me feel welcomed in the group, both now and then. And, finally, to all the special people I met in the shed, especially to Giovanni and Riccardo for still making my Dutch life richer.

I would also like to thank all the wonderful people I met around the world, especially my MetroAeroSpace family. The Lublin edition will always be the peak of trash in my PhD memories.

And now, the last thanks are for the people who have always been there.

To my parents, I owe everything to you. Thank you for always supporting me, for believing in me, but never expecting anything from me. To my sister, for all the times we've teamed together. It is always strange to me that now that we finally get along, we don't live together anymore. Thanks because I would not have been the same without my sister.

To Carmel(in)a and Filippo, you will forever be my best friends. Whatever will happen in our lives, I know we will find a way to talk about life in Filippo's car while he smokes the last cigarette of the day. All those moments, I bring them in my heart.

To Anna, I am so proud of the woman you are and so thankful for having you in my life. We've grown up a lot since we first met, and I cherish every moment, from measurement meetings at my and Leo's place to sharing the same open space in

Nice. With you, I learned how easy it is to be extremely and sincerely enthusiastic for each other's achievements. I know this friendship will last forever.

To Danila, a few years ago I wouldn't have expected to become so close friends, but here we are. You bring happiness to people's lives and deserve all the best. Don't settle for less.

And finally, to my love, Luca. I always leave you at the end because there are no words to really explain how much I am grateful to life for putting you along my way. Your love always gave me the strength and lightness I needed. Nothing would have been possible without your support, your way to make my life easier and to make me feel loved. I cannot imagine doing again all of this without you by my side. And I hope I will never have to. I love you.

Contents

Acknowledgements

List of Tables

List of Figures 1

List of Abbreviations 11

Introduction 23

List of publications 27

1 Optical Links for Integrated TNs and NTNs 30
1.1 OFLs: Advantages and challenges 34
1.2 Optical satellite links: State-of-the-art 37
1.2.1 Early proof-of-concept demonstrations 40
1.2.2 Emergence of operational optical inter-satellite links 43
1.2.3 Transition to coherent optical communications and AO systems 51
1.2.4 Toward miniaturization, quantum communication, and New Space terminals 58
1.2.5 Toward operational optical relay and feeder-link systems . . 64
1.2.6 Optical communications for small satellites and CubeSat constellations 70
1.3 Thesis' scope and summary of contributions 73

2 Link Budget Model for OFLs **78**
2.1 System and channel models for OFLs . . . 79
2.1.1 Transmitter . . . 80
2.1.2 Free-space propagation . . . 82
2.1.3 Absorption and scattering . . . 82
2.1.4 Optical turbulence . . . 86
2.1.5 Pointing errors . . . 109
2.1.6 Perturbed sky effects . . . 115
2.1.7 Receiver . . . 122
2.2 Link budget model for OFLs . . . 125
2.2.1 Downlink LEO OFL . . . 129
2.2.2 Uplink GEO OFL . . . 133
2.2.3 Dynamic downlink LEO OFL . . . 136
2.2.4 Impact of Link Distance Modeling on Beam Wander Estimation . . . 140
2.3 SNR models for OFLs . . . 145
2.3.1 Detection schemes . . . 147
2.3.2 Noise sources . . . 151
2.3.3 SNR for OOK OFLs . . . 158
2.3.4 SNR for coherent OFLs . . . 160

3 Experimental emulation of fading-affected OFLs **163**
3.1 Optical turbulence generators . . . 165
3.2 Fading generation algorithms . . . 170
3.2.1 Turbulence-induced fading generation . . . 173
3.2.2 Pointing jitter-induced fading generation . . . 176
3.3 Experimental testbed for OFLs emulation . . . 180
3.3.1 Poliba experimental testbed . . . 181
3.3.2 TeCIP experimental testbed . . . 187
3.4 Experimental results . . . 194
3.4.1 Poliba experimental campaigns . . . 195
3.4.2 TeCIP experimental campaign . . . 212

4 End-to-end modeling of OFLs exploiting digital mitigation techniques 219

4.1 Digital mitigation techniques 221

4.1.1 Forward error correction codes 221

4.1.2 Erasure codes 239

4.1.3 Interleaving 252

4.2 End-to-end OFL simulation framework 257

4.2.1 Physical layer abstraction 259

4.2.2 End-to-end OFL simulation framework: algorithm definition 272

4.2.3 Performance assessment of 100 Gbit/s coherent OFLs 275

4.3 Enhanced end-to-end OFL simulation framework with comprehensive packet-level EC modeling 285

4.3.1 EC-enabled protocol stack for OFLs 286

4.3.2 Enhanced end-to-end OFL simulation framework: algorithm definition 292

4.3.3 Performance assessment of 100 Gbit/s coherent OFLs 297

Conclusions 304

References 309

List of Tables

1.1 Major optical satellite communication missions 38
1.2 GOPEX transmitters characteristics 40
1.3 LCE specifications 43
1.4 KODEN specifications 50
1.5 TESAT LCT specifications 53
1.6 VSOTA specifications 65
1.7 LUCAS specifications 67

2.1 Coefficients of the KLN model 119
2.2 Link budget analysis for the downlink LEO OFL 131
2.3 Link budget analysis for the uplink GEO OFL 135
2.4 Beam wander parameters for the uplink GEO OFL 143

4.1 Summary of the main Consultative Committee for Space Data Systems (CCSDS) recommendations for high-data-rate optical satellite communications 234
4.2 CCSDS ad-hoc IRA codes parameters 248
4.3 Receiver parameters for the simulated LEO downlink OFL 279
4.4 Analyzed EC configurations 298

List of Figures

1.1 Global mobile network data traffic forecast (EB per month) 31
1.2 Next-generation integrated TN and NTN 3D network architecture . 32
1.3 EM spectrum 33
1.4 Trends in data rate for the EO satellites 34
1.5 Basic diagram of a FSO point-to-point link 35
1.6 Block diagram of LCE on the ETS-VI satellite 42
1.7 Block diagram of the SILEX terminals 45
1.8 Block diagram of the LUCE terminal 49
1.9 Block diagram of Alpha-Up breadboard 58
1.10 Exploded schematic view of the AeroCube-OCSD CubeSat 63
1.11 LCRD payload architecture 66
1.12 High-level block diagram of the TBIRD PTD-3 mission 72
1.13 Overview of the developed framework for the analysis and design of OFLs 75

2.1 OFL geometry 79
2.2 Amplitude profile of a Gaussian-beam wave 81
2.3 Diagram of the atmospheric layers 84
2.4 Atmospheric transmittance in a ground-to-space link at zenith. A rural aerosol model with a visibility of 23 km is considered 85
2.5 Energy cascade theory of turbulence 87
2.6 (a) C_n^2 profile as a function of altitude obtained with the HV model for different values of A and w (b) Comparison between the HV model and its modified version for $A = 1.7 \cdot 10^{-14}$ $\mathrm{m}^{-2/3}$, $w = 21$ m/s, and $h_{OGS} = 2300$ m 91

2.7 Downlink scintillation index as a function of the zenith angle for different turbulence regimes at $\lambda = 1.06$ μm 96
2.8 Downlink aperture-averaged scintillation index as a function of the receiver aperture diameter at $\lambda = 1.55$ μm 98
2.9 (a) Flattened beam profile as a function of the radial displacement r (b) Graphical representation of the beam wander-induced effective pointing error σ_{pe}. The dashed circle represents the RMS short-term spot size, W_{LT} is the long-term spot size, W_{ST} is the short-term spot size 99
2.10 Longitudinal scintillation index for a ground-to-space link as a function of beam radius according to (a) Rytov and (b) extended Rytov theories 101
2.11 Angular beam wander as a function of the transmitter beam radius for an uplink OFL at $\zeta = 90°$, $\lambda = 1.55$ μm, $A = 1.7 \cdot 10{-}14$ m$^{-2/3}$, $w = 21$ m/s 104
2.12 Absolute error between the flat-Earth and round-Earth link distance approximations as a function of the elevation angle, for an OFL between an OGS located at 2300-m altitude and a LEO satellite orbiting at 600 km 105
2.13 Short-term (dashed circle) and long-term (large circle) beam sizes . 108
2.14 Uplink (left) and downlink (right) acquisition process. Data link are represented with red arrows, while laser beacons are represented as orange cones 110
2.15 Geometry of point-ahead angle 112
2.16 Fog-induced specific attenuation as a function of visibility at $\lambda =$ 1.55 μm 117
2.17 Rain-induced specific attenuation as a function of rain rate 120
2.18 Snow-induced specific attenuation as a function of snowfall rate for wet (cyan curve) and dry (black curve) snow 121
2.19 SMF coupling efficiency as a function of (a) the number of speckles over the receiver aperture, and (b) the refractive index structure parameter at ground, considering $a = 1.12$ 125

2.20 Downlink received power for the KODEN experimental trial conducted on March 30, 2006 132
2.21 Downlink fiber coupling efficiency for the KODEN experimental campaign 133
2.22 Scintillation seen at the TDP1 as a function of the Fried's parameter measured at the T-AOGS 136
2.23 Link distance (black curve) and elevation angle (cyan curve) as a function of the time elapsed since the pass of the satellite for the dynamic downlink LEO OFL 137
2.24 Received optical power as a function of the elevation angle for the dynamic downlink LEO OFL 139
2.25 Received optical power as a function of the elevation angle for the KIODO trial on 14 June 2006 140
2.26 Scintillation index (black curve) and Fried's parameter (cyan curve) as a function of the elevation angle for the dynamic downlink LEO OFL 141
2.27 (a) Scintillation index and (b) OGS Fried's parameter as a function of the elevation angle for the KIODO trial on 14 June 2006 (KT3) . 142
2.28 (a) Beam wander variance, (b) angular beam wander, and (c) beam wander-induced loss as a function of the elevation angle for the uplink LEO OFL, evaluated considering the flat-Earth link distance approximation (black curve), the round-Earth link distance approximation (blue curve) and the exact link distance value (dashed cyan curve) 144
2.29 Block diagram of a FSO receiver chain 146

3.1 Fading time series generation method 171
3.2 Nonlinear transformation derivation 172
3.3 Scintillation-induced fading time series generation algorithm 176
3.4 Average jitter-induced pointing loss as a function of the rms pointing jitter for different transmitter aperture diameters 177
3.5 PSD of jitter-induced irradiance fluctuations 178
3.6 Pointing jitter-induced fading time series generation algorithm . . . 179

3.7 Scheme of the developed Poliba testbed for the emulation of scintillation- and pointing jitter-affected OFLs . . . 181
3.8 Scheme of the Poliba OTG calibration setup . . . 184
3.9 Laser spectrum . . . 185
3.10 VOA measured (a) transmission power and (b) attenuation as a function of applied control voltage . . . 186
3.11 VOA inverse calibration curve . . . 187
3.12 VOA measured transmission power as a function of set transmission power after calibration . . . 188
3.13 VOA sinusoidal control voltage over time before (black curve) and after (cyan curve) calibration . . . 189
3.14 (a) VOA output signal over time and (b) its spectrum with applied sinusoidal control voltage . . . 190
3.15 Scheme of the developed TeCIP testbed for the emulation of scintillation-affected OFLs . . . 191
3.16 VOA measured (a) transmission power and (b) attenuation as a function of applied control voltage . . . 192
3.17 VOA inverse calibration curve at (a) $\lambda = 1544.53$ nm and (b) $\lambda = 1545.32$ nm . . . 193
3.18 VOA measured attenuation as a function of set attenuation after calibration . . . 194
3.19 Percentage of Echo Replies lost packets as a function of the attenuation imposed on the link branch connecting the client PC to the server PC . . . 197
3.20 (a) Generated scintillation-affected time series of receiver power for the LEO downlink OFL as a function of time, together with (b) their histograms and theoretical lognormal PDF, and (c) their autocorrelation functions . . . 198
3.21 (a) Probability density functions and (b) autocorrelation functions for selected elevations in KT06-04. In (a), the bright green line marks the -3 dB threshold with respect to unity mean. In (b), the dashed red lines denote the 50% roll-offs . . . 199

3.22 Generated scintillation-affected time series of (a) attenuation and (b) control voltage for the LEO downlink OFL as a function of time. In (a), the green line marks the fading threshold 199
3.23 (a) Percentage of Echo Replies packet loss and (b) response time jitter as a function of the elevation angle for the emulated 10 GbE LEO downlink OFL 200
3.24 (a) Link distance (black curve), elevation angle (blue curve) and (b) slew rate as a function of time for the emulated downlink LEO OFL 201
3.25 Scintillation index as a function of (a) elevation angle and (b) time for the emulated downlink LEO OFL 203
3.26 (a) Scintillation correlation time and (b) bandwidth as a function of time for the emulated downlink LEO OFL 203
3.27 (a) Generated scintillation-affected time series of normalized received power as a function of time for the emulated LEO downlink OFL, together with (b) their histograms and theoretical lognormal PDFs, and (c) their PSDs 204
3.28 Generated time series of normalized received power as a function of time for the entire pass of the emulated LEO downlink OFL 205
3.29 Generated time series of (a) attenuation and (b) control voltage as a function of time for the emulated LEO downlink OFL. In (a), the green line marks the fading threshold 206
3.30 Frame error rate as a function of the elevation angle for the emulated 10GbE LEO downlink OFL 207
3.31 (a) Frame error rate and (b) outage probability as a function of the link margin for the emulated 10GbE LEO downlink OFL 208
3.32 (a) Link distance (black curve), elevation angle (blue curve) and (b) slew rate as a function of time for the emulated downlink LEO OFL 208
3.33 (a) Scintillation index and (b) correlation time as a function of time for the emulated downlink LEO OFL 209
3.34 Generated time series of normalized received power as a function of time for the entire pass of the emulated LEO downlink OFL 210

3.35 (a) Generated jitter-affected time series of normalized received power as a function of time for the emulated LEO downlink OFL, together with (b) their histograms and theoretical beta PDFs, and (c) their PSDs . . . 211
3.36 Generated time series of normalized received power as a function of time for the entire pass of the turbulence- and jitter-affected emulated LEO downlink OFL . . . 212
3.37 Frame error rate as a function of the rms pointing jitter for the emulated 10GbE LEO downlink OFL . . . 213
3.38 Pre-FEC BER as a function of the EDFA input power for the 10G (black curve) and 100G (cyan curve) links. The dashed lines mark the transceivers' sensitivity thresholds . . . 214
3.39 (a) Generated scintillation-affected time series of normalized received power as a function of time, together with (b) their histograms and theoretical lognormal PDFs . . . 215
3.40 Histograms of the generated and measured time series at $\sigma_I^2 = 0.01$ 216
3.41 Frame error rate as a function of the link margin for the emulated 10G IM/DD (solid lines) and 100G coherent (dashed lines) OFLs . 217

4.1 Block diagram of a FSO data transmission system employing channel coding . . . 223
4.2 Link scenarios showing possible optical)red) and RF (black) links . 233
4.3 Construction of a generic product code . . . 236
4.4 Graphical representation of erasure coding and decoding processes . 242
4.5 Interaction of the EC shim layer with adjacent layers . . . 249
4.6 EC processing . . . 250
4.7 Example of an ECLSA coding matrix . . . 251
4.8 LTP segment incapsulation into a UDP datagram via ECLSA . . . 252
4.9 Block interleaver . . . 253
4.10 Convolutional interleaver . . . 254
4.11 Block diagram of a CM communication system . . . 261
4.12 Block diagram of a BICM communication system . . . 262

4.13 CM MI and BICM GMI for (a) QPSK, (b) 8PSK, and (c) 16QAM modulation over the AWGN channel 271
4.14 NGMI as a function of the SNR for QPSK (black curve), 8PSK (cyan curve), and 16QAM (blue curve) modulation schemes over the AWGN channel 272
4.15 Schematic representation of the algorithm implemented in the end-to-end OFL simulation tool 274
4.16 (a) Link distance (black curve), elevation angle (blue curve) and (b) slew rate as a function of time for the simulated downlink LEO OFL 276
4.17 (a) Scintillation correlation time, (b) scintillation index, and (c) Fried's parameter as a function of time for the simulated downlink LEO OFL 277
4.18 Time series of normalized received optical power as a function of time for the simulated LEO downlink OFL at 30° elevation 278
4.19 NGMI as a function of the per-polarization received optical power at the EDFA input and OSNR 280
4.20 Unfaded optical power per polarization at the pre-amplifier input, as a function of the PHY-layer interleaver span, required to guarantee an outage probability below 10^{-3} for the simulated LEO downlink OFL at $\zeta = 30°$ 281
4.21 Illustration of the approach to model the impact of synchronization loss and re-synchronization time in the presence of deep fading events 281
4.22 Penalty in required unfaded optical power per polarization at the pre-amplifier input as a function of the re-synchronization time and synchronization loss threshold for the simulated LEO downlink OFL at $\zeta = 30°$. The analysis assumes a PHY-layer interleaver span of 70 ms 282
4.23 Average HL decoded PER as a function of the per-polarization unfaded received power at the EDFA input for the simulated LEO downlink OFL at $\zeta = 30°$. The analysis assumes oFEC channel coding without additional channel interleaver 283

4.24 Average HL decoded PER as a function of the per-polarization unfaded received power at the EDFA input for the simulated LEO downlink OFL at $\zeta = 30°$. The analysis assumes channel coding rates of 0.55, 0.77, and 0.79, respectively combined with HL EC rates of 0.91, 0.64, and 0.51 with a HL 70-ms interleaver 284
4.25 Transmitter protocol stack showing the EC shim layer operation and OTN encapsulation process for a 100 Gbit/s OFL 287
4.26 Ethernet packet format 288
4.27 Ethernet info frames encapsulation process via the EC shim layer . 289
4.28 CGMII data stream 290
4.29 OPU frame structure 291
4.30 PHY-layer processing 292
4.31 High-level representation of the workflow implemented in the enhanced end-to-end OFL simulation tool 293
4.32 EC codeword transmission time as a function of the EC configuration ID. The plot assumes a "lower" MAC client data length equal to 1500 bytes. The dashed-cyan curve corresponds to the LEO downlink OFL channel correlation time at $\zeta = 30°$ 298
4.33 Required average power at the receiver to guarantee an error-free OFL as a function of the EC configuration ID, for the LEO downlink OFL at $\zeta = 30°$. The plot assumes a "lower" MAC client data length equal to 1500 bytes 299
4.34 Percentage of (a) IT and (b) ML decoded EC codewords as a function of the unfaded received optical power for the LEO downlink OFL at $\zeta = 30°$. The plot assumes a "lower" MAC client data length equal to 1500 bytes 300
4.35 Post-EC FER as a function of the unfaded received optical power for the LEO downlink OFL at $\zeta = 30°$. The plot assumes a "lower" MAC client data length equal to 1500 bytes 300
4.36 EC codeword transmission time as a function of "lower" MAC client data length. The plot assumes EC ID = 9. The dashed-cyan curve corresponds to the LEO downlink OFL channel correlation time at $\zeta = 30°$ 301

4.37 Required average power at the receiver to guarantee an error-free OFL as a function of the "lower" MAC client data length, for the LEO downlink OFL at $\zeta = 30°$. The plot assumes EC ID = 9 . . . 302
4.38 Post-EC FER as a function of the unfaded received optical power for the LEO downlink OFL at $\zeta = 30°$. The plot assumes "lower" MAC client data lengths equal to 1500 bytes (black curve), 2500 bytes (blue curve), and 9000 bytes (cyan curve) 302

List of Abbreviations

16QAM 16-ary Quadrature Amplitude Modulation

2-PPM 2-Pulse Position Modulation

3D Three-Dimensional

4QD Four-Quadrant Detector

5G Fifth-Generation

6G Sixth-Generation

A-OGS Adaptive Optical Ground Station

ABL Atmospheric Boundary Layer

ACS Attitude Control System

ADU Application Data Unit

ALOS-4 Advanced Land Observing Satellite-4

AO Adaptive Optics

APD Avalanche Photodiode

ARQ Automatic Repeat reQuest

ARTEMIS Advanced Relay and Technology Mission Satellite

ASE Amplified Spontaneous Emission

ATP Acquisition, Tracking, and Pointing

AUDE Alpha-up and Down Experiment

AWG Arbitrary Waveform Generator

AWGN Additive White Gaussian Noise

B5G Beyond Fifth-Generation

BCH Bose, Chaudhari, and Hocquenghe

BER Bit Error Rate

BICM Bit-Interleaved Coded Modulation

BICM-ID Bit-Interleaved Coded Modulation with Iterative Decoding/Demapping

BiROS Bispectral Infrared Optical System

BMP Bit-suynchronous Mapping Procedure

BP Bundle Protocol

BPSK Binary Phase-Shift Keying

BRGC Binary Reflected Gray Code

CARO Cassegrain Adaptive Receiver Optics

CCD Charge-Coupled Device

CCSDS Consultative Committee for Space Data Systems

CLICK Laser Infrared CrosslinK

CM Coded Modulation

CNES National Center for Space Studies

COTS Commercial Off-The-Shelf

CPA Coarse Pointing Assembly

CPolSK Circular Polarization Shift Keying

CRC Cyclic Redundancy Check

CRL Communications Research Laboratory

CSA Canadian Space Agency

CubeCAT CubeSat Communication Active Terminal

CW Continuous Wave

DCO Digital Coherent Optics

DLR German Aerospace Center

DM Deformable Mirror

DP-16QAM Dual-Polarization 16-ary Quadrature Amplitude Modulation

DP-QPSK Dual-Polarization Quadrature Phase-Shift Keying

DPSK Differential Phase-Shift Keying

DQPSK Differential Quadrature Phase-Shift Keying

DRU Data Redundancy Unit

DSP Digital Signal Processing

DTE Direct-to-Earth

DTN Delay/Disruption Tolerant Network

DVB-S2 Digital Video Broadcasting–Satellite Second Generation

EC Erasure Code

ECDU Erasure Coding Data Unit

ECLSA Erasure Coding Link Service Adapter

ECLSI Erasure Coding Link Service Induct

ECLSO Erasure Coding Link Service Outduct

EDFA Erbium-Doped Fibre Amplifier

EDRS European Data Relay System

EM Electromagnetic

EO Earth Observation

ESA European Space Agency

ESM Effective SNR Mapping

ESTOL ESA Specification for Terabit/sec Optical Links

ETS-VI Engineering Test Satellite-VI

EXIT Extrinsic Information Transfer

F-IRA Flexible IRA

FCS Frame Check Sequence

FEC Forward Error Correction

FER Frame Error Rate

FFT Fast Fourier Transform

FLP Flying Laptop

FOV Field of View

FPM Fine Pointing Mirror

FrOGS French Optical Ground Station

FSO Free Space Optics

FWHM Full-Width at Half Maximum

GEO Geostationary Earth Orbit

GH Gauss-Hermite

GMI Generalized Mutual Information

GMP Generic Mapping Procedure

GOLD Ground/Orbiter Lasercomm Demonstration

GOPEX Galileo Optical Experiment

HAP Hufnagel-Andrews-Phillips

HAP High-Altitude Platform

HD Hard Decision

HICALI HIgh-speed Communication with Advanced Laser Instrument

HL Higher Layer

HV Hufnagel-Valley

HY-2 Haiyang-2

HydRON High thRoughput Optical Network

IAC Instituto de Astrofisica de Canarias

ICMP Internet Control Message Protocol

IF Intermediate Frequency

ILLUMINA-T Integrated LCRD Low Earth Orbit User Modem and Amplifier Terminal

IM/DD Intentisy Modulation/Direct Detection

IoE Internet of Everything

ION Interplanetary Overlay Network

IP Internet Protocol

IR Infrared

IRA Irregular Repeat-Accumulate

ISARA Integrated Solar Array and Reflectarray Antenna

ISS International Space Station

IT Iterative

ITU International Telecommunication Union

JAXA Japan Aerospace Exploration Agency

JPL Jet Propulsion Laboratory

KIODO Kirari's Optical Downlink to Oberpfaffenhofen

KODEN Kirari Optical Communication Demonstration Experiments with the NICT OGS

LC Liquid Crystal

LCE Laser Communication Equipment

LCRD Laser Communications Relay Demonstration

LCT Laser Communication Terminal

LDGM Low-Density Generator-Matrix

LDPC Low Density Parity-Check

LEO Low Earth Orbit

LLR Log-Likelihood Ratio

LO Local Oscillator

LoS Line-of-Sight

LSA Link Service Adapter

LTP Licklider Transmission Protocol

LUCAS Laser Utilizing Communication System

LUCE Laser Utilizing Communication Equipment

MAC Media Access Control

MAP Maximum A Posteriori

MCLCD Micius Coherent Laser Communication Demonstration

MDS Maximum Distance Separable

MEMS Micro Electro Mechanical Systems

MEMs Micro-Electromechanical

MEO Medium Earth Orbit

MI Mutual Information

MII Media Independent Interface

ML Maximum-Likelihood

ML-P Maximum-Likelihood Pivoting

MPE Maximum Permissible Exposure

MSA Multi-Source Agreement

MVE Micro Vibration Measurement Equipment

NASA National Aeronautics and Space Administration

NEP Noise Equivalent Power

NFIRE Near Field Infrared Experiment

NGMI Normalized Generalized Mutual Information

NGSO Non-Geostationary Orbit

NIC Network Interface Card

NICT National Institute of Information and Communications Technology

NIM Near-Index-Matching

NITech Nagoya Institute of Technology

Nmap Network mapper

NR New Radio

NRZ Non-Return to Zero

NTN Non-Terrestrial Network

OCSD Optical Communications and Sensor Demonstration

OCTL Optical Communications Telescope Laboratory

OFBG oFEC Block Group

oFEC open FEC

OFL Optical Feeder Link

OGS Optical Ground Station

OGS-OP Optical Ground Station Oberpfaffenhofen

OICETS Optical Intersatellite Communication Engineering Test Satellite

OISL Optical Inter-Satellite Link

OOK On-Off Keying

OPALS Optical PAyload for Lasercomm Science

OSA Optical Spectrum Analyzer

OSIRIS Optical Space Infrared Downlink System

OSNR Optical Signal-to-Noise Ratio

OTG Optical Turbulence Generator

OTN Optical Transport Network

OWC Optical Wireless Communication

PAA Point-Ahead Angle

PAM Pulse-Amplitude Modulation

PAM Point-Ahead Mechanism

PCB Printed Circuit Board

PCS Physical Coding Sublayer

PDF Probability Density Function

PDU Protocol Data Unit

PEC Packet Erasure Channel

PER Packet Error Rate

PGZ Peterson-Gorenstein-Zierler

PHY Physical layer

PIN Positive-Intrinsic-Negative

PLL Phased-Locked Loop

PMF Probability Mass Function

PN Pseudorandom Noise

Poliba Polytechnic University of Bari

PSD Power Spectral Density

PSK Phase-Shift Keying

PTD-3 Pathfinder Technology Demonstrator-3

PULSE-A Polarization-modUlated Laser Satellite Experiment

QAM Quadrature Amplitude Modulation

QC-LDPC Quasi-Cyclic LDPC

QD Quadrant Detector

QKD Quantum Key Distribution

QoS Quality of Serive

QPSK Quadrature Phase-Shift Keying

RF Radiofrequency

RIN Relative Intensity Noise

RISESAT Rapid International Scientific Experiment Satellite

rms Root Mean Square

RS Reed Solomon

RS Reconciliation Sublayer

RS-PC RS Product Code

RTT Round-Trip Time

SatComs Satellite Communications

SCCC Serially Concatenated Convolutional Code

SCIDAR Scintillation Detection and Ranging

SD Soft Decision

SDA Space Development Agency

SDU Service Data Unit

SER Symbol Error Rate

SFD Start Frame Delimiter

SFP+ Small Form-factor Pluggable Plus

SGP4 Simplified General Perturbations 4

SILEX Semiconductor Laser Inter-Satellite Link Experiment

SISO Soft-Input Soft-Output

SLM Spatial Light Modulator

SMF Single-Mode Fibre

SNR Signal-to-Noise Ratio

SOCRATES Space Optical Communications Research Advanced Technology Satellite

SOR Starfire Optical Range

SOTA Small Optical TrAnsponder

SR Strehl Ratio

SWaP Size, Weight, and Power

T-AOGS Tansportable Adaptive Optics Ground Station

TBIRD TeraByte InfraRed Delivery

TDP1 Technology Demonstrator Payload 1

TeCIP Telecommunications, Computer Engineering, and Photonics Institute

THz Terahertz

TLE Two-Line Element

TMF Table Mountain Facility

TN Terrestrial Network

UAV Unmanned Aerial Vehicle

UDP User Datagram Protocol

UV Ultraviolet

VDR Variable Data Rate

VHTS Very High Throughput Satellite

VL Visible Light

VOA Variable Optical Attenuator

VSOTA Very Small Optical Transponder

WDM Wavelength Division Multiplexing

WFS Wavefront Sensor

Introduction

The rapid evolution of Beyond Fifth-Generation (B5G) and Sixth-Generation (6G) communication systems is driving the development of a new networking paradigm in which terrestrial and non-terrestrial infrastructures operate as a unified ecosystem. In this vision, satellites, High-Altitude Platforms (HAPs), and Unmanned Aerial Vehicles (UAVs) complement terrestrial optical fiber and wireless networks, enabling ubiquitous connectivity, global service availability, and improved network resilience. Such an integrated architecture is expected to support the unprecedented traffic demands generated by emerging applications.

Within this context, Optical Wireless Communications (OWCs), and in particular Free-Space Optics (FSO), have emerged as a promising technology to overcome the limitations of conventional radio-frequency feeder links. By exploiting the vast unlicensed optical spectrum, FSO systems can provide data rates ranging from several tens to hundreds of Gigabits per second while benefiting from reduced size, weight, and power requirements, high directivity, and enhanced communication security. Optical Feeder Links (OFLs), connecting Optical Ground Stations (OGSs) with satellites, are therefore regarded as one of the key enabling technologies for extending the terrestrial optical transport network into space and for realizing the "fiber-through-the-air" paradigm envisioned for future integrated terrestrial and non-terrestrial networks.

Despite their remarkable potential, the deployment of OFLs poses several technological challenges. Unlike optical inter-satellite links, OFLs propagate through the Earth's atmosphere and are therefore affected by absorption, scattering, atmospheric turbulence, and adverse weather conditions. These phenomena, coupled with the strict pointing requirements, introduce random fluctuations of the received optical power, potentially degrading communication reliability and reducing

link availability. Moreover, the dynamic nature of Low Earth Orbit (LEO) satellite systems further complicates system design, as channel conditions continuously evolve during each satellite pass. Consequently, the successful implementation of OFLs requires accurate propagation models, reliable design methodologies, realistic experimental validation techniques, and effective mitigation strategies capable of guaranteeing high communication reliability under varying operating conditions.

Although significant progress has been achieved in recent years, many existing research efforts focus on specific aspects of OFLs, such as propagation modeling, experimental demonstrations, or communication techniques, often treating them independently. Conversely, the design of practical OFLs requires a comprehensive approach capable of linking the physical characterization of the optical channel with the evaluation of actual link performance.

This thesis has been developed following this perspective. Its primary objective is to provide methodologies and tools supporting the analysis, design, and optimization of OFLs for next-generation networks. To this end, the research combines theoretical modeling, numerical simulations, laboratory experimentation, and end-to-end communication performance evaluation.

The first objective of the thesis is to develop accurate numerical tools capable of evaluating OFL performance under realistic propagation conditions. Particular attention is devoted to the comprehensive modeling of the physical phenomena affecting optical propagation through the atmosphere and to improving the accuracy of conventional link budget analyses.

The second objective is the experimental investigation of OFLs employing commercial optical networking equipment. Since in-orbit experimental campaigns are inherently expensive and difficult to reproduce, laboratory emulation techniques are developed to realistically emulate turbulence- and jitter-induced fading under controlled conditions. These experimental platforms enable the performance assessment of Commercial Off-The-Shelf (COTS) fiber-optic transceivers operating over atmospheric optical channels.

Finally, the thesis investigates digital techniques aimed at improving communication reliability in the presence of atmospheric impairments. To this purpose, end-to-end simulation frameworks are developed to jointly model the physical layer and higher communication layers, allowing the effectiveness of advanced digital

mitigation techniques, such as packet-level erasure coding and interleaving, to be evaluated under realistic OFL operating conditions.

Overall, the original contribution of this work lies in the development of an integrated framework for OFL analysis that combines accurate physical-layer modeling, realistic experimental emulation, and end-to-end communication system evaluation. Rather than addressing these aspects independently, the proposed methodologies provide complementary tools that support the design and optimization of OFLs.

The remainder of this dissertation is organized as follows.

Chapter 1 introduces the fundamentals of OFLs and reviews the state of the art of optical satellite communications. The main characteristics, advantages, and challenges of OFLs are discussed, with particular emphasis on atmospheric propagation impairments, optical communication technologies, and the role of OFLs within future integrated terrestrial and non-terrestrial network architectures.

At the end of the chapter, an overview of the developed tools is provided.

Chapter 2 presents a comprehensive numerical framework for OFL link budget analysis. After reviewing the main propagation phenomena affecting optical links, the related mathematical models are introduced and integrated into a flexible simulation tool. The framework is validated against experimental results available in the literature, and its capabilities are exploited to investigate the limitations of the conventional beam wander model, leading to a more accurate estimation of propagation losses and link margins.

Chapter 3 focuses on the experimental investigation of turbulence- and jitter-impaired OFLs. Compact laboratory testbeds based on variable optical attenuators are developed to emulate atmospheric fading under controlled conditions. Efficient algorithms are proposed to reproduce both the statistical and temporal characteristics of turbulence-induced scintillation and pointing jitter experienced by LEO satellite links. The developed platforms are then employed to experimentally assess the performance of commercial optical transceivers under realistic atmospheric impairments.

Chapter 4 addresses the performance optimization of OFLs from a communication perspective. End-to-end simulation frameworks are developed to evaluate

the interaction between atmospheric fading, channel coding, and higher-layer digital mitigation strategies. Particular attention is devoted to packet-level erasure coding, interleaving, and their joint optimization with channel coding to improve communication reliability over turbulence-impaired links.

Finally, the conclusions summarize the main achievements, highlight the research's original contributions, and discuss possible future research directions toward the realization of reliable, high-capacity OFLs for next-generation integrated terrestrial and non-terrestrial communication networks.

List of publications

Journal articles

j1 **C. Cantore**, D. Monopoli, A. Altamura, et al., "Link budget analysis of bi-directional LEO and GEO optical feeder links advancing the beam wander model's accuracy," in *Scientific Reports*, vol. 14, no. 8579, 2024, doi: https://doi.org/10.1038/s41598-024-59198-x.

j2 I. Marasco, **C. Cantore**, G. V. Bianco, G. Bruno, A. D'Orazio and G. Magno, "Transparent Graphene-Based RIS for 6G Communications in the THz Spectrum," in *IEEE Open Journal of Antennas and Propagation*, vol. 6, no. 1, pp. 193-200, Feb. 2025, doi: 10.1109/OJAP.2024.3487793.

j3 E. Boffetti, I. Marasco, **C. Cantore**, et al., "In-Flight Pose and Electromagnetic Experimental Characterization of UAV-Mounted Metasurfaces for Next-Generation Indoor Wireless Systems," in *IEEE Internet of Things Journal*, vol. 12, no. 20, pp. 43130-43142, 15 Oct.15, 2025, doi: 10.1109/JIOT.2025.3595391.

Conference proceedings

c1 **C. Cantore**, D. Monopoli, A. Altamura, A. Mengali and M. Grande, "An accurate and efficient numerical tool for the analysis and design of optical feeder links," *2023 IEEE 10th International Workshop on Metrology for AeroSpace (MetroAeroSpace)*, Milan, Italy, 2023, pp. 534-539, doi: 10.1109/MetroAeroSpace57412.2023.10189928.

c2 G. Magno, I. Marasco, **C. Cantore**, M. Grande, G. V. Bianco and G. Bruno, "Programmable Graphene Metasurfaces for Smart Windows: achieving transparency and control," *2023 IEEE Conference on Antenna Measurements and Applications (CAMA)*, Genoa, Italy, 2023, pp. 924-926, doi: 10.1109/CAMA57522.2023.10352822.

c3 **C. Cantore**, I. Marasco, D. Monopoli and G. Magno, "Reconfigurable Fading Testbed for the Investigation of COTS Transceivers in OFLs," *2024 11th International Workshop on Metrology for AeroSpace (MetroAeroSpace)*, Lublin, Poland, 2024, pp. 315-320, doi: 10.1109/MetroAero Space 61015. 2024. 10591579.

c4 I. Marasco, **C. Cantore**, A. D'Orazio and G. Magno, "Design and analysis of a graphene-based metasurface modulator for 6G wireless communications," *2024 24th International Conference on Transparent Optical Networks (ICTON)*, Bari, Italy, 2024, pp. 1-5, doi: 10.1109/ICTON62926. 2024. 10647238.

c5 D. Monopoli, **C. Cantore**, G. Magno and A. D'Orazio, "BPM-based atmospheric turbulence propagator for optical ground-to-space links through extended Rayleigh Sommerfield theory and phase screen generation," *2024 24th International Conference on Transparent Optical Networks (ICTON)*, Bari, Italy, 2024, pp. 1-4, doi: 10.1109/ICTON62926.2024.10647985.

c6 S. Basu, L. Oliviero, G. Cossu, **C. Cantore**, A. D'Orazio and E. Ciaramella, "Prospects of Optical Wireless Communications in Non-Terrestrial Networks," *2024 24th International Conference on Transparent Optical Networks (ICTON)*, Bari, Italy, 2024, pp. 1-4, doi: 10.1109/ICTON62926.2024. 10647761.

c7 **C. Cantore**, I. Marasco, D. Monopoli, G. Magno and A. D'Orazio, "Laboratory emulation of LEO downlink optical feeder link employing commercial transceivers," *2024 24th International Conference on Transparent Optical Networks (ICTON)*, Bari, Italy, 2024, pp. 1-4, doi: 10.1109/ICTON62926. 2024. 10647497.

c8 **C. Cantore** et al., "Experimental Evaluation of Commercial OTN Transcei -vers under Emulated Weak Turbulence," *2025 International Conference on Optical Network Design and Modeling (ONDM)*, Pisa, Italy, 2025, pp. 1-3, doi: 10.23919/ONDM65745.2025.11029368.

c9 I. Marasco, **C. Cantore**, D. Monopoli and G. Magno, "Experimental Emulation of LEO Downlink OFLs Affected by Turbulence and Pointing Jitter," 2025 IEEE 12th International Workshop on Metrology for AeroSpace (MetroAeroSpace), Naples, Italy, 2025, pp. 239-244, doi: 10.1109/MetroAero Space64938.2025.11114550.

c10 **C. Cantore**, G. Magno and I. Marasco, "Metasurfaces for Transmission and Reflection in Next-Generation Communication Systems," *2025 25th Anniversary International Conference on Transparent Optical Networks (ICTON)*, Barcelona, Spain, 2025, pp. 1-4, doi: 10.1109/ICTON67126.2025.11125151.

c11 **C. Cantore**, I. Marasco, G. Magno and A. D'Orazio, "Toward UAV-Aided RIS Communications," *2025 25th Anniversary International Conference on Transparent Optical Networks (ICTON)*, Barcelona, Spain, 2025, pp. 1-4, doi: 10.1109/ICTON67126.2025.11125194.

c12 **C. Cantore**, I. Marasco, D. Monopoli, et al., "Experimental laboratory emulation of turbulence-induced fading affecting optical feeder links," *Proceedings of SPIE 13699, International Conference on Space Optics — ICSO 2024*, 136996G, 28 Jul 2025, doi: https://doi.org/10.1117/12.3075363.

c13 D. Monopoli, **C. Cantore**, A. Altamura, et al., "Emulation of ground-space optical link propagation based on multilayer turbulence models," *Proceedings of SPIE 13699, International Conference on Space Optics — ICSO 2024*, 136996F, 28 Jul 2025, doi: https://doi.org/10.1117/12.3075362.

Chapter 1

Optical Links for Integrated TNs and NTNs

The exponential growth of bandwidth-intensive services and the proliferation of emerging applications, such as holographic communications, digital twins, tactile Internet, enhanced on-board communications, and Internet of Everything (IoE), is driving an unprecedented demand for higher data rates, larger capacities, and ubiquitous connectivity [1]. As shown in Fig. 1.1, Ericsson forecasters expect global mobile data traffic to continue to increase explosively, reaching 482 Exabytes per month in 2031 [2].

In this scenario, current terrestrial telecommunication infrastructures, mainly relying on optical fiber and Radiofrequency (RF) wireless technologies, are approaching their intrinsic limits. Specifically, RF-based mobile networks face spectrum congestion, regulatory constraints, and interference issues. Moreover, the lack of telecommunication infrastructures in remote, rural, and developing regions, where fiber or terrestrial wireless connections are impractical, makes Terrestrial Networks (TNs) unable to provide global coverage.

As a result, the future Beyond Fifth-Generation (B5G) and Sixth-Generation (6G) networks are envisioned to build upon a novel paradigm, i.e., the seamless integration of TNs and Non-Terrestrial Networks (NTNs), giving rise to a Three-Dimensional (3D) architecture capable of ensuring global, resilient, high-capacity connectivity [3–5]. As depicted in Fig. 1.2, NTNs including satellites in Low Earth Orbit (LEO), Medium Earth Orbit (MEO), and Geostationary Earth Orbit (GEO), as well as aerial platforms, such as Unmanned Aerial Vehicles (UAVs) and

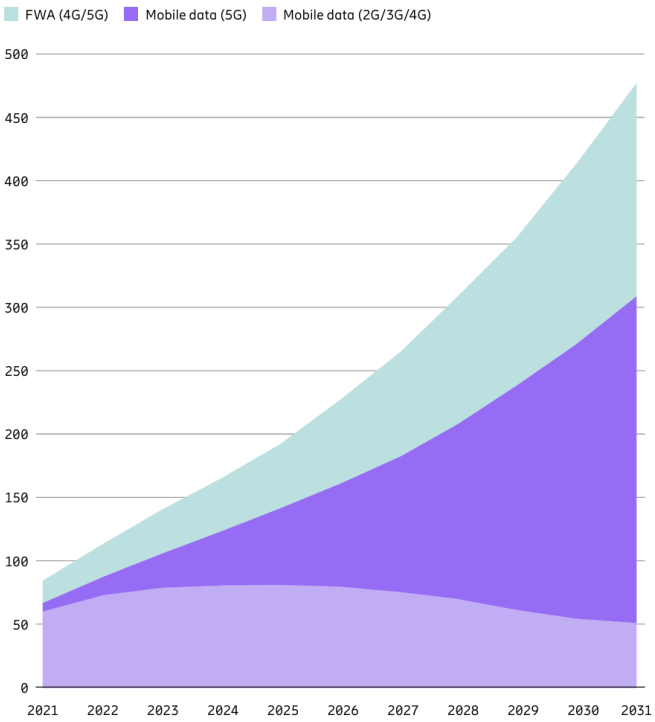


Figure 1.1 – Global mobile network data traffic forecast (EB per month) [2]

High-Altitude Platforms (HAPs), will complement terrestrial infrastructures by extending coverage to remote areas, blind spots, ships, and airplanes. Moreover, in the event of natural disasters, space-air networks can swiftly provide high-speed and stable connections, thus improving the network flexibility and resilience at reduced costs [5].

Thanks to this novel paradigm, Satellite Communications (SatComs) are evolving with respect to traditional applications such as television broadcasting, remote sensing, and navigation, where they used to act as a standalone system. On the contrary, they now represent a crucial element to make the ubiquitous availability of Internet services a reality, implying a notable social impact and taking a step forward in bridging the digital divide.

Historically, GEO has been the preferred orbit for commercial space-based communication systems. This choice mainly stems from the fixed GEO satellite position with respect to the Earth and from the intrinsic wide coverage. However, links from ground to GEO satellites suffer from higher latencies with respect to

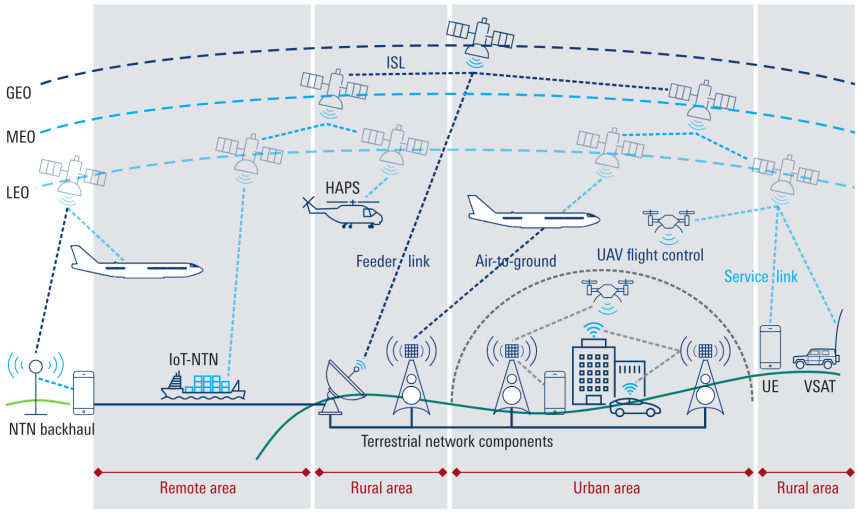


Figure 1.2 – Next-generation integrated TN and NTN 3D network architecture [6]

links involving Non-Geostationary Orbit (NGSO) platforms, as well as from poorer signal quality in terms of average received power. Consequently, the industry interest toward constellations of LEO satellites orbiting at altitudes below 2000 km increased. Indeed, lower latencies and reduced losses make them appealing candidates to provide low-latency, high-speed connectivity [7–9]. Moreover, LEO satellites benefit from lower production and launch costs. These advantages led, in recent years, to the planning and launch of mega-constellations of NGSO satellites specifically designed to provide communication services, such as Starlink, Lightspeed, OneWeb, and Amazon LEO [8, 10, 11]. Nonetheless, the dynamic nature of such constellations creates unique challenges with respect to their end-to-end performance optimization. Indeed, variable channel conditions are experienced due to the relative movement between the LEO satellite and ground terminal.

Within this integrated architecture, communication technologies operating at higher frequencies, where significantly wider bandwidths are available, can be adopted to tackle the expected massive traffic demand [5]. In this respect, Optical Wireless Communications (OWCs), operating in the Infrared (IR), Visible Light (VL), and Ultraviolet (UV) bands of the Electromagnetic (EM) spectrum as shown in Fig. 1.3, have attracted considerable attention as a promising solution to overcome the limitations of RF systems [5, 12]. Among optical wireless technologies,

Free Space Optics (FSO), which mainly operates in the IR region, is capable of long- and ultra-long-distance data transmission. By exploiting several Terahertz (THz) of unlicensed optical spectrum, FSO links can provide extremely high data rates, making them a key enabler for the realization of the so-called "fiber-through-the-air" paradigm [13, 14]. By implementing FSO links within satellite systems, high-speed connectivity could be extended to areas not reachable by fiber optics due to high cost limitations and topographical impediments [15, 16]. In addition, FSO is among the candidate technologies to address the last mile access problem, as well as to implement high-capacity backhauls in next-generation wireless networks [1, 17–19].

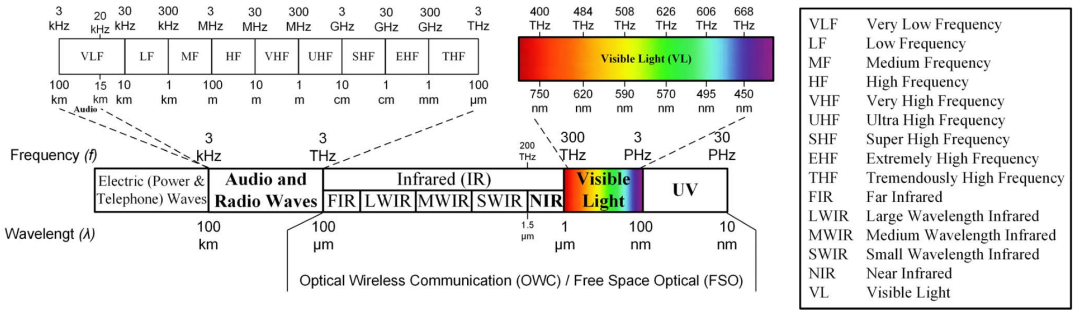


Figure 1.3 – EM spectrum [20]

A fundamental role in this vision is played by Optical Feeder Links (OFLs), which establish high-capacity bidirectional connections between Optical Ground Stations (OGSs) and satellites, seamlessly interconnecting terrestrial and space segments. Together with Optical Inter-Satellite Links (OISLs), OFLs constitute the backbone of emerging space-based optical network architectures, as also envisaged by the European Space Agency (ESA)'s High thRoughput Optical Network (HydRON) initiative. The latter aims at developing a global all-optical high-capacity transport network by deploying OISLs and OFLs to extend the terrestrial optical transport network into space [21].

Direct-to-Earth (DTE) OFLs from LEO satellites have also been considered as a solution to burst the huge amount of data collected by Earth Observation (EO) payloads to ground [15]. Indeed, EO sensors are marked by ever-increasing resolutions, frequencies, and areas of observation. Thus, the amount of acquired

information has seen a dramatic increase during the years, as highlighted in Fig. 1.4 [22]. High-data-rates DTE links are thus necessary to download these data during the short visibility time of LEO satellites.

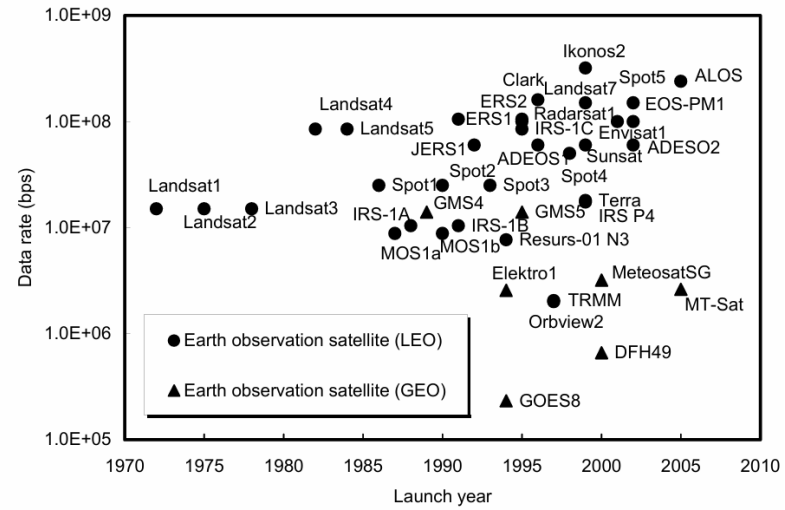


Figure 1.4 – Trends in data rate for the EO satellites [22]

1.1 OFLs: Advantages and challenges

FSO is an OWC technology based on the Line-of-Sight (LoS) transmission of modulated optical beams through an unguided medium, namely free space and/or the atmosphere, to convey information between a transmitter and a receiver. As depicted in the basic scheme of Fig. 1.5, in a typical FSO system, the information signal is modulated onto an optical carrier generated by a laser source, collimated through a transmitting telescope, and propagated through the channel toward the receiver, where it is collected, focused onto a photodetector, and converted back into the electrical domain for signal recovery. When such a link is established between an OGS and a satellite, it is referred to as an OFL. In this case, the propagation channel is inherently hybrid, consisting of both atmospheric and free-space segments, and the link can operate in two directions, i.e., uplink, or ground-to-space, and downlink, or space-to-ground, which exhibit different propagation characteristics due to the asymmetry of the propagation path. Indeed,

an uplink beam travels first across the atmosphere and then through free space, as opposed to a downlink one, which gets spread due to beam divergence before reaching the atmosphere.

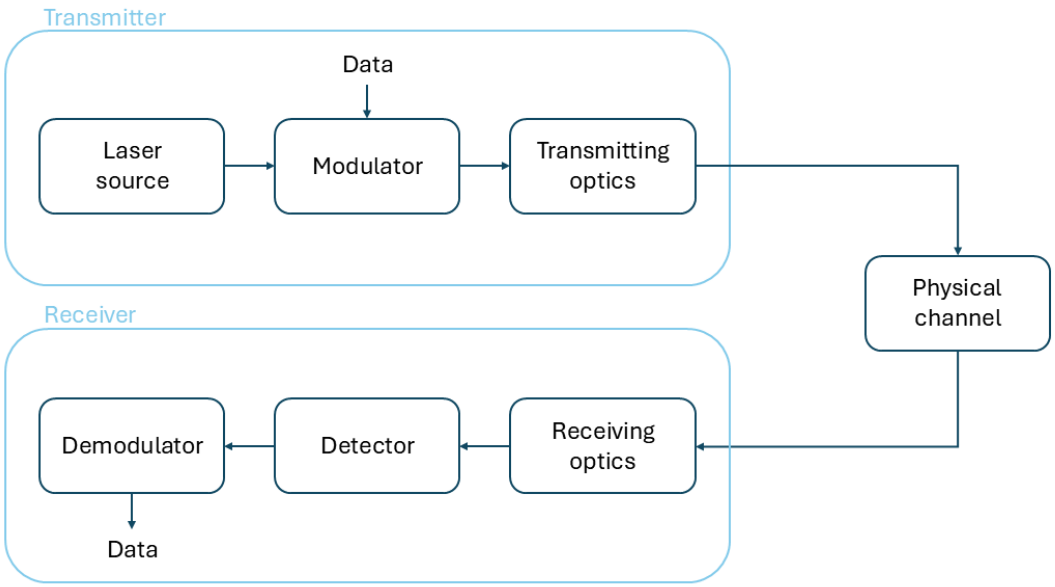


Figure 1.5 – Basic diagram of a FSO point-to-point link

OFLs are key enablers of future integrated TN and NTN networks, as they allow the extension of high-capacity optical fiber infrastructures into space. Compared to conventional RF feeder links, optical solutions offer several notable advantages [1, 14, 23, 24], i.e.:

- The optical domain provides an enormous amount of unlicensed spectral bandwidth, in the order of Terahertz, enabling data rates that can reach hundreds of Gigabits-per-second and even Terabit-per-second regimes when combined with advanced techniques such as Wavelength Division Multiplexing (WDM). This capability directly addresses the spectrum scarcity affecting RF systems.

- Optical carriers are characterized by significantly lower beam divergence, which results in higher received power density for a given transmitted power and enhances communication security by reducing the probability of interception and jamming.

- Optical terminals feature lower Size, Weight, and Power (SWaP) than RF ones, making them particularly attractive for spaceborne platforms.

- FSO systems can leverage mature technologies developed for fiber-optic communications, speeding up the short-term OFLs deployment at reduced costs. Specifically, by exploiting mature concepts such as WDM and coherent modulations, these links have the potential to achieve Terabit-per-second throughputs via a single OGS, thus reducing the complexity and cost of the ground station network with respect to the RF infrastructure.

Despite these advantages, OFLs pose several technical challenges, primarily associated with the propagation of optical signals through the Earth's atmosphere, which represents the main performance-limiting factor. Unlike OISLs, which operate entirely in free space, OFLs are affected by a variety of atmospheric impairments, including absorption and scattering, as well as hydrometeors such as fog, clouds, rain, and snow, which can introduce significant attenuation and lead to temporary link outages. Among all impairments, atmospheric turbulence is particularly detrimental. It arises from random fluctuations of the refractive index caused by temperature and pressure variations and induces stochastic distortions on the propagating wavefront. As a consequence, the received optical signal experiences phenomena such as beam spreading, beam wander, and scintillation, resulting in random fluctuations of the received power over time. These fluctuations translate into fading, which may cause bursts of errors and degrade link reliability, especially at high data rates.

Additional challenges stem from the highly directional nature of optical beams. While narrow beam divergence is beneficial in terms of efficiency and security, it also requires extremely accurate pointing, acquisition, and tracking mechanisms to maintain alignment between transmitter and receiver. Pointing errors, caused by mechanical vibrations, tracking inaccuracies, or turbulence-induced beam wander, can significantly reduce the collected optical power and contribute to random power fading.

In the optical domain, aperture averaging and Adaptive Optics (AO) systems can be exploited at the receiver to reduce the impact of turbulence. Specifically, aperture averaging consists in increasing the receiver telescope aperture so as to

average out small-scale irradiance fluctuations. Instead, building on image stabilization, AO performs closed-loop wavefront corrections.

In a complementary manner, digital mitigation techniques including Forward Error Correction (FEC) codes, Erasure Codes (ECs), Automatic Repeat reQuest (ARQ) protocols, and interleaving techniques can be adopted [25]. Among them, packet-level erasure coding schemes, implemented at Higher Layers (HLs) than the physical one, represent a promising solution to correct residual bit errors. Indeed, with respect to channel coding and interleaving, they do not require modifying the underlying Physical layer (PHY). Consequently, they can be implemented on top of existing transceivers to correct residual errors [26].

1.2 Optical satellite links: State-of-the-art

In recent decades, space-based optical communication has evolved from early experimental demonstrations into a rapidly advancing field driven by both institutional and commercial interest. Initial proof-of-concept missions, dating back to the 1990s, established the feasibility of optical downlinks and marked the beginning of sustained research into laser SatComs. Since then, a growing number of in-orbit demonstrations and technology validation programs have been conducted.

More recently, the development of dedicated payloads and operational systems has accelerated significantly, with space agencies and private companies investing in increasingly complex architectures. These efforts aim to address the growing demand for high-data-rate, secure, and spectrum-efficient communication infrastructures in space.

This section provides a review of key missions, highlighting major technological milestones and the evolution of optical communication capabilities in space. These are summarized in Table 1.1, which underlines the progressive increase in link complexity, data rate, and system maturity.

Table 1.1 – Major optical satellite communication missions

Mission	**Year**	**Link**	**Wavelength**	**Modulation**	**Data Rate**	**Key Technologies**
ETS-VI (LCE)	1994	GEO–Ground	830 nm DL, 514.5 nm UL	IM/DD	1.024 Mb/s	First bidirectional optical link, ATP, point-ahead compensation
GOLD	1995	GEO–Ground	830 nm DL, 514.5 nm UL	IM/DD	1.024 Mb/s	Spatial diversity applied to the uplink beacon, scintillation mitigation
SILEX (ARTEMIS–SPOT4)	2001	GEO–LEO	847 nm, 819 nm	OOK	50 Mb/s	First GEO-LEO OISL, autonomous ATP
ARTEMIS OGS Campaigns	2001–2006	GEO–Ground	801 nm, 819 nm	NRZ, 2-PPM	50 Mb/s UL, 2 Mb/s DL	Multi-beam uplink, turbulence characterization
OICETS (LUCE)	2005–2009	LEO–GEO, LEO–Ground	847 nm	NRZ, 2PPM	49 Mb/s, 2 Mb/s	First LEO-to-ground link, micro-vibration characterization, multi-beam beacon, FEC
TerraSAR-X/NFIRE	2008	LEO–LEO, LEO–Ground	1064 nm	BPSK	5.625 Gb/s	First coherent OISL and OFL, beaconless acquisition, Doppler shift compensation
HY-2	2011	LEO–Ground	1550 nm	IM/DD	504 Mb/s	Micro-vibration characterization
BTLS	2011	LEO-Ground	1550 nm	IM/DD	622 Mb/s	
Alphasat	2013	GEO–LEO, GEO–Ground	1064 nm	BPSK	1.8 Gb/s	First AO pre-compensated uplink, atmospheric characterization, intradyne detection
EDRS	2016	GEO–LEO	1064 nm	BPSK	1.8 Gb/s	Operational optical relay network
OPALS	2014	LEO–Ground	1550 nm	OOK	50 Mb/s	Reed–Solomon FEC, COTS-based design, AO-assisted reception
SOCRATES (SOTA)	2014	LEO–Ground	800 nm, 976 nm, 1549 nm	OOK	10 Mb/s	Miniaturized terminal, QKD precursor, LDGM coding
Micius	2016	LEO–Ground	1550 nm DL, 1064 nm UL	DPSK, PPM	5.12 Gb/s DL / 20 Mb/s UL	QKD, coherent reception
OSIRIS v1/v2	2017	LEO–Ground	1550 nm	OOK	200 Mb/s – 1 Gb/s	Miniaturized terminal for small satellites, CCSDS-compliant

Table 1.1 – continued from previous page

Mission	Year	Link	Wavelength	Modulation	Data Rate	Key Technologies
OSIRIS4CubeSat (CubeLCT)	2020	LEO–Ground	1550 nm	OOK	100 Mb/s	Miniaturized terminal for CubeSats
OSIRISv3	2020	LEO-Ground	1550 nm	OOK	10 Gb/s	High-speed terminal for LEO platforms
OCSD	2017	LEO–Ground	1064 nm	OOK	200 Mb/s	CubeSat optical communications, first optical crosslink experiment between CubeSats
VSOTA	2019	LEO–Ground	980 nm, 1540 nm	OOK	100 kb/s	Body pointing
LCRD	2021	GEO–LEO, GEO–Ground	1550 nm	PPM, DPSK	2.8 Gb/s	AO, relay network
CubeSOTA	2021	LEO–Ground, LEO-HAPs	1550 nm	OOK	Gb/s class	CubeSat optical communications
CLICK	2022	LEO–Ground, LEO–LEO	1550 nm	OOK	10 Mb/s	Low-cost CubeSat optical terminal
TBIRD	2022	LEO–Ground	1550 nm	DP-QPSK, 2-PPM	200 Gb/s	Record optical downlink from CubeSat, ARQ
CubeLCT	2022	LEO–Ground, LEO–LEO	1550 nm	OOK	Gb/s class	Integrated miniaturized LCT
CubeCAT	2023	LEO–Ground	1550 nm	OOK	1 Gb/s	Compact 1U optical communication payload
TELEO	2024	GEO–Ground	1550 nm, 1600.22 nm	DPSK, OOK	10 Gb/s	AO-assisted uplink precompensation, LDPC coding
LUCAS	2024	GEO–LEO, GEO–Ground	1560 nm, 1540 nm	DPSK, IM/DD	1.8 Gb/s	Operational optical relay, beaconless ATP, LDPC coding
HICALI	2025	GEO–Ground	1550 nm	Advanced coherent modulation	10 Gb/s	AO, feeder-link technologies, high-speed photonics

1.2.1 Early proof-of-concept demonstrations

The first major milestone in space optical communications was National Aeronautics and Space Administration (NASA)'s Galileo Optical Experiment (GOPEX) [27]. In December 1992, GOPEX demonstrated a deep-space laser uplink from ground stations located at the Table Mountain Facility (TMF), California, and the Starfire Optical Range (SOR), New Mexico, to the Galileo spacecraft during its Earth flyby en route to Jupiter. Operating at 532 nm using frequency-doubled Nd:YAG lasers coupled to Cassegrain telescopes, the experiment successfully detected transmitted optical signals over distances ranging from approximately 600 000 km to 6 000 000 km.

The transmitters characteristics are given in Table 1.2. In detail, a 15-cm subaperture of the 0.6-m TMF telescope primary mirror was illuminated by the laser beam. In this way, the large loss in signal strength due to the occultation by the secondary mirror was avoided. Instead, at the SOR facility, the beam was transmitted through the full 1.5-m aperture, while the effects of occultation by the 10-cm secondary mirror were mitigated by reconfiguring the laser resonator so that it generated a flat-top intensity profile across the beam. Although no

Table 1.2 – GOPEX transmitter characteristics [27]

	Table Mountain Facility	**Starfire Optical Range**
Wavelength	532 nm	532 nm
Pulse energy	250 mJ	350 mJ
Repetition rate	15-30 Hz	10 Hz
Pulse width	12 ns	15 ns
Beam divergence	110/60 μrad	80/40 μrad
Telescope primary mirror diameter	0.6 m	1.5 m
Telescope secondary mirror diameter	0.2 m	0.1 m

high-rate data transmission was attempted, GOPEX validated long-distance laser

beam pointing based solely on orbital predictions and demonstrated the feasibility of deep-space optical communications.

A second key milestone was achieved at the Communications Research Laboratory (CRL) with the Japanese Engineering Test Satellite-VI (ETS-VI), a GEO satellite carrying the Laser Communication Equipment (LCE) [28]. The primary objective of the mission was to validate the fundamental technologies required for future optical inter-satellite communication systems, including coarse and fine tracking subsystems, point-ahead mechanism, bidirectional laser communications based on Intentisy Modulation/Direct Detection (IM/DD) technique, satellite vibration characterization, and long-term behavior analysis of optical components in the space environment. The communication link between ETS-VI and a ground station was to be used as a representative counterpart of an inter-satellite optical link.

ETS-VI was launched on August 28, 1994. Although it was originally intended to operate in GEO, a malfunction of the satellite propulsion system prevented its insertion into the GEO orbit, leaving it in an elliptical one. The satellite was then transferred into a 3-day subrecurrent orbit. While this anomaly altered the original mission profile, it ultimately created additional opportunities for experimentation by making the spacecraft visible from a larger number of ground stations worldwide. Consequently, the mission became the first practical platform for extensive space-to-ground optical communication testing.

The LCE terminal was designed as a compact and lightweight optical communication payload, with a total mass of approximately 22 kg. It incorporated all the essential subsystems required for optical communication terminals, including a coarse pointing system, a fine-pointing mechanism, acquisition and tracking sensors, a Point-Ahead Mechanism (PAM), an Avalanche Photodiode (APD) receiver, laser diode transmitters, and a 7.5-cm telescope. A block diagram of the LCE terminal can be seen in Fig. 1.6.

The coarse tracking system consisted of a two-axis gimbal mirror and a Charge-Coupled Device (CCD) tracking sensor, enabling an acquisition range of $\pm$ 1.5° and a resolution of 0.012°. While coarse tracking could provide an accuracy of 33 μrad, the fine tracking loop achieved an accuracy of 2 μrad (3σ). The communication architecture relied on IM/DD, employing an 830 nm laser diode for

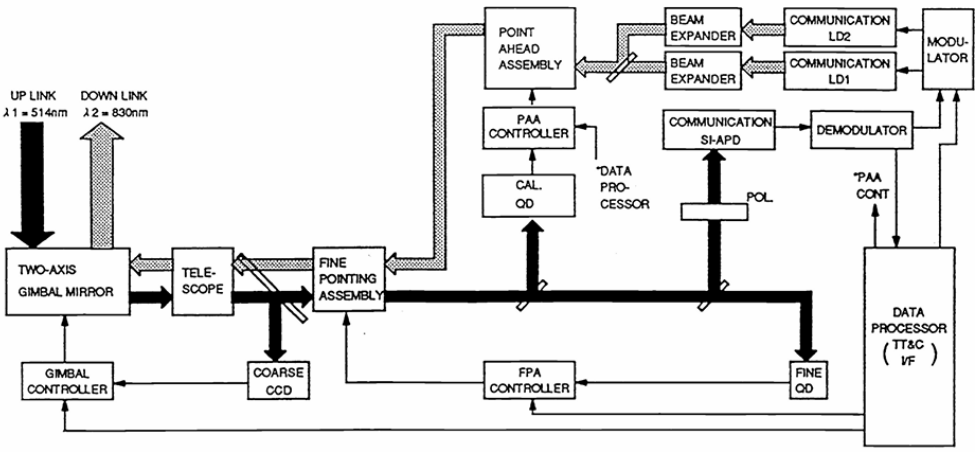


Figure 1.6 – Block diagram of LCE on the ETS-VI satellite [28]

downlink transmission and a 514.5 nm argon-ion laser for the uplink. Both uplink and downlink operated at a data rate of 1.024 Mb/s using Manchester-coded modulation. A complete list of LCE specifications is reported in Table 1.3. The CRL OGS was equipped with a 1.5-m receiving telescope, a 0.2-m transmitting telescope, and a 10-W laser. A Quadrant Detector (QD) allowed to reduce the pointing error caused by gimbal-mount jitter and laser beam wandering [29, 30].

Between 1994 and 1995, ETS-VI demonstrated the first bidirectional space-to-ground optical communication link. However, a continuous lock-on of the fine tracking loop was not achieved due to severe attenuation and scintillation of uplink laser light.

The subsequent Ground/Orbiter Lasercomm Demonstration (GOLD), jointly conducted by NASA and CRL, further investigated the performance of bidirectional optical links under different atmospheric conditions [31]. Specifically, GOLD used the 0.6-m and 1.2-m telescopes located at NASA's TMF to communicate with ETS-VI. The communication architecture remained similar to that employed in the original ETS-VI experiments. An argon-ion laser operating at 514.5 nm transmitted a 1.024 Mb/s Manchester-coded Pseudorandom Noise (PN) sequence from the ground station to the spacecraft, while the onboard GaAs laser diode transmitted a corresponding 830 nm downlink signal toward the 1.2-m ground receiver. However, GOLD extended the scope of the previous demonstrations by focusing

Table 1.3 – LCE specifications [28]

Parameter	Value
Weight	22.4 kg
Power	90.4 W
Tx/Rx telescope diameter	7.5 cm
Tx wavelength	830 nm
Average Tx power	13.8 mW
Data rate	1.024 Mb/s
Tx beam divergence	30/60 μrad
Rx wavelength	514.5 nm
Detector	Si-APD

specifically on atmospheric effects and link reliability.

A particularly important contribution of GOLD was the introduction of spatial and temporal diversity to mitigate atmospheric scintillation on the uplink beacon. Indeed, the transmitted laser beam at the OGS was splitted into two mutually incoherent beams separated by a distance larger than the atmospheric coherence, also known as Fried's parameter. Because the two beams propagated through largely independent turbulence cells, the resulting intensity fluctuations at the spacecraft receiver became partially uncorrelated, reducing the overall variance of the received signal. Measurements of acquisition times, received power statistics, and atmospheric transmission losses were collected over numerous experimental sessions between October 1995 and January 1996 and compared with theoretical models in [32].

1.2.2 Emergence of operational optical inter-satellite links

The beginning of the 21st century marked a turning point in the development of optical satellite communications. Whereas the experiments conducted during the 1990s primarily focused on validating the feasibility of optical space-to-ground links

and characterizing atmospheric propagation effects, the following decade witnessed the emergence of operational OISLs.

Specifically, OISLs between LEO and GEO spacecrafts were envisioned to mitigate the intermittent visibility constraints inherent to direct LEO-to-ground communications by enabling data relay through a geostationary satellite. In addition to extending communication availability, such relay architectures improve operational flexibility, facilitate the centralization of ground infrastructure, reduce ground-segment deployment requirements, and optimize the management of onboard data storage systems. The main technological challenge is no longer the transmission of optical signals over long distances, but rather the establishment and maintenance of highly directional communication links between independently moving spacecraft. This requires the development of autonomous Acquisition, Tracking, and Pointing (ATP) systems capable of achieving sub-microradian accuracy while compensating for relative motion, orbital uncertainties and point-ahead effects. The successful demonstrations carried out during this period laid the foundations for the current optical relay networks and satellite mega-constellations.

A decisive step was achieved through the ESA's Semiconductor Laser Inter-Satellite Link Experiment (SILEX), implemented between the GEO satellite Advanced Relay and Technology Mission Satellite (ARTEMIS) and the French LEO EO satellite SPOT-4 [33]. ARTEMIS was launched in 2001, while the first successful optical communication session was established later that year, becoming the first GEO-LEO OISL ever demonstrated in space.

The SILEX Laser Communication Terminal (LCT) was based on On-Off Keying (OOK) modulation with direct detection at 50 Mb/s, i.e., the maximum data rate the EO camera on SPOT-4 could provide. The two LCT terminals used wavelength discrimination, at 819 and 847 nm, to isolate their respective transmit and receive beams. This wavelength range was selected because it provided the best compromise between component maturity and system performance for spaceborne applications at the time of development. The ARTEMIS-to-SPOT-4 link was not modulated but used for tracking purposes only, as there was no communication receiver chain on-board the LEO terminal [34]. The architecture of the two optical terminals, whose mass and power consumption were about 100 kg and 150 W, respectively, is shown in Fig. 1.7.

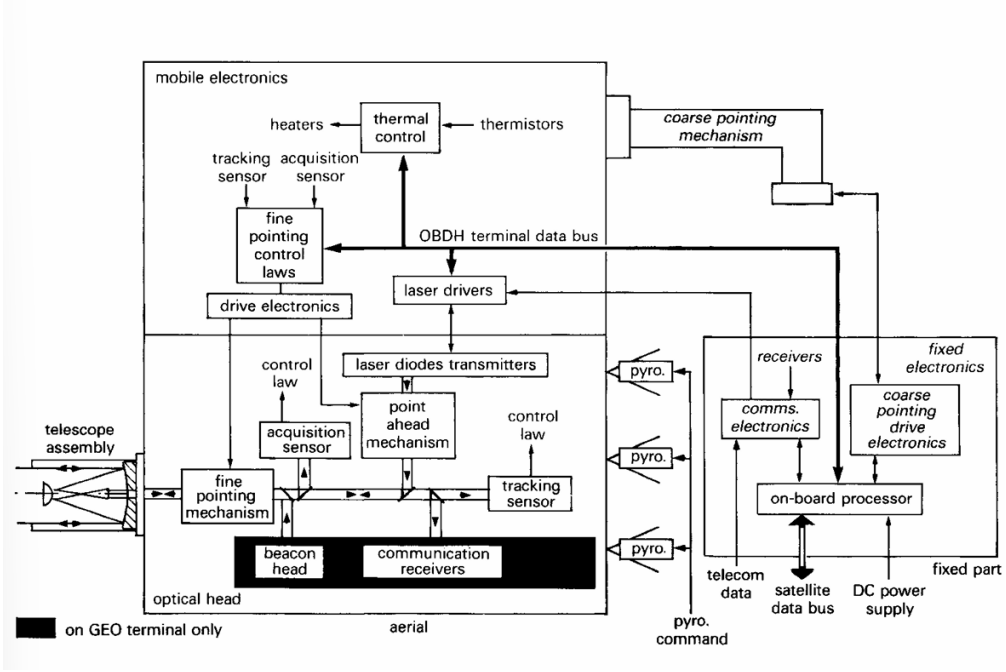


Figure 1.7 – Block diagram of the SILEX terminals [33]

The principal achievement of SILEX was not the data rate itself, but the demonstration of a stable optical link between two spacecrafts moving in different orbital regimes over distances approaching 45 000 km. To achieve this objective, SILEX implemented a sophisticated acquisition and tracking procedure based on beacon lasers. Initial coarse pointing relied on orbital predictions and spacecraft attitude information, after which beacon detection enabled progressive refinement of the pointing accuracy through multiple tracking stages. In detail, the LCT on ARTEMIS first scans the 1700 μrad uncertainty cone with a 750-μrad beacon laser following a spiral path. Upon detection of the beacon, SPOT-4 sends a communication beam back to stop the beacon scan. The two terminals then track each other and optimize their angular alignment. Once lock is achieved, fine-pointing mechanisms ensure continuous alignment throughout the communication session. The system also implemented Point-Ahead Angle (PAA) compensation to account for the finite propagation time of the optical signal. Since the satellites moved significantly during the time required for the light to travel between them, the transmitted beam had to be directed toward the predicted future position of the

receiving terminal rather than its instantaneous location. This requirement, more restrictive than in previous space-to-ground demonstrations, became one of the defining challenges of optical inter-satellite communications [35].

Analysis of the pointing performance revealed that the open-loop pointing error of the SPOT-4 terminal was significantly smaller than anticipated, highlighting the excellent attitude determination and control capabilities of the SPOT-4 platform. In contrast, the ARTEMIS terminal exhibited noticeably larger pointing errors. Nevertheless, these errors remained within the design margins established during system development and did not compromise link establishment or communication performance. The latter was evaluated through Bit Error Rate (BER) measurements. A PN sequence generated onboard the LEO satellite was transmitted to ARTEMIS via the optical link and subsequently forwarded to ESA's In-Orbit Test facility in Redu, Belgium, through the satellite's Ka-band feeder link. At the ground facility, the received sequence was compared with a locally generated reference pattern to identify transmission errors. Over a cumulative observation period of 56 minutes, a BER of $8.9 \cdot 10^{-10}$ was measured. This value corresponded to the noise error floor of the communication receiver, indicating that virtually no performance degradation was introduced by the optical link itself [36].

The operational capabilities of the system were further demonstrated through the transmission of EO images acquired by SPOT-4. Owing to the outstanding communication performance, image data were relayed through ARTEMIS and delivered in real time to the SPOTIMAGE operations center in Toulouse, France. Continuous image transmission sessions lasting up to 20 minutes were successfully achieved, with the received images exhibiting no observable degradation [36].

ARTEMIS was also used to conduct bidirectional space-to-ground optical links with the ESA's OGS located at the Instituto de Astrofisica de Canarias (IAC) Teide Observatory. Between November and December 2001, while ARTEMIS was still undergoing orbit-raising maneuvers, the first eight bidirectional optical communication sessions were successfully completed [37]. Particular attention was devoted to evaluating the closed-loop tracking system of the OGS, which employed a Fine Pointing Mirror (FPM) to compensate for turbulence-induced image motion. Measurements confirmed the effectiveness of the tracking loop in maintaining stable coupling despite atmospheric perturbations. Simultaneously, fluctuations of the

received downlink power were recorded and analyzed. The resulting power spectra exhibited the characteristic low-pass behavior associated with optical wave propagation through atmospheric turbulence. In addition, parameters such as wavelength stability, polarization state, and communication performance were monitored throughout the campaign. The transmitted wavelength remained within the nominal operating range during all experiments, although variations of up to approximately 2 nm were observed both between different communication sessions and within individual links. The state of polarization exhibited remarkable stability, while BER measurements revealed a broader variability, largely driven by changing atmospheric conditions and pointing performance.

The downlink relied on 2-Pulse Position Modulation (2-PPM) at 2 Mb/s. To mitigate turbulence-induced fading in the uplink, the OGS employed four mutually incoherent transmit beams. Analysis of the irradiance recorded onboard ARTEMIS confirmed the effectiveness of this approach, with the measured irradiance statistics closely following the log-normal distribution. Despite relatively low Signal-to-Noise Ratios (SNRs) in uplink, successful communication sessions were achieved during both nighttime and daytime operations.

Following the completion of the orbit-raising campaign, communication experiments resumed in 2003 and continued extensively over the following years, resulting in more than one hundred successful optical link sessions. This large experimental dataset provided an unprecedented opportunity to investigate long-term optical link performance and to validate propagation models under a wide variety of atmospheric conditions. Indeed, a series of propagation experiments was conducted to evaluate the influence of beam divergence and transmitter diversity on communication performance. In several campaigns, these measurements were complemented by simultaneous atmospheric characterization using a Scintillation Detection and Ranging (SCIDAR) instrument. The availability of refractive-index structure parameter profiles enabled direct correlation between measured communication performance and atmospheric turbulence conditions.

Across all experiments, the average downlink BER was measured to be approximately $9.8 \cdot 10^{-7}$. Temporal variations within individual communication sessions were also significant, with BER fluctuations typically spanning a factor of 6.5 and, in extreme cases, reaching a factor of 20. These results highlighted the

highly dynamic nature of the atmospheric optical channel and the importance of adaptive mitigation strategies. Although the best uplink measured BER values were in the range of 10^{-5}–10^{-6}, most experiments exhibited BER levels exceeding 10^{-3}. Detailed analysis revealed that atmospheric turbulence alone could not account for the observed performance degradation. Instead, a significant fraction of the impairment was attributed to imperfections in the modulation quality of the ground-based laser transmitter [38].

Irradiance fluctuations were measured using a Four-Quadrant Detector (4QD) operating at a sampling frequency of 1 kHz. Owing to the relatively large receiving aperture of the OGS, aperture averaging substantially reduced turbulence-induced intensity fluctuations, resulting in scintillation indices typically ranging between 0.001 and 0.01. A strong correlation was observed between scintillation intensity and communication performance. In particular, the lowest BER values were consistently achieved when the scintillation index remained below approximately 0.004.

Although SILEX represented a major milestone in the validation of OISL, its relatively large mass (157 kg) and modest data rate (50 Mb/s) limited its competitiveness with contemporary RF systems. These constraints were largely driven by the low output power of the available 830 nm laser diodes, which necessitated large 25-cm apertures on both terminals. Recognizing the need for more compact and efficient user terminals, ESA initiated the development of lightweight LCTs. Several architectures were investigated, including optically pre-amplified direct-detection systems at 1550 nm. Ultimately, coherent systems based on Nd:YAG lasers were favored due to the greater technological maturity, reduced susceptibility to radiation-induced degradation, superior immunity to background light, and ability to operate even with the Sun within the receiver field of view [39].

Building upon SILEX, the Japanese Optical Intersatellite Communication Engineering Test Satellite (OICETS) satellite carrying the Laser Utilizing Communication Equipment (LUCE) terminal established in 2005 the first bidirectional OISL with ARTEMIS. OICETS also became a cornerstone for space-to-ground optical communication research through campaigns involving National Institute of Information and Communications Technology (NICT), German Aerospace Center (DLR), ESA, and NASA [40].

On August 23, 2005, OICETS was successfully launched and injected into a sun-synchronous orbit at the altitude of 610 km [41]. As can be seen in Fig. 1.8, LUCE consists of two parts, i.e., (i) the externally mounted optical assembly (LUCE-O), which incorporated a 26-cm Cassegrain telescope on a two-axis gimbal, and (ii) the internal electronics unit (LUCE-E), responsible for ATP and communication functions. The complete terminal had a mass of approximately 130 kg and consumed between 230 W and 320 W during operation. OICETS also carried a Micro Vibration Measurement Equipment (MVE) for characterizing spacecraft-induced disturbances. The system employed intensity modulation and direct detection, using 2-PPM at 2.048 Mb/s in the forward link (ARTEMIS-to-OICETS) and Non-Return to Zero (NRZ) modulation at 49.4 Mb/s in the return link (OICETS-to-ARTEMIS). Acquisition and tracking were achieved through a combination of coarse (0.3 Hz) and fine (200 Hz) tracking loops, together with a dedicated point-ahead mechanism [41, 42].

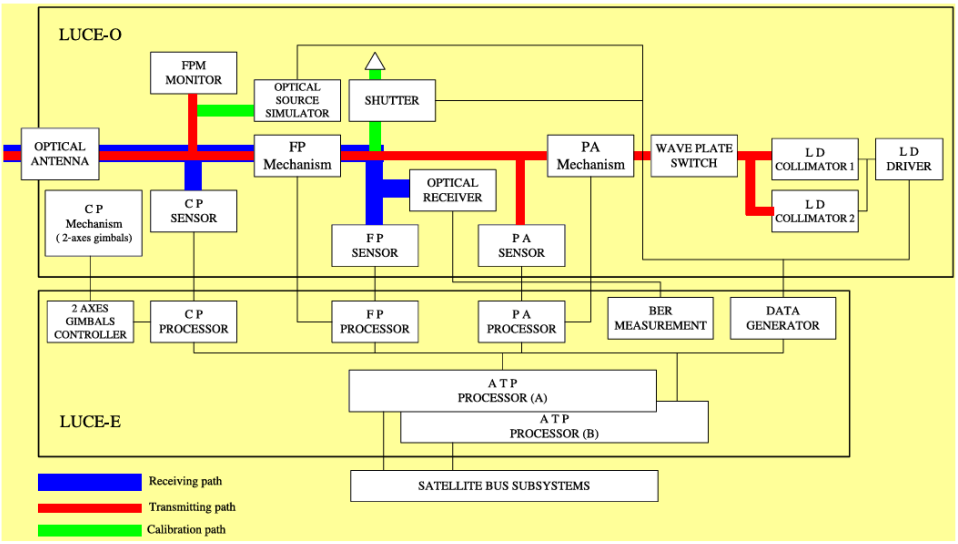


Figure 1.8 – Block diagram of the LUCE terminal [41]

Compared with SILEX, OICETS provided a more comprehensive assessment of optical inter-satellite communication technologies. Particular attention was devoted to the performance of acquisition and tracking algorithms, which achieved

an overall accuracy of ±1 μrad [42]. Moreover, in-orbit calibration of bias pointing error was tested, allowing optimization of communication performance [43].

The first successful LEO-to-ground link was demonstrated in 2006 in the context of the Kirari Optical Communication Demonstration Experiments with the NICT OGS (KODEN). In this campaign, a 1.5-m telescope was used for uplink beacon transmission, with a divergence angle of 9 mrad at 808 nm, fully covering the open pointing error of the OGS. Instead, the uplink communication beam had a divergence angle of 204 μrad, sufficient to cover the PAA of the satellite, and was further divided into four parallel beams to mitigate turbulence. To receive the downlink beam, a 20-cm telescope was initially used, later substituted by a 31.8-cm sub-aperture of the 1.5-m telescope [44]. An overview of the KODEN specifications is found in Table 1.4.

Table 1.4 – KODEN specifications [44]

	Uplink beams		**Downlink beam**
	Beacon	**Communication**	
Wavelength	808 nm	815 nm	847 nm
Beam divergence angle (FWHM)	9 mrad	204 μrad	5.5 μrad
Transmitted power (at telescope aperture)	30 W (max)	10 mW	53 mW
Signal format	CW	2-PPM	NRZ
Data rate	-	2.048 Mb/s	49.3724 Mb/s
Polarization	Random	LHCP, Random	LHCP
Number of beams	1	4	1
Rx aperture diameter	26 cm	26 cm	20 cm/31.8 cm

The KODEN campaign contributed to the understanding of turbulence-induced effects over varying elevation angles. Several experiments also investigated diver-

sity and coding techniques for atmospheric mitigation. Multi-beam uplink configurations were tested to reduce scintillation effects, while the performance of advanced FEC schemes also evaluated [45]. These investigations represented some of the earliest practical studies of techniques that would later become central components of high-availability OFL systems, including site diversity, aperture averaging, coding gain exploitation, and adaptive transmission strategies.

Additional optical communication campaigns were conducted between 2008 and 2009 with OGSs operated by NICT, DLR, ESA, and NASA/Jet Propulsion Laboratory (JPL). These experiments aimed to compare atmospheric propagation effects and communication performance across different ground terminals. Measurements of scintillation index, irradiance statistics, power spectral density, autocovariance functions, and BER showed good agreement among the stations, with irradiance distributions closely following the theoretical log-normal model. Notably, the Kirari's Optical Downlink to Oberpfaffenhofen (KIODO) experiment with DLR's OGS in Oberpfaffenhofen demonstrated reliable LEO-to-ground optical communications at 50 Mb/s and highlighted the benefits of spatial diversity and aperture averaging for scintillation mitigation [46]. The joint demonstrations continued until September 2009, when Japan Aerospace Exploration Agency (JAXA) stopped the OICETS signal [47].

1.2.3 Transition to coherent optical communications and AO systems

While SILEX and OICETS demonstrated the feasibility of optical inter-satellite communications using IM/DD architectures, their achievable data rates remained limited to a few tens of Megabits per second. To overcome these limitations, the DLR initiated the development of a new generation of LCTs based on coherent optical communication techniques [48]. The resulting terminal, developed by TESAT-Spacecom with contributions from EADS Astrium and Zeiss Optronik, represented a major technological leap in optical satellite communications and laid the foundation for all subsequent European optical relay systems.

The TESAT LCT adopted homodyne Binary Phase-Shift Keying (BPSK) modulation operating at a wavelength of 1064 nm. Unlike direct-detection systems,

coherent reception combines the received optical field with a local oscillator laser. This approach significantly improves receiver sensitivity and enables operation at substantially higher data rates while maintaining moderate optical transmit power. Furthermore, coherent detection offers excellent immunity to background illumination and allows operation even in the presence of strong solar radiation, making it particularly attractive for operational inter-satellite communication networks [49].

To support coherent operation, TESAT developed a highly stable space- qualified Nd:YAG laser source operating at 1064 nm and able to compensate for Doppler shifts up to ±10 GHz. The laser output was coupled into a polarization-maintaining Single-Mode Fibre (SMF) and phase-modulated by an electro-optical modulator before transmission at speeds up to 10 Gb/s. The resulting communication beam was amplified to an optical output power of 0.7 W and transmitted through a compact telescope system. The complete terminal consisted of a single integrated unit with a mass of roughly 30 kg and an average power consumption of approximately 130 W, representing a dramatic reduction in size and power requirements compared with previous optical communication terminals, while simultaneously increasing the achievable throughput by two orders of magnitude [50].

Another innovative feature of the TESAT architecture was the implementation of beaconless acquisition. Rather than relying on dedicated acquisition beacons, the communication beam itself was used for acquisition, tracking, and communication [51]. This significantly simplified the terminal architecture and reduced system complexity while maintaining highly reliable link establishment. The TESAT LCT main features are summarized in Table 1.5.

The first in-orbit validation of the new technology was performed aboard the German EO satellite TerraSAR-X, launched in June 2007 at 512-km altitude. In January 2008, the terminal entered operational service and became the first coherent laser communication system ever deployed in space. In a first verification step, SAR data were transmitted to a ground-based terminal at a speed of 5.625 Gb/s. Shortly thereafter, a series of experiments was conducted with the U.S. Near Field Infrared Experiment (NFIRE) satellite, orbiting at 495 km, creating the first coherent high-data-rate OISL between two spacecrafts [52]. The first successful communication session took place on February 21, 2008. During this experiment, the two satellites established an error-free bidirectional optical link for

Table 1.5 – TESAT LCT specifications [51]

Parameter	**Value**
Wavelength	1064 nm
Waveform	Coherent BPSK
Data rate	5.625 Gb/s
Terminal mass	32 kg
Terminal power	120 W
Peak transmit power	0.7 W
Doppler range	±10 GHz
Field of regard	±180 degrees Az. & El.
Maximum angular tracking rate	4 degrees/second
Field of view	10 mrad

133 s while their separation varied between approximately 3800 and 4900 km. The acquisition process, including coarse pointing and closed-loop tracking, required approximately 43 s, while frequency and phase locking were completed within an additional 30 s. Subsequent experiments progressively reduced these acquisition times and demonstrated increasingly robust autonomous operation. In later campaigns, full-duplex communication links could routinely be established in less than 30 s [49].

The TerraSAR-X/NFIRE experiments also generated valuable information regarding pointing stability and terminal dynamics. Analysis of LoS disturbances showed total pointing jitter values between approximately 5.6 and 6.8 μrad Root Mean Square (rms), with a significant contribution arising from vibrations associated with the azimuth bearing mechanism of the terminal. Despite these disturbances, communication performance remained unaffected, demonstrating the effectiveness of the terminal's fine-pointing and tracking subsystems [51].

In parallel with the inter-satellite demonstrations, DLR and TESAT initiated a series of satellite-to-ground experiments to investigate the feasibility of coherent

optical communication through the atmosphere. Ground version of the LCT were deployed at OGSs in Hawaii and Tenerife, where bidirectional 5.625 Gb/s links were established with NFIRE. In detail, the terminal aperture was halved (i.e., 125 mm) to mitigate scintillation [49]. Indeed, since AO was not employed at the OGS, the reduced aperture was essential to operate at small Fried's parameters. The space-to-ground campaign demonstrated worse pointing performance than the OISL one, which was attributed to the different geometry of the LCT gimbals in the two configurations [53]. Moreover, the LEO-to-ground BER was still low as for the OISL but increased due to beam distortion, with degraded performance in uplink. Specifically, BERs higher than 10^{-5} were measured. The OGS 60-cm aperture was sufficient to collect enough photons while keeping the optical phase nearly constant, making homodyne reception possible. In contrast, in a GEO-to-ground link, a larger telescope would be required to collect enough power, reducing the homodyne detection sensitivity if the wave distortion is not compensated by AO [48].

The Chinese Haiyang-2 (HY-2) mission in 2011 further advanced optical downlink technology by demonstrating a 504 Mb/s IM/DD downlink at 1550 nm while characterizing spacecraft micro-vibrations and their impact on pointing stability [54]. During the same period, the BTLS terminal aboard the Russian segment of the International Space Station (ISS) demonstrated optical downlinks at rates up to 622 Mb/s, further confirming the viability of high-rate optical transmission through the atmosphere [55].

Following the success of the TerraSAR-X/NFIRE campaign, the next major milestone was represented by the launch of Alphasat in 2013. Its Technology Demonstrator Payload 1 (TDP1), derived from the TESAT LCT architecture, served as a precursor to the European Data Relay System (EDRS) [56]. Operating in GEO, it validated autonomous acquisition and coherent optical communications for future relay-network applications. The payload consisted of a coherent optical terminal operating at 1064 nm together with a Ka-band communication subsystem used to forward data to ground stations. While the Ka-band feeder link supported transmission rates up to 600 Mb/s, the optical relay link enabled bidirectional communication at rates up to 1.8 Gb/s, demonstrating the significant capacity advantage offered by laser communications.

The TDP1 terminal retained the key architectural features of the TESAT coherent communication concept, including homodyne BPSK modulation, coherent detection, beaconless acquisition, and autonomous link establishment. Indeed, the entire acquisition process was performed without human intervention. After receiving orbital information and link scheduling parameters from the ground segment, the terminal autonomously performed pre-heating, coarse pointing, spiral search acquisition, tracking, frequency acquisition, and phase locking before initiating data transmission. This degree of autonomy was a critical requirement for future operational relay systems, where hundreds of optical links would eventually need to be established each day.

The first phase of the TDP1 mission focused on commissioning and calibration activities. Initial space-to-ground optical links were established with ESA'sOGS in Tenerife during late 2013. These experiments verified the accuracy of the terminal pointing system and demonstrated the effectiveness of the autonomous search algorithm. The first successful detections confirmed that the predicted spacecraft ephemerides and coarse pointing models were sufficiently accurate for optical acquisition. Subsequent calibration campaigns enabled progressive refinement of the pointing models, reducing acquisition times and improving overall link reliability [57].

The most significant achievement of the mission occurred in November 2014, when the first OISL between Alphasat and the Sentinel-1A EO satellite was successfully established. This experiment constituted the first demonstration of the complete EDRS relay concept and represented the first operational GEO–LEO optical communication link intended for routine service provision. The optical link operated over distances approaching 45,000 km and achieved stable, error-free communication with measured BER values below 10^{-10} while using only 1.1 W of transmitted optical power [58]. Remarkably, these results were obtained without relying on the Reed Solomon (RS) coding scheme normally implemented within the Sentinel communication chain, highlighting the substantial link margin provided by the coherent architecture. The commissioning results further confirmed the exceptional performance of the TESAT LCT. Whereas the original specification allocated up to 55 s for the acquisition sequence, several demonstrations achieved complete acquisition and communication establishment in less than 20 s. These

results demonstrated not only the reliability of beaconless acquisition but also the suitability of the technology for operational relay services involving a large number of daily communication sessions.

Following the successful validation with Sentinel-1A, additional relay demonstrations were performed with Sentinel-2A, whose optical terminal was commissioned in 2015. These campaigns confirmed the interoperability of multiple LCT-equipped spacecraft and verified the capability of the relay architecture to support different classes of EO payloads. The resulting system became the technological foundation for routine data-relay operations within the Copernicus programme.

The operational successor to TDP1 was EDRS. Developed as a public–private partnership between ESA and Airbus Defence and Space, EDRS was conceived as a permanent space-based communication infrastructure capable of providing near-real-time delivery of large EO datasets [59–61]. The first operational node, EDRS-A, was launched aboard the Eutelsat 9B satellite in January 2016, followed by EDRS-C [62]. Positioned at 9°E and 31°E longitude, respectively, the two GEO satellites provide coverage over Europe, Africa, the Middle East, and surrounding regions. Together they formed the first operational optical relay constellation in space. Compared with earlier LEO–LEO demonstrations, the GEO terminals incorporate larger apertures, higher optical transmit power, improved telescope transmission efficiency, and dedicated channel coding to compensate for the substantially greater propagation distance. By 2017, several Sentinel terminals had already entered continuous operational service, routinely performing approximately ten optical relay sessions per day with individual link durations ranging from 5 to 20 minutes [63]. The successful operation of these links demonstrated that optical communications had progressed beyond experimental validation and had become a practical component of a large-scale space communication infrastructure. Fully automated planning and network management software enabled routine operation without continuous operator intervention, marking a significant step toward future optical communication networks and relay constellations.

From 2015, further space-to-ground links were established between Alphasat and the Tansportable Adaptive Optics Ground Station (T-AOGS), co-located with the ESA one [63]. The T-AOGS exploits AO in the receive path, while its transmitter aperture diameter can vary between three different options, i.e., 35 mm, 48

mm, and 95 mm [64]. Measurement results show that, thanks to the AO system coupled with the use of a RS FEC code, the downlink is outage-free. Instead, the uplink suffers from fades leading to significant outage times [64–66].

Given these considerations, ESA developed the Alpha-Up breadboard, whose architecture is depicted in Fig. 1.9, to be used in 2022 for demonstrating pre-compensation of the uplink beam using closed-loop, high-speed AO in a common transmit/receive aperture [67]. The mission demonstrated both tip/tilt and full pre-compensation. The results outline the benefits of full pre-compensation under strong turbulence. However, the advantage is less evident under weak turbulence, since there is little higher-order wavefront error to compensate for [68]. This was the first optical uplink with higher-order wavefront pre-compensation towards a GEO satellite. Later on, the Alpha-up and Down Experiment (AUDE) project was established, with the goal of characterizing the impact of both pre- and post-compensation AO between the ESA OGS and Alphasat. Starting on September 2023, several trials were conducted with different AO modes [69]. A gain in SMF coupling efficiency together with a variance reduction in uplink irradiance were observed with full correction. Despite a significant increase of the average received power at Alphasat was not recognized, the fading depth was remarkably reduced.

Similar AO experiments were conducted between Alphasat and the DLR OGS in Oberpfaffenhofen [70], further confirming that large beam can be effectively pre-distorted and transmitted with reduced power, thus providing a power efficient way of establishing bidirectional OFL with GEO satellites.

In addition to AO demonstrations, the Alphasat space-to-ground campaigns were crucial to establish the performance of homodyne feeder links at Gigabit-per-second data rates. Nonetheless, to achieve even faster rates, higher-order coherent modulation formats would be beneficial. As the complexity of the Phased-Locked Loop (PLL) increases with the modulation order, a promising alternative is intradyne detection which, thanks to advances in digital signal processing, offers lower complexity, faster frequency acquisition, and greater robustness to atmospheric fading. In 2023, TESAT conducted a series of GEO-to-ground experiments between Alphasat and the T-AOGS, directly comparing homodyne and intradyne reception under similar atmospheric conditions. The results showed comparable receiver performance, while the intradyne architecture exhibited improved resilience

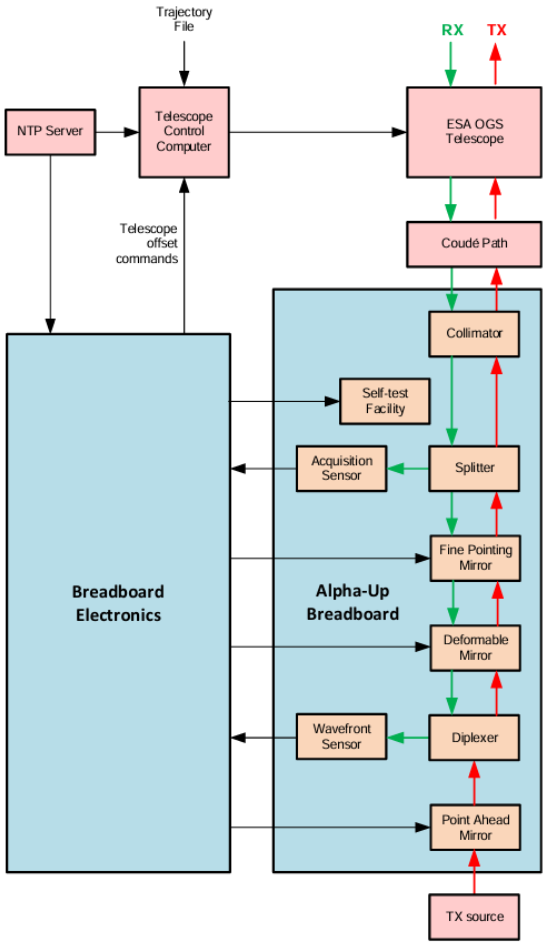


Figure 1.9 – Block diagram of Alpha-Up breadboard [68]

to turbulence-induced signal outages, faster link re-acquisition, and reduced implementation complexity, highlighting its potential for future high-capacity OFLs [62].

1.2.4 Toward miniaturization, quantum communication, and New Space terminals

The period following 2014 marked a profound transformation in the development of optical satellite communications. While previous efforts had focused primarily on demonstrating high-performance laser links using relatively large and complex terminals, the new generation of missions emphasized miniaturization, cost reduction, compatibility with small satellites, and the exploration of novel applications

such as quantum communications. As a result, optical communication technologies began to transition from specialized demonstrations conducted on dedicated spacecrafts to versatile payloads capable of supporting a broad range of missions, from EO and broadband communications to secure quantum networks.

A first milestone was NASA's Optical PAyload for Lasercomm Science (OPALS), installed aboard the ISS. The primary objective of OPALS was to demonstrate that a relatively simple and low-cost optical terminal based largely on Commercial Off-The-Shelf (COTS) components could provide reliable high-rate optical downlinks from LEO [71]. Operating at 1550 nm and employing OOK modulation together with CCSDS-standardized RS FEC coding, OPALS successfully transmitted high-definition video, telemetry, and test data streams to the Optical Communications Telescope Laboratory (OCTL) at data rates between 33 and 50 Mb/s. The gimbaled terminal relied on beacon-assisted acquisition and tracking, using a 976 nm uplink beacon transmitted from the ground station. Instead, the OOK modulation format was selected for the implied simplicity in the receiver design and the availability of commercial components for driver and synchronization electronics [72]. Apart from coding, the system relied on aperture averaging and looping of the transmitted video to provide diversity against turbulence, as well as a multi-beam beacon.

During its operational campaign in 2014, eighteen successful communication sessions were completed, including several daytime passes, demonstrating the robustness of optical communications under realistic operational conditions [73, 74]. Beyond the initial technology demonstration, OPALS was subsequently used to investigate several aspects of OFL performance. Extended mission campaigns characterized the vibration environment of the ISS and assessed its impact on optical pointing stability [75]. Furthermore, one of the first demonstrations of AO-assisted optical communications from space was conducted using a Boeing AO testbed installed at OCTL [76]. In March 2015, atmospheric distortions affecting the received optical signal were successfully corrected in real time, allowing for the first time efficient coupling of the downlink signal into a SMF despite the high slew rate characterizing the LEO link [77]. This experiment highlighted the importance of AO for future coherent OFLs and anticipated technologies that would later be investigated more extensively in the Alphasat campaigns.

While OPALS focused on demonstrating practical space-to-ground optical communications, Japan pursued the development of highly miniaturized optical terminals through the Space Optical Communications Research Advanced Technology Satellite (SOCRATES) mission [78]. Launched in 2014 and inserted into a sun-synchronous orbit at 600 km, the 48-kg microsatellite carried the Small Optical TrAnsponder (SOTA), a compact optical communication terminal specifically designed for small spacecraft. One of the principal goals of the project was to demonstrate that meaningful optical communication capabilities could be implemented within the stringent mass, volume, and power constraints typical of microsatellites.

The SOTA terminal had a mass of only 6.2 kg and consumed less than 40 W, making it one of the smallest optical communication payloads ever flown at the time [78]. The system employed multiple laser transmitters operating at wavelengths of 800 nm, 975 nm, and 1549 nm, thereby enabling both conventional communication experiments and investigations related to quantum communications. Unlike previous systems, SOTA was specifically designed to evaluate the suitability of the 1.5 μm wavelength region for satellite optical communications. This wavelength range was particularly attractive because of the maturity of terrestrial fiber-optic technologies and the availability of low-cost commercial components [79]. For what concerns turbulence mitigation, error correction via RS and Low-Density Generator-Matrix (LDGM) codes was implemented.

The engineering model of SOTA included a fork mount gimbal and five apertures. In detail, the acquisition and tracking sensors shared the same 23-mm aperture, while the 1.55 μm Tx/Rx aperture wss 50 mm wide. Of the remaining three apertures, one wss coupled with the 975 nm laser, and the other two were used for the Quantum Key Distribution (QKD) experiments. For the downlink, two data rates could be selected, i.e., 1 Mb/s and 10 Mb/s.

Between 2014 and 2016, SOTA successfully established optical links with several international OGSs operated by NICT, DLR, National Center for Space Studies (CNES), ESA, and Canadian Space Agency (CSA). Communication experiments were conducted at data rates up to 10 Mb/s, while extensive measurements of atmospheric propagation effects were collected. The campaigns provided valuable information on scintillation, irradiance statistics, and wavelength-dependent propagation effects [80–82]. To characterize coding performance, the BER was

measured both before and after applying the FEC code, showing that the LDGM scheme can correct errors extending up to 35% of the data, slightly lower than the theoretical 38% value [83].

In addition to classical communications, SOTA became one of the first space-borne platforms used to investigate quantum communication concepts. Dedicated experiments exploited polarization-encoded optical signals transmitted in the 800 nm band to evaluate the feasibility of satellite-based QKD. Measurements demonstrated that polarization states could be preserved through atmospheric propagation with sufficient fidelity to support future quantum communication protocols [84]. These experiments effectively bridged the fields of optical communications and quantum information science, paving the way for subsequent dedicated quantum communication missions.

The most prominent of these was the Chinese Micius, launched in 2016 as part of the Quantum Experiments at Space Scale program. Although Micius is primarily known for its groundbreaking quantum communication demonstrations, it also carried a sophisticated coherent optical communication terminal. The Micius Coherent Laser Communication Demonstration (MCLCD) established a duplex optical link between the satellite and a dedicated OGS in Nanshan, China. The downlink employed coherent communication at 1550 nm using Differential Phase-Shift Keying (DPSK) modulation and supported data rates up to 5.12 Gb/s, while the uplink used a 1064 nm 16-PPM signal at 20 Mb/s [85].

The coherent transmitter incorporated a highly stable narrow-linewidth laser source combined with a master-oscillator power-amplifier architecture capable of delivering nearly 3 W of optical power. During in-orbit demonstrations, the system achieved an average downlink BER of approximately $1.9 \cdot 10^{-9}$ over a communication session lasting 306 s, despite the absence of AO compensation. At the same time, the uplink BER was below 10^{-6}. The mission therefore demonstrated that coherent multi-gigabit optical communications between LEO satellites and ground stations is feasible using relatively compact terminals.

In parallel with these developments, the increasing popularity of CubeSats and small satellites stimulated the emergence of highly-compact optical communication payloads. Among the most influential programs was DLR's Optical Space Infrared

Downlink System (OSIRIS), initiated to address the growing demand for high-throughput DTE communications from small EO satellites. The program adopted a New Space philosophy based on extensive use of commercial components, low power consumption, and highly compact system architectures.

The first OSIRIS demonstrations, known as OSIRISv1 and OSIRISv2, were conducted aboard the Bispectral Infrared Optical System (BiROS) and Flying Laptop (FLP) satellites. OSIRISv1 achieved data rates of up to 200 Mb/s using body pointing alone with star cameras as reference, while OSIRISv2 increased the throughput to 1 Gb/s through tighter beam divergence and beacon-assisted pointing [86]. The CCSDS standard for optical OOK was adopted for what concerns physical layer parameters [87].

Building on these successes, DLR developed OSIRIS4CubeSat, later known as CubeLCT, i.e., a miniaturized optical terminal with dimensions smaller than $10 \times 10 \times 3$ cm^3, a mass of only 395 grams, and power consumption below 10 W [88]. Despite its compact size, the terminal supported optical downlinks of up to 100 Mb/s with only 150 mW of transmission power, demonstrating that laser communication systems could be integrated into even the smallest satellite platforms. To this end, OSIRIS4CubeSat relied on a hybrid pointing approach, i.e., while the CubeSat bus had to provide a pointing accuracy within $\pm 1^\circ$, the terminal was equipped with a highly precise pointing unit which compensated for the residual offsets of the platform's Attitude Control System (ACS).

At the same time, OSIRISv3 was developed to target the highest possible data rates from small LEO spacecrafts. While aiming at 10 Gb/, the lower input data rates of the EO payload constituted the bottleneck. Nonetheless, the adoption of a mass memory to buffer mission data before downlink transmission overcame this problem. Differently from OSIRISv1 and v2, OSIRISv3 used a Coarse Pointing Assembly (CPA) combined with a larger aperture to achieve the desired data rates. This translated to a 5 kg terminal with 50 W of power consumption [86, 89].

Another important contribution to CubeSat optical communications came from NASA's Optical Communications and Sensor Demonstration (OCSD). The mission employed two 1.5-U CubeSats and aimed to demonstrate optical downlinks from CubeSats to 30-cm ground terminals while simultaneously validating proximity-

navigation technologies [90]. However, an additional 80-cm OGS was also utilized [91, 92].

A schematic view of the AeroCube-OCSD, which embarked the optical payload, is shown in Fig. 1.10. The downlink laser beam is amplitude-modulated at 1064 nm and amplified. While a two-stage amplifier was flown in the AeroCube-OCSD-A demonstrator, a one-stage laser was used for the AeroCube-OCSD-B and -C, reducing the output power from 6 W to 2 W, and limiting the data rate to 600 Mb/s [92, 93].

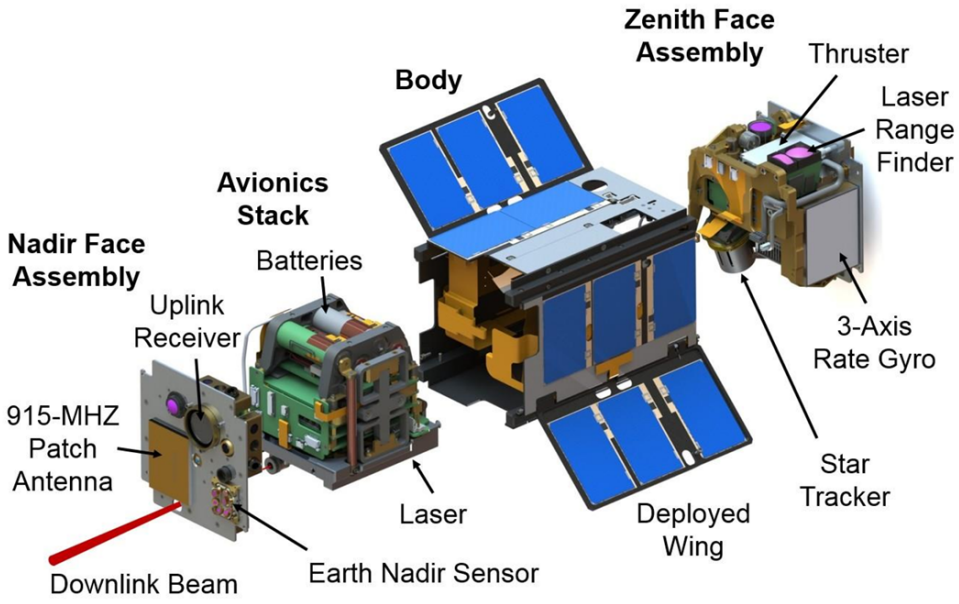


Figure 1.10 – Exploded schematic view of the AeroCube-OCSD CubeSat [91]

The AeroCube-B and -C were launched on November 13, 2017, and deployed to a nominal height of 450 km. The platform architecture did not encompass a gimbal or any internal beam steering hardware to reduce SWaP and costs. Nonetheless, this solution required milliradian beam divergence to sustain the body steering approach, thus reducing optical intensity. Consequently, the Aerospace Corporation developed cm-scale star trackers to provide the necessary attitude references, making the uplink beacon not necessary. Nor a downlink beacon was employed, making closed-loop pointing possible by using the incoming communication signal [94]. BER measurements were performed at 50, 100, and 200 Mb/s. During

the best pass, about 77% of the time intervals were error free, while 92% had BERs below 10^{-6}. Instances of higher BER could be observed, presumably due to transient pointing errors.

In addition to achieving optical communication links from LEO, OCSD participated in one of the first CubeSat optical crosslink pointing experiments. Together with the Integrated Solar Array and Reflectarray Antenna (ISARA) satellite, the mission demonstrated the ability of small spacecraft to perform autonomous optical acquisition and tracking based on precision ephemerides and onboard sensors. These experiments showed that optical crosslinks could eventually become feasible even within CubeSat constellations, despite the nearby targets and relevant slew rates made pointing and tracking a challenging task [95].

The trend toward extreme miniaturization continued with Japan's Very Small Optical Transponder (VSOTA), flown aboard the Rapid International Scientific Experiment Satellite (RISESAT) micro-satellite in 2019. VSOTA can be regarded as the successor to SOTA, maintaining the objective of providing optical communication capabilities for small satellites while further reducing size, mass, and complexity. The complete terminal weighed only about 700 g and employed laser transmitters at 980 nm and 1540 nm [96]. The VSOTA specifications are summarized in Table 1.6. Although the supported data rates were relatively modest, ranging from a few kilobits per second to approximately 100 kb/s [97], the mission focused on validating body-pointing-based optical communications, simplified terminal architectures, and low-cost implementations suitable for widespread deployment. In particular, the ACS of RISESAT was required to achieve an attitude pointing accuracy of 0.1° at 980 nm and 0.04° at 1540 nm [98].

1.2.5 Toward operational optical relay and feeder-link systems

The period beginning in 2020 represents a new phase in the evolution of optical satellite communications. Whereas the preceding decade was largely dedicated to demonstrating the feasibility of optical relay architectures and miniaturized communication terminals, later developments focused on transforming these technologies into operational communication infrastructures. Attention shifted toward

Table 1.6 – VSOTA specifications [96]

Parameter	**Value**
Mass	0.7 kg
Power consumption	<10 W
Link distance	<2000 km
Wavelengths	980 nm/1550 nm
Beam spread angle	3.5 mrad/1.3 mrad
Transmission power	270 mW/40 mW
Waveform	NRZ

OFLs, motivated by the rapidly increasing capacity demands of broadband satellite networks and EO missions. As a consequence, the principal technological challenges was no longer limited to acquisition and tracking but increasingly involved atmospheric turbulence mitigation, AO, advanced coding techniques, and the implementation of highly reliable optical gateways capable of supporting multi-Gigabit and eventually Terabit-class communication services.

One of the most important milestones of this period was NASA's Laser Communications Relay Demonstration (LCRD), launched in December 2021. The mission aimed at demonstrating bidirectional FSO links between GEO and ground, characterizing the system performance under variable conditions, and testing standards for optical relay links [99]. The payload employs two independent optical space terminals connected through an onboard switching unit, enabling bidirectional optical communications between GEO and ground stations as well as relay configurations involving airborne and spaceborne users. Each terminal incorporates a 10-cm Cassegrain telescope mounted on a two-axis gimbal, together with integrated modems and autonomous ATP functions. The high-level payload architecture is shown in Fig. 1.11. The modem was originally designed to support both PPM and DPSK communication formats, with uncoded rates up to 2.88 Gb/s. With FEC coding, the user data rates range between 2 Mb/s and 1.24 Mb/s.

Dedicated optical ground stations were deployed in Haleakalā, Hawaii, and

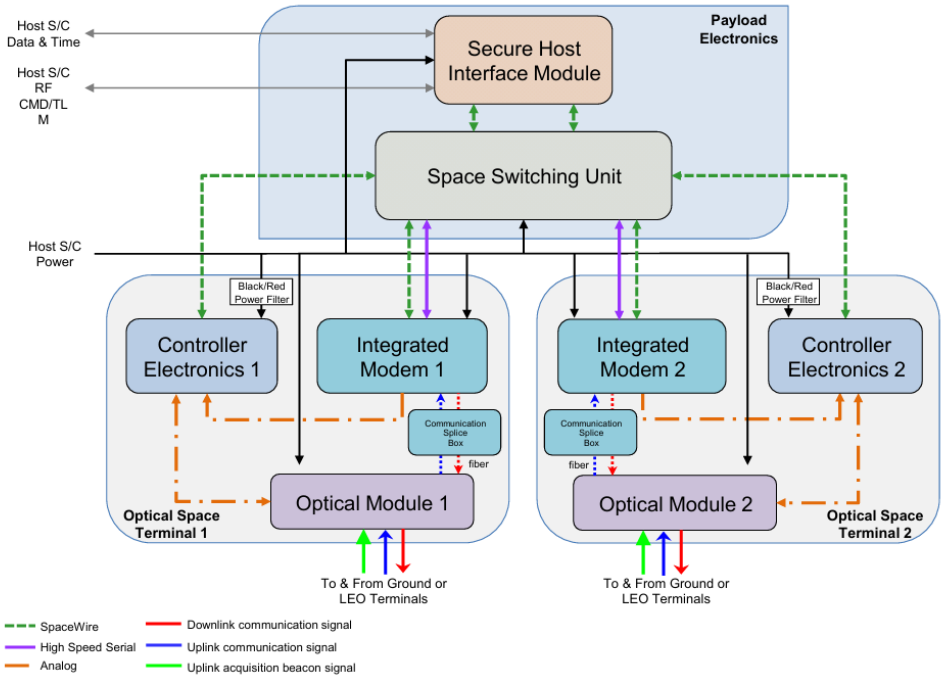


Figure 1.11 – LCRD payload architecture [99]

at the OCTL facility in California. The latter, also-called OGS1, is the primary ground terminal for the experiment and features a 1-m telescope with a AO system. In uplink, four beams separated by at least 20 cm are used to reduce turbulence effects on the beacon, while a 20-μrad single beam with tip/tilt correction is used for communication [99, 100].

The mission supports DTE, relay, and loopback configurations, allowing researchers to isolate and analyze the individual effects of uplink and downlink propagation. Experimental campaigns demonstrated the capability to transfer approximately 40 Gbit of data in only a couple of minutes under favorable atmospheric conditions [101], while simultaneously generating one of the most comprehensive datasets available on turbulence-induced fading, beam wander, scintillation, and link availability in GEO OFLs for both uplink and downlink transmission directions.

Regarding relay operations, the first user of LCRD was the Integrated LCRD Low Earth Orbit User Modem and Amplifier Terminal (ILLUMINA-T) onboard

the ISS [102, 103]. Between 2023 and 2024, physical layer and networking experiments were conducted. The former focused on ATP and link performance characterization, while the latter were devoted to data routing using the Delay/ Disruption Tolerant Network (DTN) protocols [103].

In parallel, Japan advanced the development of operational optical relay services through the Laser Utilizing Communication System (LUCAS) [104]. Conceived as the successor to OICETS and inspired by the European EDRS architecture, LUCAS was developed to provide high-speed optical relay services between GEO and LEO satellites. The GEO relay satellite carrying the LUCAS terminal was launched in November 2020, while user terminals were subsequently integrated into EO missions such as Advanced Land Observing Satellite-4 (ALOS-4). The system employs OISL operating in the 1550 nm wavelength band, leveraging the extensive technological ecosystem developed for terrestrial fiber-optic communications. Bidirectional communication rates of up to 1.8 Gb/s are supported, while the feeder link continues to rely on Ka-band RF communications to guarantee high service availability under adverse weather conditions. The main specification of LUCAS are reported in Table 1.7.

Table 1.7 – LUCAS specifications [105]

Parameter	**Value**	
	Return link (LEO-GEO-GND)	Forward link (GND-GEO-LEO)
Pre-FEC data rate	2.5 Gb/s	60 Mb/s
Post-FEC data rate	1.8 Gb/s	50 Mb/s
Link quality (BER)	10^{-5}	10^{-6}
Wavelength	1560 nm	1540 nm
Modulation	DPSK	IM/DD

The LUCAS architecture introduces several innovations compared with earlier optical relay systems. Both GEO and LEO terminals employ beaconless acquisition techniques, using wavelength and polarization multiplexing to separate transmitted and received optical signals. Optical powers of approximately 3 W are com-

bined with compact apertures of 140 mm and 90 mm for GEO and LEO terminals, respectively. Extensive in-orbit testing confirmed the effectiveness of the acquisition and tracking architecture, with average acquisition times of approximately 50 s and residual tracking errors below one microradian [105]. In September 2024, the first OISL between LUCAS and ALOS-4 was successfully established, followed shortly thereafter by real-time transmission of SAR data through the complete relay chain. During one demonstration, more than thirty minutes of continuous observation data were transmitted in real time through the optical relay system, confirming the readiness of the architecture for operational EO services.

Although LUCAS employs RF feeder links operationally, the system has also become an important experimental platform for OFL research. Joint campaigns conducted by JAXA and NICT established bidirectional GEO-to-ground optical links between LUCAS and the NICT OGS in Okinawa. These experiments investigated atmospheric propagation effects at 1540 nm and 1560 nm, validating both lognormal and Gamma–Gamma channel models and quantifying aperture-averaging effects through simultaneous measurements with 5-cm and 1-m receiving apertures [106, 107]. The experiments confirmed that large-aperture telescopes substantially reduce scintillation and increase channel coherence times. These results led NICT and JAXA, in collaboration with Nagoya Institute of Technology (NITech), to test a FEC-coded OFL data transmission by implementing both the Digital Video Broadcasting–Satellite Second Generation (DVB-S2) and Fifth-Generation (5G) New Radio (NR) Low Density Parity-Check (LDPC) next-generation codes. The results confirmed the superiority of the LDPC codes with respect to the RS one [108].

The increasing maturity of optical relay systems has also stimulated the development of next-generation communication terminals intended for large-scale optical networking. TESAT has expanded its LCT portfolio through the SCOT family, targeting applications ranging from CubeSat constellations to GEO relay satellites. The SCOT80 terminals are currently deployed within the U.S. Space Development Agency (SDA)'s LEO constellation [62], while larger SCOT135 terminals target communication rates up to 100 Gb/s over GEO-scale distances [62]. At the opposite end of the spectrum, the SCOT20 terminal aims to bring opti-

cal communications to CubeSat-class platforms through highly compact terminals capable of supporting both space-to-ground links and inter-satellite links [62].

A further step is represented by the HIgh-speed Communication with Advanced Laser Instrument (HICALI) program developed by NICT. Scheduled for launch aboard ETS-9, HICALI aims to demonstrate bidirectional 10-Gb/s-class optical communications between GEO and ground using 1.5-μm laser technology. In contrast to earlier missions, HICALI is explicitly designed as a feeder-link technology demonstrator and focuses on validating advanced modulation formats, high-speed photonic components, and atmospheric mitigation techniques [109]. To support these experiments, NICT has developed a dedicated ground infrastructure known as HICALI-GATE, consisting of multiple OGSs distributed across Japan, including fixed and transportable facilities [110].

At the same time, Europe has initiated one of the most ambitious OFL programs to date through the TELEO demonstrator [111]. Developed by Airbus and CNES, TELEO was conceived as an in-orbit precursor for future Terabit-class OFLs intended for Very High Throughput Satellite (VHTS) systems. The payload was integrated aboard the BADR-8 GEO satellite, launched in 2023, and is accompanied by a dedicated network of OGSs including ESA's Adaptive Optical Ground Station (A-OGS), the French Optical Ground Station (FrOGS), and ONERA's FEELINGS facility.

The TELEO payload incorporates a flight terminal prototype featuring a 260-mm telescope, a 5-W optical amplifier, and a transceiver operating at 10 Gbaud downlink NRZ-DPSK and uplink NRZ-OOK. The terminal relies on a beacon at 1600.22 nm for ATP. Downlink experiments performed during 2024 successfully demonstrated AO-assisted reception and SMF coupling, while uplink campaigns focused on AO pre-compensation techniques [112–114]. Particular attention was devoted to the interaction between atmospheric fading and modern coding schemes based on LDPC codes and long interleavers, highlighting the importance of jointly optimizing optical and digital mitigation techniques.

1.2.6 Optical communications for small satellites and CubeSat constellations

In parallel with the development of operational optical relay infrastructures, the early 2020s witnessed a rapid expansion of optical communication technologies toward small satellites and CubeSat platforms. Advances in photonic integration, miniaturized pointing systems, and low-power laser transmitters enabled optical terminals that previously required tens of kilograms of mass and hundreds of watts of power to be implemented on spacecraft weighing only a few kilograms. These developments are particularly relevant for future distributed satellite architectures, where optical links are expected to provide high-capacity connectivity between large constellations of small spacecraft.

One of the first demonstrations of this new generation of terminals was the previously mentioned CubeLCT, which was flown aboard a 3U CubeSat. Designed specifically for nanosatellite and CubeSat applications, CubeLCT integrates a complete optical communication system including telescope, acquisition and tracking sensors, communication electronics, and laser transmitter within a compact package. This was possible thanks to a new design concept in which the Printed Circuit Board (PCB) is used as optical bench. The terminal, operating in the C-band, adopted the CCSDS optical OOK standard combined with RS coding [115].

DLR decided to adapt the CubeLCT technology into the OISL domain, thus starting the project CubeISL. The objective of CubeISL was to enable bidirectional 100 Mb/s links over distances up to 1500 km, while improving DTE capabilities up to 1 Gb/s [88]. Another version of the terminal, namely OSIRIS4QUBE, was developed to extend the LCT capabilities from classical FSO communication to QKD on CubeSats [116].

Another development was the CubeSat Communication Active Terminal (CubeCAT) mission, which also sought to validate miniaturized optical communication hardware in orbit using a CubeSat platform. With a 1U volume, an effective 1 kg mass, and a 1 Gb/s data rate, CubeCAT recently achieved the highest bitrate for a terminal of its size, weight, and power [117].

Similarly, the Laser Infrared CrosslinK (CLICK) program was designed to demonstrate low-cost optical crosslinks between CubeSat-class spacecrafts [118].

The program investigated compact pointing systems, integrated photonic architectures, and autonomous link establishment procedures. The first CLICK paylaod, namely CLICK-A, was launched on the ISS in 2022 and demonstrated the terminal capability to achieve sufficient fine pointing accuracy without pointing feedback. Other two terminals, CLICK-B and CLICK-C, will be deployed to validate crosslink performance [119].

Another important mission is the CubeSOTA one, developed by NICT [120]. Building upon the heritage of the SOTA and VSOTA experiments, CubeSOTA aims to demonstrate optical LEO-HAP and LEO-ground links. In detail, LEO-HAP links could provide an alternative to the hundreds of RF gateways required to bring mega-constellation traffic down to Earth. Indeed, this architecture can potentially decouple the negative effects due to long distance and atmospheric impairments. This is possible thanks to the LEO-HAP link being exempt from atmospheric turbulence, while the shorter HAP-to-ground link can exploit high-power Erbium-Doped Fibre Amplifier (EDFA) and larger apertures to overcome atmospheric impairments while still providing hundreds of Gb/s data rates. Moreover, CubeSOTA is envisioned to demonstrate the first ground-to-LEO uplink combining EDFA and SMF coupling. Lastly, CubeSOTA will showcase the narrowest laser beam transmission from a CubeSat thanks to its 9-cm telescope and beam divergence control system.

Among the most significant demonstrations of high-rate optical communications from small satellites was NASA's TeraByte InfraRed Delivery (TBIRD) mission. Integrated aboard the Pathfinder Technology Demonstrator-3 (PTD-3) CubeSat launched in 2022, TBIRD was specifically developed to investigate extremely high-throughput optical downlinks from LEO. The terminal, shown in Fig. 1.12, relies on high-speed solid state drives to feed 100 Gb/s COTS fiber transceivers. The 1550 nm outputs from the two coherent transceivers are coupled by means of a WDM multiplexer and sent through a 1 W EDFA. Thus, the space terminal is capable of transferring 200 Gb/s data through a 22-mm aperture [121]. However, the commercial transceivers alone would not make this possible due to turbulence-induced fading. Thus, an ad-hoc ARQ protocol was designed and implemented onboard to make the link error-free [122]. Specifically, the ARQ protocol exploits the uplink beam to concurrently transmit 2-PPM-modulated feedback

messages at 5 kb/s, while also serving as a beacon. Spatial diversity and RS coding are used in uplink to combat fading.

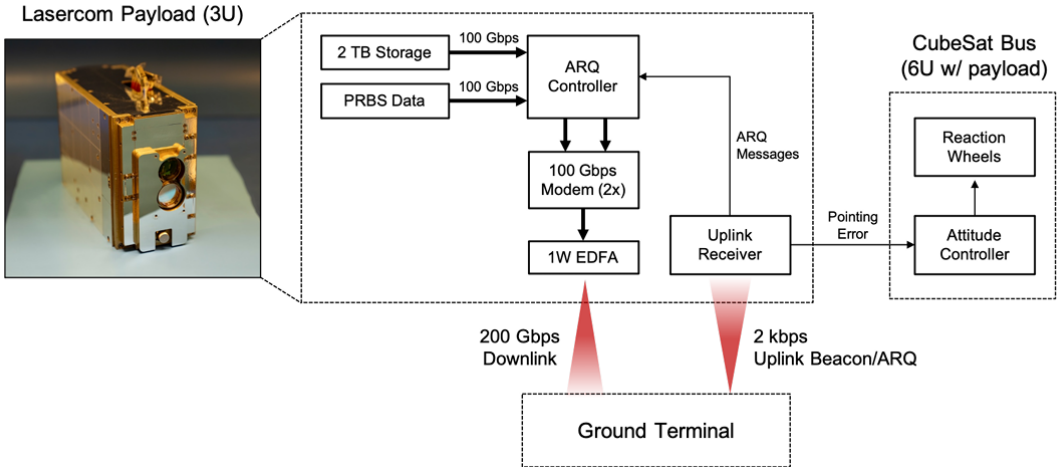


Figure 1.12 – High-level block diagram of the TBIRD PTD-3 mission [121]

Pointing relies entirely on the bus reaction wheels, while the beacon-assisted ATP allows the terminal to achieve the required fine pointing accuracy.

A 6U CubeSat developed by Tyvak Nanosatellite hosts the TBIRD 3U payload. Instead, a 40-cm telescope with back-end AO is used at the ground facility.

Orbiting at an altitude of 500 km, the system successfully achieved record-breaking transmission rates of up to 200 Gb/s from a CubeSat platform [123]. The highest data volume delivered during a single pass was 4.8 TB over 5 minutes, when Doppler compensation was active [124]. These results represented an increase of several orders of magnitude compared with earlier CubeSat optical communication demonstrations and established a new benchmark for space-to-ground optical communications. The mission demonstrated that optical links could provide data rates comparable to terrestrial fiber-optic systems while remaining compatible with the severe size and power constraints of small satellites.

A last interesting mission is the Polarization-modUlated Laser Satellite Experiment (PULSE-A) one that aims to investigate the feasibility of Circular Polarization Shift Keying (CPolSK) OFLs [125]. An advantage of this modulation format is its ability to be detected regardless of variations in transmitter and receiver orientations, making it appealing for dynamic scenarios.

1.3 Thesis' scope and summary of contributions

The state of the art reviewed in the previous sections shows that optical satellite communications have undergone remarkable progress over the last three decades. OISLs have evolved from experimental demonstrations to operational systems and are currently deployed in commercial satellite networks. In contrast, OFLs, despite their recognized potential for supporting future integrated TN and NTN, remain largely at the demonstration stage. While several successful experiments have validated the feasibility of high-capacity optical links between space and ground, fully operational OFL systems are still limited, and many technological challenges remain open.

A major difficulty lies in the strong dependence of OFL performance on atmospheric propagation conditions. Unlike fiber-optic channels, whose characteristics are essentially static, optical wireless channels are affected by atmospheric turbulence and pointing impairments which introduce random fluctuations in the received signal. The problem is further exacerbated in LEO satellite scenarios, where the continuous variation of the satellite elevation angle results in a time-varying propagation geometry and therefore in a non-stationary channel. Consequently, the design of OFLs cannot rely solely on hardware developments or qualitative assessments of atmospheric effects but requires accurate engineering tools capable of predicting system performance under realistic operating conditions.

In this context, the link budget represents one of the fundamental instruments for OFL design. Starting from the characteristics of the transmitter, the propagation channel, and the receiver, the link budget allows the estimation of the received optical power and the evaluation of link feasibility. Such an analysis must account for all relevant gain and loss mechanisms, including geometric spreading, atmospheric attenuation, turbulence-induced effects, pointing errors, and hardware impairments. However, because the atmospheric channel is inherently stochastic, the received power cannot be treated as a deterministic quantity. Instead, it must be characterized through suitable statistical models capable of describing the temporal evolution of fading and its impact on communication performance metrics such as SNR, BER, Frame Error Rate (FER), and link availability.

Although analytical and numerical models provide valuable insight into system behavior, experimental validation remains essential. The growing availability of COTS transceivers developed for terrestrial fiber-optic communications offers an attractive opportunity to accelerate the deployment of OFLs. Nevertheless, these devices are inherently designed for channels whose impairments differ substantially from those encountered in FSO propagation. In particular, turbulence-induced scintillation generates power fluctuations occurring over timescales of milliseconds, which are several orders of magnitude longer than the bit duration and may result in burst errors and frame losses. Therefore, the suitability of such transceivers for OFL applications must be carefully assessed through dedicated experimental investigations.

Direct testing through field campaigns is often impractical due to their high cost, limited availability, and poor repeatability. Consequently, laboratory testbeds capable of reproducing realistic atmospheric fading conditions become key enablers. By generating controlled and repeatable turbulence- and jitter-induced fading conditions, these platforms allow systematic testing of communication equipment and mitigation strategies over a wide range of operating scenarios. The importance of such approaches has been demonstrated in several recent missions, including TBIRD, where channel emulators were extensively employed during system validation and protocol development prior to launch [126].

The need for reliable performance prediction extends beyond the PHY layer. Experimental demonstrations have shown that coding, interleaving, retransmission schemes, and other digital mitigation techniques can significantly improve link availability and throughput in the presence of atmospheric fading. However, the design and optimization of these techniques require a detailed characterization of fade statistics, including fade depth, duration, and temporal correlation. As a result, accurate numerical tools capable of evaluating the interaction between atmospheric impairments and communication protocols are increasingly required to support the design of future OFL systems.

The objective of this thesis is to address these challenges by developing a set of complementary numerical and experimental tools that support the design, validation, and optimization of OFLs. Rather than focusing on a single aspect of the communication chain, the proposed approach covers the entire PHY layer, from

optical propagation and link budget analysis to experimental validation and assessment of digital mitigation techniques. The developed framework is summarized in Fig. 1.13 and consists of three main contributions.

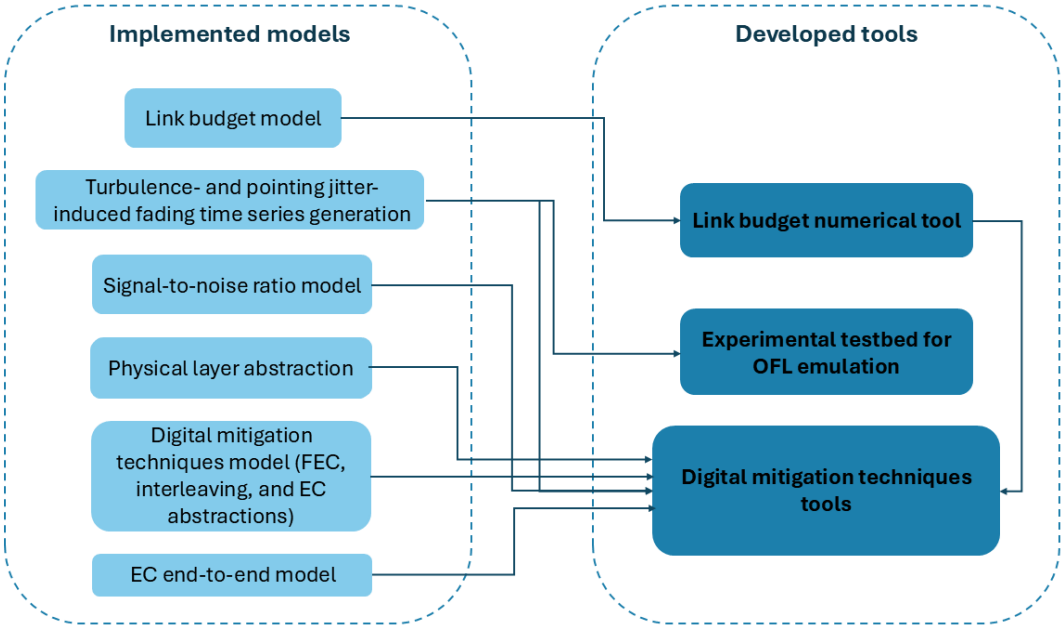


Figure 1.13 – Overview of the developed framework for the analysis and design of OFLs

The first contribution is a flexible Matlab-based tool for the design and performance evaluation of both ground-to-space and space-to-ground OFLs. At the core of the tool lies a comprehensive link budget model specifically developed to accurately quantify atmospheric propagation impairments while accounting for the fundamental differences between uplink and downlink propagation. Particular emphasis has been placed on turbulence-induced effects, including scintillation, beam spreading, beam wander, as well as on pointing losses. Furthermore, a dedicated investigation of beam wander modeling has been conducted, highlighting for the first time the impact of commonly adopted geometrical approximations on the accuracy of performance predictions. The developed model has been validated through comparison with measurement results reported in several experimental campaigns and provides a versatile framework for OFL dimensioning and feasibil-

ity assessment. The methodology, implementation details, and validation results are presented in Chapter 2.

The second contribution addresses the experimental validation of communication equipment through the development of an all-fiber OFL channel emulator. The proposed testbed is capable of reproducing both turbulence- and pointing-jitter-induced fading by generating realistic time-varying attenuation profiles representative of specific propagation scenarios. Unlike existing solutions, the developed platform combines flexibility, repeatability, and ease of configuration, enabling systematic performance evaluations under controlled laboratory conditions. The testbed has been employed to experimentally assess the behavior of commercial IM/DD and coherent fiber-optic transceivers under realistic OFL fading conditions, providing valuable insight into their suitability for future space applications. The architecture of the emulator, the adopted fading generation methodology, and the obtained experimental results are discussed in Chapter 3.

The third contribution concerns the development of end-to-end numerical tools for the design and evaluation of digital mitigation techniques. To this end, additional modules have been integrated with the link budget framework to provide a complete abstraction of the PHY layer and to estimate HL performance metrics, including FER. The resulting framework enables the analysis of the combined effects of atmospheric fading, receiver noise, channel coding, and interleaving. Building upon this abstraction, two complementary tools have been developed. The first, implemented entirely in Matlab, relies on analytical abstractions of both PHY and HL error-control mechanisms, enabling rapid system-level evaluations. The second, implemented through a combined Matlab/C architecture, performs a complete simulation of HL EC coding, providing higher accuracy at the expense of increased computational complexity. Together, these tools enable the design and optimization of cross-layer mitigation techniques for OFLs, a topic that remains largely unexplored and not yet fully standardized. The tools' implementation and application are presented in Chapter 4.

Overall, the work presented in this thesis contributes to the development of a comprehensive design methodology for OFLs by combining accurate propagation modeling, realistic experimental validation, and advanced performance assessment tools. The proposed framework provides support throughout the entire design

process, from preliminary link dimensioning to the evaluation of communication equipment and mitigation strategies, thereby contributing to the maturation of OFL technologies for future integrated TN/NTN communication networks.

Chapter 2

Link Budget Model for OFLs

The design and performance assessment of OFLs require accurate prediction of the received optical power in both transmission directions. Unlike OISLs, OFLs are strongly influenced by atmospheric propagation effects that also differ from the ones experienced by RF feeder links, introducing large fluctuations in the received signal. Consequently, the development of reliable link budget models is essential for evaluating link feasibility, dimensioning system parameters, and estimating achievable performance under different operational conditions.

The received optical power depends not only on transmitter and receiver characteristics and on free-space propagation losses, but also on a variety of atmospheric phenomena acting on different spatial and temporal scales. Absorption and scattering attenuate the optical signal along its path through the atmosphere, while hydrometeors such as clouds, fog, rain, and snow can introduce severe additional losses. Furthermore, atmospheric turbulence causes random fluctuations of the refractive index that distort the optical wavefront and give rise to effects such as scintillation, beam spreading, beam wander, and SMF coupling efficiency degradation. The impact of these phenomena differs between uplink and downlink transmissions because of the asymmetric distribution of turbulence along the propagation path.

Firstly, this chapter reviews the literature models describing the impact that each element composing the OFL has on the propagating beam. Then, these models are combined to develop a flexible, comprehensive OFL link budget model capable of supporting the design of both space-to-ground and ground-to-space OFLs.

Subsequently, the proposed model and its numerical Matlab-based implementation are validated through comparison with results from representative OFL campaigns, demonstrating their capability to accurately predict system performance and supporting their use for the design and analysis of future OFL systems.

To conclude the chapter, the noise sources impairing OFLs are reviewed and exhaustive SNR models are presented. The SNR models have been implemented to extend the link budget tool capabilities and have been essential to develop the OFL PHY layer abstraction, later presented in Chapter 4.

2.1 System and channel models for OFLs

In the following, the geometrical parameters depicted in Fig. 2.1 will be used. Specifically, L is the link distance, i.e., the distance between the OGS and the satellite, H and h_{OGS} are the satellite and OGS altitudes, respectively, ζ the link elevation angle, i.e., the angle between the local horizontal plane at the OGS and the LoS to the satellite , R_E is the mean Earth radius, and d_{ATM} is the atmospheric propagation length.

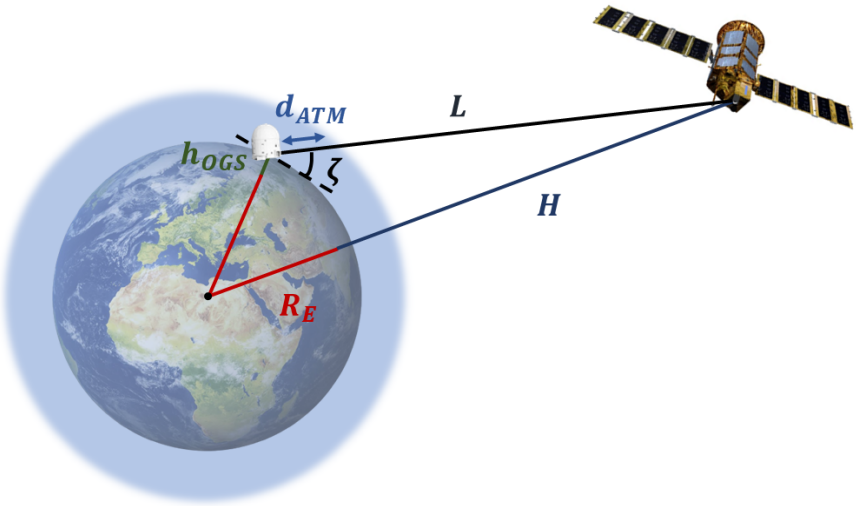


Figure 2.1 – OFL geometry

2.1.1 Transmitter

The transmitter is responsible for converting the source information into an optical signal, which encompasses the generation, shaping, and launching of the optical beam towards the receiver. From a link budget perspective, the transmitter determines the amount of optical power injected into the channel as well as the initial spatial characteristics of the propagating beam, which directly influence several propagation impairments experienced along the atmospheric path.

A typical OFL transmitter consists of a laser source, an electro-optic modulator, beam conditioning optics, a booster amplifier, and a transmitting telescope. The laser generates the optical carrier at the operating wavelength λ, while the telescope expands and collimates the beam in order to reduce its divergence and maximize the power collected by the receiver.

In detail, the beam emitted from the laser source can be modeled as a lowest-order TEM_{00} Gaussian-beam wave with effective beam radius, or spot size, W_0 [m] [127]. As shown in Fig. 2.2, W_0 denotes the radius at which the field amplitude falls to $1/e$ of that on the beam axis. Assuming the transmitter plane at $z = 0$, the emitted field can be expressed as

$$U_0(r, 0) = a_0 \exp\left(-\frac{r^2}{W_0^2} - \frac{ikr^2}{2F_0}\right) \tag{2.1}$$

where a_0 $[(W/m^2)^{1/2}]$ is the field amplitude, r is the radial distance from the beam center, k is the wave number, and F_0 [m] is the phase front radius of curvature. For a collimated beam, $F_0 = \infty$.

The beam spot size has its minimum value at the waist which, for a collimated beam, corresponds to W_0 and is related to the telescope aperture , D_T [m], by

$$D_T^2 = 8W_0^2 \tag{2.2}$$

Due to diffraction, the emitted beam will diverge with half-divergence angle $\theta_{e^{-2}}/2$ [rad], i.e., the radial angular distance where the intensity falls to $1/e^2$ of its peak value, given by

$$\frac{\theta_{e^{-2}}}{2} = \frac{\lambda}{\pi W_0} \tag{2.3}$$

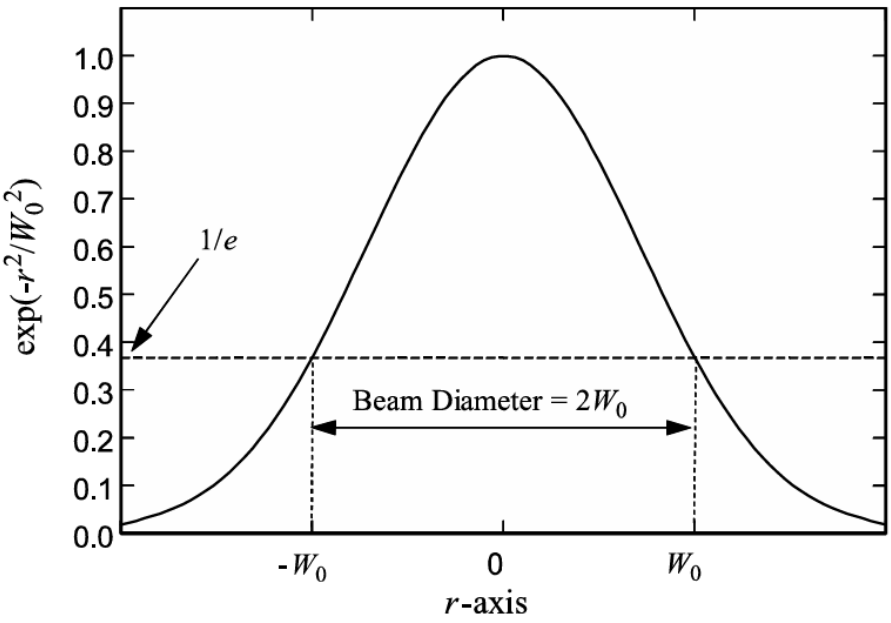


Figure 2.2 – Amplitude profile of a Gaussian-beam wave [127]

which is also related to the Full-Width at Half Maximum (FWHM) divergence angle θ_{FWHM} as

$$\frac{\theta_{e^{-2}}}{2} = \frac{\theta_{FWHM}}{\sqrt{2\ln 2}} \tag{2.4}$$

For the purpose of link budget analysis, the transmitter can be represented through three terms, i.e., the transmitted optical power P_T, the transmitter chain efficiency η_T, and the telescope gain G_T.

As shown in Eq. (2.5), the transmitting telescope's gain can be derived from the source solid emission angle Ω_T and depends on the operating wavelength and telescope aperture diameter D_T [128].

$$G_T = \frac{4\pi}{\Omega_T} \cong \left(\frac{4D_T}{\lambda}\right)^2 \tag{2.5}$$

The above expression implies that larger transmitter apertures or shorter wavelengths lead to higher gains. Nonetheless, as evident from Eq. (2.3), a larger aperture will also lead to a reduced beamwidth, thus making the link more prone to pointing errors.

2.1.2 Free-space propagation

An electromagnetic wave experiences diffraction which causes the beam to progressively expand as it propagates, thus reducing the optical power density at the receiver. In OFLs, where propagation distances can range from several hundred kilometers for LEO satellites to tens of thousands of kilometers for GEO systems, free-space loss L_{FS} represents one of the dominant contributions to the overall link attenuation. According to the Friis law

$$L_{FS} = \left(\frac{\lambda}{4\pi L}\right)^2 \tag{2.6}$$

The link distance L depends on the link geometry and varies with the satellite altitude and elevation angle. A coarse approximation based on the flat-Earth assumption, which is often encountered in optical beam propagation theory, is

$$L \cong (H - h_{OGS}) \sec(\xi) \tag{2.7}$$

where ξ [°] is the zenith angle between the OGS and the satellite, i.e., $\xi = 90 - \zeta$. A more accurate link distance approximation, derived as described in [129], but without neglecting the OGS altitude, is given by

$$L \cong -(R_E + h_{OGS}) \sin(\zeta) + [(R_E + H)^2 - (R_E + h_{OGS})^2 \cos^2(\zeta)]^{\frac{1}{2}} \tag{2.8}$$

As can be observed from Eq. (2.6), the free-space loss increases quadratically with the propagation distance and decreases with longer wavelengths. Therefore, despite the high directivity achievable with optical systems, the large distances involved in satellite communications make free-space attenuation a fundamental component of the OFL link budget.

2.1.3 Absorption and scattering

The atmosphere is a heterogeneous medium composed primarily of water vapor, carbon dioxide, nitrous oxide, carbon monoxide, and ozone, together with suspended particles such as aerosols, dust, and pollutants. The concentration of these constituents varies with altitude, geographical location, season, and meteorological conditions, making the atmospheric channel inherently variable.

As reported in Fig. 2.3, the atmosphere, which extends up to several hundred kilometers above the Earth's surface, can be divided into four primary layers, i.e.:

1. The troposphere, extending up to 11 km, is characterized by a decreasing air temperature that reaches -55°C. The next 9 km constitute the tropopause, over which the temperature stays constant. Together, the troposphere and tropopause form the lower atmosphere

2. The stratosphere extends from 20 km to 48 km. In this region, the temperature tends to increase with altitude due to UV sunlight absorption by the ozone. Another isothermal layer at about -3°C, known as stratopause, separates the stratosphere from the mesosphere

3. The mesosphere extends up to 80 km and features a decreasing temperature. It is followed by the mesopause, i.e., a third isothermal layer, which divides the mesosphere and the thermosphere. The stratosphere and mesosphere, together with the stratopause and mesopause, are commonly grouped into the so-called middle atmosphere

4. The last layer, i.e., the thermosphere, extends up to about 600 km. In this region, the Sun's energy causes a strongly increasing temperature. Most of the ionosphere and exosphere are included in the thermosphere, with the ionosphere extending from about 70 km up to around 1000 km.

As the optical beam propagates through the atmosphere, its interaction with molecules and particles leads to attenuation of the transmitted power. The two main physical mechanisms responsible for this are absorption and scattering. Absorption occurs when part of the optical energy is transferred to atmospheric molecules and converted into internal energy through molecular excitation processes. The entity of this effect strongly depends on the operating wavelength and on the concentration and size of the involved molecules. For this reason, optical communication systems are typically designed to operate within atmospheric transmission windows, where absorption losses are minimized.

Scattering, on the other hand, is caused by the interaction of the optical wave with molecules and particles suspended in the atmosphere, resulting in a redistribution of the optical energy away from the propagation direction. Depending

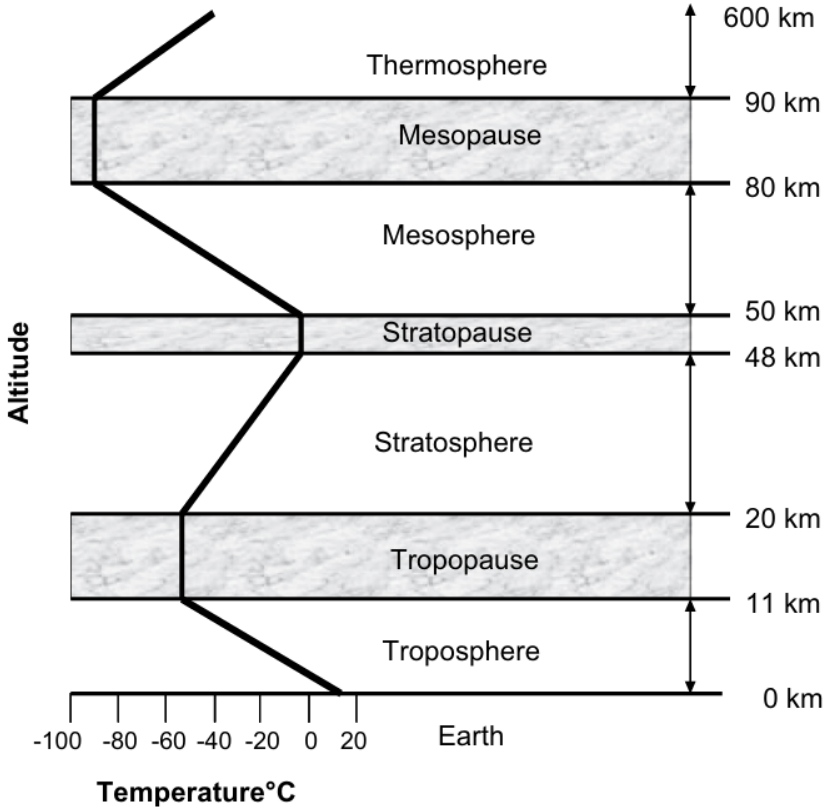


Figure 2.3 – Diagram of the atmospheric layers [127]

on the size of the scattering particles relative to the optical wavelength, different scattering regimes can be identified. Rayleigh scattering occurs when the particle dimensions are smaller than the signal's wavelength and is mainly associated with atmospheric molecules. Mie scattering arises when particle sizes are comparable to the wavelength and is typically generated by suspended aerosol particles. In this case, the scattered radiation is mainly concentrated in the forward direction. Finally, scattering induced by larger particles can be described by means of geometric optics.

Absorption and scattering are commonly grouped into a single phenomenon referred to as atmospheric extinction. The resulting atmospheric transmittance, τ_{ATM} [dB], can be described through the Beer–Lambert law as [130]

$$\tau_{ATM} = 10 \log_{10} \exp \left[- \int_0^{d_{ATM}} \alpha(\lambda, r) dr \right] \tag{2.9}$$

where $\alpha(\lambda, r)$ [m^{-1}] is the altitude- and wavelength-dependent atmospheric extinction coefficient. At lower elevations, reduced transmittance will be experienced due to the increased distance traveled through the atmosphere.

Atmospheric radiative transfer simulation packages, such as LOWTRAN, MODTRAN, and FASCODE, enable atmospheric transmittance calculations for different atmospheric conditions. For example, Fig. 2.4 shows the transmittance spectrum for a ground-to-space link and two h_{OGS} values, i.e., 0 km (sea level) and 2 km. Since the atmospheric density decreases with altitude, higher transmittance is observed for $h_{OGS} = 2$ km [131]. This suggests that locating the OGS at higher heights can effectively reduce extinction losses. Moreover, the plot evidences that a transmission window appears around 1550 nm, thus endorsing the increasing number of missions relying on this wavelength. Other factors supporting this choice include the possibility to transmit at higher power levels and the increased Maximum Permissible Exposure (MPE) for eye safety with respect to shorter wavelengths [128].

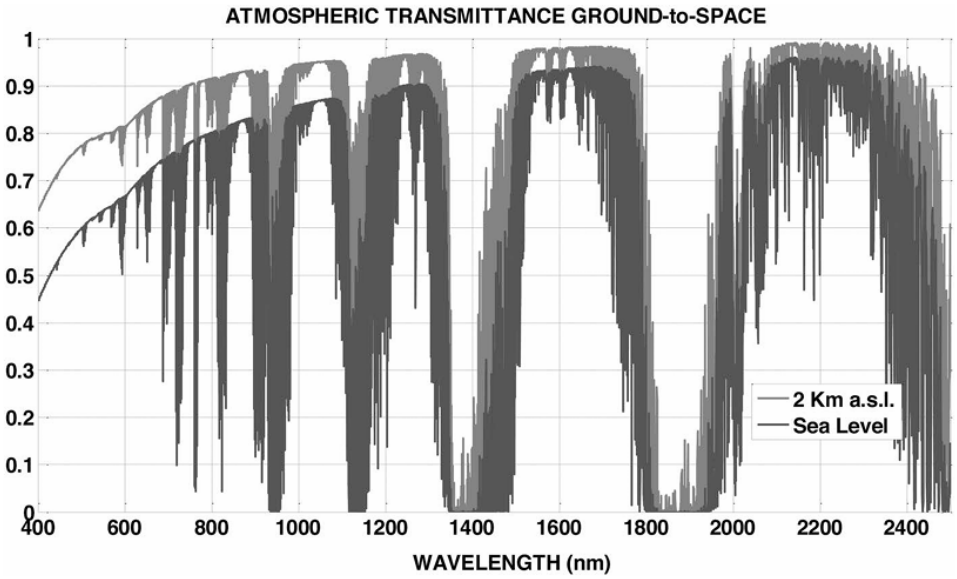


Figure 2.4 – Atmospheric transmittance in a ground-to-space link at zenith. A rural aerosol model with a visibility of 23 km is considered [131]

2.1.4 Optical turbulence

The propagation of an optical beam through the atmosphere is strongly influenced by atmospheric turbulence, which constitutes one of the main performance-limiting factors in OFLs. Atmospheric turbulence originates from the uneven heating of the Earth's surface caused by incident solar radiation. As a result, air masses located close to the ground generally exhibit higher temperatures than those at greater altitudes. The continuous exchange and mixing of warm and cold air masses generates random fluctuations in temperature and pressure throughout the atmosphere. Since the refractive index of air depends on its thermodynamic state, these fluctuations translate into random variations of the atmospheric refractive index, both in space and time. Such variations perturb the phase and amplitude of the propagating optical wave, giving rise to several degradation effects that will be discussed in the following sections. It is important to note that, unlike absorption and scattering, which mainly introduce deterministic attenuation, optical turbulence requires a statistical modeling of its effects.

A physical understanding of optical turbulence can be obtained by considering the atmosphere as a viscous fluid. Depending on the flow conditions, the motion of the fluid can be classified as either laminar or turbulent. In a laminar regime, the flow velocity exhibits a regular and predictable behavior, with adjacent fluid layers moving smoothly relative to each other. Conversely, in a turbulent regime, the flow becomes highly irregular and is characterized by random sub-flows known as turbulent eddies [127].

According to Richardson's cascade theory, when the wind velocity increases up to exceeding the critical Reynolds number, turbulent eddies are formed. As shown in Fig. 2.5, inertial forces cause the larger eddies to break up into smaller ones, forming a continuum of eddy sizes comprised between an outer scale L_0 and an inner scale l_0. Both scales vary with altitude, with typical values near ground ranging from 10 m to 100 m for what concerns L_0, and between 1 mm and 10 mm for what regards l_0 [128]. Eddies bigger than L_0 belong to the so-called input range, where the energy is injected into turbulence. Instead, eddies between the two scales define the inertial range, where turbulence is fully developed. Finally,

eddies smaller than the inner scale belong to the dissipation range, in which the residual energy is dissipated by viscous forces in the form of heat.

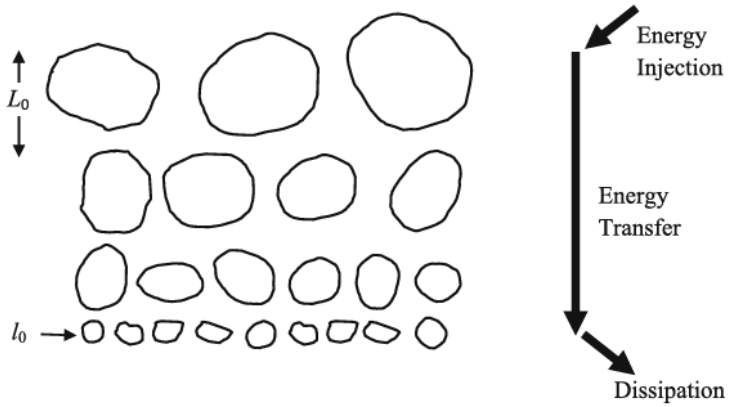


Figure 2.5 – Energy cascade theory of turbulence [128]

From a mathematical perspective, the atmospheric refractive index n can be represented as a random field

$$n(\mathbf{R}, t) = n_0 + n_1(\mathbf{R}, t) \tag{2.10}$$

where $n_0 = \langle n(\mathbf{R}, t) \rangle \cong 1$ is the mean value of n and $n_1(\mathbf{R}, t)$ represents its random deviation from the mean value [127]. Nonetheless, time variations are usually suppressed in the treatment of optical wave propagation, leading to the following dependence of n upon temperature and pressure fluctuations

$$n(\mathbf{R}) \cong 1 + 79 \cdot 10^{-6} \frac{P(\mathbf{R})}{T(\mathbf{R})} \tag{2.11}$$

In Eq. (2.11), P [mbars] is the pressure and T [K] is the temperature.

The theoretical framework most commonly adopted to describe turbulence is based on Kolmogorov's statistical theory, which assumes that the related random field is statistically homogeneous and isotropic within the inertial subrange. Under this hypothesis, the refractive-index structure function $D_n(R)$ is given as

$$D_n(R) = \langle [n(\mathbf{R}_1) - n(\mathbf{R}_2)]^2 \rangle = \begin{cases} C_n^2 R^{2/3}, & l_0 \ll R \ll L_0 \\ C_n^2 l_0^{-4/3} R^2, & R \ll l_0 \end{cases} \tag{2.12}$$

where $\mathbf{R}_1$ and $\mathbf{R}_2$ are two points in space separated by distance $R = |\mathbf{R}_2 - \mathbf{R}_1|$, $\langle ... \rangle$ is an ensemble average, and C_n^2 [$\mathrm{m}^{-2/3}$] is the refractive-index structure constant

or parameter. Starting from Eq. (2.12), it is possible to derive the 3D spatial power spectrum of the refractive-index random field, $\Phi_n(\kappa)$, as

$$\Phi_n(\kappa) = 0.033 \cdot C_n^2 \cdot \kappa^{-11/3} \quad \frac{1}{L_0} \ll \kappa \ll \frac{1}{l_0} \tag{2.13}$$

Equation (2.13) highlights that the Kolmogorov spectrum, despite being widely adopted in theoretical calculations, is limited to the inertial subrange. Other models have been proposed in the literature to extend the Kolmogorov spectrum, such as the Von Karman, Tatarskii, and modified Hill bump ones [127, 132].

The structure parameter C_n^2 is a measure of turbulence strength. Typically, under weak turbulence $C_n^2 \sim 10^{-16}$ m$^{-2/3}$ or less, while in strong turbulence $C_n^2 \sim 10^{-13}$ m$^{-2/3}$ or more [132]. Moreover, the parameter is not constant but exhibits significant variations both in time and space. Near the Earth's surface, measurements performed over 24-hour periods typically reveal a pronounced diurnal cycle. During daytime, solar radiation heats the ground, which in turn transfers heat to the surrounding air. The resulting temperature gradients generate convective motions and thermal plumes that increase the intensity of atmospheric turbulence. Consequently, C_n^2 usually reaches its maximum values around midday, when the temperature difference between the ground and the overlying air masses is largest. During nighttime, the atmosphere becomes more stable and C_n^2 generally assumes lower values. Minimum turbulence levels are commonly observed around sunrise and sunset, when the temperatures of the ground and the surrounding air become nearly equal and thermal convection is substantially reduced.

The vertical distribution of turbulence is closely related to the structure of the atmosphere. The Atmospheric Boundary Layer (ABL), which extends from the Earth's surface up to approximately 1–2 km of altitude during daytime, is the region where atmospheric dynamics are primarily driven by heat exchange with the ground. Within this layer, optical turbulence is generally strongest, with typical daytime values of C_n^2 ranging between 10^{-14} and 10^{-13} m$^{-2/3}$ [127]. Over relatively uniform terrain, the turbulence strength decreases with altitude according to a power law proportional to approximately $h^{-4/3}$, where h [m] denotes the height above ground level. Above complex terrains, such as mountainous regions, a slower decay has been observed. During nighttime, when the atmosphere is more stable, the decrease of turbulence strength with altitude is typically less pronounced [127].

For horizontal FSO links operating at approximately constant altitude, it is often reasonable to assume a uniform turbulence strength along the propagation path and therefore treat C_n^2 as a constant parameter. Conversely, for slant and vertical propagation paths, such as those encountered in OFLs, the optical beam traverses atmospheric layers characterized by significantly different turbulence levels. In these cases, the refractive-index structure parameter must be modeled as a function of altitude, and appropriate altitude-profile models are required to accurately describe the atmospheric channel.

Several empirical models have been developed to represent the vertical profile of C_n^2 based on experimental measurements. These models constitute a fundamental input for the calculation of turbulence-induced effects. Among the available formulations, the Hufnagel-Valley (HV) model is the most widely adopted in the analysis of OFLs. Its expression is given in Eq. (2.14), where w [m/s] is the rms wind speed and A [$m^{-2/3}$] is the nominal value of the structure parameter at ground level [127].

$$\begin{aligned} C_n^2(h) = 0.00594 \left(\frac{w}{27}\right)^2 (10^{-5}h)^{10} \exp\left[-\frac{h}{1000}\right] \\ + 2.7 \cdot 10^{-16} \exp\left[-\frac{h}{1500}\right] + A \exp\left[-\frac{h}{100}\right] \end{aligned} \tag{2.14}$$

The particular set of parameters $A = 1.7 \cdot 10^{-14}$ [$m^{-2/3}$] and $w = 21$ [m/s] defines the so-called HV-5/7 model which, for a wavelength of 0.5 μm, predicts a 5-cm atmospheric coherence length and a 7-μrad isoplanatic angle, where the latter represents the angular distance over which the optical turbulence remains unchanged. The HV-5/7 model is recommended by the International Telecommunication Union (ITU) for nighttime observations [133]. Multiples of this model, denoted as MxHV-5/7, can eventually be used to represent different turbulence strengths.

For OFLs involving OGSs located above sea level, a modified version of the HV model, reported in Eq. (2.15), is often employed to account for the actual station altitude and for the corresponding reduction of the near-ground turbulence

contribution [134].

$$C_n^2(h) = A \cdot \exp\left[-\frac{h_{OGS}}{700}\right] \cdot \exp\left[-\frac{(h-h_{OGS})}{100}\right] + 5.94 \cdot 10^{-53} \cdot \left(\frac{w}{27}\right)^2 \cdot h^{10} \exp\left[-\frac{h}{1000}\right] + 2.7 \cdot 10^{-16} \exp\left[-\frac{h}{1500}\right] \tag{2.15}$$

Several other C_n^2 models can be found in the literature, some of them being modifications of the HV model, such as the Hufnagel-Andrews-Phillips (HAP) profile, and others being site-dependent models representative of specific OGS locations [127,132]. The advantage of the models of Eqs. (2.14) and (2.15) is that they can easily be adapted to the specific atmospheric conditions by leveraging the A and w parameters. In detail, the rms wind speed can estimated by means of the Bufton wind model as

$$w = \left[\frac{1}{15 \cdot 10^3} \int_{5 \cdot 10^3}^{20 \cdot 10^3} V^2(h) dh\right]^2 \tag{2.16}$$

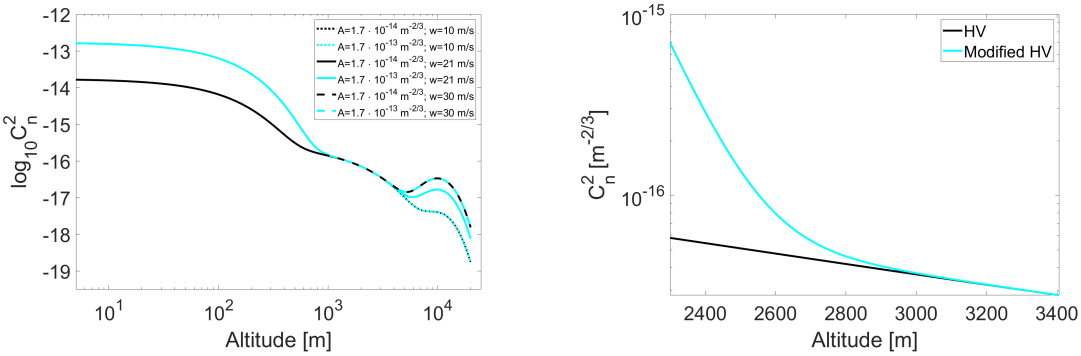
where

$$V(h) = \omega_s h + V_g + 30 \exp\left[-\left(\frac{h-9400}{4800}\right)^2\right] \tag{2.17}$$

In Eq. (2.17), V_g [m/s] is the ground wind speed and ω_s [rad/s] is the slew rate associated with the satellite moving with respect to an observer on the ground.

Figure 2.6a shows the refractive index structure parameter as a function of altitude for different combinations of A and w values. The plot highlights that the A value at ground does not considerably affects the turbulence profile above 1 km, while the wind speed has a significant impact around 10 km. Additionally, Fig. 2.6b compares the HV model and its modified version for an OGS located at 2300 m. Clearly, the modified model induces an increase of the structure parameter near the OGS, while the two curves converge as the altitude increases.

Another fundamental parameter used to characterize atmospheric turbulence is the atmospheric coherence length, commonly referred to as Fried's parameter and denoted by r_0 [m]. Physically, r_0 represents the largest effective telescope diameter for image resolution [132]. As the Fried's parameter quantifies the spatial coherence



(a) (b)

Figure 2.6 – (a) C_n^2 profile as a function of altitude obtained with the HV model for different values of A and w (b) Comparison between the HV model and its modified version for $A = 1.7 \cdot 10^{-14}$ m$^{-2/3}$, $w = 21$ m/s, and $h_{OGS} = 2300$ m

of the optical wavefront, it provides a direct measure of turbulence severity. Smaller values of r_0 correspond to stronger turbulence conditions.

Despite the laser beam typically being characterized by a Gaussian profile, the downlink beam can be well approximated by a plane wave, while the uplink one by a spherical wave. At the OGS, the Fried's parameter can be expressed as [135]

$$\begin{aligned} r_{0_{OGS}} &= \left[\frac{16.71}{\lambda^2}\int_0^L C_n^2(r)\left(1-\frac{r}{L}\right)^{5/3} dr\right]^{-\frac{3}{5}} \\ &\approx \left[0.423k^2\sec(\xi)\int_{h_{OGS}}^H C_n^2(h)\,dh\right]^{-\frac{3}{5}} \end{aligned} \tag{2.18}$$

where the weighting factor $(1 - r/L)$ in the integrand is negligible since $r \ll L$ where C_n^2 is nonzero, and thus the coherence length reduces to the plane wave one. Instead, at the satellite

$$\begin{aligned} r_{0_{sat}} &= \left[\frac{16.71}{\lambda^2}\int_0^L C_n^2(r)\left(\frac{r}{L}\right)^{5/3} dr\right]^{-\frac{3}{5}} \\ &= \left[0.423k^2\sec(\xi)\int_{h_{OGS}}^H C_n^2(h)\left[\frac{h-h_{OGS}}{H-h_{OGS}}\right]^{5/3} dh\right]^{-\frac{3}{5}} \end{aligned} \tag{2.19}$$

Equation (2.19) is valid for a spherical wave, and the last expression can be obtained by using the approximation of Eq. (2.7) for the link distance.

2.1.4.1 Optical wave propagation through turbulence

When an electromagnetic wave propagates through a random medium such as the atmosphere, both its amplitude and phase suffer from stochastic fluctuations, giving rise to wavefront distortions.

The propagation of a monochromatic optical field through a turbulent atmosphere is governed by the stochastic Helmholtz equation, i.e.,

$$\nabla^2\mathbf{E} + k^2 n^2(\mathbf{R})\mathbf{E} + s\nabla \log n(\mathbf{R}) = 0 \tag{2.20}$$

in which ∇^2 is the Laplacian operator and the refractive index appears as a random quantity [127]. Under the assumptions typically adopted in atmospheric optics, namely (i) negligible depolarization and backscattering effects, (ii) statistical homogeneity along the propagation direction, and (iii) paraxial approximation, Eq. (2.20) can be simplified to

$$\nabla^2 U + k^2 n^2(\mathbf{R})U = 0 \tag{2.21}$$

However, even in this simplified formulation, an exact analytical solution is generally not available, making it necessary to resort to approximate propagation theories.

Among the various approaches proposed in the literature, the Born and Rytov approximations constitute the most widely used analytical frameworks. The Born approximation models turbulence as a perturbation of the free-space field by expressing the optical field as the sum of an unperturbed component and a series of correction terms of increasing order. Although mathematically tractable, this approach is accurate only for weak turbulence conditions and relatively short propagation distances, which limits its applicability to OFLs.

A more effective description is provided by the Rytov approximation, which models turbulence-induced perturbations through fluctuations of the complex phase of the optical field. In contrast to the additive formulation adopted by Born, the Rytov approach introduces multiplicative perturbations and generally provides better agreement with experimental observations. For this reason, it has become the standard analytical framework for the study of atmospheric optical propagation. However, the validity of the conventional Rytov theory is restricted to weak

fluctuation regimes. The turbulence regime is commonly characterized through the Rytov variance, σ_R^2, which quantifies the strength of irradiance fluctuations experienced by a propagating wave. When the Rytov variance remains below unity, turbulence-induced distortions are weak and the conventional Rytov approximation provides accurate predictions. However, as turbulence intensity increases, the assumptions underlying the theory progressively break down and more advanced formulations become necessary.

To overcome these limitations, the extended Rytov theory was developed to describe optical wave propagation under moderate-to-strong turbulence conditions [127]. This theory is based on the observation that turbulent eddies of different sizes affect the optical wave through distinct physical mechanisms. Large-scale eddies mainly induce refractive effects, such as beam wander, whereas small-scale eddies produce diffractive effects, including scintillation and turbulence-induced beam spreading. This separation of turbulence effects, commonly referred to as the two-scale model, allows the refractive index to be decomposed into independent large-scale and small-scale contributions.

Within this framework, the optical field is represented as the product of the free-space field and two independent perturbation terms accounting for small-scale and large-scale effects, respectively. By introducing an effective turbulence spectrum that selectively includes the eddy scales contributing to each phenomenon, the extended Rytov theory provides analytical expressions that remain valid beyond the weak-fluctuation regime.

Starting from the mentioned theories, the second- and fourth-order moments of the random field can be derived to characterize the common impairments affecting the beam propagation, including:

1. Turbulence-induced beam spreading, i.e., beam divergence beyond pure diffraction, leading to a reduction of the power collected at the receiver

2. Beam wander, i.e., the angular deviation of the spot from the LoS

3. Scintillation, i.e., irradiance fluctuations observed within the beam cross section, leading to random power fades.

The analytical treatment of each phenomenon will be addressed in the following sections. It is worth stressing that the related mathematical models will vary between the two transmission directions. As anticipated, due to the asymmetry of the atmospheric channel, beam wander and additional beam spreading are negligible in downlink. At the same time, the transverse correlation width of irradiance, ρ_c, can be smaller than the receiver aperture D_R only in the downlink direction, thus making aperture averaging of irradiance fluctuations feasible [127].

2.1.4.2 Scintillation

When turbulent eddies have characteristic dimensions comparable to the beam size, they act as randomly distributed lenses that continuously focus and defocus different portions of the optical wavefront. As a result, the optical energy is redistributed within the beam cross-section, producing random fluctuations of the received irradiance, known as scintillation.

Unlike atmospheric absorption or scattering, scintillation does not modify the average optical power received over sufficiently long observation intervals. Instead, it causes temporal fluctuations of the instantaneous received power around its mean value. These fluctuations can become particularly severe under strong turbulence and may cause the received signal to temporarily fall below the receiver sensitivity threshold, resulting in communication outages. Consequently, scintillation has a direct impact on the availability and reliability of OFLs.

The severity of scintillation is commonly quantified through the scintillation index σ_I^2, defined as the normalized variance of the received irradiance, i.e.,

$$\sigma_I^2(\mathbf{r}, L) = \frac{\langle I^2(\mathbf{r},\mathbf{L})\rangle}{\langle I(\mathbf{r}, L)\rangle^2} - 1 \tag{2.22}$$

In Eq. (2.22), $I(\mathbf{r}, L)$ is the irradiance at the observation point $\mathbf{r}$ in the receiver plane ($z = L$).

According to the Rytov approximation, the scintillation index can be expressed as a function of the wave log-amplitude variance $\sigma_\chi^2(\mathbf{r}, L)$

$$\sigma_I^2(\mathbf{r}, L) = \exp\left[4\sigma_\chi^2(\mathbf{r}, L)\right] - 1 = \exp\left[\sigma_{\ln I}^2\right] - 1 \cong 4\sigma_\chi^2(\mathbf{r}, L) \tag{2.23}$$

In the above expression, σ^2_{lnI} is the variance of log irradiance. Moreover, it is possible to decompose σ^2_I into the sum of a radial and a longitudinal component, that is

$$\sigma^2_I(\mathbf{r}, L) = \sigma^2_{I,r}(\mathbf{r}, L) + \sigma^2_{I,l}(L) \tag{2.24}$$

where the radial component $\sigma^2_{I,r}(\mathbf{r}, L)$ describes off-axis scintillation and is null at $\mathbf{r} = 0$, while the longitudinal term $\sigma^2_{I,l}(L)$ is related to on-axis scintillation and is constant across the beam cross section [127].

In downlink, considering the plane wave approximation and Rytov theory, the total scintillation index is given by [127]

$$\sigma^2_I(r, L) = \sigma^2_R = 2.25 \cdot k^{7/6} \cdot \sec^{11/6}(\xi) \int_{h_{OGS}}^{H} C_n^2(h)(h - h_{OGS})^{5/6} dh \tag{2.25}$$

Instead, according to the extended Rytov theory, the normalized irradiance can be expressed as

$$\hat{I} = \frac{I}{\langle I \rangle} = XY \tag{2.26}$$

where X and Y are statistically independent terms due to large- and small-scale eddies, respectively. They have unit means and σ^2_X and σ^2_Y variances. Thus, it is possible to express the scintillation index as

$$\sigma^2_I = (1 + \sigma^2_X)(1 + \sigma^2_Y) = \exp\left[\sigma^2_{\ln X} + \sigma^2_{lnY}\right] - 1 \tag{2.27}$$

In downlink, Eq. (2.27) specializes to

$$\sigma^2_{I,l}(L) = \exp\left[\frac{0.49\sigma^2_R}{\left(1 + 1.11\sigma_R^{12/5}\right)^{7/6}} + \frac{0.51\sigma^2_R}{\left(1 + 0.69\sigma_R^{12/5}\right)^{5/6}}\right] - 1 \tag{2.28}$$

Figure 2.7 depicts the variation of the downlink longitudinal scintillation index with zenith for the two propagation theories and different turbulence regimes. The plot highlights that the validity of the Rytov theory reduces to lower zenith angles as the turbulence strength increases. Moreover, for shorter wavelengths, the validity of weak fluctuation theory would be further limited to even smaller zenith angles.

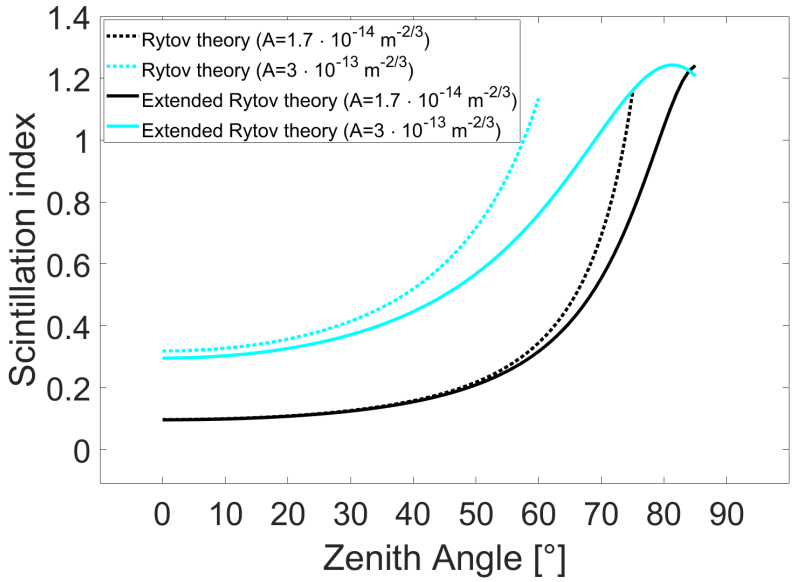


Figure 2.7 – Downlink scintillation index as a function of the zenith angle for different turbulence regimes at $\lambda = 1.06$ μm

The transverse correlation width of irradiance, ρ_c, also depends on the adopted theory and is defined as the $1/e$, $1/e^2$, or zero crossing point of the normalized covariance function

$$b_I(\rho, L) = \frac{B_I(\rho, L)}{B_I(0, L)} \tag{2.29}$$

In Eq. (2.29), $\rho = 2r$ is the distance between two points symmetrically located with respect to the optical axis. According to the Rytov theory

$$b_I(\rho, L) = \frac{\mu_{3d}(\rho)}{\mu_{3d}(0)} \tag{2.30}$$

where

$$\begin{aligned}\mu_{3d}(\rho) = \mathfrak{Re} \int_{h_{OGS}}^{H} C_n^2(h) \Bigg[& \gamma^{5/6} \left[\Lambda\gamma + i(1-\bar{\Theta}\gamma)\right]^{5/6} \\ & \times {}_1F_1\left\{-\frac{5}{6}; 1; -\frac{kp^2(1-\bar{\Theta}\gamma - i\Lambda\gamma)^2}{4L\gamma\left[\Lambda\gamma + i(1-\bar{\Theta}\gamma)\right]}\right\} \\ & - (\Lambda\gamma^2)^{5/6} {}_1F_1\left\{-\frac{5}{6}; 1; -\frac{k\rho^2}{4L\Lambda}\left(\frac{1-\bar{\Theta}\gamma}{\gamma}\right)^2\right\}\Bigg] dh\end{aligned} \tag{2.31}$$

In Eq. (2.31), ${}_1F_1(a;c;x)$ is the confluent hypergeometric function, $\gamma = (h - h_{OGS})/(H - h_{OGS})$, and Λ and $\bar{\Theta}$ are the output plane beam parameters defined in [127]. Under weak irradiance fluctuations, the correlation width can be approximated by means of the following empirical formula

$$\rho_c \cong \sqrt{\frac{45 \cdot 10^3 \sec(\xi)}{k}} \quad \sigma_R^2 \ll 1, 0^\circ \leq \xi < 50^\circ \tag{2.32}$$

Instead, by adopting the extended Rytov theory, the covariance function is expressed as

$$B_I(\rho) = \exp\left[\frac{\mu_{4d}(\rho)}{\mu_{4d}(0)}\sigma^2_{\ln X} + 0.99\left(\frac{k\rho^2\eta_Y}{L}\right)^{5/12} K_{5/6}\left(\sqrt{\frac{k\rho^2\eta_Y}{L}}\right)\sigma^2_{\ln Y}\right] - 1 \tag{2.33}$$

where $K_\upsilon(x)$ is the modified Bessel function of the second kind and

$$\mu_{4d}(\rho) = \int_{h_{OGS}}^{H} \frac{C_n^2(h)}{\gamma^{1/3}\left(1 - \frac{5\gamma}{8}\right)^{7/5}} {}_1F_1\left[\frac{7}{5}; 1; \frac{-k\rho^2\eta_X}{8L\gamma^{5/3}\left(1 - \frac{5\gamma}{8}\right)}\right] dh \tag{2.34}$$

$$\eta_X = \frac{0.92}{1 + 1.11\sigma_R^{12/5}} \tag{2.35}$$

$$\eta_Y = 3\left(1 + 0.69\sigma_R^{12/5}\right) \tag{2.36}$$

$$\sigma^2_{\ln X} = \frac{0.49\sigma_R^2}{\left(1 + 1.11\sigma_R^{12/5}\right)^{7/6}} \tag{2.37}$$

$$\sigma^2_{\ln Y} = \frac{0.51\sigma_R^2}{\left(1 + 0.69\sigma_R^{12/5}\right)^{5/6}} \tag{2.38}$$

If it ρ_c is smaller than the receiving aperture diameter D_R, the aperture will average out the intensity fluctuations, thus leading to decreased scintillation index and improved link performance. The aperture-averaged scintillation index, assuming the Rytov theory, can be expressed as

$$\sigma_I^2(D_R) = 8.70k^{7/6}(H - h_{OGS})^{5/6}\sec^{11/6}(\xi) \mathfrak{Re}\int_{h_{OGS}}^{H} C_n^2(h)\left[\left(\frac{kD_R^2}{16L} + i\frac{h - g_{OGS}}{H - h_{OGS}}\right)^{5/6} - \left(\frac{kD_R^2}{16L}\right)^{5/6}\right] dh \tag{2.39}$$

Instead, if the extended Rytov theory is used

$$\sigma_I^2(D_R) = \exp\left[\frac{0.49\sigma_R^2}{\left(1+0.65d^2+1.11\sigma_R^{12/5}\right)^{7/6}} + \frac{0.51\sigma_R^2\left(1+0.69\sigma_R^{12/5}\right)^{-5/6}}{1+0.90d^2+0.62d^2\sigma_R^{12/5}}\right] - 1 \tag{2.40}$$

with

$$d = \sqrt{\frac{kD_R^2}{4L}} \tag{2.41}$$

being the circular aperture radius scaled by the Fresnel length $F = \sqrt{L/k}$. Figure 2.8 shows the aperture-averaged scintillation index as a function of D_R for two different zenith angles. The curves have been evaluated according to Eq. (2.39).

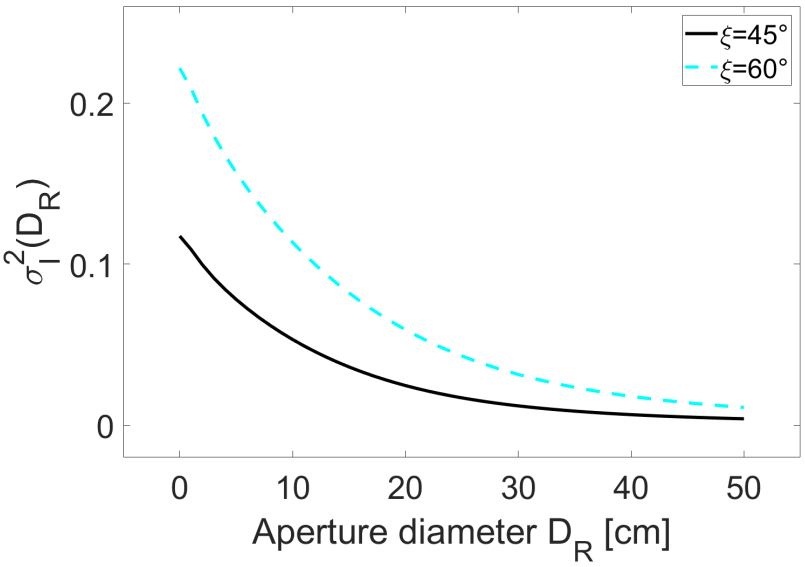
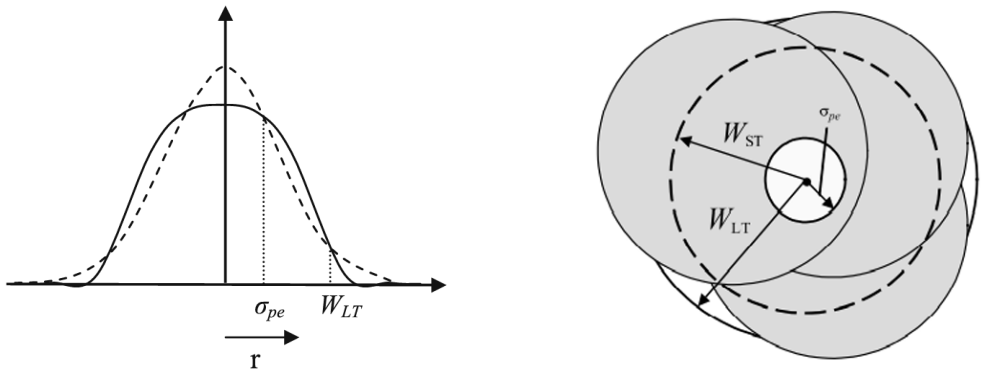


Figure 2.8 – Downlink aperture-averaged scintillation index as a function of the receiver aperture diameter at $\lambda = 1.55$ μm

As expected, the advantage offered by aperture averaging increases with D_R and with decreasing zenith angle.

In uplink, it can be proved that the transverse correlation width equals tens of meters or even more [127], which is certainly larger than D_R at the satellite. Thus, the detector acts as a point receiver, and the longitudinal scintillation index is enough to characterize scintillation. However, as shown in Fig. 2.9, beam wander

induces beam flattening, with the beam maximum extending over a circumference of radius σ_{pe}. The overall effect of σ_{pe}, which can be thought as an effective



(a) (b)

Figure 2.9 – (a) Flattened beam profile as a function of the radial displacement r [128] (b) Graphical representation of the beam wander-induced effective pointing error σ_{pe}. The dashed circle represents the RMS short-term spot size, W_{LT} is the long-term spot size, W_{ST} is the short-term spot size [127]

pointing error, is an increased longitudinal scintillation index. According to the Rytov theory [132]

$$\begin{aligned}\sigma_{pe}^2 &= 7.25\,(H-h_{OGS})^2\sec^3(\xi)\,W_0^{-1/3} \\ &\quad\cdot\left[1-\left(\frac{K_0^2W_0^2}{1+K_0^2W_0^2}\right)^{1/6}\right]\int_{h_{OGS}}^{H}C_n^2(h)\left(1-\frac{h-h_{OGS}}{H-h_{OGS}}\right)^2 dh \\ &\cong 0.54\,(H-h_{OGS})^2\sec^2(\xi)\left(\frac{\lambda}{2W_0}\right)^2\left(\frac{2W_0}{r_0}\right)^{5/3}\left[1-\left(\frac{K_0^2W_0^2}{1+K_0^2W_0^2}\right)^{1/6}\right]\end{aligned} \tag{2.42}$$

where r_0 is given in Eq. (2.18) [135], the last approximation is valid for a collimated beam and

$$K_0 = \frac{2\xi}{\pi} \tag{2.43}$$

For an untracked Gaussian beam, the longitudinal scintillation index derived from

the Rytov theory can be expressed as [127]

$$\sigma_{I,l}^2(L)_{untracked} = 5.95\left(H - h_{OGS}\right)^2 \sec^2(\xi)\left(\frac{2W_0}{r_0}\right)^{5/3}\left(\frac{\alpha_{pe}}{W}\right)^2 + 8.70\mu_{3u}k^{7/6}\left(H - h_{OGS}\right)^{5/6}\sec^{11/6}(\xi) \tag{2.44}$$

In Eq. (2.44), $\alpha_{pe} = \sigma_{pe}/L$ is the jitter-induced angular pointing error, while

$$\mu_{3u} = \mathfrak{Re}\int_{h_{OGS}}^{H} C_n^2(h)\left\{\gamma^{5/6}\left[\Lambda\gamma + i(1-\bar{\Theta}\gamma)\right]^{5/6} - \Lambda^{5/6}\gamma^{5/3}\right\}dh \tag{2.45}$$

In Eq. (2.45), $\gamma = 1 - (h - h_{OGS})(H - h_{OGS})$ and W is the beam radius at the receiver due to diffraction [127]. Instead, by adopting the extended Rytov theory

$$\sigma_{I,l}^2(L)_{untracked} = 5.95\left(H - h_{OGS}\right)^2 \sec^2(\xi)\left(\frac{2W_0}{r_0}\right)^{5/3}\left(\frac{\alpha_{pe}}{W}\right)^2 + \exp\left[\frac{0.49\sigma_{bu}^2}{\left(1 + (1+\Theta)\,0.56\sigma_{bu}^{12/5}\right)^{7/6}} + \frac{0.51\sigma_{bu}^2}{\left(1 + 0.69\sigma_{bu}^{12/5}\right)^{5/6}}\right] - 1 \tag{2.46}$$

where $\Theta = 1 - \bar{\Theta}$ and σ_{bu}^2 is defined in Eq. (2.47).

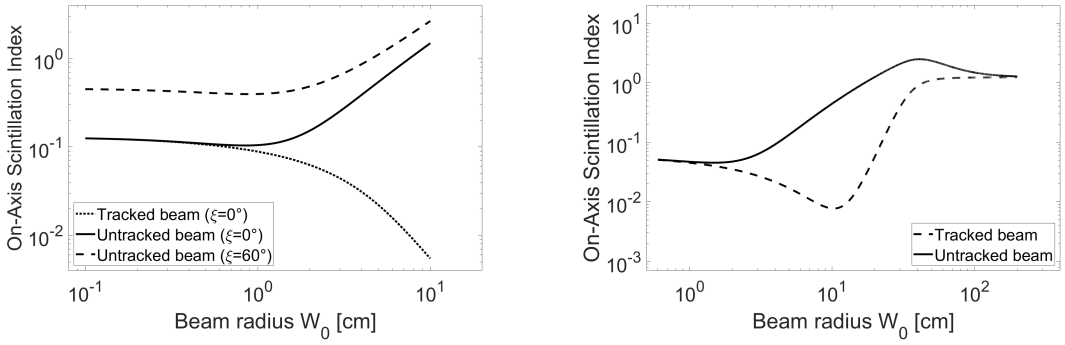
Tracking a beam could imply tracking the beam hot spot or removing the wavefront tilt. If removal of the rms hot spot displacement is assumed, the longitudinal scintillation index derived from the Rytov theory becomes

$$\sigma_{I,l}^2(L)_{tracked} \equiv \sigma_{bu}^2 = 8.70\mu_{3u}k^{7/6}\left(H - h_{OGS}\right)^{5/6}\sec^{11/6}(\xi) \tag{2.47}$$

while the one obtained through the extended Rytov theory is

$$\sigma_{I,l}^2(L)_{tracked} = \exp\left[\frac{0.49\sigma_{bu}^2}{\left(1 + (1+\Theta)\,0.56\sigma_{bu}^{12/5}\right)^{7/6}} + \frac{0.51\sigma_{bu}^2}{\left(1 + 0.69\sigma_{bu}^{12/5}\right)^{5/6}}\right] - 1 \tag{2.48}$$

Figures 2.10a and 2.10b depict the uplink longitudinal scintillation index versus the transmitter beam radius for tracked and untracked beams evaluated through Rytov and extended Rytov expressions, respectively. Figure 2.10a is evaluated at $\lambda = 840$ nm and for two different zenith angles, i.e., 0° and 60°. Instead, in



(a) (b)

Figure 2.10 – Longitudinal scintillation index for a ground-to-space link as a function of beam radius according to (a) Rytov and (b) extended Rytov theories

Fig. 2.10b, $\lambda = 1.6$ μm and $\xi = 0°$ are assumed. All the curves are evaluated by modeling turbulence with the HV model with parameters $A = 1.7 \cdot 10^{-14}$ m$^{-2/3}$ and $w = 21$ m/s.

The two plots outline that tracked and untracked beams' curves overlap for small beam radii, while they tend to diverge as the beam radius increases. This suggests that on-axis scintillation could be strongly reduced by tracking the beam and increasing the beam size. Nonetheless, the tracked curves are based on the hypothesis of complete beam wander removal, which is usually difficult to achieve [127]. Instead, for the untracked case, there is a small reduction in beam wander for moderate beam sizes, followed by increasing scintillation as the beam radius further enlarges, eventually reaching saturation. Moreover, as the zenith angle increases, increased scintillation can be observed.

The relevance of scintillation extends beyond the characterization of atmospheric turbulence. Indeed, the scintillation index is a key parameter in the evaluation of communication performance metrics such as the SNR and the BER. Since deep irradiance fades can significantly increase the probability of detection errors, appropriate mitigation strategies are required to guarantee the desired quality of service.

A basic approach consists in introducing a scintillation fade margin, defined as a surplus of transmitted optical power that compensates for turbulence-induced

fading events. The required fade margin can be estimated from the statistical distribution of the received irradiance and from the target outage probability [136].

In the literature, several distributions have been proposed to model the Probability Density Function (PDF) of irradiance, $p_I(I)$. Among them, the lognormal one is widely recognized to be valid under weak turbulence or when, even if irradiance does not obey the lognormal PDF, aperture averaging brings the received power back to lognormal statistics [127, 137, 138]. According to this model

$$p_I(I) = \frac{1}{I\sqrt{2\pi}\sigma_{\ln I}} \exp\left\{\left\{-\frac{\left[\ln(I) + \frac{1}{2}\sigma^2_{\ln I}\right]^2}{2\sigma^2_{\ln I}}\right\}\right\} \quad I > 0 \tag{2.49}$$

Many demonstrations validated the above model, especially concerning downlink OFLs [82, 106]. In this case, an analytical expression for the required fade margin, L_{SI} [dB], can be found in [138], according to which

$$L_{SI} = 4.343\left\{\mathrm{erf}^{-1}\left(2\rho_{thr} - 1\right)\left[2\ln\left(\sigma_I^2 + 1\right)\right]^{\frac{1}{2}} - \frac{1}{2}\ln\left(\sigma_I^2 + 1\right)\right\} \tag{2.50}$$

In Eq. (2.50), ρ_{thr} is the desired fraction of outage time, i.e., the probability that the received optical power falls below the sensitivity threshold.

It should be noted, however, that the lognormal assumption may become inaccurate under severe turbulence conditions, where the received irradiance can exhibit more complex statistical behavior. In such cases, the gamma-gamma model is more accurate [127], while the gamma and modulated gamma models are considered more appropriate for uplink tracked and untracked beams, respectively [132]. Furthermore, scintillation-induced fading represents only one of the mechanisms affecting link availability. Additional impairments, including pointing and tracking errors and synchronization losses caused by deep fades can further degrade system performance. Consequently, the fade margin estimated from scintillation alone should be regarded as a first-order design parameter rather than a complete solution to guarantee the required link availability. As discussed in Chapter 1, it is typically complemented by additional mitigation techniques such as AO, forward error correction, and diversity schemes.

2.1.4.3 Beam wander

Beam wander arises from the interaction between the optical beam and turbulent eddies whose characteristic dimensions are larger than the beam size. These large-scale refractive-index inhomogeneities randomly deflect the beam from its nominal propagation direction, resulting in a distorted short-term Gaussian profile, in which the beam centroid and hot spot are distinct points [139].

The importance of beam wander strongly depends on the propagation direction. In downlink, the optical beam propagates through most of its path in free space and enters the turbulent atmosphere only after having expanded considerably. Consequently, its diameter at the atmospheric entrance is generally larger than the outer scale of turbulence, making beam wander negligible. In uplink, on the contrary, the beam traverses the atmosphere while still relatively narrow and therefore remains susceptible to large-scale turbulent eddies. As a result, significant centroid displacements can be observed at the satellite receiver, potentially reaching several hundreds of meters [127].

Eddies bigger than the atmospheric coherence length primarily affect the phase of the optical wavefront. The resulting wavefront tilts are translated into angular deviations of the beam trajectory and ultimately into random displacements of the beam centroid. Moreover, the short-term displacements translate into a larger long-term spot size, thus leading to an increased diffraction loss. Instead, turbulent structures with dimensions larger than the beam size but smaller than the atmospheric coherence length contribute to irradiance fluctuations, increasing the on-axis scintillation experienced by the received signal, as already explained in Section 2.1.4.2 [140].

According to the reciprocity principle, beam wander observed at the receiver can be modeled as an equivalent random angular tilt introduced at the transmitter. The severity of the phenomenon is commonly quantified through the beam wander variance, $\langle r_c^2 \rangle$, defined as the variance of the beam-centroid displacement relative to the LoS. For a collimated Gaussian beam propagating through Kolmogorov turbulence and assuming an infinite outer scale, the beam wander variance can be

expressed as [127]

$$\langle r_c^2 \rangle = 0.54(H - h_{OGS})^2 \sec^2(\xi) \left(\frac{\lambda}{2W_0}\right)^2 \left(\frac{2W_0}{r_0}\right)^{5/3} \tag{2.51}$$

An alternative, equivalent metric is the rms angular beam wander, θ_{BW} [rad], defined as

$$\theta_{BW} = \frac{\sqrt{\langle r_c^2 \rangle}}{L}. \tag{2.52}$$

This quantity, which represents the equivalent angular deviation of the transmitted beam, provides a direct measure of the pointing error induced by turbulence. Figure 2.11 illustrates the angular beam wander as a function of the transmitter beam radius for an uplink collimated beam at $\lambda = 1.55$ μm. As suggested by the

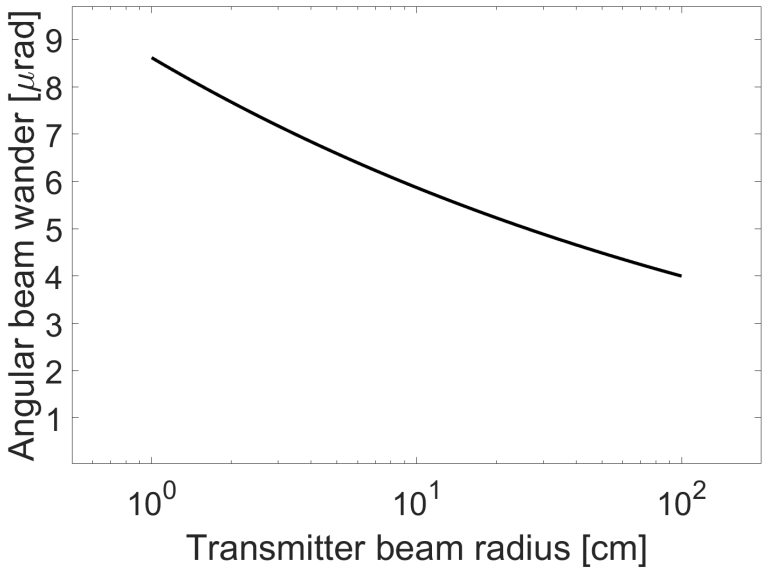


Figure 2.11 – Angular beam wander as a function of the transmitter beam radius for an uplink OFL at $\zeta = 0°$, $\lambda = 1.55$ μm, $A = 1.7 \cdot 10{-}14$ m$^{-2/3}$, $w = 21$ m/s

plot, angular beam wander is typically on the order of few microradians, but it can increase at lower elevations.

Since the beam wander variance scales with the square of the propagation distance, an accurate evaluation of the slant range is essential. Nonetheless, in the commonly adopted model of Eq. (2.51), the propagation distance is approximated

using the flat-Earth approximation of Eq. (2.7), which is sufficiently accurate only for small zenith angles. However, for low-elevation links, the curvature of the Earth becomes significant, and more accurate geometrical models, as the one of Eq. (2.8), should be adopted.

Fig. 2.12 shows the absolute error between the flat-Earth and round-Earth link distance approximations, as a function of the elevation angle, for an OFL between an OGS located at 2300 m of altitude and a LEO satellite orbiting at 600 km. The error curve highlights that the flat-Earth approximation accuracy rapidly decreases with the elevation angle. The absolute error is zero only at $\zeta = 90°$,

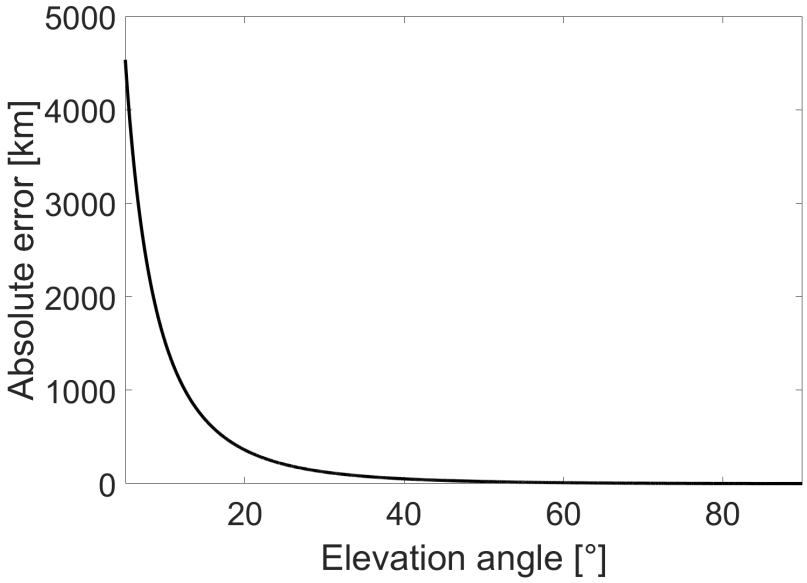


Figure 2.12 – Absolute error between the flat-Earth and round-Earth link distance approximations as a function of the elevation angle, for an OFL between an OGS located at 2300-m altitude and a LEO satellite orbiting at 600 km

where the two approximations return the same results. A complete analysis about the relationship between link distance and the beam wander accuracy is provided in Section 2.2.4.

Beam wander affects system performance in several ways. First, it increases the temporal variability of the received power by enhancing scintillation effects. Second, the short-term random displacement of the beam centroid and the motion of the hot spot around it introduce turbulence-induced pointing errors that may

reduce the amount of optical power collected by the receiver. Consequently, beam wander must be properly accounted for in OFL link budget analyses.

Several countermeasures can reduce the impact of beam wander. The simplest approach consists of increasing the beam divergence, thereby reducing the probability that the beam misses the receiver aperture. However, this solution simultaneously decreases the received power density, which is generally undesirable. A more effective approach relies on fast-tracking systems, which continuously compensate for turbulence-induced beam deviations.

Beam tracking can be interpreted as the lowest-order implementation of an AO system [141]. Indeed, the phase of the optical wave received through a circular aperture can be decomposed into orthogonal spatial modes represented by Zernike polynomials, with the lowest-order modes corresponding to wavefront tilts. Specifically, the first Zernike mode relates to the averaging effect of a circular aperture, the next two modes are associated with the vertical and horizontal wavefront tilts, and the subsequent modes describe higher-order aberrations. By measuring these tilts and applying the appropriate correction through a fast-steering mirror, beam wander can be substantially reduced, while a Deformable Mirror (DM) can compensate for higher-order distortions [142]. In OFLs, the required information is typically obtained from a downlink beacon transmitted by the satellite, whose wavefront distortions are measured at the OGS and used to estimate the correction to be applied to the outgoing uplink beam. As an alternative, a laser guide star could be exploited but, unfortunately, it would not allow measuring tip-tilt because the lights would travel up and down through the same path [136].

The effectiveness of AO correction is nevertheless limited by several factors. The correction remains valid only within the isoplanatic angle, θ_0 [rad], which can be estimated as

$$\theta_0 = \frac{\cos^{8/5}(\xi)}{\left[2.91k^2 \int_{h_{OGS}}^{H} C_n^2(h)(h - h_{OGS})^{5/3} dh\right]^{3/5}} \tag{2.53}$$

However, the PAA separating the uplink and downlink propagation paths may exceed the isoplanatic angle, reducing the correlation between the two channels and degrading the achievable correction [127]. Anisoplatism particularly affects LEO systems, with PAA values typically ranging between 20 μrad at the horizon

and 50 μrad at zenith [136]. Nonetheless, also in GEO links the lateral speed between the OGS and the satellite leads to PAAs varying between 17 μrad and 20 μrad, which can make the AO pre-distortion ineffective [143].

Additional limitations arise from the finite bandwidth of the AO system, which must operate at rates comparable to or greater than the Greenwood frequency in order to effectively track the temporal evolution of atmospheric turbulence [144]. The Greenwood frequency, f_{T_G}, can be computed as

$$f_{T_G} = 2.31\lambda^{-6/5}\left[\int_0^L C_n^2(r)V^{5/3}(r)dr\right]^{3/5} \tag{2.54}$$

On the other hand, the tilt component of the phase has a more slowly time characteristic with respect to the whole phase distortion [144], i.e.,

$$f_{T_G,tilt} = 0.331D^{-1/6}\lambda^{-1}\sec^{1/2}(\xi)\left[\int_{g_{OGS}}^H C_n^2(h)V^2(h)dh\right]^{1/2} \tag{2.55}$$

In Eq. (2.55), D is the diameter of the tracking aperture.

Finally, the pre-compensation techniques require the OGS to receive and transmit across the same aperture, which imposes strong isolation requirements [136].

Although beam tracking and AO can significantly reduce beam wander, residual pointing errors generally remain. For this reason, beam wander continues to play an important role in the performance assessment and link-budget modeling of both tracked and untracked OFLs.

2.1.4.4 Turbulence-induced beam spreading

In addition to scintillation and beam wander, atmospheric turbulence causes a progressive broadening of the optical beam during propagation. This phenomenon originates from the interaction between the optical wave and turbulent eddies whose characteristic dimensions are smaller than the beam diameter. These small-scale refractive-index fluctuations perturb the phase front of the propagating wave, introducing additional diffraction beyond that experienced during free-space propagation. In addition, the beam wander-induced short-term beam displacement prompts a widened long-term spot radius, as shown in Fig. 2.13 [127]. As a consequence, the optical beam reaches the receiver with a larger spot size than predicted

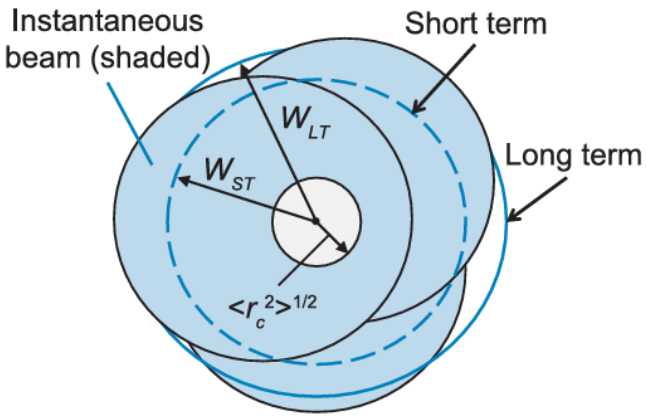


Figure 2.13 – Short-term (dashed circle) and long-term (large circle) beam sizes [132]

by diffraction alone. Since the optical power is distributed over a wider area, the on-axis irradiance decreases, reducing the amount of optical power collected by a finite receiving aperture.

The effect can be understood by distinguishing between the short-term and long-term behavior of the received beam. As illustrated in Fig. 2.13, the short-term beam corresponds to the instantaneous beam profile observed over time intervals shorter than the characteristic turbulence evolution time. In this case, the beam broadening is solely due to free-space diffraction and to the additional spreading generated by small-scale turbulence. The corresponding short-term beam radius, W_{ST} can therefore be expressed as

$$W_{ST}^2 = W^2 + W^2 T_{SS} \tag{2.56}$$

where W denotes the receiver beam radius resulting from free-space propagation and the second term represents the contribution of small-scale turbulence-induced spreading.

Over longer observation intervals, the random motion of the beam centroid caused by beam wander further increases the effective beam size observed at the receiver. The resulting long-term beam radius, W_{LT}, is given by

$$W_{LT}^2 = W_{ST}^2 + W^2 T_{LS} \tag{2.57}$$

where the last term corresponds to the variance of the beam-centroid displacement and accounts for the contribution of large-scale eddies. Thus, the long-term beam profile includes the combined effects of both small-scale and large-scale turbulent eddies.

The collected power reduction produced by turbulence-induced beam spreading is commonly quantified through the Strehl Ratio (SR), defined as the ratio between the on-axis mean irradiance in the presence of turbulence and the corresponding irradiance in the absence of atmospheric distortions at the receiver image plane. Physically, the SR measures the extent to which turbulence reduces the concentration of optical energy around the beam center. A value of SR equal to one corresponds to ideal diffraction-limited propagation, while smaller values indicate increasing wavefront degradation.

The turbulence-induced spreading loss, L_{SR}, can be expressed in terms of the SR as [127]

$$L_{SR} = \left[1 + \left(\frac{D_T}{r_{0_{Tx}}}\right)^{5/3}\right]^{-6/5} \qquad 0 \leq \frac{D_T}{r_{0_{Tx}}} < \infty \tag{2.58}$$

The above expression highlights the central role played by the ratio between the transmitter aperture and the atmospheric coherence length. When the aperture diameter is significantly smaller than r_0, the transmitted wavefront remains nearly coherent, and turbulence-induced spreading is limited. Conversely, when D_T exceeds the coherence length, distortions become increasingly important, leading to a substantial reduction of the on-axis irradiance.

As for beam wander, the additional beam broadening introduced by turbulence is generally negligible in downlink. In uplink, however, it becomes a significant source of power loss.

2.1.5 Pointing errors

The extremely narrow beam divergences employed in OFLs, combined with the limited Field of View (FOV) of optical receivers, require the transmitter and receiver to maintain an accurate LoS alignment throughout the communication session [25]. Unlike RF systems, where beamwidths are typically several orders of magnitude larger, optical communication systems often operate with divergences

of only a few microradians [145]. Consequently, even very small angular deviations can result in a substantial reduction of the received optical power and, in severe cases, complete loss of the communication link.

The challenge of maintaining accurate pointing is further exacerbated by the large propagation distances involved and by the relative motion between the OGS and the satellite. For this reason, OFLs rely on dedicated ATP systems [146]. In detail, before the start of the data transmission, the transmitter optics must be properly aligned with the receiver optics i.e., a correct pointing must be ensured. Moreover, the receiver detector must be aligned with the angle of arrival of the incident wave. The last operation is called spatial acquisition, while the preservation of pointing and acquisition for the entire link duration is called spatial tracking. Typically, coarse pointing is achieved using satellite ephemeris data and navigation systems, such as star trackers or the global positioning system. Then, as highlighted in Chapter 1, initial acquisition is usually performed by means of a closed-loop mechanism. The overall acquisition procedure is schematized in Fig. 2.14. Specifically, in uplink, acquisition starts when a beacon is sent from the

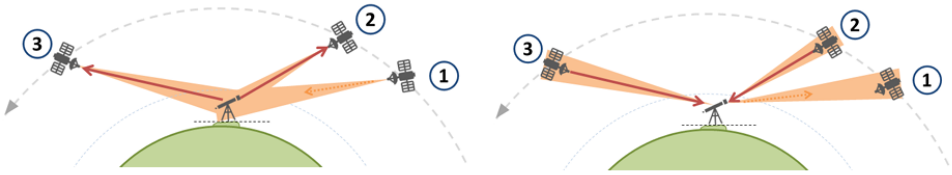


Figure 2.14 – Uplink (left) and downlink (right) acquisition process. Data link are represented with red arrows, while laser beacons are represented as orange cones [147]

satellite to the OGS. Then, the OGS tracks the beacon and points its communication beam to the satellite. In downlink, an analogous procedure is performed, where the roles of the satellite and OGS are exchanged. Typically, the beacon follows a spiraling search pattern. Bi-directional and beaconless acquisitions are also possible. Finally, fine tracking systems continuously compensate for residual misalignments and maintain the optical beam aligned with the target.

The sensitivity of OFLs to pointing errors originates from the Gaussian irradiance profile of the transmitted beam [127]. Since the optical intensity decreases

rapidly with increasing radial distance from the beam center, even small angular deviations may significantly reduce the power collected by the receiver. Furthermore, because turbulence-induced scintillation generally increases away from the optical axis, pointing errors can also modify the fading statistics of the received signal and further degrade link performance.

Pointing errors are generally classified into three categories, i.e., (i) static errors, (ii) dynamic errors, and (iii) random errors.

Static pointing errors are deterministic angular offsets that remain approximately constant during a communication session and are independent of the link elevation angle. These errors typically originate from mechanical misalignments within the transmitter optics, assembly tolerances, calibration inaccuracies, or structural deformations of the optical terminal. Since they introduce a constant angular bias, $\Delta\theta$ [rad], with respect to the LoS, their effect is a systematic displacement of the beam footprint at the receiver.

Dynamic pointing errors vary with time and depend on the geometry of the optical link. A major source of dynamic errors is the uncertainty in the determination of the satellite position. OGSs commonly rely on orbital information derived from ephemeris data or Two-Line Element (TLE) sets. However, these data are affected by prediction errors that increase with time since the last orbit update. For example, the mean along-track error (that is, the error along the direction of the satellite trajectory) can potentially range from few meters when the TLE data are recent, up to more than 5 km after three days of satellite motions and more than 24 km after seven days [147, 148]. Additional inaccuracies may arise from time-synchronization errors, reference-frame transformations, and tracking system imperfections. Consequently, the actual satellite position may differ from the predicted one, introducing a time-varying pointing offset.

Another important source of dynamic error is associated with the PAA. Because of the finite speed of light, c, and the relative motion between the satellite and the OGS, and considering the narrow laser beam divergence, the transmitted beam must be directed toward the future position of the receiver rather than its instantaneous location. The required PAA depends on the tangential velocity of the satellite, v_{sat} [m/s], and on the link distance. Assuming that the link distance does not change during a round-trip time $\tau = 2L/c$, the satellite runs

through a distance equal to τv_{sat} [149]. Neglecting the Earth rotation, between two consecutive uplink and downlink transmissions, an angular separation

$$\theta_{PAA}(\zeta) = \frac{\tau v_{sat}(t)}{L} = \frac{2v_{sat}(t)}{c} \tag{2.59}$$

occurs. This concept is illustrated in Fig. 2.15. In practice, the PAA varies during the link duration due to the satellite orbit. Thus, in practical systems, when a constant correction is applied, a residual pointing error arises whose magnitude generally increases as the beam divergence decreases and elevation angle increases.

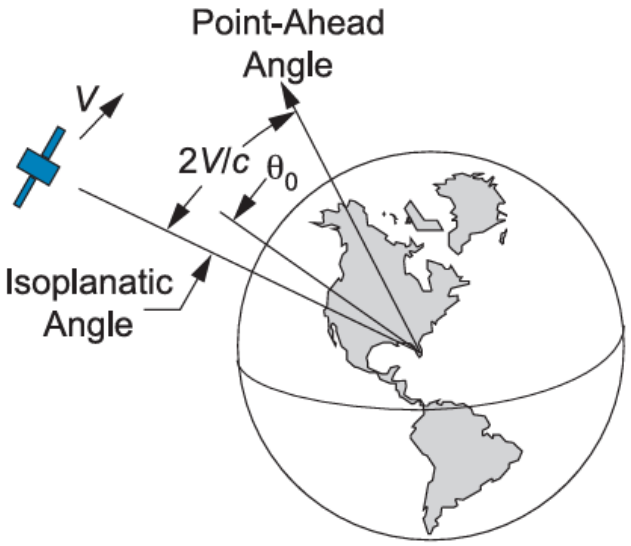


Figure 2.15 – Geometry of point-ahead angle [132]

Random pointing errors, commonly referred to as pointing jitter, are stochastic fluctuations of the beam direction around its nominal pointing angle. Pointing jitter can be either elevation-dependent or independent and leads to received intensity fluctuations. These fluctuations are caused by a variety of mechanisms, including tracking sensor noise, servo-control imperfections, mechanical vibrations, structural oscillations, and atmospheric turbulence.

As previously discussed, turbulence-induced beam wander constitutes one of the main contributors to pointing jitter in uplink OFLs. Additional jitter sources may originate from the satellite platform itself. Internal disturbances include

attitude-control noise, reaction wheel vibrations, thruster operations, antenna steering mechanisms, solar-array drives, and other onboard subsystems. External disturbances arise from environmental effects such as solar radiation pressure, satellite structure bending due to temperature gradients and to elastic forces of tension, gravitational perturbations, and micrometeorite impacts [146]. The combined action of these mechanisms results in a random displacement of the beam footprint and corresponding fluctuations of the received optical power.

The impact of pointing errors on link performance is commonly quantified through the associated pointing loss. Deterministic pointing errors introduce a fixed reduction of the received power, whereas random pointing errors must be characterized statistically.

The loss induced by deterministic pointing errors can be evaluated starting from the knowledge of the related angular deviation, $\Delta\theta$, and beam half-divergence angle as [147]

$$L_{pointing,static} = exp\left[-2\left(\frac{\Delta\theta}{\frac{\theta_{e^{-2}}}{2}}\right)^2\right] \tag{2.60}$$

For what concerns pointing jitter, the pointing error is statistically described by Gaussian distributions of both azimuth and elevation uncertainties. The radial pointing error θ equals the rms of the elevation and azimuth angles, θ_V and θ_H, i.e., $\theta = \sqrt{\theta_V^2 + \theta_H^2}$. If the standard deviations of azimuth and elevation angles are $\sigma_V = \sigma_H = \sigma_{jitt}$, and both azimuth and elevation processes are zero-mean, independent, and identically distributed, the radial pointing error angle θ is modeled by a Rician distribution [150], i.e.,

$$f(\theta, \phi) = \frac{\theta}{\sigma_{jitt}^2} \exp\left(-\frac{\theta^2 + \phi^2}{2\sigma_{jitt}^2}\right) I_0\left(\frac{\theta\phi}{\sigma_{jitt}^2}\right) \tag{2.61}$$

In Eq. (2.61), I_0 is the modified Bessel function of order zero and ϕ is the bias error angle. In the absence of a deterministic bias, the distribution reduces to a Rayleigh law, i.e.,

$$f(\theta) = \frac{\theta}{\sigma_{jitt}^2} \exp\left(-\frac{\theta^2}{2\sigma_{jitt}^2}\right) \tag{2.62}$$

In this last case, the irradiance follows the beta distribution [151], i.e.,

$$p_I(I) = \beta \cdot I^{\beta-1} \tag{2.63}$$

with parameter

$$\beta = \frac{\left(\frac{\theta_{e^{-2}}}{2}\right)^2}{4\sigma_{jitt}^2} \tag{2.64}$$

This statistical model allows the average pointing loss to be estimated as

$$L_{pointing,random} = \frac{\left(\frac{\theta_{e^{-2}}}{2}\right)^2}{\left(\frac{\theta_{e^{-2}}}{2}\right)^2 + 4\sigma_{jitt}^2} \tag{2.65}$$

where σ_{jitt} is the jitter standard deviation. If errors stemming from platform vibration and beam wander are independent and normally distributed, their standard deviation can be added in quadrature to obtain the overall pointing jitter, σ_{tot}^2, as

$$\sigma_{tot}^2 = \sigma_{jitt}^2 + \theta_{BW}^2 \tag{2.66}$$

In practical systems, deterministic and random pointing errors generally coexist. Their combined effect can significantly increase the probability of deep fades and, consequently, degrade the BER and link availability [150]. In [147], a comprehensive pointing-loss model accounting for both constant angular biases and stochastic jitter contributions has been defined, according to which

$$L_{pointing,static+random} = \frac{\left(\frac{\theta_{e^{-2}}}{2}\right)^2}{\left(\frac{\theta_{e^{-2}}}{2}\right)^2 + 4\sigma_{jitt}^2} \cdot \exp\left[-2\frac{\Delta\theta_{tot}^2}{\left(\frac{\theta_{e^{-2}}}{2}\right)^2 + 4\sigma_{jitt}^2}\right]. \tag{2.67}$$

In Eq. (2.67), $\Delta\theta_{tot}$ is the total pointing bias accounting for PAA error, orbit uncertainties, and other static errors.

The mitigation of pointing errors requires a careful trade-off between optical design and tracking performance. As for beam wander, increasing the beam divergence reduces sensitivity to pointing inaccuracies by enlarging the illuminated area at the receiver. However, this approach simultaneously decreases the received power density and may lead to an unacceptable link margin penalty. For this reason, the preferred solution consists in improving the accuracy and bandwidth of the ATP system. In general, the residual pointing uncertainty must remain significantly smaller than the beam divergence angle to avoid excessive power losses. Consequently, the design of OFLs requires an accurate characterization of all pointing-error contributions and their incorporation into the overall link budget model.

2.1.6 Perturbed sky effects

In addition to molecular absorption, scattering, and optical turbulence, the propagation of an optical beam through the atmosphere can be severely affected by adverse weather conditions. Hydrometeors such as fog, clouds, rain, and snow interact with the optical wave through absorption and scattering mechanisms, causing additional attenuation of the transmitted signal. Depending on the meteorological conditions, these phenomena can introduce losses ranging from a few decibels per kilometer to several hundreds of decibels per kilometer, potentially leading to temporary link outages.

The severity of hydrometeor-induced attenuation depends on the size, concentration, and spatial distribution of atmospheric particles, as well as on the operating wavelength. Accurate modeling of these effects is therefore essential for the design and availability assessment of OFLs. Among the various weather-related impairments, fog and clouds generally represent the most critical conditions for FSO communications, while rain and snow typically produce less severe, although still significant, attenuation.

2.1.6.1 Fog and clouds

Fog is widely recognized as the most detrimental atmospheric phenomenon for optical communications. The reason lies in the fact that fog droplets typically have dimensions comparable to optical wavelengths, resulting in highly efficient scattering processes described by the Mie theory. Under dense fog conditions, attenuation levels can exceed several hundreds of decibels per kilometer, rendering the optical link temporarily unavailable [152].

Clouds affect optical propagation through mechanisms analogous to those occurring in fog. Since cloud droplets exhibit similar optical properties, both phenomena can be modeled using common attenuation frameworks based on atmospheric extinction coefficients.

A rigorous description of fog attenuation can be obtained from Mie scattering theory by integrating the extinction contribution of individual droplets over the particle-size distribution [153]. The resulting extinction coefficient, $\beta_{fog,clouds}(\lambda)$

[km^{-1}], is

$$\beta_{fog,clouds}(\lambda) = \int_{r_1}^{r_2} \pi r^2 Q_{ext}\left(m, \frac{r}{\lambda}\right) n(r) dr \tag{2.68}$$

where m is the droplet refractive index, r is the droplet radius, Q_{ext} is the extinction efficiency, and $n(r)$ is the particle-size distribution that represents the number of fog particles per unit volume and per unit of radius increment. However, detailed information on particle-size distributions is rarely available in practical applications, making empirical approaches more attractive.

For this reason, fog attenuation is commonly modeled using the concept of visibility, V [km], defined as the distance at which the radiance of a reference beam operating at 0.55 μm decreases to a specified fraction of its initial value. Visibility measurements are routinely provided by meteorological stations and therefore constitute a convenient parameter for attenuation prediction.

Based on the Beer–Lambert law, the fog extinction coefficient can be expressed as a function of visibility and wavelength through a power-law relationship. The wavelength dependence is described by the scattering coefficient as

$$\beta_{fog,clouds}(\lambda) = \frac{3.91}{V}\left(\frac{\lambda}{0.55}\right)^{-q} \tag{2.69}$$

where the size distribution coefficient q value depends on the adopted empirical model. Among the most widely used formulations are the Kruse, Kim, and Al Naboulsi models. The Kruse model represents one of the earliest visibility-based approaches, according to which

$$q = \begin{cases} 1.6 & V \geq 50 \text{ km} \\ 1.3 & 6 \text{ km} \leq V < 50 \text{ km} \\ 0.585V^{1/3} & V < 6 \text{ km} \end{cases} \tag{2.70}$$

while the Kim model extends its validity to low-visibility conditions, i.e.,

$$q = \begin{cases} 1.6 & V \geq 50 \text{ km} \\ 1.3 & 6 \text{ km} \leq V < 50 \text{ km} \\ 0.16V + 0.34 & 1 \text{ km} \leq V < 6 \text{ km} \\ V - 0.5 & 0.5 \text{ km} \leq V < 1 \text{ km} \\ 0 & V < 0.5 \text{ km} \end{cases} \tag{2.71}$$

The Kim model implies that for low visibilities, the extinction coefficient is wavelength-independent while, for higher visibilities, the attenuation decreases as the operating wavelength increases.

The Al Naboulsi model was specifically developed for fog and distinguishes between advection and convection fog, accounting for their different microphysical characteristics. This model is valid for wavelengths between 0.69 μm and 1.55 μm and for visibilities between 50 m and 1 km. The related specific attenuation, A_{fog} [dB/km], is computed as

$$A_{fog} = \begin{cases} 4.343 \cdot \frac{0.11478\lambda + 3.8367}{V} & \text{advection} \\ 4.343 \cdot \frac{0.18126\lambda^2 + 0.13709\lambda + 3.7502}{V} & \text{convection} \end{cases} \tag{2.72}$$

In all the above equations, V is in kilometers and λ in microns. Knowing the in-fog/clouds propagation length, $l_{fog/clouds}$ [km], it is possible to compute the fog/clouds-induced loss, $L_{fog/clouds}$ [dB], as

$$L_{fog/clouds} = A_{fog} l_{fog} = 10 \log_{10} \exp\left(-\beta_{fog/clouds}(\lambda) l_{fog/clouds}\right) \tag{2.73}$$

As shown in Fig. 2.16, these models generally predict attenuation values that decrease with increasing visibility, reflecting the reduced concentration of scattering particles in the atmosphere.

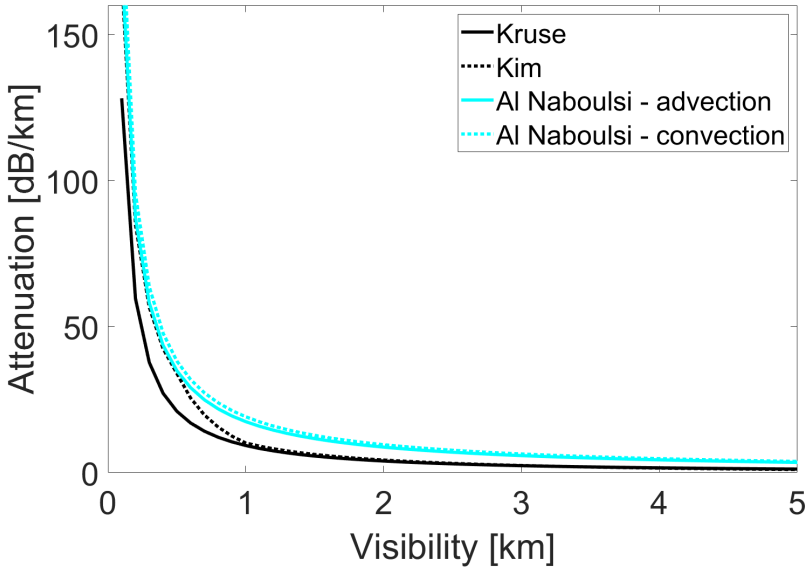


Figure 2.16 – Fog-induced specific attenuation as a function of visibility at $\lambda = 1.55$ μm

2.1.6.2 Rain

Rain affects optical propagation through both scattering and absorption by raindrops. In contrast to fog droplets, raindrops are typically larger than the optical wavelength. Consequently, the interaction between the optical wave and the particles can be accurately described using geometric optics, resulting in a scattering process that is nearly wavelength independent within the optical communication bands.

Although rain attenuation is generally less severe than fog attenuation, it can still introduce significant losses, typically ranging from approximately 1 dB/km to 10 dB/km depending on the rainfall intensity [25]. These attenuation levels are comparable to those experienced by millimeter-wave communication systems, which explains why several models originally developed for RF applications have also been adapted for optical links.

The attenuation caused by rain is commonly expressed as a power-law function of the rainfall rate, R [mm/h] [154]. Thus, the related extinction coefficient in dB/km is

$$\beta_{rain} = \gamma R^{\alpha} \tag{2.74}$$

In Eq. (2.74), γ and α are parameters dependent on the raindrop-size distribution whose values can be empirically estimated.

The derivation of this relationship originates from the raindrop-size distribution, which describes the number of drops of a given diameter per unit volume. Among the available models, the Marshall and Palmer one is the most widely adopted and assumes an exponential distribution of drop diameters, leading to $\gamma = 0.365$ and $\alpha = 0.63$ [155]. Other formulations, such as the Carbonneau model, according to which $\gamma = 1.076$ and $\alpha = 0.67$ [156], and the Korai, Luini and Nebuloni (KLN) model, have been proposed based on extensive experimental observations and regional climatological data [157]. In detail, the KLN model relies on the definition of the so-called shape parameter, μ, that can assume integer values between -3 and 8 and is related to the adopted raindrop-size distribution. Assuming a gamma distribution, the parameters listed in Table 2.1 have been derived.

Table 2.1 – Coefficients of the KLN model [157]

μ	γ	α
-3	4.0684	0.2077
-2	2.2838	0.4050
-1	1.5921	0.5506
0	1.2924	0.6436
1	1.1394	0.7057
2	1.0505	0.7497
3	0.9938	0.7823
4	0.9551	0.8074
5	0.9273	0.8273
6	0.9065	0.8435
7	0.8905	0.8569
8	0.8779	0.8682

As an alternative to the above-mentioned models, rain attenuation can also be computed based on visibility through the Atlas model [158], i.e.,

$$\beta_{rain} = \frac{2.9}{V} \tag{2.75}$$

As for fog, the rain-induced loss, L_{rain} [dB], is obtained by multiplying Eq. (2.74) by the in-rain propagation length, l_{rain} [km].

Regardless of the adopted formulation, all models predict an increase in attenuation with increasing rainfall rate, as clearly visible in Fig. 2.17 . Consequently, rain-induced losses become particularly relevant in tropical and subtropical regions characterized by intense precipitation events.

2.1.6.3 Snow

Snow attenuation depends on both the snowfall rate, S [mm/h], and the physical characteristics of snowflakes. Since snowflakes are generally larger and more irregular than raindrops, they can produce stronger attenuation effects, with typical

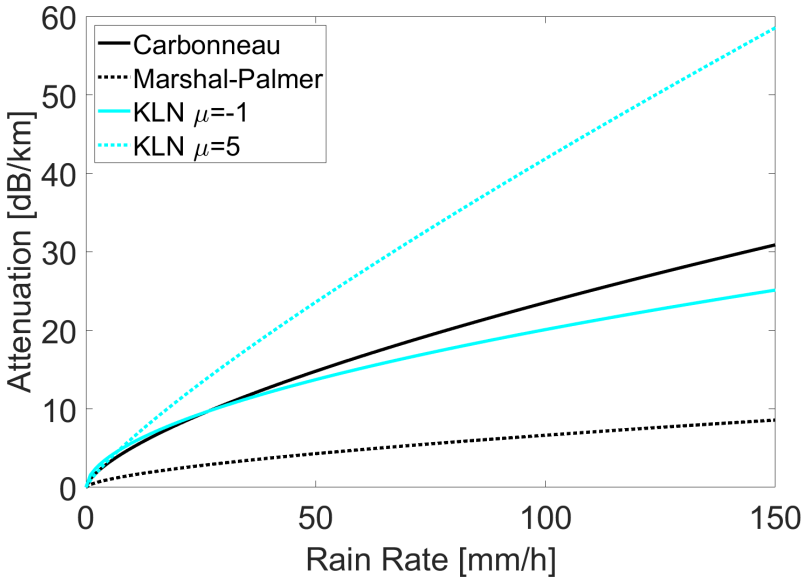


Figure 2.17 – Rain-induced specific attenuation as a function of rain rate

values ranging from a few decibels per kilometer to several tens of decibels per kilometer [159].

The interaction between optical radiation and snow particles is more complex than in the case of rain because snowflakes exhibit highly variable shapes, densities, and water contents. For this reason, attenuation models usually distinguish between dry snow and wet snow.

The specific attenuation due to snowfall is commonly expressed through a power-law relationship involving the snowfall rate [156], as

$$\beta_{snow} = aS^b \tag{2.76}$$

$$a = \begin{cases} 5.42 \cdot 10^{-5}\lambda + 5.4958776 & \text{dry snow} \\ 1.023 \cdot 10^{-4}\lambda + 3.7855466 & \text{wet snow} \end{cases} \tag{2.77}$$

$$b = \begin{cases} 1.38 & \text{dry snow} \\ 0.72 & \text{wet snow} \end{cases} \tag{2.78}$$

where the coefficients a and b depend on the operating wavelength, expressed in nanometers, and on the type of snow. A comparison between wet and dry snow-induced losses in shown in Fig. 2.18. Alternative empirical formulations based

solely on visibility measurements are also available and are often preferred when direct snowfall-rate data are unavailable. For example, according to [128],

$$\beta_{snow} = \frac{58}{V} \tag{2.79}$$

Also in this case, the overall snow-induced loss, L_{snow} [dB], is obtained by multiplying the related specific attenuation by the in-snow propagation length, l_{snow} [km].

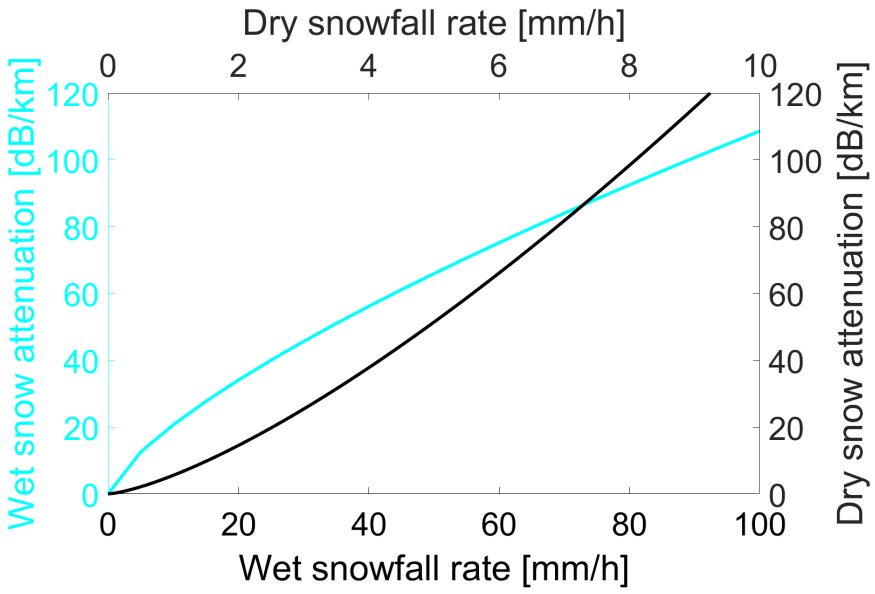


Figure 2.18 – Snow-induced specific attenuation as a function of snowfall rate for wet (cyan curve) and dry (black curve) snow

Although snow events occur less frequently than rain in many geographical regions, they can significantly degrade optical communication performance because of the large dimensions of snowflakes and their ability to partially obstruct the optical beam. Consequently, snowfall statistics must be considered when assessing the long-term availability of OFLs in cold-climate environments.

It is important to highlight that the above hydrometeor-related models provide a first-order approximation to evaluate the losses involved in OFLs. To better refine their applicability to slant paths, published works propose to define several horizontal layers of clouds within the Earth's atmosphere [160–162]. For each layer,

thickness and visibility are defined as input parameters to be used in the above equations. A more accurate prediction can be obtained by exploiting tools such as MODTRAN, which can also model fog, clouds, and rain.

In summary, the attenuation introduced by fog, clouds, rain, and snow can severely reduce the availability of OFLs. Several mitigation techniques have therefore been proposed in the literature, including the deployment of geographically distributed OGS networks, dynamic routing of optical traffic toward locations experiencing favorable weather conditions, and hybrid RF/optical communication architectures. In particular, hybrid systems exploit the complementary behavior of optical and RF links, switching to RF transmission when adverse weather conditions prevent reliable optical communication.

2.1.7 Receiver

The receiver subsystem is responsible for collecting the optical power and converting it into an electrical signal suitable for subsequent processing. In OFLs, the receiver typically consists of a telescope, optical filtering and coupling optics, and a photodetection stage. The characteristics of the receiving optics directly influence the amount of collected optical power and therefore play a fundamental role in the overall link budget.

After propagation through free space and the atmosphere, only a fraction of the transmitted optical power is intercepted by the receiver aperture. Assuming far-field propagation, the received power, P_R can be related to the receiver collecting area, A_R, as

$$P_R = \frac{G_T P_T A_R}{4\pi R^2} \tag{2.80}$$

In analogy with RF systems, the receiving telescope can be characterized by a receiver gain, G_R, which is related to the effective collecting area according to

$$G_R = \frac{4\pi A_R}{\lambda^2} \tag{2.81}$$

For a circular receiver aperture of diameter D_R

$$G_R = \left(\frac{\pi D_R}{\lambda}\right)^2 \tag{2.82}$$

The receiver gain therefore increases quadratically with the aperture diameter and decreases with the square of the operating wavelength. A larger receiving aperture allows a greater fraction of the incoming optical beam to be collected, thereby improving the received signal level. However, increasing the aperture diameter also results in a larger collection of background radiation, which may degrade the SNR, especially in daytime operations.

Practical receiver systems are further characterized by an optical efficiency factor, η_R, accounting for losses introduced by the telescope optics, filters, mirrors, lenses, and detector coupling stages. This factor is included in the link budget to represent the fraction of collected optical power that effectively reaches the detection subsystem.

In coherent optical communication systems and in pre-amplified receivers, the collected optical beam is typically coupled into a SMF before amplification and photodetection. The efficiency of this process is quantified by the SMF coupling efficiency η_F, defined as the ratio between the average optical power coupled into the fiber and the average optical power in the receiver plane.

For an ideal diffraction-limited wavefront, efficient coupling can be achieved through proper matching between the incoming optical field and the fundamental mode supported by the fiber. However, atmospheric turbulence introduces phase distortions that reduce the spatial coherence of the received wavefront, thereby degrading the achievable coupling efficiency.

The coupling efficiency can be expressed as the overlap integral between the received optical field and the fiber mode profile [163]. For a partially coherent optical wave, it can be written as

$$\eta_F = \frac{\left\langle \left| \int_A U_i(\boldsymbol{r}) U_m^*(\boldsymbol{r}) d\boldsymbol{r} \right|^2 \right\rangle}{\left\langle \int_A \left| U_i(\boldsymbol{r}) \right|^2 d\boldsymbol{r} \right\rangle} \tag{2.83}$$

In Eq. (2.83), $U_i(\boldsymbol{r})$ is the optical field at the receiver plane, $U_m(\boldsymbol{r})$ is the normalized fiber-mode profile, and the integrals are evaluated over the receiver aperture area.

The exact evaluation of this quantity requires knowledge of the mutual coherence function of the received optical field and generally leads to a computationally demanding four-dimensional integral. To obtain a tractable model suitable

for link budget calculations, the mutual coherence function is commonly approximated by a Gaussian distribution characterized by the spatial coherence radius $\rho_0 = 0.48 r_0$ [127]. Under this assumption, the coupling efficiency can be expressed as

$$\eta_F = 8a^2 \int_0^1 \int_0^1 \exp\left[\left(-a^2 - \frac{A_R}{A_C}\right)\left(x_1^2 + x_2^2\right)\right] \cdot I_0\left(\frac{2A_R}{A_C} x_1 x_2\right) x_1 x_2 \, dx_1 \, dx_2 \tag{2.84}$$

where $A_C = \pi \rho_0^2$ is the spatial coherence area of the incident wave, also known as speckle size, the ratio A_R/A_C is the number of speckles over the receiver aperture area, and the parameter a is given by

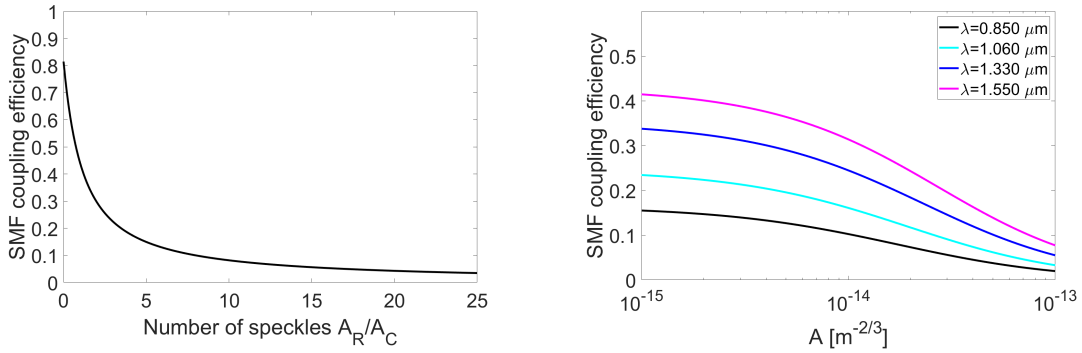
$$a = \frac{D_R}{2} \frac{\pi W_m}{\lambda f} \tag{2.85}$$

with W_m [m] being the fiber-mode field radius at the fiber end face and f [m] the receiver focal length. As turbulence strength increases, the spatial coherence radius decreases, causing the number of speckles to increase and consequently reducing the coupling efficiency.

Regarding the a parameter, it can be demonstrated that its optimum value for a fully coherent wave is $a = 1.12$, which leads to a maximum coupling efficiency of 0.815. Instead, for a partially coherent wave, the optimum value will depend on the number of speckles. Nevertheless, if the ratio D_R/f can be manipulated to satisfy the condition $a = 1.12$, an analogous result can be obtained [163].

Although more general formulations exist, the Gaussian approximation has been shown to provide excellent accuracy while significantly reducing the computational burden. For this reason, it is commonly adopted in OFL analyses.

Figure 2.19a depicts the SMF coupling efficiency as a function of the number of speckles over the receiving aperture, while Fig. 2.19b depicts the same quantity as a function of turbulence strength at ground and for different wavelengths. The dependence of η_F on atmospheric conditions highlights the strong impact of optical turbulence on coherent optical communication systems. Stronger turbulence, longer propagation paths, or shorter operating wavelengths generally lead to smaller coherence radii and therefore lower coupling efficiencies. Conversely, longer wavelengths and weaker turbulence conditions tend to preserve



(a) (b)

Figure 2.19 – SMF coupling efficiency as a function of (a) the number of speckles over the receiver aperture, and (b) the refractive index structure parameter at ground, considering $a = 1.12$

wavefront coherence, improving the fraction of power that can be successfully coupled into fiber. As a result, the SMF coupling efficiency constitutes an additional turbulence-dependent loss term that must be included in the link budget whenever fiber coupling is required. In coherent and pre-amplified OFLs, this contribution may become comparable to other turbulence-induced impairments and therefore represents an important factor in the accurate prediction of system performance.

2.2 Link budget model for OFLs

During this research work, a novel link-budget model has been developed to support the design and performance evaluation of both uplink and downlink OFLs under a wide range of operating conditions. The model integrates the propagation phenomena discussed in the previous sections into a unified framework, accounting for atmospheric attenuation, optical turbulence, hydrometeor-induced losses, pointing impairments, and transmitter and receiver effects. Particular attention was devoted to the accurate modeling of turbulence-induced phenomena and to the asymmetry between uplink and downlink propagation, which is often overlooked in existing literature. The developed model has been implemented to build a Matlab-based link budget numerical tool.

Unlike many previously published OFL link budget models, which are generally

tailored to specific scenarios or rely on simplified assumptions, the developed tool provides a high degree of flexibility. Moreover, the tool enable the analysis of both static and dynamic communication scenarios, ranging from GEO OFLs to rapidly varying LEO OFLs.

According to the developed model, the received optical power, P_R [W], can be expressed as the product of transmitter's gain and efficiency, channel transmission losses, and receiver's gain and efficiencies. In its most general form, the implemented model evaluates the received power as

$$P_R = P_T G_T \eta_T G_R \eta_R \eta_F \tau_{ATM} L_{pointing} L_{SR} L_{FS} L_{fog/clouds} L_{rain} L_{snow} \tag{2.86}$$

where

- P_T is the transmitted optical power
- G_T and G_R are the transmitter and receiver telescope gains, respectively
- η_T and η_R represent the transmitter and receiver optical efficiencies, respectively
- η_F is the SMF coupling efficiency
- τ_{ATM} accounts for molecular absorption and atmospheric scattering
- $L_{pointing}$ represents losses due to pointing errors
- L_{SR} is the turbulence-induced beam spreading loss
- L_{FS} is the free-space propagation loss
- $L_{fog/clouds}$, L_{rain}, and L_{snow} describe attenuation caused by hydrometeors.

Different terms contribute to uplink and downlink propagation. For uplink transmissions, the received power includes the effects of beam wander, which is combined with other pointing errors in the $L_{pointing}$ term, and turbulence-induced beam spreading, which are negligible in downlink.

The available link margin can then be computed as

$$LM = P_R - S_R \tag{2.87}$$

where S_R is the receiver sensitivity, and both P_R and S_R are expressed in dB. The link margin represents the excess received power available to counteract fading and determines the achievable link availability for a given modulation and coding scheme.

A key objective of the developed tool was to provide a flexible framework capable of adapting to different mission scenarios and environmental conditions. To this end, several alternative models have been implemented for each propagation phenomenon. For what concerns atmospheric turbulence, the tool supports both the classical Rytov theory and the extended Rytov formulation. The former is applicable under weak turbulence conditions and offers reduced computational complexity, whereas the latter remains valid across all turbulence regimes and is therefore preferred when strong turbulence is expected.

Several atmospheric turbulence profiles can be selected to describe the vertical evolution of the refractive-index structure parameter, enabling the analysis of different geographical locations and climatic conditions. Furthermore, the tool automatically accounts for aperture averaging effects in downlink scenarios whenever the receiver aperture becomes larger than the transverse irradiance correlation width.

Particular attention was devoted to beam wander, which is one of the major contributors to uplink performance degradation. The developed implementation goes beyond conventional formulations by allowing three different approaches for the evaluation of the propagation distance appearing in the beam wander variance expression, i.e., (i) the classical flat-Earth approximation, (ii) the improved geometrical approximation accounting for Earth curvature and OGS altitude, and (iii) the exact link distance value. The latter can be easily retrieved in Matlab by knowing the OGS coordinates and satellite orbital parameters.

The tool can evaluate both tracked and untracked beam configurations, allowing the user to quantify the benefits of beam tracking.

Pointing losses are evaluated through a comprehensive framework capable of distinguishing between deterministic and random pointing impairments.

To maximize applicability to different climatic regions, the multiple empirical attenuation models presented in Section 2.1.6 have been incorporated to describe

adverse weather conditions. The possibility of selecting between them is particularly important because their validity ranges strongly depend on local meteorological conditions.

A further strength of the developed tool is the capability to analyze dynamic OFL scenarios. For LEO satellite communications, the link geometry changes continuously during a pass. Consequently, the propagation distance, elevation angle, atmospheric path length, turbulence strength, and pointing requirements become time-dependent. The tool reconstructs the satellite trajectory and evaluates the link budget at multiple time instants throughout the pass, enabling temporal analyses of received power and turbulence-related quantities.

In addition, parametric sweeps involving up to two independent variables can be performed, providing a useful capability for sensitivity analyses and system optimization studies.

The developed model extends the state of the art in several respects.

First, most existing OFL link budget analyses focus on specific scenarios of interest and consider either uplink or downlink propagation [134, 164]. Additionally, they often rely on a single propagation theory (i.e., Rytov or extended Rytov) [134, 137, 165]. In contrast, the proposed framework supports both propagation directions, fully modeling the differences between them, and incorporates both Rytov and extended Rytov formulations.

Furthermore, several turbulence-induced effects are frequently neglected or described through simplified analytical models that sacrifice accuracy for mathematical convenience, despite their significant impact on the performance of atmospheric FSO links. Specifically, beam wander is frequently neglected or only partially considered in published models [137, 156, 165, 166]. On the contrary, the developed implementation explicitly accounts for both the direct pointing loss induced by beam wander and its contribution to scintillation enhancement. Moreover, the accuracy of the beam wander model is investigated and enhanced in the proposed tool through dedicated geometrical models.

Also with regard to pointing losses, many literature approaches employ simplified models that do not distinguish between deterministic and random error sources [134,137,156,164–167]. The proposed tool separately models these impair-

ments and evaluates their combined effect through statistically consistent formulations.

Likewise, perturbed sky effects are often omitted [134, 164, 165]. The implemented framework instead allows the user to select among multiple validated models for fog, clouds, rain, and snow, thereby increasing applicability across different climatic environments.

Finally, unlike most published studies that evaluate only static scenarios, the developed tool supports time-varying LEO links and dynamic orbit-dependent analyses.

Overall, the resulting framework provides a comprehensive and highly configurable environment for OFL design, enabling accurate performance estimation across a wide range of propagation conditions and system architectures. It therefore represents a significant advancement over conventional link budget methodologies and constitutes the foundation for all numerical investigations presented in the remainder of this thesis.

In the next subsections, the validation results of the proposed model are shown. In detail, both GEO and LEO campaigns have been taken as reference to perform link budget analyses and compare the outcomes with experimental, published measurements. Finally, in Section 2.2.4, the implications that the different degrees of link distance approximation have on the beam wander model's accuracy are investigated.

2.2.1 Downlink LEO OFL

The KODEN campaign, jointly conducted by JAXA and NICT, represented the first successful bidirectional optical communication demonstration between a LEO satellite and a ground station [168].

The experimental campaign was carried out between 2006 and 2009 using the OICETS satellite, also known as Kirari, orbiting at an altitude of approximately 610 km [169]. The satellite was equipped with the LUCE optical terminal, featuring a transmitting telescope with an aperture diameter $D_T = 26$ cm and operating at a wavelength of 847 nm. The transmitted optical power was $P_T = 100$ mW, while the transmitter optical efficiency was $\eta_T = -2.7$ dB. The receiving terminal

was the NICT OGS located in Koganei, Tokyo, at an altitude of 122 m above mean sea level. During the considered measurement campaign, the receiving telescope aperture diameter was $D_R = 20$ cm and the receiver optical efficiency was equal to $\eta_R = -8.1$ dB. Nonetheless, after May 2006, a 31.8-cm sub-aperture of the 1.5-m transmitting telescope was used for reception [169].

A particular aspect of the KODEN experiment was the investigation of the SMF coupling degradation under atmospheric turbulence [170]. Consequently, the SMF coupling efficiency was explicitly included in the link budget evaluation, providing an additional validation metric for the developed model.

The reference experimental data correspond to measurements acquired on 30 March 2006 [168]. Since the exact timing information necessary to reconstruct the complete satellite pass is not available, the analysis was performed for a representative operating condition corresponding to an elevation angle of $\zeta = 25°$, for which atmospheric transmittance measurements were reported in [168]. Specifically, a measured atmospheric transmittance of 0.45 was therefore adopted in the link budget calculations.

To accurately reproduce the atmospheric conditions at the NICT site, a variation of the HV turbulence profile was developed in [169] based on local measurements. The resulting refractive-index structure parameter profile is expressed as

$$\begin{aligned} C_n^2(h) = M \cdot 0.00594 \left(\frac{w}{27}\right)^2 (10^{-5}h)^{10} \exp\left[-\frac{h}{1000}\right] \\ + 2.7 \cdot 10^{-16} \exp\left[-\frac{h}{1500}\right] + A \exp\left[-\frac{h}{100}\right] \end{aligned} \tag{2.88}$$

where the experimentally derived parameters are $M = 0.2$, $A = 9.0 \cdot 10^{-14}$ m$^{-2/3}$, and $w = 21$ m/s. This turbulence model was implemented within the numerical tool to enable a direct comparison between simulated and measured quantities.

Considering the relatively low elevation angle, which increases the optical path through the turbulent atmosphere and enhances turbulence effects, the extended Rytov theory was adopted for the computation of scintillation-related quantities. The scintillation fade margin was evaluated assuming a target outage probability $\rho_{thr} = 10^{-4}$, corresponding to a link availability of 99.99%.

Additional losses due to fog, clouds, rain, or snow were not included in the analysis since the measured atmospheric transmittance already incorporates the attenuation associated with the meteorological conditions experienced during the experiment [168].

Regarding pointing performance, the KODEN campaign employed a tracking system capable of removing the initial pointing bias before the communication phase. Consequently, only residual tracking jitter is considered. Based on the experimental measurements, a pointing jitter standard deviation of 2.0 μrad is assumed in the simulations [169].

The performed link budget analysis for the described downlink LEO OFL is reported in Table 2.2.

Table 2.2 – Link budget analysis for the downlink LEO OFL

Output parameter	**Value**
Transmitted power P_T	20 dBm
Free space loss L_{FS}	-265.32 dB
Transmitter telescope gain G_T	121.78 dB
Receiver telescope gain G_R	117.41 dB
Extinction loss τ_{ATM}	-3.80 dB
Turbulence-induced beam spreading loss L_{SR}	—
Pointing loss $L_{pointing}$	-2.53 dB
Scintillation margin L_{SI}	-9.13 dB
SMF coupling efficiency η_F	74 dB
Received optical power P_R	-36.98 dBm

The obtained results demonstrate an excellent agreement between the numerical predictions and the experimental observations. Indeed, the computed average received optical power is equal to -36.98 dBm, which falls within the range of the measured values reported during the KODEN campaign that, for convenience, are shown in Fig. 2.20 [168]. Similarly, the estimated SMF coupling loss of -13.74

dB is fully consistent with the experimentally observed values, which ranged between -11 dB and -18 dB depending on atmospheric conditions, as shown in Fig. 2.21 [170].

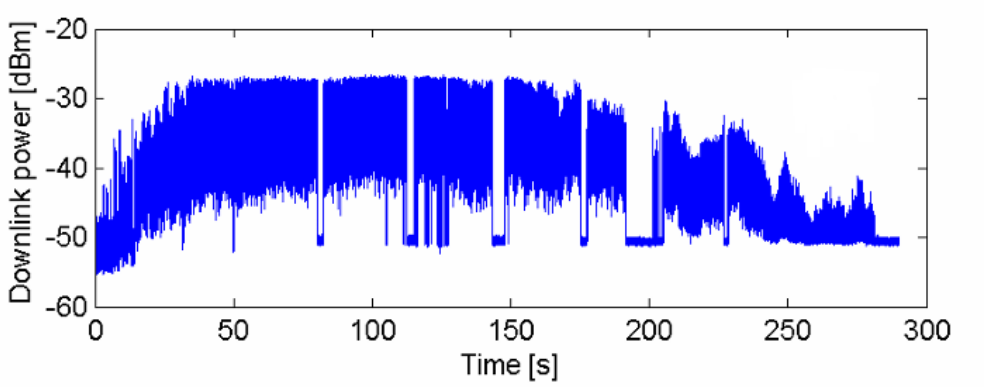


Figure 2.20 – Downlink received power for the KODEN experimental trial conducted on March 30, 2006 [168]

The turbulence-related quantities predicted by the model also show remarkable agreement with measurements [169]. In particular, the numerical tool estimates a Fried's parameter of 4.62 cm at the OGS and a scintillation index of 0.32. The latter value was obtained by automatically accounting for aperture averaging effects at the receiver. Indeed, the computed transverse irradiance correlation width was found to be smaller than the receiver aperture diameter, thus activating the aperture-averaging correction implemented in the model.

The results highlight the significant impact of atmospheric turbulence on the performance of LEO OFLs. Although the average received power remains compatible with successful communication, the estimated scintillation margin demonstrates that turbulence-induced fading cannot be neglected during system design. The link margin must be sufficiently large to ensure that the instantaneous received power remains above the receiver sensitivity despite the fluctuations induced by scintillation. This requirement becomes even more critical in practical LEO scenarios, where the satellite elevation angle continuously varies during the pass, causing corresponding variations in turbulence impairments.

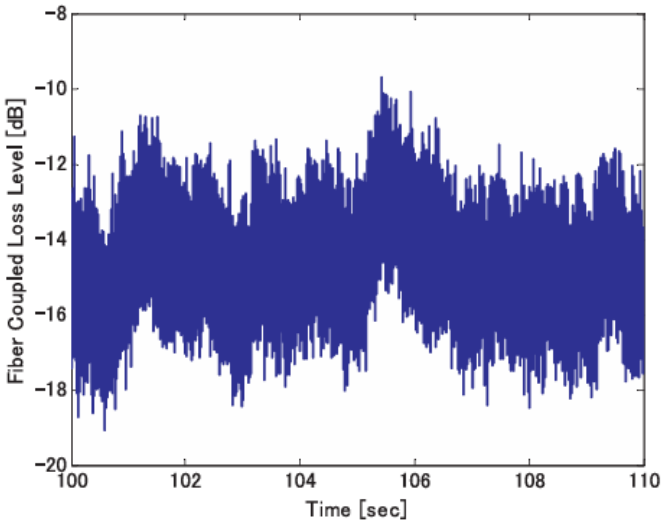


Figure 2.21 – Downlink fiber coupling efficiency for the KODEN experimental campaign [170]

2.2.2 Uplink GEO OFL

The accuracy of the developed link budget model whas been further assessed by considering an uplink OFL towards a GEO satellite. In particular, the analyzed scenario reproduces the optical communication experiments conducted between Tesat's T-AOGS and the TDP1 LCT onboard the Alphasat satellite [64].

The validation has been performed considering the same operating conditions as the experimental campaign conducted on 26 April 2018. Starting from the publicly available TLE data describing the Alphasat orbit, downloadable at [171], and from the geographical coordinates of the OGS, it is possible to reconstruct the link geometry at the time of the measurements. The T-AOGS was co-located with the ESA ground station in Tenerife, at an altitude of 2450 m above mean sea level [64]. The analysis has been performed at the beginning of the acquisition interval, corresponding to 01:05:48 UTC, resulting in a satellite altitude of approximately 35 800 km, an elevation angle of 32.9°, and a link distance of 38 368 km.

The T-AOGS transmitter is capable of operating with three different aperture diameters, namely 35 mm, 48 mm, and 95 mm. During the considered experiment, the smallest aperture was selected, corresponding to a transmitter beam radius

$W_0 = 15.6$ mm. The optical signal was transmitted at a wavelength of 1064 nm with an optical power of 50 W and a transmitter efficiency of -1.5 dB [172].

On the receiver side, the TDP1 terminal employs a telescope with an aperture diameter of 135 mm and adopts a coherent homodyne detection architecture [64]. Consequently, the SMF coupling efficiency has been included among the link budget contributions, as its degradation due to atmospheric turbulence can significantly affect the received optical power.

Pointing performance represents a critical aspect of GEO OFLs due to the extremely narrow beam divergences involved. Experimental measurements indicate that the residual tracking error of the satellite terminal during communications exhibited a rms value $\sigma_{jitt} = 0.07$ μrad [65]. In addition, the alignment of the T-AOGS was manually optimized before each communication session, limiting the residual static pointing error to $\Delta\theta_{OGS} = 10$ μrad [173]. Therefore, both deterministic and random pointing contributions have been included in the numerical analysis.

The atmospheric transmittance has been assumed equal to 0.92, consistently with measurements previously reported for the Tenerife site under comparable atmospheric conditions [174]. Since the analyzed experiment was conducted under clear-sky conditions, additional attenuation due to fog, clouds, rain, or snow has not been considered.

To accurately characterize atmospheric turbulence, the Maui3 refractive-index structure parameter profile was adopted. Although originally developed for the Maui observatory, this profile has been shown to provide a good representation of the turbulence conditions experienced at the Tenerife site [175]. The corresponding model, which is reported in Eq. (2.89), has been implemented within the numerical tool, enabling a fair comparison between simulated and experimental results.

$$C_n^2(h) = \begin{cases} 10^{-9.4010-1.5913h-0.0606h^2} & 3.048 \text{ km} < h \leq 4.2 \text{ km} \\ \quad -17.1273 - 0.0332h - 0.0015h^2 & \\ \quad +0.9061 \exp\left[-\frac{1}{2}\left(\frac{h-15.0866}{5.2977}\right)^2\right] & \\ 10 & 4.2\,\text{km} < h \leq 25\,\text{km} \\ \exp\left[-\frac{h-25}{5}\right] & h > 25 \text{ km} \end{cases} \tag{2.89}$$

As in the previous LEO downlink case, the extended Rytov theory has been selected for the evaluation of turbulence-induced effects. This choice is justified by the relatively low elevation angle, which increases the atmospheric path length and may lead to turbulence conditions outside the strict validity range of classical Rytov theory.

The scintillation margin has been computed assuming a target link availability of 99.99%. Furthermore, the analysis has been performed considering an untracked beam configuration, allowing the complete impact of beam wander and turbulence-induced pointing fluctuations to be evaluated.

The resulting link budget, reported in Table 2.3, predicts an average received optical power of -43.94 dBm, in excellent agreement with the experimentally measured value of -42.6 dBm [64].

Table 2.3 – Link budget analysis for the uplink GEO OFL

Output parameter	**Value**
Transmitted power P_T	46.99 dBm
Free space loss L_{FS}	-293.13 dB
Transmitter telescope gain G_T	102.38 dB
Receiver telescope gain G_R	112.01 dB
Extinction loss τ_{ATM}	-0.36 dB
Turbulence-induced beam spreading loss L_{SR}	-0.68 dB
Beam wander and pointing loss $L_{pointing}$	-5.16 dB
Scintillation margin L_{SI}	-9.74 dB
SMF coupling efficiency η_F	-4.50 dB
Received optical power P_R	-43.94 dBm

The turbulence-related quantities computed by the tool also exhibit a strong agreement with experimental observations. In particular, a turbulence coherence length $r_0 = 11.46$ cm and a scintillation index $\sigma_I^2 = 0.37$ were obtained. Both

values are consistent with the measurements reported during the experimental campaign [64], and shown in Fig. 2.22, providing further validation of the implemented turbulence models.

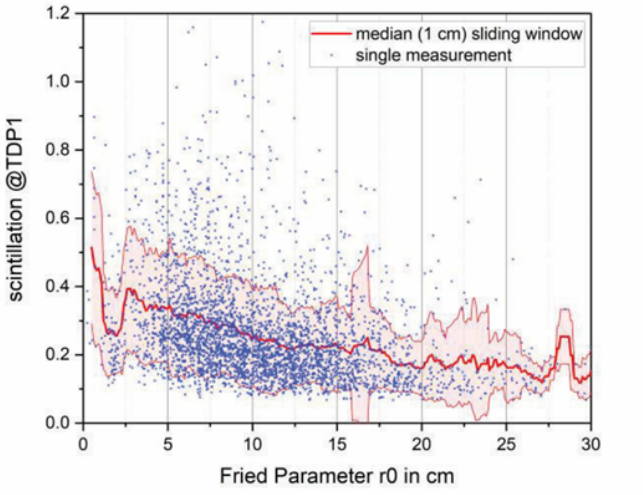


Figure 2.22 – Scintillation seen at the TDP1 as a function of the Fried's parameter measured at the T-AOGS [64]

2.2.3 Dynamic downlink LEO OFL

To further assess the capabilities of the developed model and tool in dynamic operating conditions, a complete LEO pass has been analyzed. In detail, downlink transmission is considered based on the KIODO experiment. The campaign, carried out in 2006 through a collaboration between DLR, JAXA, and NICT, represented the first successful LEO optical downlink demonstration in Europe. During the campaign, the LUCE terminal installed onboard the OICETS satellite transmitted an optical beam toward the Optical Ground Station Oberpfaffenhofen (OGS-OP), located near Munich [176].

Unlike the static validation scenarios previously presented, the KIODO experiment provides an ideal benchmark for demonstrating the dynamic analysis capabilities of the developed tool. The exact acquisition start time, i.e., 01:04 UTC on 14 June 2006, and the communication duration of approximately 380 s are known from the literature [176], enabling a complete reconstruction of the

satellite pass. By exploiting the parametric sweep functionalities implemented in the numerical framework, the received optical power was evaluated over the entire communication interval.

The satellite orbit was reconstructed in Matlab starting from the corresponding TLE data, while the geographical coordinates of the OGS-OP were used to determine the time evolution of the link geometry [177]. Link distance and elevation angle, shown in Fig. 2.23, were computed at a sampling frequency of 1 Hz throughout the satellite pass. As expected, the continuously changing geometry of the LEO link resulted in significant variations of both quantities. In particular, lower elevation angles corresponded to longer propagation distances and a larger atmospheric path length, whereas the minimum link distance was achieved near the highest elevation angles.

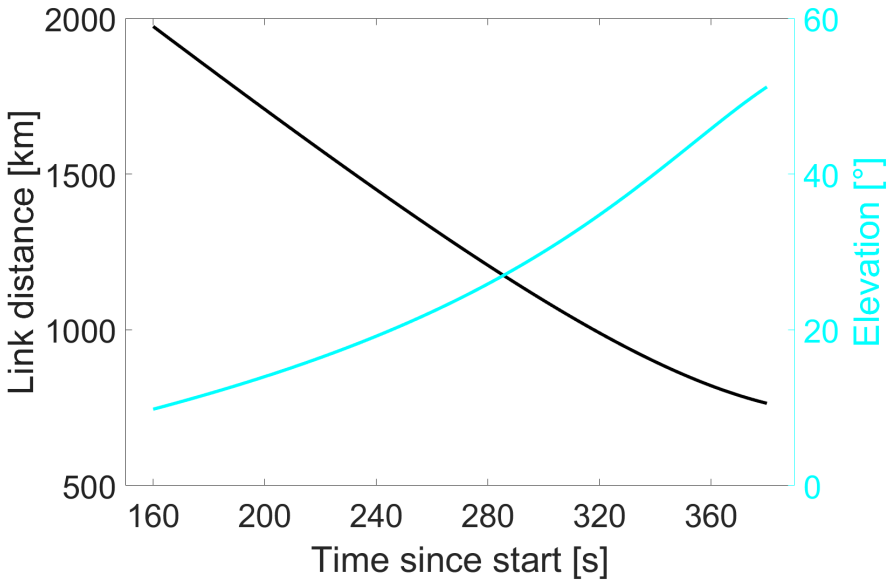


Figure 2.23 – Link distance (black curve) and elevation angle (cyan curve) as a function of the time elapsed since the pass of the satellite for the dynamic downlink LEO OFL

The transmitter characteristics are equal to those employed in the KODEN experiments. Specifically, the LUCE terminal transmitted an optical beam with a power of 100 mW at a wavelength of 847 nm through a telescope with an aperture diameter of 26 cm [168]. The receiving terminal at OGS-OP employed a 40

cm aperture telescope followed by a direct-detection receiver chain [176]. Consequently, no SMF coupling losses were included in the link budget calculation [177]. Since specific measurements of the transmitter and receiver optical efficiencies were not available for this experiment, a transmitter efficiency of -2.7 dB, consistent with previous LUCE-based analyses [168], was assumed, while the receiver efficiency was set equal to 0 dB.

The maximum rms tracking error reported for the experiment was $\sigma_{jitt} = 0.7$ μrad and was included in the pointing error model [178]. Concerning atmospheric losses, an atmospheric transmittance of 0.19 was adopted according to experimental observations [178]. Since the measurements were performed during clear-sky nighttime conditions, no additional attenuation due to fog, clouds, rain, or snow was considered [176].

The turbulence characterization was based on measurements of the refractive-index structure parameter collected during the KIODO campaign [178]. The best-fitting turbulence profile derived from experimental scintillation data has been implemented within the numerical tool, that is, the HV model with parameters $A = 2.20 \cdot 10^{-12}$ m$^{-2/3}$ and $w = 10$ m/s [179]. Moreover, the extended Rytov theory was proven to give better accuracy and, therefore, has been used for the analysis [179].

The resulting received optical power, depicted in Fig. 2.24, has been evaluated as a function of elevation angle. The simulated trend closely reproduces the behavior observed during the experimental campaign, which is shown in Fig. 2.25 [176]. In particular, the received power increases as the satellite approaches its maximum elevation and decreases again as the satellite moves away from zenith. Although the simulated values are approximately 8 dB higher than the measured ones, this discrepancy can reasonably be attributed to the uncertainty associated with the transmitter and receiver efficiency assumptions, whose actual values are not available in the published experimental reports.

The results clearly highlight the strong dependence of the received optical power on the instantaneous link geometry. Since the transmitted optical power remained constant throughout the pass, the varying propagation distance produced significant fluctuations in the received signal level. This observation demonstrates that

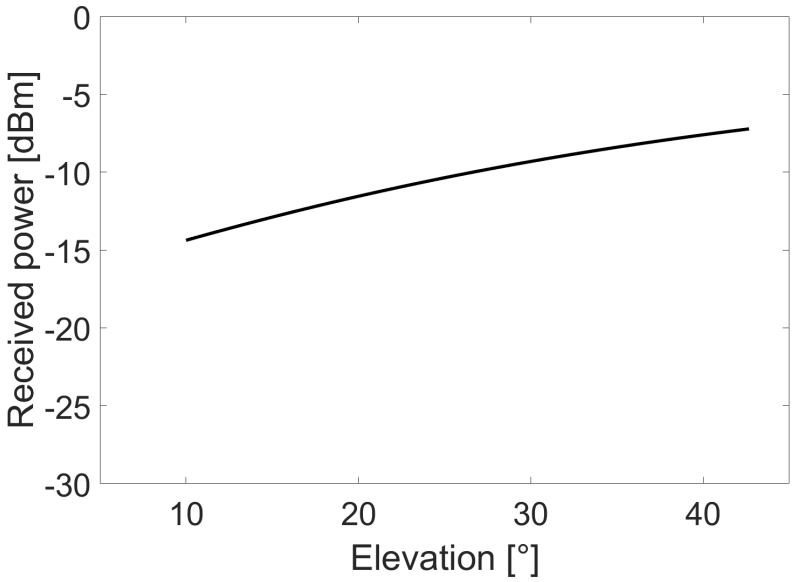


Figure 2.24 – Received optical power as a function of the elevation angle for the dynamic downlink LEO OFL

the design of LEO OFLs must account for the entire range of operational elevation angles.

To further validate the turbulence modeling capabilities of the tool, the Fried's parameter and scintillation index have also been evaluated as function of the elevation angle. The numerical results, shown in Fig. 2.26, confirm the expected physical behavior. As the elevation angle increases, the atmospheric path length decreases, resulting in reduced turbulence effects. Consequently, the scintillation index decreases while the Fried's parameter increases, indicating a larger atmospheric coherence length and improved wavefront quality.

The predicted trends have been found to be in good agreement with the experimental measurements reported during the KIODO campaign [176], shown in Fig. 2.27. In particular, the scintillation index shows excellent agreement with the measured values over the entire range of elevation angles. A slight overestimation of the Fried's parameter is instead observed [178]. This discrepancy can be explained by the fact that the adopted turbulence profile had been originally optimized to reproduce the measured scintillation statistics rather than the atmospheric coherence length [179]. Nevertheless, the overall agreement between

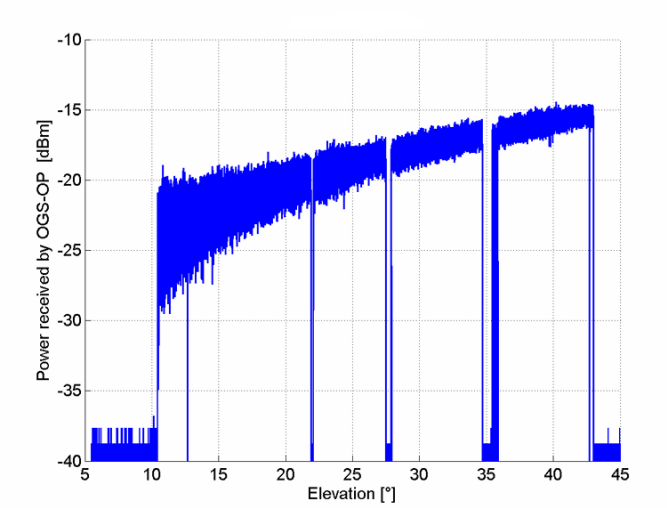


Figure 2.25 – Received optical power as a function of the elevation angle for the KIODO trial on 14 June 2006 [176]

numerical predictions and experimental observations confirms the capability of the proposed tool to accurately model the evolution of OFLs performance under realistic dynamic LEO operating conditions.

2.2.4 Impact of Link Distance Modeling on Beam Wander Estimation

One of the original contributions of the developed OFL link budget tool concerns the investigation of the impact of link distance modeling on the accuracy of beam wander predictions. As discussed in Section 2.1.4.3, conventional beam wander formulations typically rely on a simplified approximation of the slant-path propagation distance. Although this assumption is commonly adopted in the literature, its influence on the accuracy of beam wander estimates was not previously quantified.

To assess this effect, a comparative analysis has been performed considering the GEO uplink scenario presented in Section 2.2.2. The same system configuration, atmospheric conditions, and turbulence parameters have been adopted, while the beam wander variance, previously computed by using the conventional flat-Earth approximation of Eq. (2.7), has now been evaluated using two additional

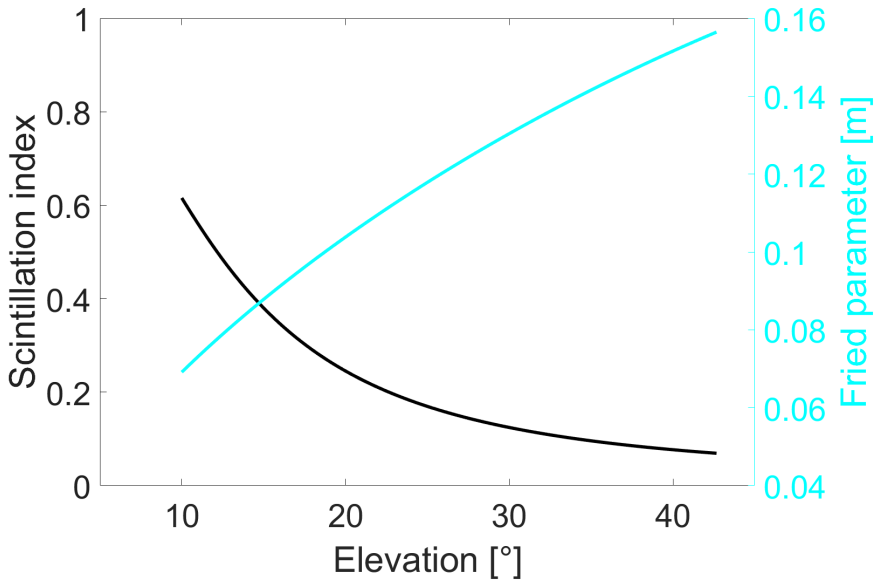
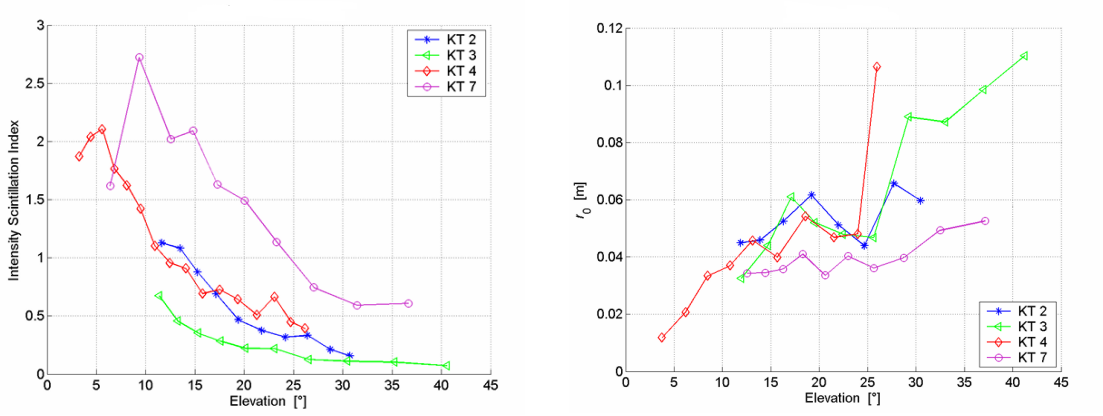


Figure 2.26 – Scintillation index (black curve) and Fried's parameter (cyan curve) as a function of the elevation angle for the dynamic downlink LEO OFL

approaches for the propagation distance, i.e., the improved geometrical approximation of Eq. (2.8) and the exact slant-path distance obtained from orbital reconstruction. For the latter case, the satellite orbit was reconstructed from the corresponding TLE data and the exact OGS coordinates, allowing the propagation distance to be computed through Matlab built-in orbital mechanics functions. The resulting beam wander variance, angular beam wander, and beam wander loss have then been compared for the three approaches, as shown in Table 2.4.

The analysis' outcomes reveal that the conventional approximation systematically overestimates the beam wander effect. As a consequence, both the beam wander variance and the angular displacement of the beam centroid are predicted to be larger than their actual values, leading to an excessive estimation of the associated pointing loss. In contrast, the improved approximation developed in this work produces correct results, which aligned to those obtained using the exact propagation distance. For the considered GEO scenario, the difference between the improved approximation and the exact link distance value was approximately 1 km, corresponding to a relative error of only 0.0029%, whereas the conventional approximation introduced an error of about 71.8%.



(a) (b)

Figure 2.27 – (a) Scintillation index and (b) OGS Fried's parameter as a function of the elevation angle for the KIODO trial on 14 June 2006 (KT3) [176]

These results demonstrate that the proposed geometrical approximation provides a highly accurate alternative when the exact orbital information is unavailable during preliminary system design activities. In such cases, the improved approximation enables significantly more reliable beam wander and link budget estimations without requiring detailed satellite ephemeris information.

Although the differences observed in the GEO scenario are already significant, the impact of the link distance approximation becomes even more pronounced at lower elevation angles. As previously shown in Fig. 2.12, the error associated with the conventional approximation increases rapidly as the elevation angle decreases. This aspect is particularly relevant for communications involving LEO satellites, where the elevation angle continuously varies during the satellite pass and can reach low values.

To investigate this effect, an additional uplink LEO scenario has been analyzed using the same geometry considered for the dynamic downlink experiment discussed previously. For this purpose, the actual multi-beam transmission employed during the experimental KIODO campaign was replaced by a single uplink beam in order to isolate the beam wander contribution. The NICT OGS was assumed to transmit at a wavelength of 815 nm with a transmitter beam radius of 0.25 cm, consistently with the parameters reported in [168].

Table 2.4 – Beam wander parameters for the uplink GEO OFL

Link distance	**Output parameter**		
	Beam wander variance $\langle r_c^2 \rangle$	**Angular beam wander** θ_{BW}	**Beam wander loss** L_{BW}
Conventional approximation $L = 65\,908.14$ **km**	$3.1203 \cdot 10^5$	14.5590 μrad	-4.4787 dB
More accurate approximation $L = 38\,368.91$ **km**	$1.0575 \cdot 10^5$	8.4757 μrad	-2.0726 dB
Exact value $L = 38\,367.80$ **km**	$1.0574 \cdot 10^5$	8.4757 μrad	-2.0726 dB

The exact acquisition start time of the considered experiment, i.e., the trial of 30 March 2006, was not available in the literature. However, it is known that the trial occurred around midnight (local time) and lasted 4 minutes and 41 seconds [168]. Thus, a transmission start time of 00:36:15 local time has been selected. This choice resulted in a simulated satellite pass spanning elevation angles between 16.02° and 47.67°, maintaining consistency with the reported communication duration and safety constraints that restricted optical transmissions to elevation angles above 15° [169]. The atmospheric channel and turbulence parameters have been assumed equal to those adopted in the dynamic downlink analysis.

The resulting beam wander variance, angular beam wander, and beam wander loss have been evaluated throughout the satellite pass using the three propagation distance models. In detail, the obtained plot for the beam wander variance is shown in Fig. 2.28a, while the angular beam wander and beam wander loss are depicted in Figs. 2.28b and 2.28c, respectively. The comparison clearly shows that the improved approximation (blue curves) and the exact distance solution (dashed cyan curves) produce overlapping results over the entire range of elevation angles. Conversely, the conventional approximation (black curves) consistently overestimates all beam wander-related quantities.

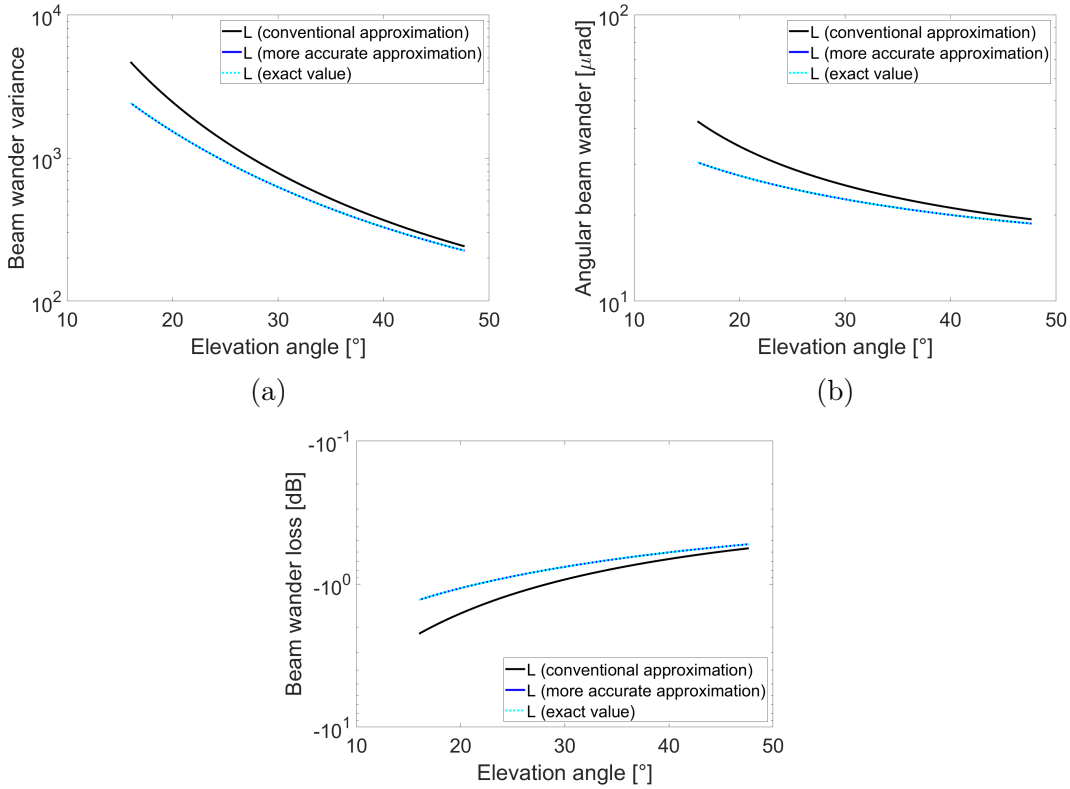


Figure 2.28 – (a) Beam wander variance, (b) angular beam wander, and (c) beam wander-induced loss as a function of the elevation angle for the uplink LEO OFL, evaluated considering the flat-Earth link distance approximation (black curve), the round-Earth link distance approximation (blue curve) and the exact link distance value (dashed cyan curve)

Furthermore, the discrepancy between the conventional and accurate solutions has been found to strongly depend on the elevation angle. The largest deviations occur at the beginning and end of the satellite pass, where the elevation angle is lowest and the propagation distance is longest. As the satellite approaches higher elevations, the error progressively decreases, following the same trend previously observed in the geometrical comparison between the different distance models.

These findings highlight the importance of accurately modeling the propagation distance when evaluating beam wander effects in OFLs. An incorrect estimation of beam wander not only leads to an inaccurate prediction of the associated power

loss but also affects the estimation of the hot spot displacement at the receiver. Since this displacement must be compensated by the tracking system to maintain accurate transmitter–receiver alignment, errors in beam wander prediction may directly impact pointing system design and overall link performance.

Overall, the results demonstrate that the improved geometrical approximation developed in this research achieves high accuracy while preserving the simplicity required for practical engineering applications. Consequently, its adoption enables more reliable beam wander predictions and more accurate optical link budget analyses.

2.3 SNR models for OFLs

While the link budget provides a first assessment of the feasibility of an OFL by estimating the average received optical power, the SNR represents another important performance metric. Indeed, the SNR directly determines the achievable BER, receiver sensitivity and, ultimately, the maximum data throughput that can be supported by the communication system. For this reason, SNR analysis constitutes a fundamental step in the design and optimization of OFLs.

In FSO systems, random variations of the received optical power are experienced, thus leading to the definition of both instantaneous and average SNRs. Specifically, the estimation of the average SNR requires accounting for both the mean received power, obtained through the link budget analysis presented in the previous sections, and the various noise sources introduced by the receiver chain.

The SNR strongly depends on the adopted detection architecture and modulation format. As depicted in Fig. 2.29, after collection by the receiving telescope, the optical signal is typically filtered by an optical band-pass filter with bandwidth B_o [Hz], centered at the operating wavelength λ. The filter is used to reduce the amount of background radiation entering the receiver. By neglecting the dashed block in Fig. 2.29, the filtered optical signal $p(t)$ is then converted into an electrical current $i(t)$ by a photodetector and subsequently amplified and processed through electronic circuitry. Depending on the receiver architecture, the optical signal may also be optically pre-amplified before photodetection. Moreover, in the

case of coherent detection, the optical signal is mixed with a Local Oscillator (LO) field prior to conversion into the electrical domain.

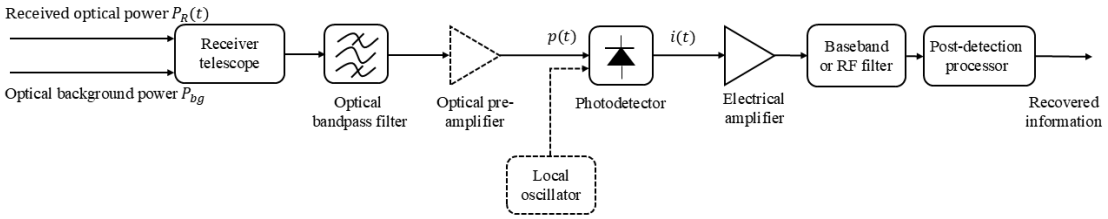


Figure 2.29 – Block diagram of a FSO receiver chain

Thus, the two main detection approaches which are commonly adopted in optical communication systems are IM/DD and coherent detection. In the former, the electrical current generated by the photodetector is directly proportional to the received optical power. This approach is characterized by a relatively simple implementation and is widely employed in practical systems. Instead, coherent receivers enable the recovery of both amplitude and phase information from the optical signal, allowing the use of advanced modulation formats and generally providing superior sensitivity compared with direct-detection architectures.

The optical-to-electrical conversion process is usually performed by semiconductor photodetectors, most commonly Positive-Intrinsic-Negative (PIN) photodiodes or APDs [128]. These devices are characterized by high quantum efficiencies, wide operating bandwidths, and low intrinsic noise [131]. In the case of APDs, an internal avalanche multiplication mechanism provides additional gain at the expense of increased multiplication noise. Therefore, the choice between PIN and APD photodetectors depends on the specific receiver architecture and operating conditions.

Additional receiver components may further influence the SNR performance. Optical pre-amplifiers, such as EDFAs, can significantly improve receiver sensitivity by amplifying the optical signal before photodetection, although they also introduce Amplified Spontaneous Emission (ASE) noise. Similarly, electrical am-

plifiers increase the amplitude of the generated photocurrent while contributing to thermal and electronic noise.

Each element of the receiver chain introduces specific noise contributions, including shot noise, thermal noise, background noise, multiplication noise, and ASE noise. The relative importance of these contributions depends on the receiver architecture, operating wavelength, optical bandwidth, electrical bandwidth, and received optical power.

The following sections present the mathematical models adopted to evaluate each noise contribution and the overall SNR equations. These models have been implemented in Matlab and integrated within the link budget tool, enabling the estimation of the SNR for different modulation formats and detection schemes. The SNR modeling presented here constitutes the basis for the OFL PHY layer abstraction presented in Chapter 4.

2.3.1 Detection schemes

The receiver architecture plays a fundamental role in determining the performance of an OFL, as it directly affects the achievable sensitivity and SNR. The two main detection approaches, i.e., direct detection and coherent detection, are reviewed here. While direct-detection receivers can only operate in conjunction with intensity modulation schemes, coherent receivers enable the use of amplitude-, phase-, and frequency-modulated signals by recovering the full optical field information.

Direct-detection systems are characterized by a relatively simple implementation and lower complexity, which made them the most widely adopted solution in past experimental OFLs. In particular, IM/DD schemes based on OOK remain among the most common approaches due to their simplicity and robustness [130]. Coherent receivers, on the other hand, offer significantly higher sensitivities thanks to the mixing between the received optical signal and a LO laser. Consequently, coherent detection becomes particularly attractive for power-limited systems and very-high-capacity links, where receiver sensitivity is a critical design parameter [128].

Before discussing the different receiver architectures, it is useful to briefly review the photodetection process. Both PIN and APD photodiodes operate under

reverse bias, converting incident photons into electron-hole pairs that generate an electrical current $i(t)$ in the external circuit. The conversion process can occur only when the photon energy, $E = hf$, exceeds the semiconductor bandgap energy E_g, resulting in a cut-off wavelength given by

$$\lambda_{cut-off} = \frac{hc}{E_g} \tag{2.90}$$

where h is Planck's constant, c is the speed of light in vacuum, and $f = c/\lambda$ is the operating frequency [131].

A key figure of merit of a photodetector is its responsivity R [A/W], defined as the ratio between the generated photocurrent and the incident optical power. It can be expressed as

$$R = \frac{\eta q}{hf} \tag{2.91}$$

where η is the photodetector's quantum efficiency and q is the electron charge. For a PIN diode, the responsivity is always below unity. Instead, in APDs, the primary photocurrent undergoes an internal avalanche multiplication process, leading to an average gain factor M. Consequently, the average photocurrent, i [A], generated by an incident optical power P_R [W] can be written as

$$i = RMP_R \tag{2.92}$$

For PIN photodiodes, $M = 1$, whereas APDs typically provide multiplication gains ranging from 50 to 300 [159]. Although this internal amplification improves receiver sensitivity, its stochastic nature also introduces additional multiplication noise. For this reason, APDs are mainly employed in direct-detection systems, while PIN photodiodes are generally preferred in coherent receivers, where the required gain is already provided by the LO.

The linear relationship between incident optical power and generated photocurrent expressed by Eq. (2.92) is valid only below the detector saturation power. Furthermore, although the operating wavelength must remain below the cut-off wavelength, the quantum efficiency may still decrease at shorter wavelengths due to scattering effects and reduced effectiveness of the antireflection coating away from its design wavelength [180].

2.3.1.1 Direct detection

In IM/DD systems, information is conveyed through the modulation of the optical intensity. The received optical field can be represented as

$$E_s(t) = S(t)\cos\left(\omega_c t + \theta_c\right), \tag{2.93}$$

where $S(t)$ is the modulated field amplitude, ω_c is the optical carrier angular frequency, and θ_c is the carrier phase [180].

The photodetector responds to the incident optical power rather than to the optical field itself. The average optical power associated with the received field is therefore proportional to the squared field amplitude, i.e.,

$$P_R = \frac{s}{\eta_0}\langle E_s^2\rangle = \frac{s}{\eta_0}S^2(t)\langle\cos^2(\omega_c t)\rangle = \frac{s}{2\eta_0}S^2(t), \tag{2.94}$$

where s is the detector area, η_0 is the free-space impedance, and $\langle ...\rangle$ denotes the time average. The generated photocurrent becomes

$$i_s = RMP_R = RM\frac{s}{2\eta_0}S^2(t) \tag{2.95}$$

The above expression highlights a fundamental characteristic of direct detection, i.e., the generated current contains information only about the received optical power, while the carrier phase and frequency are completely lost during the photodetection process. The mean-square value of the useful signal current can therefore be expressed as

$$\langle i_s^2\rangle = (RMP_R)^2. \tag{2.96}$$

2.3.1.2 Coherent heterodyne detection

In coherent receivers, the incoming optical field is combined with the radiation generated by a LO before photodetection. This operation enables the recovery of both amplitude and phase information carried by the optical signal.

For heterodyne detection, the LO frequency differs from the carrier frequency. The LO field can be written as

$$E_L(t) = E_{LO}\cos\left(\omega_L t + \theta_L\right), \tag{2.97}$$

where ω_L and θ_L are the LO angular frequency and phase, respectively.

After optical mixing, the total incident power on the photodetector becomes

$$P = \frac{s}{\eta_0}\langle[S(t)\cos(\omega_c t + \theta_c) + E_{LO}\cos(\omega_L t + \theta_L)]^2\rangle \tag{2.98}$$

While, the generated current is

$$i_s = RM\left\{P_R + P_{LO} + 2\sqrt{P_R P_{LO}}\cos[\omega_{IF}t + (\theta_c - \theta_L)]\right\} \tag{2.99}$$

where $\omega_{IF} = \omega_c - \omega_L$ is the Intermediate Frequency (IF) and P_{LO} is the LO power [180]. According to Eq. (2.99), the generated current contains three contributions, i.e., (i) a signal term, (ii) a LO term, and (iii) a beating term. The additional term at $\omega_c + \omega_L$ that should appear in the above expression is filtered out.

The beating component contains the complete information associated with the received optical field. Its mean-square value is

$$\langle i_s^2\rangle = 2(RM)^2 P_R P_{LO} \tag{2.100}$$

Unlike direct detection, the useful signal scales with the product of the received signal power and the LO power. Since the LO power can be made significantly larger than the received signal power, coherent receivers achieve substantially higher sensitivities, particularly under weak-signal conditions.

In practical FSO systems, imperfect overlap between the received wavefront and the LO mode may reduce the beating efficiency [131]. This effect is accounted for through the heterodyne efficiency $\eta_{\text{heterodyne}}$, leading to

$$i_s = RM\left[P_R + P_{LO} + 2\sqrt{P_R P_{LO}\eta_{\text{heterodyne}}}\cos\left(\omega_{IF}t + \theta_c - \theta_L\right)\right] \tag{2.101}$$

When both the received signal and the LO are coupled into the same SMF fiber before photodetection, the modal mismatch is inherently removed at the photodetector and the heterodyne efficiency becomes equal to the SMF coupling efficiency already introduced in the link budget analysis.

2.3.1.3 Coherent homodyne detection

Homodyne detection represents a special case of coherent reception in which the LO frequency is equal to the optical carrier frequency, resulting in $\omega_{IF} = 0$. The output current therefore becomes

$$i_s = RM\left[P_R + P_{LO} + 2\sqrt{P_R P_{LO}}\cos\left(\theta_c - \theta_L\right)\right]. \tag{2.102}$$

If the receiver employs a PLL to maintain synchronization between the incoming signal and the LO, the phase difference can be forced close to zero, maximizing the beating term. Under this condition, the mean-square signal current becomes

$$\langle i_s^2 \rangle = 4(RM)^2 P_R P_{LO} \tag{2.103}$$

Compared with heterodyne reception, the useful signal power is doubled, corresponding to an SNR improvement of 3 dB [180]. This makes homodyne detection the most sensitive coherent architecture. However, the requirement for accurate phase tracking and synchronization significantly increases receiver complexity and imposes stringent stability requirements on both the received signal and the LO.

2.3.2 Noise sources

The performance of an OFL is not determined solely by the received signal power but also by the various noise mechanisms affecting the detection process. Noise contributions arise from both the optical channel and the transmitter/receiver hardware and combine with the useful signal at the receiver, ultimately limiting the achievable SNR.

Some noise sources are signal-dependent, meaning that their magnitude varies with the received optical power level. Others originate from the receiver electronics and are largely independent of the incident radiation. A comprehensive SNR analysis requires the identification and accurate modeling of all relevant noise contributions.

In the following subsections, the principal noise sources encountered in FSO communication systems are reviewed and the corresponding mathematical models are presented. These models have been implemented in Matlab as modular functions, forming the building blocks of the SNR evaluation tool developed during this work.

2.3.2.1 Shot noise

Shot noise originates from the discrete nature of the photodetection process. Since optical radiation is composed of individual photons, the generation of photoelectrons within the detector is inherently random, resulting in fluctuations of the photocurrent. These fluctuations constitute the shot noise component.

Assuming a uniform photon arrival rate, the photocurrent can be modeled as a stationary random process obeying Poisson statistics and composed of individual elementary pulses [181]. Under this assumption, the shot noise exhibits a white Power Spectral Density (PSD) over the frequency range of interest. For a PIN photodiode, the mean-square shot noise current is given by

$$\langle i_{\text{shot}}^2 \rangle = 2qRP_R B \tag{2.104}$$

where P_R [W] is the average optical power incident on the detector, and B [Hz] is the electrical receiver bandwidth [131]. This expression is valid provided that the optical power variations are much slower than the response time of the detection circuit.

In conventional direct-detection receivers, shot noise is often less significant than thermal and other electronic noise contributions because of the relatively low received optical powers. In coherent receivers, however, the LO introduces an additional shot noise contribution [131]. Since the LO power is typically much larger than the received signal power, its associated shot noise can become the dominant noise source [159]. The corresponding mean-square current is

$$\langle i_{\text{shot,LO}}^2 \rangle = 2qRP_{\text{LO}} B \tag{2.105}$$

When an APD is employed, the stochastic multiplication process introduces additional fluctuations in the output current, commonly referred to as excess noise. This effect is characterized by the excess noise factor F, which is generally expressed as

$$F = M^x \tag{2.106}$$

where x is the excess noise index, whose value depends on the semiconductor material and typically lies between 0 and 1 [128]. For PIN photodiodes, $M = 1$ and consequently $F = 1$.

Taking into account avalanche multiplication, the signal-related shot noise variance becomes

$$\langle i_{\text{shot}}^2 \rangle = 2qRM^2FP_RB \tag{2.107}$$

while the LO contribution in coherent receivers is

$$\langle i_{\text{shot,LO}}^2 \rangle = 2qRM^2FP_{\text{LO}}B \tag{2.108}$$

Equations (2.107) and (2.108) show that the useful signal power scales as M^2, whereas the shot noise variance scales as $M^2F = M^{2+x}$. Consequently, increasing the avalanche gain does not indefinitely improve receiver performance, since the excess noise eventually counteracts the benefits of signal amplification and may lead to a reduction in the achievable SNR.

2.3.2.2 Dark current shot noise

Even in the absence of incident optical radiation, a photodetector exhibits a small reverse leakage current, commonly referred to as the dark current and here denoted by I_d [A]. This current originates from carrier generation mechanisms unrelated to photon absorption, such as thermal excitation and material defects. Since the generation of these carriers is a random process, the dark current gives rise to an additional shot noise component that is independent of the received optical power [128].

For a PIN photodiode, the mean-square dark current shot noise is given by

$$\langle i_d^2 \rangle = 2qI_dB \tag{2.109}$$

The total dark current is generally composed of a bulk component, I_{db}, and a surface leakage component, I_{ds}. In APDs, only the bulk current experiences avalanche multiplication, while the surface current remains unaffected [181]. Consequently, the dark current shot noise variance for an APD can be expressed as

$$\langle i_d^2 \rangle = 2qM^2FI_{db}B + 2qI_{ds}B \tag{2.110}$$

The magnitude of the dark current depends on several device characteristics, including the semiconductor material, operating temperature, detector size, and manufacturing quality. In general, photodetectors fabricated from large band-gap materials exhibit lower dark currents. Furthermore, dark current can be reduced by cooling the detector and minimizing its active area.

2.3.2.3 Thermal noise

Thermal noise, also known as Johnson noise, arises from the random motion of thermally excited carriers within conductive materials at temperatures above absolute zero. Unlike shot noise, thermal noise is independent of the optical signal and is characterized by a flat PSD over the frequency range of interest, making it a white noise process. For a receiver circuit with equivalent load resistance R_L [Ω] operating at temperature T [K], the thermal noise variance can be expressed as

$$\langle i_{\text{th}}^2 \rangle = \frac{4kTB}{R_L} \tag{2.111}$$

where k is the Boltzmann constant.

Thermal noise represents one of the main electronic noise contributions in optical receivers. In practical systems, thermal noise is often considered together with other signal-independent electronic noise sources through the concept of Noise Equivalent Power (NEP). The NEP is defined as the optical power per square root electrical receiver bandwidth that generates an output current equal to the internally generated electronic noise [131]. Using this parameter, the total electronic noise variance can be written as

$$\langle i_{\text{el}}^2 \rangle = R^2 \text{NEP}^2 B \tag{2.112}$$

where the NEP is expressed in $\text{W}/\sqrt{\text{Hz}}$. This formulation provides a convenient way to account for the combined effect of thermal and other receiver electronics noise contributions in SNR calculations.

2.3.2.4 Background noise

Background optical radiation collected by the receiving telescope represents an important source of noise in FSO systems. This unwanted optical power originates from natural sources such as the sky, the Sun, the Moon, and other celestial bodies. In most OFL applications, the dominant contribution is provided by diffuse sky radiance, whereas localized sources are generally neglected except in specific scenarios such as deep-space optical communications [128].

The background optical power, P_{bg} [W], collected by the receiver can be expressed as

$$P_{\text{bg}} = N_f \Omega_{\text{FOV}} \eta_R A_R B_O \tag{2.113}$$

where N_f [W/m^{2}srad Hz] is the spectral radiance of the background source, Ω_{FOV} [srad] is the receiver FOV solid angle, η_R is the receiver efficiency, A_R [m^2] is the receiver area, and B_O [Hz] is the optical filter bandwidth [128, 134]. By expressing the receiver area in terms of the aperture diameter D_R, the collected background power becomes

$$P_{\text{bg}} = N_f \left(\frac{\pi D_R \theta_{\text{FOV}}}{4} \right)^2 \eta_R B_O \tag{2.114}$$

The angular FOV θ_{FOV} [rad] of the receiver is determined by the focal length f [m] and the diameter d [m] of the photodetector active area or of the SMF, according to [134, 136]

$$\theta_{\text{FOV}} = 2 \arctan \left(\frac{d}{2f} \right). \tag{2.115}$$

Once incident on the photodetector, the background radiation generates several noise contributions [182]. The first one is the background shot noise [131], whose variance is given by

$$\langle i_{\text{bg}}^2 \rangle = 2qRM^2 F P_{\text{bg}} B \tag{2.116}$$

In addition to shot noise, photodetection gives rise to beat noise terms. The spectral components of the background light can interfere with one another, generating background-background beat noise, $\langle i_{\text{bg-bg}}^2 \rangle$, and can also beat with the received information signal or, in coherent receivers, with the LO field, generating signal-background, $\langle i_{\text{bg-sig}}^2 \rangle$ and LO-background $\langle i_{\text{bg-LO}}^2 \rangle$ noise terms. The background-background beat noise variance can be expressed as

$$\langle i_{\text{bg-bg}}^2 \rangle = R^2 M^2 M_{\text{pol}} N_{\text{back}}^2 (2B_O - B) B \tag{2.117}$$

where N_{back} is the peak PSD per mode of the background radiation at the detector and M_{pol} is the number of spatial and polarization modes of background light collected by the receiver. When the receiver FOV is smaller than the solid angle subtended by the background source at the receiver, the number of collected modes is

$$M_{\text{pol}} = \frac{2\Omega_{\text{FOV}}}{\Omega_{\text{DL}}} \tag{2.118}$$

In Eq. (2.118), Ω_{DL} is the diffraction-limited telescope FOV, i.e.,

$$\Omega_{\mathrm{DL}} = \frac{\lambda^2}{A_R} \tag{2.119}$$

If the background source subtends a smaller solid angle than the receiver FOV, Ω_{FOV} must be replaced by the source solid angle Ω_{S}. The background spectral density per mode is given by

$$N_{\mathrm{back}} = N_f \lambda^2 \tag{2.120}$$

The beating between the received signal and the background radiation produces an additional noise contribution whose variance is

$$\langle i^2_{\mathrm{bg-sig}} \rangle = 4R^2 M^2 P_R N_{\mathrm{back}} B \tag{2.121}$$

Finally, the LO-background beat noise variance is [183]

$$\langle i^2_{\mathrm{bg-LO}} \rangle = 4R^2 M^2 P_{\mathrm{LO}} N_{\mathrm{back}} B \tag{2.122}$$

Since the LO power is generally much larger than the received signal power, this contribution can become significant in coherent detection systems, particularly when operating with a large FOV or under strong background illumination conditions.

2.3.2.5 ASE noise

When an EDFA is inserted before photodetection, the received signal is affected by ASE noise. This noise originates from the spontaneous emission process occurring within the amplifier and is amplified together with the useful signal, degrading the receiver performance.

Since the optical bandwidth of the received signal is typically much smaller than the ASE spectral bandwidth, the in-band ASE contribution can be modeled as a white noise process. Under this assumption, the ASE power, P_{ASE} [W], collected within the optical filter bandwidth can be expressed as

$$P_{\mathrm{ASE}} = (G-1) n_{\mathrm{spon}} m_t \frac{hc}{\lambda} B_O \tag{2.123}$$

where G is the EDFA gain and m_t is the number of transverse modes, equal to 2 for a SMF [184].The population inversion factor n_{spon} is related to the EDFA noise figure NF_{EDFA} through

$$n_{\text{spon}} = \frac{NF_{\text{EDFA}}}{2}. \tag{2.124}$$

For an ideal amplifier, the best achievable NF_{EDFA} value is 3 dB [184].

At the EDFA output, it is possible to defined an Optical Signal-to-Noise Ratio (OSNR) as

$$\text{OSNR} = \frac{GP_R}{P_{\text{ASE}}} \tag{2.125}$$

The ASE power contributes to shot noise during the photodetection process, leading to a current variance given by

$$\langle i^2_{\text{ASE}} \rangle = 2qRP_{\text{ASE}}B \tag{2.126}$$

Besides shot noise, ASE gives rise to additional beat noise terms. The first contribution originates from the beating between the amplified signal and ASE spectral components that fall within the electrical receiver bandwidth. The corresponding signal-spontaneous beat noise variance is

$$\langle i^2_{\text{ASE}-\text{sig}} \rangle = \frac{2GR^2P_RP_{\text{ASE}}B}{B_O} \tag{2.127}$$

A second contribution arises from the beating among ASE spectral components themselves, generating the spontaneous-spontaneous beat noise variance

$$\langle i^2_{\text{ASE}-\text{ASE}} \rangle = \frac{1}{2}R^2P^2_{\text{ASE}} \left(2 - \frac{B}{B_O}\right) \frac{B}{B_O} \tag{2.128}$$

Finally, ASE noise can also interact with the optical background radiation collected by the receiver. The resulting spontaneous-background beat noise variance is

$$\langle i^2_{\text{ASE}-\text{bg}} \rangle = \frac{1}{2}R^2P_{\text{ASE}}GN_{\text{back}} \left(2 - \frac{B}{B_O}\right) B \tag{2.129}$$

These additional noise contributions are specific to optically pre-amplified receivers and can become dominant when high amplifier gains are employed.

2.3.2.6 Relative intensity noise

Laser sources exhibit a finite degree of coherence, which is determined by the relative contributions of stimulated and spontaneous emission processes within the optical field. In particular, spontaneous emission gives rise to both phase and amplitude fluctuations in the emitted radiation.

The intensity fluctuations of the optical signal are commonly described in terms of Relative Intensity Noise (RIN) [181]. These fluctuations translate into photocurrent variations at the receiver, whose variance can be expressed as

$$\langle i_{\mathrm{RIN}}^2 \rangle = R^2 M^2 P_R^2 \cdot \mathrm{RIN} \cdot B \tag{2.130}$$

where RIN [Hz^{-1}] denotes the RIN coefficient of the laser source. In coherent detection systems, the contribution of the LO laser must also be considered. The associated intensity noise follows an analogous expression, with variance given by

$$\langle i_{\mathrm{RIN,LO}}^2 \rangle = R^2 M^2 P_{\mathrm{LO}}^2 \cdot \mathrm{RIN}_{\mathrm{LO}} \cdot B \tag{2.131}$$

where $\mathrm{RIN}_{\mathrm{LO}}$ is the RIN coefficient of the LO.

2.3.3 SNR for OOK OFLs

OOK is the most commonly adopted modulation format in IM/DD FSO communication systems because of its implementation simplicity. In OOK modulation, binary information is conveyed through the presence or absence of optical power. A logical 1 is transmitted by turning the laser source on, whereas a logical 0 is represented by the absence of optical radiation. In this work, NRZ OOK modulation is considered, meaning that the optical signal remains at a constant level throughout the entire bit interval, T_{b} [s], when a logical 1 is transmitted.

At the receiver, the detected photocurrent is compared with a decision threshold to recover the transmitted bits. In the absence of atmospheric turbulence, the optimum threshold is located midway between the current levels associated with the two symbols. However, turbulence-induced irradiance fluctuations alter the statistical distribution of the received signal, making a fixed threshold suboptimal. For this reason, adaptive thresholding schemes should be preferred in OFLs, adjusting the decision level according to the channel conditions [128, 159]. This

issue is specific to intensity modulation formats, whereas phase- and frequency-modulated systems are inherently less sensitive to signal amplitude fluctuations.

For an NRZ OOK signal, the photocurrent generated by the photodetector can be expressed as

$$i_s(t) = RMP_R A(t) \tag{2.132}$$

where P_R is the received optical power corresponding to bit 1 and $A(t)$ represents OOK modulation, assuming values equal to 1 or 0 depending on the transmitted symbol [180]. Since $A^2(t) = A(t)$, the mean square signal current becomes

$$\langle i_s^2 \rangle = \frac{1}{2}(RMP_R)^2 \tag{2.133}$$

For an APD-based receiver without optical pre-amplification, the total noise variance is

$$\begin{aligned}\left\langle i_{\text{noise}}^2 \right\rangle = {} & 2qM^2F\left(\frac{1}{2}RP_R + I_{db} + RP_{bg}\right)B + 2qI_{ds}B + 4M^2R^2\frac{1}{2}P_R N_{back}B \\ & + M^2R^2M_{pol}N_{back}^2(2B_O - B)B + \frac{4kTB}{R_L} + \frac{1}{4}R^2M^2P_R^2 \cdot RIN \cdot B\end{aligned} \tag{2.134}$$

The above expression includes shot noise, dark-current noise, signal-background beat noise, background-background beat noise, thermal noise, and RIN. Alternatively, thermal and dark-current noise can be represented through the NEP, an option that has also been implemented in the numerical tool.

When a PIN photodiode is employed, the same formulation applies by setting $M = F = 1$ and replacing the APD bulk and surface dark-current terms with a single dark-current contribution.

If an optical pre-amplifier is inserted before photodetection, the average signal current becomes

$$\langle i_s^2 \rangle = \frac{1}{2}(RGP_R)^2 \tag{2.135}$$

while the total noise variance is given by

$$\begin{aligned}\left\langle i_{\text{noise}}^2 \right\rangle = 2q\left(\frac{1}{2}GRP_R + I_d + GRP_{bg} + RP_{ASE}\right)B + 4R^2\left(\frac{1}{2}G^2P_RN_{back}\right)B \\ + R^2M_{pol}G^2N_{back}^2(2B_O - B)B + 2R^2\left(\frac{1}{2}GP_RP_{ASE}\right)\frac{B}{B_O} \\ + \frac{1}{2}R^2P_{ASE}^2\left(2 - \frac{B}{B_O}\right)\frac{B}{B_O} + \frac{1}{2}R^2P_{ASE}GN_{back}\left(2 - \frac{B}{B_O}\right)B \\ + \frac{4kTB}{R_L} + \frac{1}{4}R^2G^2P_R^2 \cdot RIN \cdot B\end{aligned} \tag{2.136}$$

In this case, the model includes ASE shot noise as well as signal-spontaneous, spontaneous-spontaneous, and spontaneous-background beat noise contributions. A PIN photodiode is assumed, as commonly adopted in optically pre-amplified receivers.

2.3.4 SNR for coherent OFLs

Coherent modulation formats offer significant advantages in terms of receiver sensitivity and spectral efficiency. Their ability to exploit both the amplitude and phase of the optical carrier enables a more efficient use of the available bandwidth compared with intensity modulation schemes. Owing to these benefits, coherent modulation techniques have become standard in modern optical fiber communication networks and are increasingly being investigated for space-based FSO links [131, 185].

Among coherent modulation formats, Phase-Shift Keying (PSK) and Quadrature Amplitude Modulation (QAM) are particularly attractive for space optical communications. In PSK systems, information is encoded in discrete phase variations of the optical carrier. More generally, in an M-PSK scheme, each symbol is represented by one of M equally spaced phase states [186]. The transmitted signal can therefore be expressed as

$$\begin{aligned}s(t) &= A\sum_{k=0}^{N-1} g(t-kT)\left[\cos\Delta\phi_k\cos\omega_s t - sin\Delta\phi_k\sin\omega_s t\right] \\ &= A\sum_{k=0}^{N-1} g(t-kT)\cos(\omega_s t + \Delta\phi_k)\end{aligned} \tag{2.137}$$

where A is the signal amplitude, N is the number of transmitted symbols, T is the symbol duration, $g(t)$ denotes the pulse shape, ω_s is the optical carrier angular frequency, and $\Delta\phi_k = \pi(2k-1)/M$, with $k = 1, 2, ..., M$, identifies the phase associated with the k-th symbol. Instead, QAM combines amplitude and phase modulation by varying the amplitues of two orthogonal carriers.

Current coherent space communication systems, such as EDRS, employ BPSK combined with homodyne detection. Although BPSK provides improved receiver sensitivity, its spectral efficiency remains comparable to that of OOK. A more bandwidth-efficient alternative is Quadrature Phase-Shift Keying (QPSK), where the carrier phase assumes four possible values, namely $\pm\pi/4$ and $\pm 3\pi/4$. Since each symbol conveys two bits, the required symbol rate is halved with respect to binary schemes, resulting in a doubling of spectral efficiency. For example, ESA Specification for Terabit/sec Optical Links (ESTOL) consider Dual-Polarization Quadrature Phase-Shift Keying (DP-QPSK) to enable 100 Gbit/s and 200 Gbit/s optical links, while Dual-Polarization 16-ary Quadrature Amplitude Modulation (DP-16QAM) is proposed to deliver even higher data rates [187].

By denoting the average received power per modulation symbol as P_R, the mean-square signal current for an heterodyne receiver is

$$\langle i_s^2 \rangle = 2R^2 P_R P_{LO} \tag{2.138}$$

The corresponding SNR is obtained by dividing Eq. (2.138) by the total noise variance, that is

$$\begin{aligned}\left\langle i_{\text{noise}}^2 \right\rangle = {} & 2q(P_R R + RP_{LO} + I_d + RP_{bg})B + 4R^2 P_R N_{back} B + 4R^2 P_{LO} N_{back} B \\ & + R^2 M_{pol} N_{back}^2 (2B_O - B)B + \frac{4kTB}{R_L} \\ & + R^2 P_R^2 \cdot RIN \cdot B + R^2 P_{LO}^2 \cdot RIN_{LO} \cdot B\end{aligned} \tag{2.139}$$

which includes the contributions of shot noise, dark-current shot noise, signal-background beat noise, LO-background beat noise, background-background beat noise, thermal noise, and RIN.

In coherent receivers, the LO RIN often becomes a dominant impairment. This issue can be mitigated through balanced detection, which suppresses the DC com-

ponents of the photocurrent and substantially reduces intensity-noise contributions. In such configurations, the RIN terms in Eq. (2.139) can generally be neglected [185].

If optical pre-amplification is adopted, the mean square signal current becomes

$$\langle i_s^2 \rangle = 2R^2 G P_R P_{LO} \tag{2.140}$$

By neglecting RIN and background noise, the noise variance is

$$\begin{aligned} \left\langle i_{\text{noise}}^2 \right\rangle = 2q(P_R G R + R P_{LO} + I_d + R P_{ASE})B + \frac{1}{2} R^2 P_{ASE}^2 (2B_O - B)\frac{B}{B_O^2} \\ + \frac{2GR^2 P_R P_{ASE} B}{B_O} + \frac{2R^2 P_{LO} P_{ASE} B}{B_O} + \frac{4kTB}{R_L} \end{aligned} \tag{2.141}$$

When homodyne detection is adopted and the LO is phase-locked to the received signal, the mean-square signal current becomes

$$\langle i_s^2 \rangle = 4R^2 P_R P_{LO} \tag{2.142}$$

which is twice the value obtained in the heterodyne case. As a consequence, the homodyne SNR is 3 dB higher and can be expressed as

$$SNR_{homodyne} = 2SNR_{heterodyne} \tag{2.143}$$

Chapter 3

Experimental emulation of fading-affected OFLs

The increasing interest in OFL for future satellite communication systems has stimulated the development of high-capacity optical terminals capable of supporting data rates ranging from several Gigabits per second to hundreds of Gigabits per second. Recent demonstrations, such as NASA's TBIRD mission, have shown that commercial optical fiber communication equipment can be successfully employed in space-to-ground optical links, enabling the exploitation of mature photonic technologies and reducing the cost and complexity of terminal development. The possibility of reusing COTS transceivers originally designed for fiber-optic networks is particularly attractive for the rapid deployment of optical communication infrastructures in integrated TNs and NTNs networks.

Nonetheless, OFLs operate in a propagation environment that differs substantially from that encountered in optical fiber systems. While fiber channels are characterized by relatively stable transmission conditions, OFLs face random impairments that introduce significant fluctuations in the received optical power. Atmospheric turbulence and pointing instabilities generate time-varying fading that can severely affect communication performance. The resulting power fluctuations may persist for time intervals in the order of milliseconds, which are several orders of magnitude longer than the symbol duration of modern high-speed communication systems. Consequently, fading events may cause extended error bursts, frame losses, and link outages that are not typically experienced in conventional fiber-optic networks.

As discussed in Chapter 2, the severity of turbulence-induced scintillation depends on several factors, including the turbulence strength, propagation geometry, receiver aperture size, and satellite elevation angle. In OFLs involving LEO satellites, the relative motion between the spacecraft and the OGS further introduces a dynamic evolution of channel conditions throughout the satellite pass. In addition, pointing jitter caused by mechanical vibrations, tracking errors, and turbulence-induced beam wander contributes to received-power fluctuations. The combined effect of scintillation and pointing errors results in a fading channel whose statistical and temporal characteristics vary continuously during link operation.

Therefore, the design of reliable OFL systems requires not only accurate channel models and link-budget analyses but also an experimental assessment of the behavior of communication hardware and protocols under realistic fading conditions. Such verification is particularly important when commercial transceivers are considered, as these devices have been developed for guided optical channels and do not incorporate mechanisms specifically designed to cope with turbulence-induced outages. Understanding their response to fading is essential for evaluating their suitability for OFL applications and for identifying the need for additional mitigation techniques at the physical or higher layers.

Direct testing in operational links is often impractical. Field experiments require favorable atmospheric conditions, access to specialized OGSs and, in the case of satellite links, the availability of communication opportunities that are limited in duration and difficult to reproduce. Moreover, the stochastic nature of atmospheric turbulence prevents the execution of repeatable measurements under controlled channel conditions. These limitations make field campaigns unsuitable for systematic testing and optimization of communication equipment.

Laboratory-based channel emulation provides an effective alternative. By reproducing the statistical and temporal characteristics of the fading process within a controlled environment, turbulence emulators enable repeatable and flexible performance evaluations without the constraints associated with real atmospheric propagation. Such platforms allow communication terminals to be exposed to a wide range of channel conditions, including scenarios corresponding to different turbulence regimes, pointing-error levels, and link geometries. As a result,

hardware performance, protocol robustness, and mitigation techniques can be investigated before deployment in operational systems.

This Chapter presents an experimental testbed specifically developed to emulate the fading affecting OFLs and to assess the performance of commercial optical transceivers under realistic channel conditions. The emulator reproduces the power fluctuations generated by atmospheric scintillation and pointing jitter, enabling controlled testing of communication equipment over a broad range of fading scenarios. First, the state of the art of optical turbulence generation is reviewed. Subsequently, the methods adopted to synthesize representative fading time series are described. The architecture and implementation of the developed experimental setups are then presented in detail, followed by the experimental procedures and measurement results obtained from transceiver testing campaigns.

3.1 Optical turbulence generators

Several approaches have been proposed in the literature to emulate atmospheric turbulence and the resulting fading affecting FSO links. These approaches can be broadly classified into four categories, i.e., (i) turbulent fluid chambers, (ii) passive phase screens, (iii) active phase screens, and (iv) Variable Optical Attenuator (VOA)-based Optical Turbulence Generators (OTGs).

Turbulent fluid chambers generate atmospheric turbulence by physically producing refractive index fluctuations inside a confined propagation volume [188]. Their operating principle relies on the dependence of the atmospheric refractive index on temperature and pressure variations [127]. Typically, turbulence is generated by mixing fluid flows maintained at different temperatures, producing random refractive index inhomogeneities that distort the optical wavefront.

The turbulence strength can be controlled by adjusting the temperature gradient and the fluid velocity. In addition, different vertical turbulence profiles may be generated by stacking multiple chambers or by forcing the optical beam to perform multiple passes through the same chamber. The temporal evolution of turbulence can also be reproduced according to Taylor's frozen turbulence hypothesis, which assumes that turbulent eddies can be considered frozen in space and blown across the observation path by the transverse wind. This assumption derives from the

consideration that the time scale associated with advection (i.e., 1 to 10 ms) is typically faster than the one associated with the eddies' turnover (i.e., on the order of 10 s) [127,188]. Consequently, the turbulence temporal behavior is generated by blowing the turbulent medium through an aperture perpendicular to the propagation path [188].

Air is the most commonly adopted fluid because it naturally reproduces the Kolmogorov turbulence spectrum characteristic of the atmosphere. However, the relatively weak dependence of the air refractive index on temperature (dn/dT of the order of $10^{-6}/^{\circ}C$) requires either long propagation distances or large temperature differences to induce significant wavefront distortions [189]. Water-based chambers have also been proposed, exploiting a refractive-index temperature sensitivity approximately two orders of magnitude larger than that of air [188]. Nevertheless, water introduces additional drawbacks, including absorption in the IR region, possible leakage issues, and turbulence statistics that differ from those encountered in atmospheric propagation [188, 189].

Numerous experimental demonstrations based on turbulent chambers have been reported in the literature, including investigations of modulation formats, diversity techniques, coherent transmission systems, and turbulence mitigation strategies [190–200]. However, most reported setups are limited to weak or moderate turbulence conditions because of practical constraints on chamber dimensions and achievable temperature gradients [193–195]. Furthermore, these systems are often bulky, generate heat that must be dissipated away from the optical bench and, most importantly, produce inherently random turbulence realizations [188]. As a consequence, performing repeatable experiments under identical channel conditions is challenging. For OFLs, these limitations become particularly severe because the turbulence conditions vary continuously during the satellite pass and may not be accurately reproduced by a static chamber.

Passive phase screens reproduce turbulence-induced wavefront distortions by means of transparent or reflective optical elements whose surface profile introduces a predetermined optical path difference to the incident wavefront [188, 201]. By designing the phase pattern according to Kolmogorov turbulence statistics, a single screen can emulate the effect of a turbulent layer. $C_n^2(h)$ profiles can be represented by employing multiple phase screens distributed along the optical path [188].

Temporal evolution is typically generated by rotating the phase screens [189]. Since the phase pattern is fixed, the generated turbulence realization eventually repeats itself after a complete revolution. This limitation can be mitigated by employing multiple screens rotating at different angular velocities.

The design of phase screens requires preserving key propagation parameters of the real optical link, including the Rytov variance σ_R^2, the Fresnel number $D^2/\lambda L$, and the ratio between receiver aperture diameter and atmospheric coherence length D_R/r_0 [202]. When these parameters are properly matched, the emulator can accurately reproduce the wavefront distortions experienced in the actual propagation scenario.

Compared with turbulent fluid chambers, passive phase screens are considerably more compact, generate no heat, and provide fully deterministic and repeatable channel conditions. Their main limitation is the lack of reconfigurability. Once fabricated, the phase pattern cannot be modified, and changes in turbulence strength can only be achieved by varying the beam size incident on the screen or by replacing the optical element [188].

An additional challenge is represented by chromaticity. Conventional diffractive phase screens introduce wavelength-dependent distortions, limiting their applicability over broad spectral ranges [188]. Near-Index-Matching (NIM) techniques have been proposed to overcome this issue by exploiting the refractive index difference between carefully selected materials, thus enabling nearly achromatic operation. Nevertheless, experimental studies have shown that NIM-based phase screens mainly reproduce turbulence-induced phase distortions and are generally unable to generate significant intensity fluctuations [201].

Active phase screens extend the concept of passive phase plates by introducing reconfigurable optical elements capable of dynamically modifying the imposed phase pattern. These devices are typically implemented through Liquid Crystal (LC) Spatial Light Modulators (SLMs) or DMs.

Because the phase pattern can be updated electronically, active phase screens can generate time-varying wavefront distortions without requiring any mechanical movement. This flexibility enables the emulation of different turbulence realizations and propagation conditions using the same hardware platform.

Despite their versatility, active phase screens exhibit several limitations. LC-SLMs generally provide refresh rates on the order of hundreds of hertz, which may be insufficient to accurately reproduce the temporal dynamics of turbulence-induced scintillation. Moreover, their finite spatial resolution limits the representation of high-spatial-frequency aberrations associated with strong turbulence [188]. DMs avoid chromaticity issues but are typically characterized by an even lower spatial frequency and significantly higher costs.

Similarly to passive phase screens, active devices are primarily designed to reproduce wavefront distortions. Therefore, they are particularly suitable for studies involving AO correction [203], as well as propagation of vortex beams [204], multiplexed spatial modes [202, 205], and multiemitter beams [206]. Specifically, a phase-screen-based turbulence emulator representative of low elevation LEO-to-ground OFLs was reported in [203].

A fundamentally different approach consists of reproducing turbulence effects directly in terms of the received optical power fluctuations experienced by the communication system. In this case, the optical channel is emulated using an electronically-controlled fiber-coupled VOA whose attenuation is dynamically varied according to a predefined fading time series.

The rationale behind this approach is that atmospheric turbulence ultimately manifests itself as temporal variations of the received optical power. Therefore, rather than reproducing the physical propagation process and the associated wavefront distortions, the emulator directly recreates the resulting fading process observed at the receiver. The desired attenuation sequence can be derived from analytical channel models, numerical simulations, or experimental recordings.

The first implementations of this concept were proposed for the emulation of fog-induced attenuations and were subsequently extended to include turbulence-induced scintillation [207, 208]. More recent systems have been employed to test commercial transceivers [209], photodetectors [208], FEC and interleaving techniques [210–212], ARQ protocols [213], diversity architectures [214], and photon-counting receivers [215] for space-based optical links. Depending on the implementation, attenuation can be imposed through Micro Electro Mechanical Systems (MEMS)-based VOAs, electro-optic modulators, Mach-Zehnder modulators, or acousto-optic modulators.

Compared with other OTG architectures, VOA-based emulators offer several advantages. Since the entire setup is fiber-coupled, they are extremely compact and can be directly integrated with commercial optical communication equipment. Furthermore, they are fully deterministic and allow identical channel realizations to be reproduced repeatedly, enabling fair comparisons among different hardware and protocol configurations.

The emulator dynamic range determines the maximum achievable fading depth, whereas the modulator bandwidth establishes the highest reproducible fluctuation frequency [215]. Considering that turbulence coherence times are typically in the millisecond range, bandwidths of a few kilohertz are generally sufficient to reproduce the temporal behavior of OFL fading.

Another important advantage is the possibility of extending the emulator beyond turbulence-induced scintillation. Since pointing jitter also manifests itself as a time-varying attenuation process, its effects can be incorporated by generating attenuation sequences derived from suitable pointing-error statistical models and combining them with turbulence-induced fading. As a result, the same hardware architecture can reproduce the joint effects of scintillation and pointing instabilities without requiring additional optical components.

A limited number of experimental platforms capable of jointly emulating turbulence and pointing jitter have been reported in the literature. In [216], disturbance mirrors are employed to physically reproduce platform vibrations while scintillation is generated through attenuation profiles derived from computationally intensive wave-optics simulations. Although such approaches provide high physical fidelity, they increase both system complexity and computational burden. Conversely, fiber-based attenuation emulators can generate both turbulence- and pointing-induced fading through computationally efficient stochastic models, allowing the creation of very long fading sequences with negligible computational cost. Furthermore, they facilitate the emulation of dynamic scenarios in which the fading statistics evolve continuously, enabling systematic investigations of the impact of different pointing-jitter levels and turbulence conditions on communication performance.

3.2 Fading generation algorithms

The operation of the VOA-based emulators described in the previous section relies on the generation of attenuation time series representative of the fading experienced in OFLs. Several approaches for generating such time series can be found in the literature. The simplest solution consists of reproducing experimentally recorded vectors of received power acquired during field campaigns [208, 210, 211, 217]. This approach guarantees that the generated fading faithfully reproduces a real propagation scenario. However, it is inherently limited by the availability of measurement data, which are typically collected under a restricted set of atmospheric conditions and geographical locations. Moreover, experimental datasets are often associated with OGSs located at astronomical sites characterized by particularly favorable seeing conditions. As a consequence, relying exclusively on recorded power vectors does not provide the flexibility required to investigate the large variety of turbulence regimes and operating conditions that may occur in practical OFLs.

An alternative approach consists of generating fading vectors through wave-optics simulations [209, 218]. In this case, atmospheric turbulence is reproduced by numerically propagating the optical wavefront through a sequence of random phase screens representing turbulent layers. Although this methodology provides high physical fidelity and allows the simultaneous evaluation of wavefront distortions and intensity fluctuations, it is computationally demanding. The generation of long-duration fading sequences may require significant processing time and memory resources, especially when multiple turbulence conditions or complete satellite passes must be considered.

To overcome these limitations, the emulator developed in this research adopts a statistical time-series synthesis approach based on the method originally proposed by Gujar et al. [219]. The technique exploits the fact that a random fading process is completely characterized by its PDF and PSD. Consequently, instead of reproducing the physical propagation process itself, the algorithm directly generates random time series exhibiting the same statistical and temporal characteristics as the received irradiance. Compared with wave-optics simulations, this method drastically reduces the computational complexity while preserving the quantities

that are most relevant for communication-system performance evaluation, namely fade depths, fade durations, and temporal correlation properties. Furthermore, it enables the generation of arbitrarily long fading vectors and allows the channel statistics to be continuously modified during the simulated satellite pass.

As schematized in Fig. 3.1, the synthesis procedure begins with the generation of a Gaussian random signal $X(t)$ characterized by zero mean and unit variance. Since the PSD of a Gaussian process is flat over the entire frequency range, a suitable linear filter is subsequently applied to shape its temporal characteristics according to the desired PSD. The resulting intermediate process $X_{\text{int}}(t)$ preserves its Gaussian statistics while exhibiting the target PSD. Finally, a nonlinear transformation is applied to the intermediate signal to shape its PDF. If the nonlinear system is relatively smooth, the final output will be characterized by a PSD close to a scaled version of the desired one [219].

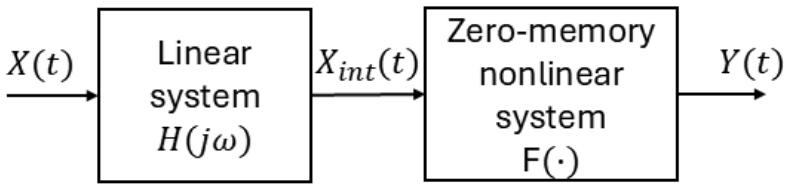


Figure 3.1 – Fading time series generation method

The transfer function of the linear system, $H(s)$, is chosen such that

$$|H(j\omega)| = \left[\frac{\Phi_{int}(\omega)}{\Phi_X(\omega)}\right]^2 \tag{3.1}$$

where $\Phi_X(\omega)$ and $\Phi_{int}(\omega)$ are the PSDs of $X(t)$ and $X_{\text{int}}(t)$, respectively [219].

Instead, the zero-memory nonlinearity $F(\cdot)$ can be seen as the composition of two functions, $P(\cdot)$ and $f(\cdot)$ [220], as shown in the block diagram of Fig. 3.2.

The intermediate signal has a Gaussian distribution $p_{X_{int}}(x)$, i.e.,

$$p_{X_{int}}(x) = \frac{1}{\sqrt{2\pi}} \exp\left[-\frac{x^2}{2}\right] \tag{3.2}$$

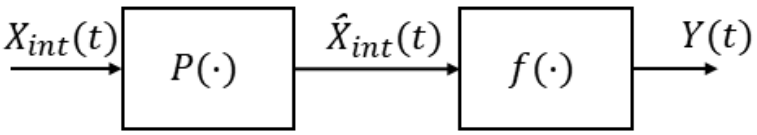


Figure 3.2 – Nonlinear transformation derivation

If $\hat{X}_{int} = P(X_{int})$, with $P(x)$ being the cumulative distribution

$$P(x) = \int_{-\infty}^{x} p_{X_{int}}(\lambda) d\lambda \tag{3.3}$$

then, the PDF of the random variable $\hat{X}_{int}$ is uniform in the interval $(0, 1)$. Similarly, if $Y = f(\hat{X}_{int})$ has the target PDF, $p_Y(y)$, the cumulative distribution $Q(y)$ is related to $f^{-1}(\cdot)$ as

$$Q(y) = \int_{-\infty}^{y} p_Y(\lambda) d\lambda = f^{-1}(y) \tag{3.4}$$

Therefore, for $Y(t)$ to have the desired PDF, $f(\cdot)$ must be chosen to satisfy Eq. (3.4). Finally, the overall nonlinear function is given by

$$F(x) = f[P(x)] \tag{3.5}$$

The adoption of the described algorithm to generate scintillation time series representative of OFLs was first proposed and validated in [221]. Then, Giggenbach et al. extended this approach to jointly model the impact of scintillation and pointing jitter [222]. According to [222], random variables modeling scintillation- and jitter-induced fading ($P_{scint}(t)$ and $P_{jitter}(t)$, respectively) can be independently generated and then multiplied for combination. Indeed, atmospheric scintillation and pointing jitter originate from independent physical mechanisms and are therefore assumed statistically independent. Under this assumption, the overall normalized received power can be expressed as

$$P_{fading}(t) = P_{scint}(t) P_{jitter}(t) \tag{3.6}$$

The resulting time series simultaneously reproduces the statistical distribution and temporal behavior of both impairments. In the following, the generation of scintillation- and jitter-induced fading time series will be further detailed.

3.2.1 Turbulence-induced fading generation

The statistical distribution of turbulence-induced received power depends on the propagation scenario and turbulence regime. For downlink OFLs, the received signal often benefits from aperture averaging at the OGS. Under these conditions, experimental measurements have repeatedly shown that the received power is accurately described by a lognormal distribution, even when moderate turbulence levels are present [221]. Moreover, the lognormal PDF may also apply to uplink OFLs under weak turbulence conditions.

The focus of the performed experimental measurements is on downlink OFLs from LEO satellites. Therefore, the normalized received power $P_{scint}(t)$ is modeled through the lognormal PDF of Eq. (2.49).

The parameters of the distribution are related to the scintillation index σ_I^2 through

$$\sigma_{\ln I}^2 = \ln\left(\sigma_I^2 + 1\right) \tag{3.7}$$

$$\mu_{\ln I} = -\frac{\sigma_{\ln I}^2}{2} \tag{3.8}$$

where $\sigma_{\ln I}^2$ is the variance of log irradiance as defined in Eq. (2.23), and $\mu_{\ln I}$ is the mean of log irradiance.

The scintillation index can be easily computed through the link budget tool presented in Chapter 2, accounting for turbulence strength, aperture averaging, satellite elevation angle, and atmospheric conditions.

Regarding the temporal characteristics, the PSD of received irradiance exhibits a low-pass behavior. At low frequencies the spectrum remains approximately constant, whereas beyond a cutoff frequency ω_c it decreases according to a $-8/3$ power-law slope [127]. For a point receiver, ω_c, also known as Fresnel frequency, can be retrieved from the mean transverse wind speed $V_\perp$ as

$$\omega_c = \frac{V_\perp}{\sqrt{L/k}} \tag{3.9}$$

Nevertheless, large-aperture receivers induce a low-pass filtering effect, shifting ω_c towards lower frequencies [127, 221]. In this case, the PSD cutoff frequency and slope can be efficiently estimated by using the engineering approximation developed by Yura [223]. As a starting point, the concepts of effective turbulent propagation length and effective rms wind speed are introduced. The former is evaluated as

$$L_{eff} = \left(\frac{18 \int_0^L C_n^2[h(s)] s^2 ds}{11 \int_0^L C_n^2[h(s)] s^{5/6} ds} \right)^{6/7} \tag{3.10}$$

while the latter is given by

$$V_{eff} = \left(\frac{\int_0^L C_n^2[h(s)] s^{5/6} G(s,a) V^2[h(s)] ds}{11 \int_0^L C_n^2[h(s)] s^{5/6} G(s,a) ds} \right)^{1/2} \tag{3.11}$$

In Eq. (3.11), $V(h)$ is the wind speed that can be modeled according to Eq. (2.16), and $G(s,a)$ is a weighted integral of the Kolmogorov refractive index spectrum, approximated by

$$G(s,a) \simeq \frac{1}{1 + 0.754(a^2 k/s)^{7/6}} \tag{3.12}$$

where a is the receiving aperture radius. Given the above quantities, it is possible to evaluate the aperture-averaged downlink correlation time, τ_c [s], i.e., the lag at which the autocovariance falls to 0.315 of its peak value [223], as

$$\tau_c(a) = \frac{\sqrt{L_{eff}/k}}{V_{eff}} \sqrt{1 + \eta_{eff}^2} \tag{3.13}$$

where

$$\eta_{eff} = a \sqrt{k/L_{eff}} \tag{3.14}$$

Now, the aperture-averaged downlink characteristic scintillation angular frequency bandwidth can be computed as

$$\omega_F(\eta_{eff}) = \frac{\omega_F(0)}{\sqrt{1 + \eta_{eff}^2}} \tag{3.15}$$

with $\omega_F(0) = V_{eff} \sqrt{k/L_{eff}}$ and $\eta_{eff} = a\sqrt{k/L_{eff}}$. The corresponding frequency value in Hertz can be obtained by dividing Eq. (3.15) by 2π [223].

By exploiting the above approximate model, an engineering PSD model is developed in [224]. Specifically, based on the value of η_{eff}, three regimes can be identified, i.e.,

- a small-aperture regime, when $\eta_{eff} < 1/4$
- an intermediate regime, when $1/4 \leq \eta_{eff} \geq 3$
- a large-aperture regime, when $\eta_{eff} > 3$.

In each case, the PSD is modeled as

$$\Phi(\omega) = \frac{1}{1 + (\omega/\omega_{cut-off})^{\alpha}} \tag{3.16}$$

where $\omega_{cut-off}$ is the 3-dB cutoff frequency and α is the logarithmic slope. The cutoff frequency can be derived from ω_F as

$$\omega_{cut-off} = K(\alpha)\omega_F(\eta_{eff}) \simeq 2.32^{1-2.86\alpha^{-2}}\omega_F(\eta_{eff}) \tag{3.17}$$

In the intermediate range, the PSD is well described by an $\alpha = 17/3$ law. For small apertures, this slope underestimates the high-frequency spectral content. Instead, a value $\alpha = 3$ is better suited. Finally, for large apertures, $\alpha = 4$ best fits the low frequency content near the cutoff [224].

To reproduce this behavior, a low-pass filter with squared magnitude $G^2(\omega) = \Phi(\omega)$ shall be adopted as linear transformation in the fading generation algorithm. If α is an even integer number, the required gain is achieved by a Butterworth filter of order $\alpha/2$. In [224], it is shown that using $\alpha = 4$ and $\alpha = 6$ in the small and intermediate regimes, respectively, gives a reasonable approximation, enabling the use of widely available digital filter design tools.

To summarize, once the desired PSD has been defined, the white Gaussian process is filtered using a low-pass filter whose frequency response approximates the theoretical scintillation spectrum. The filtered signal is then normalized to zero mean and unit variance, obtaining $X_{\text{int,n}}(t)$. Finally, the exponential nonlinear transformation

$$Y(t) = P_{scint}(t) = \exp\left[\mu_{\ln I} + \sigma_{\ln I} X_{\text{int,n}}(t)\right] \tag{3.18}$$

is applied. This operation converts the Gaussian process into a lognormally distributed random process while preserving, to a good approximation, the desired temporal spectrum [221, 222]. The resulting time series represents the normalized received power fluctuations induced by atmospheric turbulence. The overall algorithm is depicted in Fig. 3.3, showing the PDF and PSD of the synthesized signal at each step.

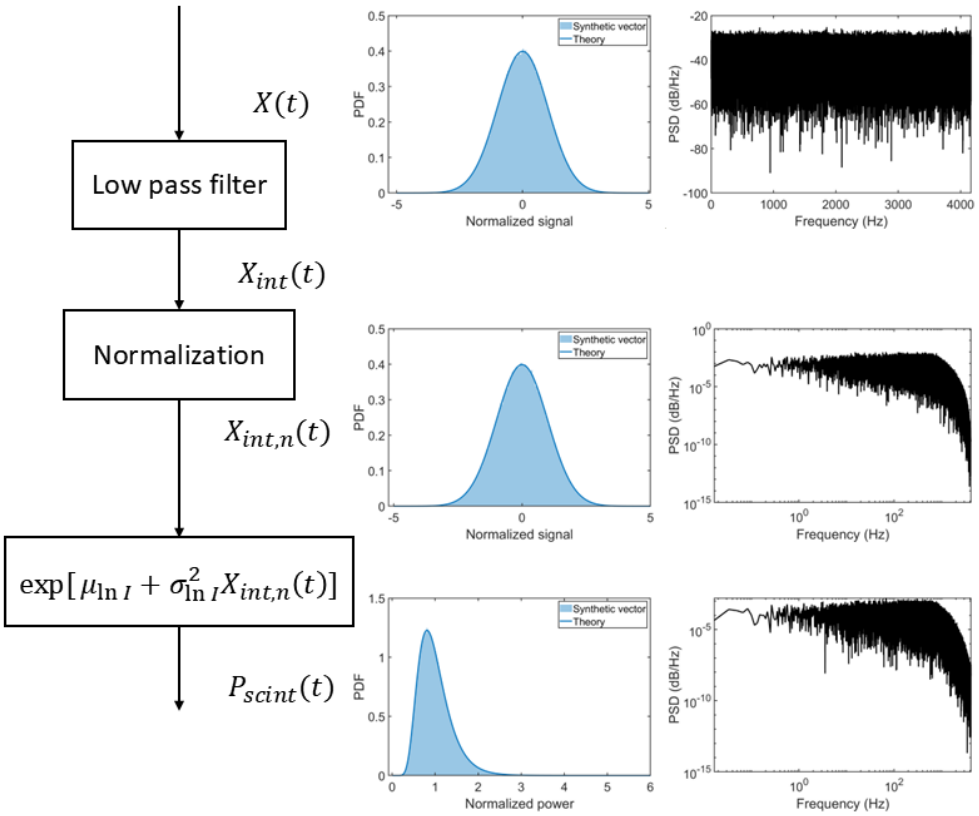


Figure 3.3 – Scintillation-induced fading time series generation algorithm

3.2.2 Pointing jitter-induced fading generation

In addition to scintillation, OFLs are affected by pointing jitter arising from platform microvibrations, tracking inaccuracies, structural resonances, and beam wander effects. These disturbances produce random angular deviations of the transmitted beam from the nominal LoS, causing fluctuations of the collected optical power.

In this work, pointing jitter arising from platform microvibrations has been considered. Indeed, since downlink OFLs have been analyzed, beam wander is negligible.

The pointing error can be modeled through two independent angular deviations, corresponding to the two orthogonal azimuth and elevation errors. Assum-

ing uncorrelated and identically, Gaussian-distributed errors in the two directions, the resulting radial pointing error follows a Rician distribution. Nonetheless, as highlighted in Section 2.1.5, the Rician distribution reduces to a Rayleigh PDF in the absence of bias errors. In the last case, the received irradiance follows a beta distribution, with parameter β given in Eq. (2.64).

The beta-distributed received power is characterized by an average value, i.e., an average pointing loss, equal to $\beta/\beta + 1$, which is equivalent to Eq. (2.65). As shown in Fig. 3.4, this loss becomes more prominent as the rms pointing error σ_{jitt} increases and/or the transmitting telescope aperture D_T widens.

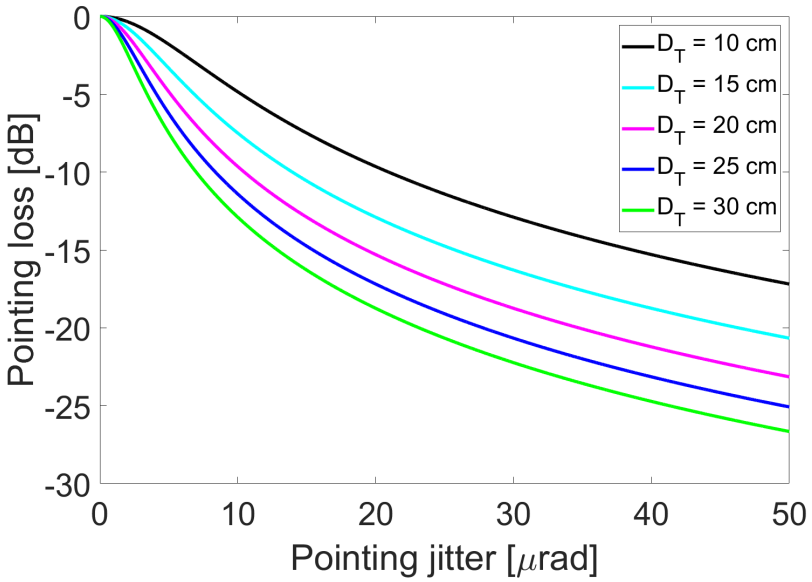


Figure 3.4 – Average jitter-induced pointing loss as a function of the rms pointing jitter for different transmitter aperture diameters

Several measurements performed on space optical terminals have shown that spacecraft microvibration spectra exhibit a low-pass behavior, with most of the disturbance energy concentrated below a few tens of Hertz [131, 151]. Building on these measurements, ESA defined the PSD of Eq. (3.19), which was used as a specification for the SILEX terminal.

$$\Phi(f) = \frac{160}{1 + f^2} \tag{3.19}$$

The above model implies a rms pointing jitter $\sigma_{jitt} \approx 16$ μrad and a slope of 20 dB/decade. A generalization of Eq. (3.19) is

$$\Phi(f) = \frac{2\sigma_{jitt}^2}{\pi \left[1 + \left(\frac{f}{f_{cutoff}}\right)^2\right]} \tag{3.20}$$

An analogous model was also developed by JAXA for the PSD of transients caused by thruster firing [131], i.e.,

$$\Phi(f) = \frac{160}{1 + (f/10)^2} \tag{3.21}$$

which implies a rms value of 50 μrad. At the same time, microvibration measurements conducted during the OICETS trials well matched other space demonstrations and related analytical models, including the one of Eq. (3.19) [151]. The in-orbit measurements revealed that more than 90% of the frequency components fall within frequencies lower than 10 Hz. As shown in Fig. 3.5, the PSD can be modeled using a first-order Butterworth filter consistent with the ESA models of Eqs. (3.19) and (3.20).

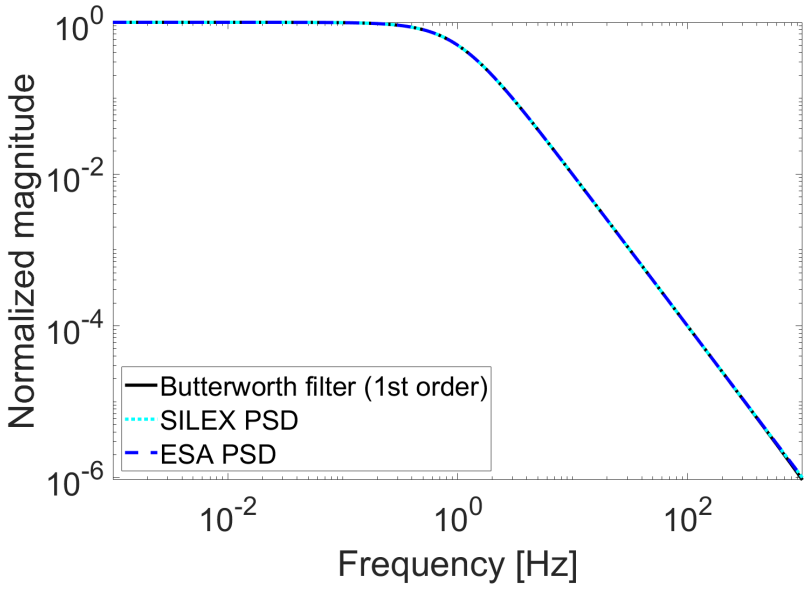


Figure 3.5 – PSD of jitter-induced irradiance fluctuations

Based on the above considerations, jitter-induced fading time series can be synthesized starting from two zero-mean, unity-standard-deviation Gaussian random signals $X_1(t)$ and $X_2(t)$, which represents orthogonal pointing errors. As shown in the scheme of Fig. 3.6, the two signals are low-pass filtered by means of first-order Butterworth filters. Specifically, a 1 Hz cutoff frequency has been selected based on Eq. (3.19). The two filtered signals are normalized and converted into a radial

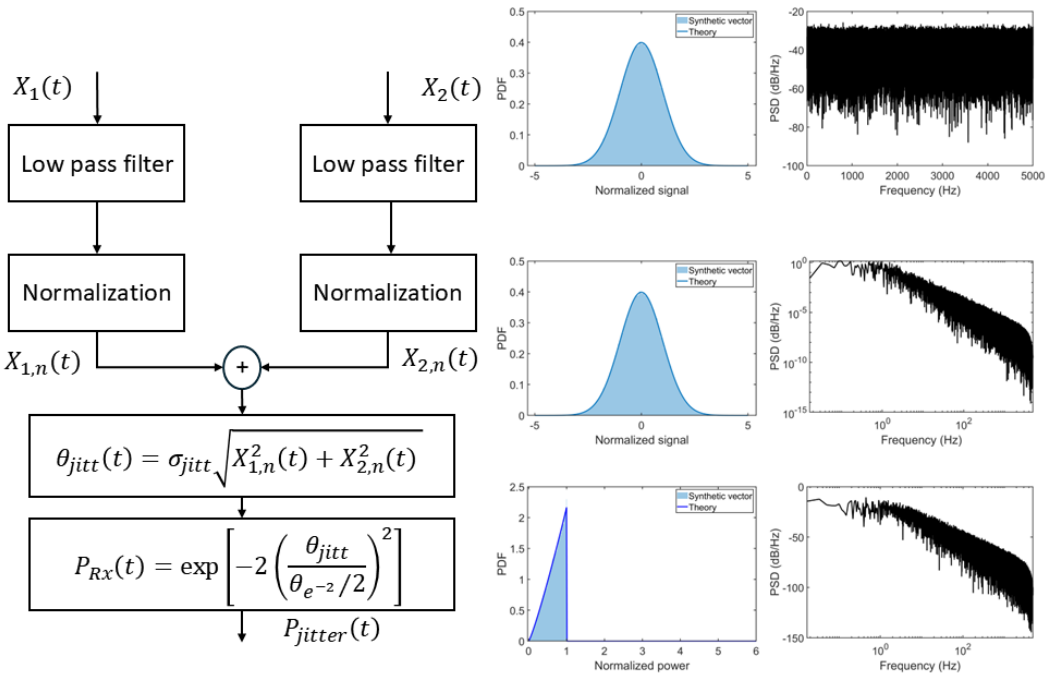


Figure 3.6 – Pointing jitter-induced fading time series generation algorithm

angular pointing error of desired standard deviation σ_{jitt} as

$$\theta_{jitt} = \sigma_{jitt}\sqrt{X_{1,n}^2 + X_{2,n}^2} \tag{3.22}$$

Assuming a Gaussian far-field beam profile, the received irradiance at an angular deviation θ [rad] from the beam center can be expressed as

$$I(L,\theta) = I(L,0)\exp\left[-2\left(\frac{\theta}{\theta_{e^{-2}}/2}\right)^2\right] \tag{3.23}$$

Consequently, the beta-distributed normalized received power affected by pointing jitter becomes

$$P_{jitter}(t) = \exp\left[-2\left(\frac{\theta_{jitt}(t)}{\theta_{e^{-2}}/2}\right)^2\right] \tag{3.24}$$

This model directly links the severity of pointing-induced fading to the ratio between beam divergence and pointing-jitter variance. Larger angular jitter or narrower optical beams therefore result in stronger power fluctuations and higher average pointing losses.

After generation and multiplication of the scintillation- and jitter-related time series, the resulting fading signal simultaneously reproduces the statistical distribution and temporal behavior of both impairments. Furthermore, since all the parameters governing the generation process are directly linked to physical quantities such as turbulence strength, receiver aperture diameter, wind speed, beam divergence, and pointing-jitter variance, the generated fading vectors can be readily adapted to different OFL configurations and satellite mission scenarios.

The computational complexity of the proposed procedure is extremely low, since it only requires the generation of Gaussian random processes, digital filtering operations, and simple nonlinear transformations. Consequently, very long fading sequences can be produced in a few seconds, enabling the emulation of complete LEO satellite passes and the systematic testing of communication equipment under a wide range of channel conditions.

3.3 Experimental testbed for OFLs emulation

To assess the performance of commercial optical transceivers, two complementary experimental platforms were developed. The first setup, implemented at the Polytechnic University of Bari (Poliba), was designed to characterize 10 Gbit/s IM/DD Ethernet-based commercial transceivers under emulated donwlink OFL fading conditions. The second setup, realized at the Telecommunications, Computer Engineering, and Photonics Institute (TeCIP) facilities of Scuola Superiore Sant'Anna, extends the experimental investigation to coherent optical communication systems. Although sharing the same fading generation methodology, the two

platforms differ in the employed hardware and in the investigated communication scenarios.

3.3.1 Poliba experimental testbed

The first experimental platform was developed at Poliba to investigate the performance of commercial 10 Gigabit Ethernet (10GbE) optical transceivers under emulated OFL fading conditions. A schematic representation of the testbed is shown in Fig. 3.7.

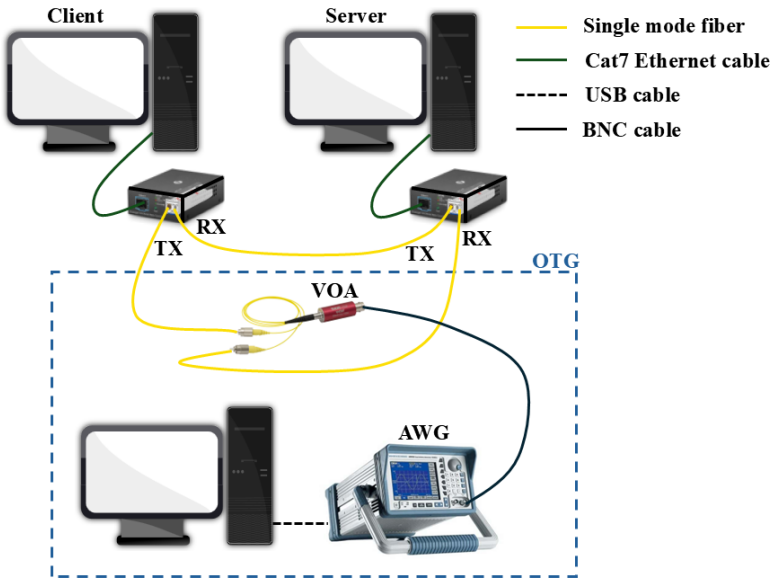


Figure 3.7 – Scheme of the developed Poliba testbed for the emulation of scintillation- and pointing jitter-affected OFLs

The core of the setup consists of the fiber-coupled OTG described in the previous sections. Specifically, the emulator relies on a Thorlabs V1550F MEMS-based VOA [225], whose attenuation is dynamically controlled to reproduce the temporal evolution of turbulence- and pointing-jitter-induced fading. The selected device operates over a broad wavelength range, from 1250 nm to 1650 nm, with a DC-to-1 kHz modulation bandwidth. This bandwidth is sufficient to reproduce the temporal dynamics of atmospheric fading typically encountered in OFLs, whose characteristic fluctuation frequencies typically lie well below 1 kHz.

The attenuation imposed by the VOA is determined by an externally applied control voltage. The corresponding voltage waveforms are generated offline in Matlab from the synthesized fading time series described in Section 3.2 and are subsequently uploaded to a 14-bit Arbitrary Waveform Generator (AWG) connected to the control computer through a USB interface. The AWG drives the VOA through a BNC connection, thereby converting the generated fading vectors into time-varying optical attenuations.

Apart from the fading emulator, the experimental platform comprises two PCs acting as traffic generator and receiver, respectively. Both computers are equipped with 10GbE Network Interface Cards (NICs), which are connected through Cat7 Ethernet cables to two unmanaged media converters. The media converters enable the electrical-to-optical conversion of the Ethernet frames by hosting the commercial optical transceivers under test.

The investigated transceivers are standard 10GbE Small Form-factor Pluggable Plus (SFP+) modules operating at a central wavelength of 1310 nm. The devices employ intensity modulation with OOK modulation and direct detection. Although the documented interest in the atmospheric transmission window around 1550 nm, the use of 1310 nm commercial transceivers does not affect the validity of the experimental assessment. Indeed, turbulence-induced fading exhibits only a weak dependence on wavelength, while equivalent commercial transceivers based on the same transmission architecture are also available for operation in the C-band. Moreover, despite the specific setup wavelength, fading conditions representative of the 1550-nm window can still be emulated by properly generating the fading profiles.

SMF patch cords interconnect the two optical transceivers. The backward communication path, from the server PC to the client PC, bypasses the fading emulator and provides an error-free return channel. Conversely, the forward direction, corresponding to the emulated downlink OFL, passes through the VOA-based OTG, where the synthesized attenuation profiles are imposed on the transmitted optical signal.

In preliminary tests, Internet Control Message Protocol (ICMP) Echo Request packets were sent from the server PC to the client one. In such way, Echo Reply packets experience fading. By running the Wireshark packet sniffing tool on the

server PC, measurements of response times and reply packet losses were made, enabling the quantification of the end-to-end link performance under fading. This configuration ensures that all Echo Requests reach the client PC, while the loss of Echo Replies is only due to fading conditions.

Subsequently, to better evaluate communication performance in a constant bitrate transmission, the setup has been update so that the client computer generates User Datagram Protocol (UDP) traffic using the iPerf2 software operating in client mode. At the same time, the second computer executes iPerf2 in server mode. The generated UDP datagrams are encapsulated on a one-to-one basis into Ethernet frames, so that the percentage of lost datagrams reported by the server directly corresponds to the Ethernet frame loss ratio. During the experimental campaign, the transmission rate was set to 1 Gbit/s. Although the adopted hardware supports 10 Gbit/s operation, this reduced rate was selected to avoid packet losses associated with memory throughput limitations of the host computers rather than with the optical communication system itself.

In the last configuration, to prevent unintended datagram losses, the socket buffer size has been optimized by comparing the number of received frames reported by the Dumpcap network traffic capture tool with that measured by the iPerf server. Furthermore, Dumpcap was used to verify that Ethernet traffic generated by background applications is negligible compared with the traffic produced by iPerf.

3.3.1.1 OTG calibration

The capability of the proposed OTG to faithfully reproduce arbitrary fading profiles depends on the accuracy with which the VOA converts the applied control voltage into the desired optical attenuation. Since the attenuation-versus-voltage characteristic of the employed MEMS-based VOA is nonlinear, a preliminary calibration procedure was carried out before performing the communication experiments. The calibration was conducted at the operating wavelength of the experimental setup, namely 1310 nm, with the setup of Fig. 3.8.

Specifically, a Continuous Wave (CW) laser diode operating at 1330 nm was employed as a source to characterize the VOA. Before performing the calibration, the laser operating point has been optimized to guarantee stable optical power

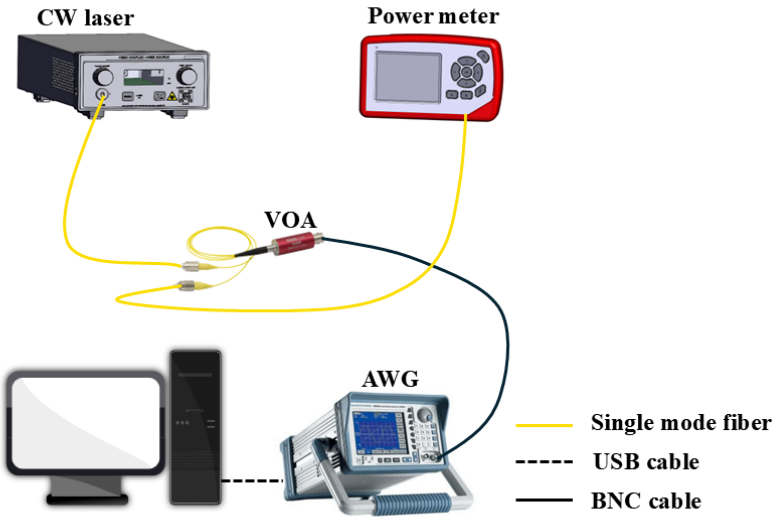


Figure 3.8 – Scheme of the Poliba OTG calibration setup

throughout the measurements. In detail, the laser bias current was set to 15.7 mA, providing an average optical power of 2 mW while ensuring excellent temporal stability thanks to the laser diode and temperature controller.

The emitted wavelength was also verified using an Optical Spectrum Analyzer (OSA). As shown in Fig. 3.9, the measured central wavelength is equal to 1310.535 nm.

The characterization of the VOA was performed by launching the stabilized 2 mW CW optical signal into the device input fiber while applying constant control voltages covering its entire operating range (i.e., 0 to 5 V). Voltage values with increments of 0.5 V have been considered. For each applied voltage, the optical power at the VOA output was measured by means of a power meter and normalized with respect to the input power, obtaining the transmission characteristic reported in Fig. 3.10a. Specifically, the transmission power, T_{VOA} [%], was derived as

$$T_{VOA} = \frac{P_{VOA,out}}{P_{VOA,in}} \cdot 100 \tag{3.25}$$

where $P_{VOA,in}$ is the optical power in input to the VOA, i.e., 2 mW, and $P_{VOA,out}$ is the optical power at the VOA output. Figure 3.10b shows the same characteristic

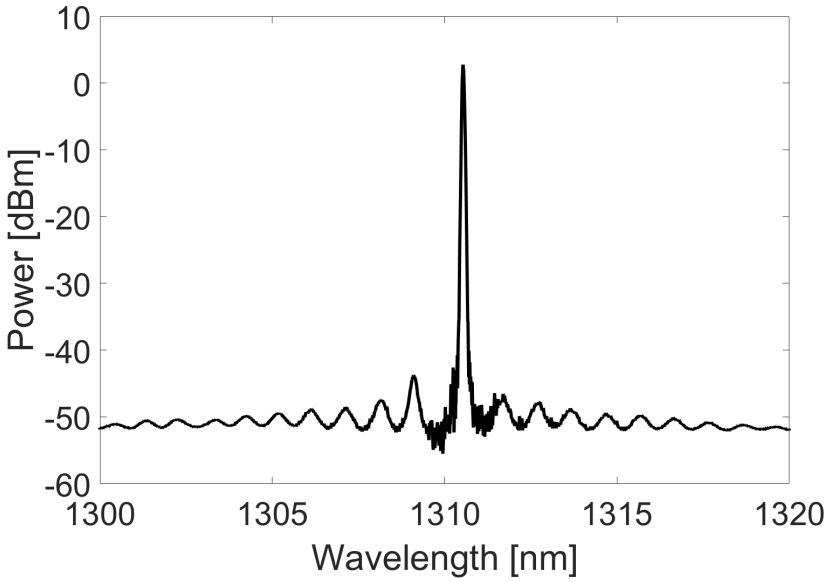


Figure 3.9 – Laser spectrum

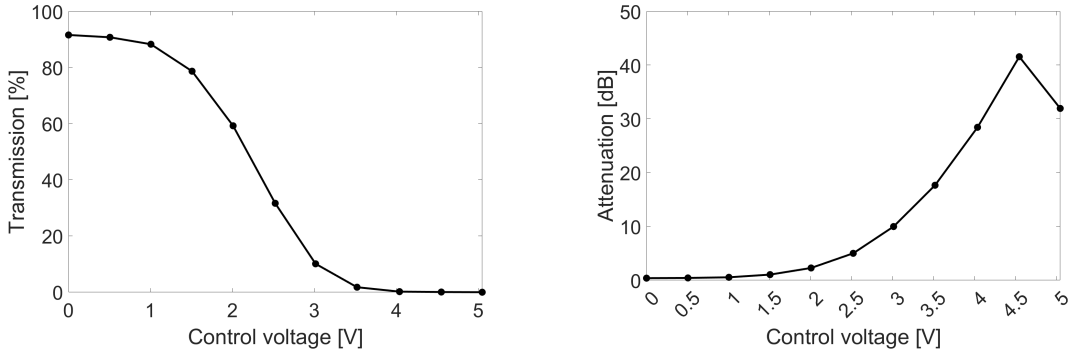
in terms of attenuation, A_{VOA} [dB], i.e.,

$$A_{VOA} = 10 \log_{10} \left(\frac{P_{VOA,in}}{P_{VOA,out}} \right) \tag{3.26}$$

As expected, the transmission decreases monotonically with increasing control voltage, although following a markedly nonlinear trend. The measured characteristic demonstrates that the device can reproduce transmission coefficients ranging from approximately 91.5% down to 0.007%, corresponding to attenuations between approximately 0.4 dB and 40 dB. This attenuation range comfortably exceeds the fade depths expected in the OFL scenarios investigated throughout this research.

Although the manufacturer specifies an operating voltage range extending up to 5 V, only voltages between 0 V and 4.5 V have been retained for the emulator operation. Beyond this limit, the measured characteristic loses its monotonic behavior because of the increased noise associated with deeper attenuations. Restricting the usable operating range guarantees a one-to-one correspondence between control voltage and optical attenuation, which is essential for the accurate reproduction of arbitrary fading profiles.

Since the measured VOA characteristic is nonlinear, the desired attenuation cannot be directly translated into the corresponding control voltage. Therefore,



(a) (b)

Figure 3.10 – VOA measured (a) transmission power and (b) attenuation as a function of applied control voltage

the inverse transfer function of the experimental characteristic was numerically computed in Matlab. To this end, a shape-preserving piecewise cubic interpolation method has been employed. Unlike conventional cubic spline interpolation, this algorithm preserves the monotonicity of the experimental data while preventing spurious oscillations between adjacent samples. The resulting inverse calibration curve is shown in Fig. 3.11. The computed curve was subsequently incorporated into the AWG control software. Consequently, every attenuation sample generated by the fading synthesis algorithms is automatically converted into the corresponding VOA control voltage before being transferred to the AWG.

The accuracy of the proposed calibration procedure has been experimentally verified by selecting ten transmission values uniformly distributed over the calibrated operating range. For each target transmission, the corresponding control voltage is obtained through the inverse calibration function, applied to the VOA, and the resulting optical transmission is experimentally measured.

Figure 3.12 compares the measured transmission values with the corresponding target values. The excellent agreement between the two datasets demonstrates the effectiveness of the calibration procedure. A linear regression performed on the experimental results yielded an R-squared of 0.9993, indicating a highly linear relationship between the desired and measured transmission coefficients. This result confirms that the nonlinear behavior of the MEMS-based VOA has been effectively compensated.

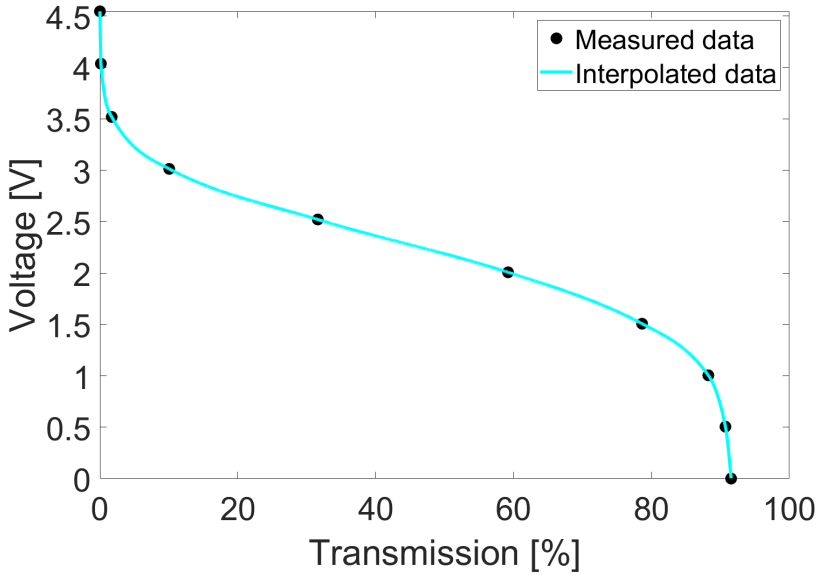


Figure 3.11 – VOA inverse calibration curve

The validity of the calibration curve has been further tested by applying a sinusoidal control voltage

$$v(t) = 1.75\sin(2\pi 20t) + 2.25 \tag{3.27}$$

whose amplitude varies between 0.5 and 4 V at a frequency of 20 Hz. In Fig. 3.13, the above control voltage before (black curve) and after (cyan curve) calibration is shown. The corresponding VOA output signals were measured by replacing the power meter by a photodetector connected to an oscilloscope. The recorded signals are shown in Fig. 3.14a. Moreover, their Fast Fourier Transform (FFT) is plotted in Fig. 3.14b.

Clearly, the calibration process allows preserving the sinusoidal signal shape in output from the VOA. This is further supported by the FFT, showing the complete suppression of higher-order harmonics after calibration.

3.3.2 TeCIP experimental testbed

A second experimental testbed was developed at the TeCIP facilities of Scuola Superiore Sant'Anna to investigate the performance of commercial Optical Trans-

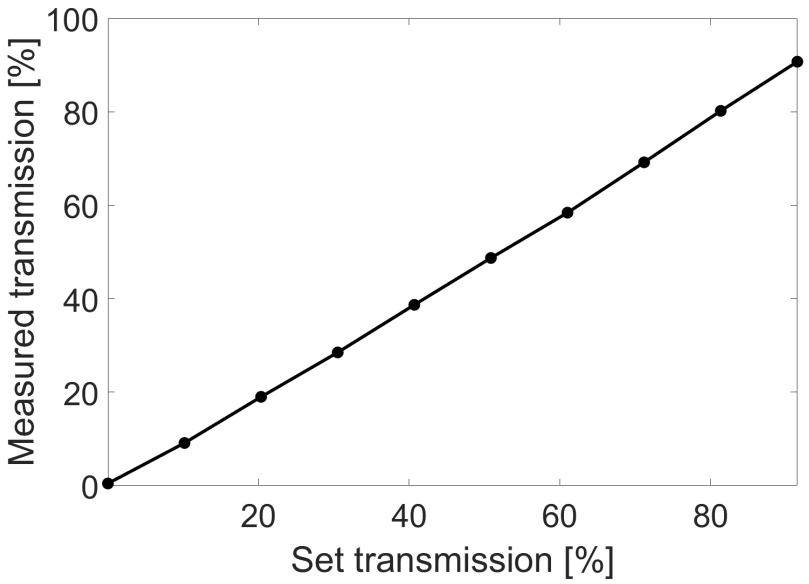


Figure 3.12 – VOA measured transmission power as a function of set transmission power after calibration

port Network (OTN) transceivers under emulated OFL fading conditions. Indeed, coherent solutions implementing terrestrial OTN standards are currently employed in fiber networks and, thus, their deployment in space networks is the obvious choice to easily extend the terrestrial network into space, delivering hundreds of Gigabits per second by means of compact and energy-efficient pluggable transceivers. Following this rationale, coherent modulations, such as DP-QPSK, are currently considered in specifications regarding the development of OISLs and OFLs [187, 226].

Compared with the testbed presented in the previous subsection, this setup extends the experimental investigation to both IM/DD and coherent transmission systems, allowing the assessment of commercial equipment operating at line rates up to 100 Gb/s. A schematic representation of the experimental testbed is reported in Fig. 3.15.

Traffic generation and performance monitoring are performed by a Spirent N4U traffic generator and analyzer equipped with 1 Gigabit Ethernet (1GbE) interfaces. During the experiments, the Spirent continuously generates Ethernet frames at a rate of one frame every microsecond while simultaneously counting the transmitted

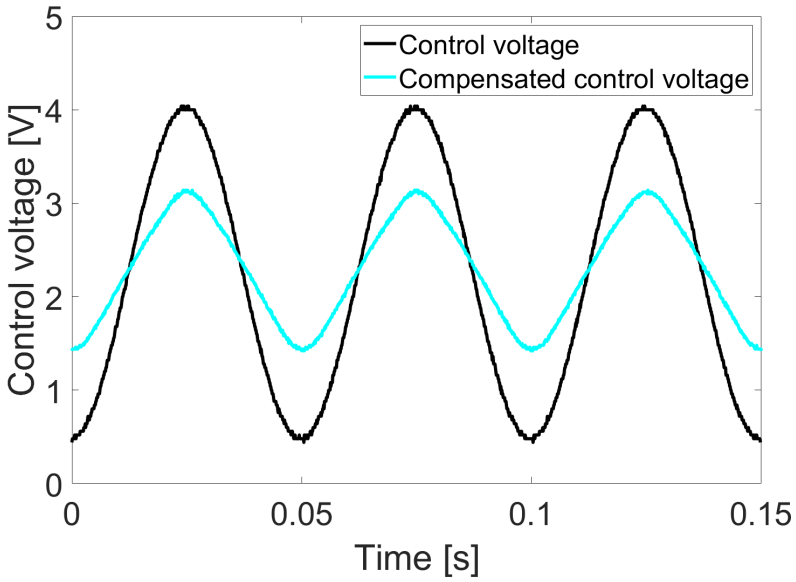
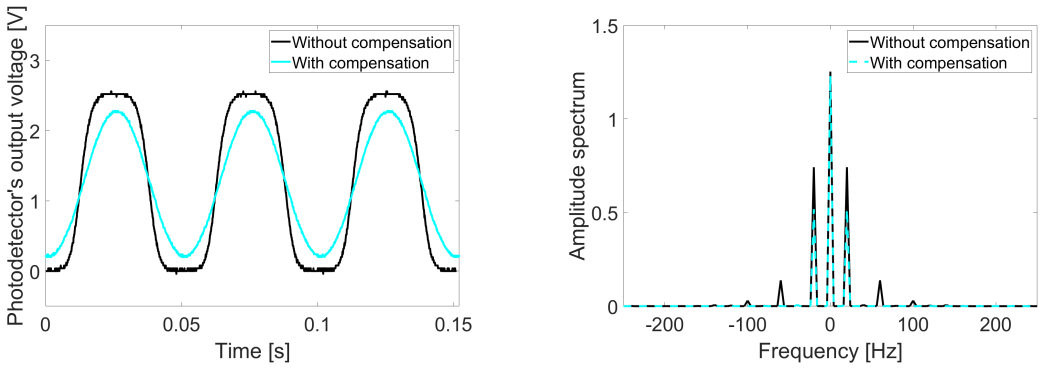


Figure 3.13 – VOA sinusoidal control voltage before (black curve) and after (cyan curve) calibration

and correctly received frames. The difference between these two quantities directly provides the number of lost frames associated with the emulated fading conditions.

The traffic generator interfaces are connected to a programmable switch, whose primary function is to maintain the communication interfaces continuously active throughout the measurement campaign while properly forwarding the incoming Ethernet traffic towards the OTN equipment under test. Depending on the considered experiment, the switch is alternatively connected to one of two pairs of commercial muxponders implementing either 10 Gb/s or 100 Gb/s optical transmission.

The 10 Gb/s optical link employs commercial transceivers based on intensity modulation with OOK, operating at a central wavelength of 1545.32 nm. Conversely, the 100 Gb/s configuration adopts coherent transceivers operating at 1544.53 nm and employing DP-QPSK modulation. The availability of both transmission technologies enables a direct comparison between conventional intensity-modulated systems and modern coherent optical communication equipment under identical channel conditions.



(a) (b)

Figure 3.14 – (a) VOA output signal over time and (b) its spectrum with applied sinusoidal control voltage

Before entering the OTG, the optical signal passes through a manually controlled VOA, which sets the optical power launched into the fading emulator to the same average value for the two transmission configurations (i.e., 10 Gb/s and 100 Gb/s). This operation is necessary because the transfer characteristic of the employed VOA was found to depend slightly on the incident optical power. Consequently, to guarantee that both transmission systems experience identical fading conditions, the experimental campaign has been carried out separately for the 10 Gb/s and 100 Gb/s configurations.

As for the Poliba setup, the fading emulator employs a voltage-controlled MEMS-based VOA. The attenuation profiles are generated offline in Matlab according to the synthesis procedure presented in Section 3.2 and uploaded to an AWG, which drives the VOA through its analog control input. By dynamically varying the applied control voltage, the optical turbulence generator reproduces the desired turbulence-induced attenuation time series.

At the emulator output, the optical signal is split by a 30:70 fiber coupler. The 70% branch is connected to an OSA or, alternatively, to a photodetector followed by a real-time oscilloscope, allowing continuous monitoring of the faded optical signal during the experiments. The remaining 30% branch is routed through a manually-adjustable VOA before entering a low-noise EDFA. This additional attenuator allows the average optical power at the EDFA input to be accurately adjusted, ensuring operation at the desired receiver operation point. Following

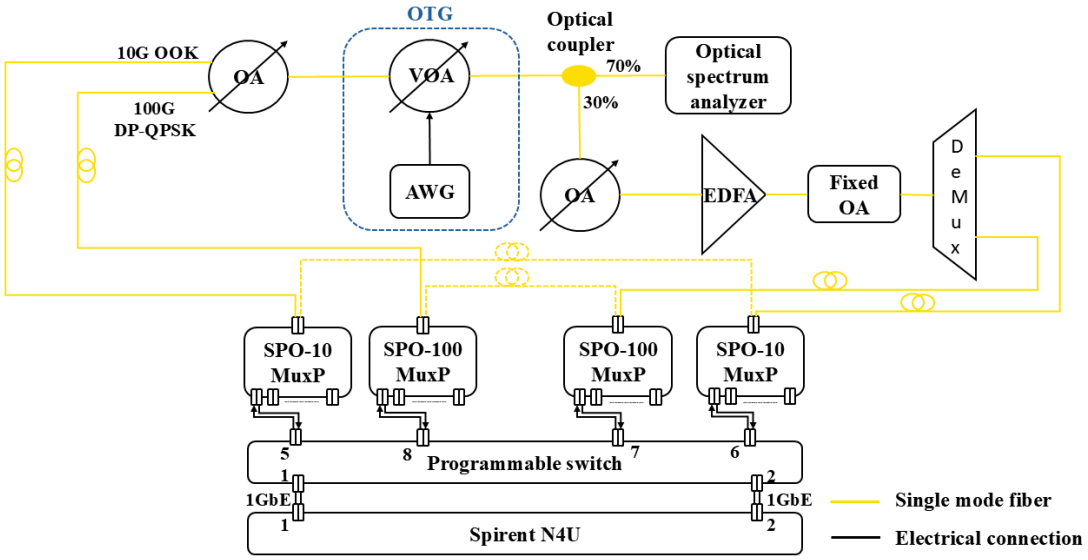


Figure 3.15 – Scheme of the developed TeCIP testbed for the emulation of scintillation-affected OFL

amplification, a second attenuator reduces the signal power to prevent receiver saturation before the signal is delivered to the demultiplexer and the corresponding transceiver.

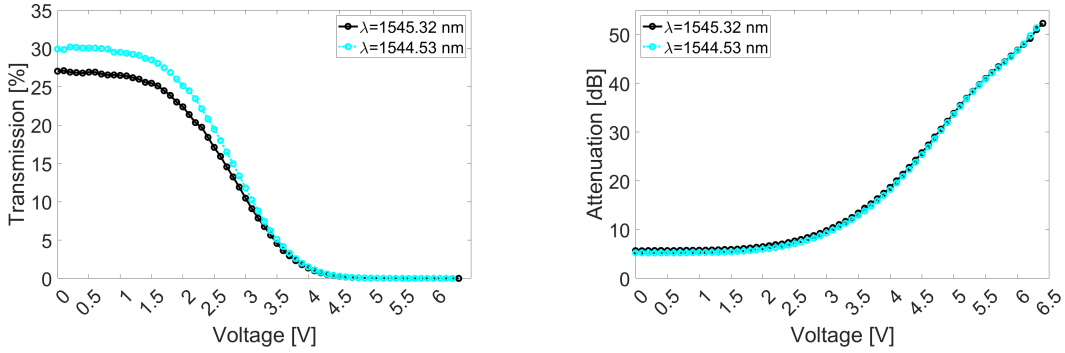
3.3.2.1 OTG calibration

As for the Poliba OTG, the VOA has been experimentally characterized to determine the relationship between the applied control voltage and the resulting optical attenuation.

The employed VOA operates over the C band, i.e., from 1530 nm to 1570 nm, and accepts control voltages between 0 V and 6.5 V. Since the communication experiments involved commercial transceivers operating at 1545.32 nm and 1544.53 nm, the characterization has been carried out at both wavelengths to verify the possible wavelength dependence of the device response.

Also in this case, the calibration has been performed by launching a CW optical signal with known power into the VOA input while applying constant control voltages spanning the entire operating range with a resolution of 0.1 V. The optical

power at the VOA output was measured by means of an optical power meter and converted into attenuation values with respect to the reference input power. Specifically, a tunable laser source was employed. The resulting transmission power and attenuation characteristics measured at the two operating wavelengths are reported in Figs. 3.16a and 3.16b, respectively.



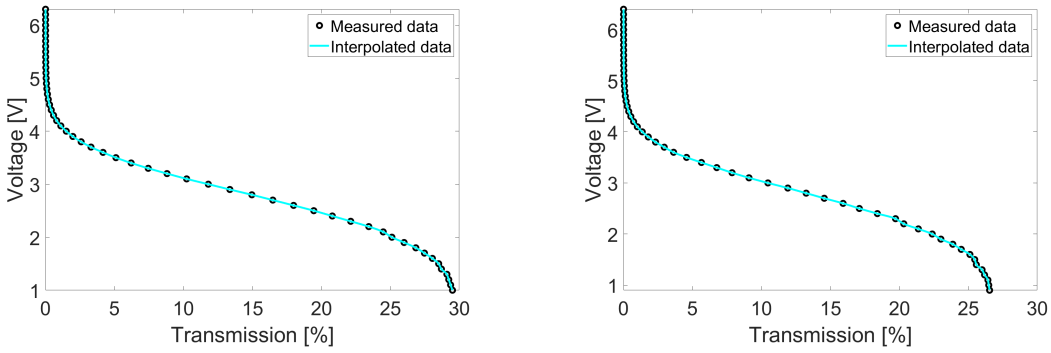
(a) (b)

Figure 3.16 – VOA measured (a) transmission power and (b) attenuation as a function of applied control voltage

Minor differences can be observed among the curves at the two wavelengths, indicating that the VOA response does not strongly depend on the wavelength within the considered portion of the C-band. An insertion loss of approximately 5.5 dB can be appreciated when no control voltage is applied, whereas the maximum achievable attenuation exceeds 52 dB at the highest control voltages. This dynamic range is largely sufficient to reproduce the fade depths typically experienced in OFLs.

A closer inspection of the transmission characteristic reveals small fluctuations at the extremes of the control voltage range, resulting in a slight loss of monotonicity. Thus, the usable operating range was restricted to voltages above 1 V and below 6.3 V. These limits correspond to attenuation ranges of approximately 5.75-52.3 dB and 5.30-51.4 dB at the two wavelengths, respectively.

To compensate for the nonlinear device response, the inverse transfer function was computed in Matlab using the shape-preserving piecewise cubic interpolation method. The obtained inverse curves are shown in Figs. 3.17a and 3.17b for the two operating wavelengths, respectively.



(a) (b)

Figure 3.17 – VOA inverse calibration curve at (a) $\lambda = 1544.53$ nm and (b) $\lambda = 1545.32$ nm

As for the Poliba setup, the accuracy of the calibration procedure has been experimentally verified by selecting ten attenuation values uniformly distributed over the usable operating range. The corresponding control voltages, computed through the inverse interpolation function, were applied to the VOA, and the resulting attenuations have been experimentally measured. Figure 3.18 compares the measured attenuation values with the target ones for $\lambda = 1544.53$ nm. The linear regression performed on the experimental data yields an R-squared exceeding 0.9999. A small, negligible offset of -0.24 dB can also be observed. Overall, these outcomes confirm the effectiveness of the adopted calibration procedure for accurately reproducing arbitrary attenuation profiles. Analogous results characterize the other wavelength.

Finally, the temporal response of the OTG has been characterized by measuring the frequency response of the VOA. To this aim, a CW optical signal has been launched into the device while sinusoidal control voltages with increasing frequency have been applied through the AWG. The resulting optical signal has been detected by a high-speed photodiode and analyzed using a spectrum analyzer. The measured 3-dB bandwidth is approximately 500 Hz, lower than the 1-kHz one of the Thorlabs' VOA.

Although this bandwidth is sufficient to reproduce most of the atmospheric fading dynamics, it was possible to verify that the finite frequency response of the VOA introduces a slight smoothing of rapidly varying attenuation profiles,

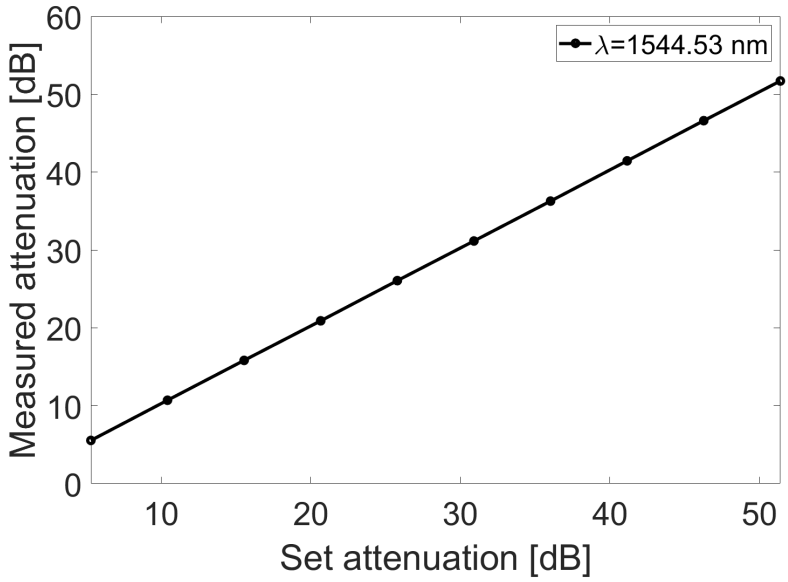


Figure 3.18 – VOA measured attenuation as a function of set attenuation after calibration

especially for deeper attenuation values. Since the latter are essential to faithfully evaluate the link performance, a predistortion stage has been performed for each reproduced fading time series. As will be shown in Section 3.4.2, the control voltage sequences have been pre-equalized by empirically adjusting the AWG offset and peak-to-peak settings, allowing the measured VOA output power to accurately reproduce the PDF of the synthesized fading time series.

3.4 Experimental results

This section presents the experimental results obtained from two independent measurement campaigns carried out using the testbeds described in the previous section. Although both platforms rely on the same principle of fading emulation, they target different communication scenarios and complementary objectives.

The experimental measurements performed at Poliba focus on the characterization of commercial 10GbE transceivers operating with IM/DD, assessing their performance under emulated turbulence- and pointing-jitter-induced fading representative of downlink OFLs from LEO satellites. Conversely, the measurement

campaign conducted at the TeCIP extends the analysis to OTN equipment, including both IM/DD and coherent commercial transceivers. In this case, the effect of turbulence-induced fading on different transceivers' architectures has been assessed.

In the following, the adopted experimental procedures are described and the obtained results discussed, highlighting the impact of the emulated channel impairments on the performance of the considered communication systems.

3.4.1 Poliba experimental campaigns

The experimental campaign carried out using the testbed developed at Poliba was organized into three successive phases of increasing complexity. The first experiments were conceived as a preliminary validation of the OTG and investigated the impact of turbulence-induced fading on basic network connectivity by transmitting ICMP Echo request packets under representative downlink LEO OFL conditions at different satellite elevation angles.

Building upon these initial tests, a second measurement campaign employed continuous UDP traffic generated by the iPerf2 tool to evaluate the frame loss performance of commercial 10 Gigabit Ethernet transceivers. Both fixed-elevation scenarios and complete LEO satellite passes were emulated, allowing the dynamic evolution of turbulence conditions during the satellite transit to be reproduced.

Finally, the experimental investigation was extended to account for the combined effect of atmospheric turbulence and pointing jitter. By simultaneously emulating both impairments, the last set of experiments provides a more realistic assessment of the performance achievable by commercial optical transceivers in practical OFL scenarios.

3.4.1.1 Preliminary results

The first experimental campaign was conceived as a preliminary validation of the developed testbed and of the proposed fading synthesis methodology. The objective was to verify whether turbulence-induced fading alone is sufficient to affect the

operation of commercial optical transceivers designed for terrestrial fiber-optic networks and to provide an initial assessment of their behavior under representative OFL conditions.

To this end, ICMP Echo Request packets were periodically transmitted from the server PC to the client one, while the synthesized fading profiles were applied only to the opposite communication direction, namely from the client PC to the server one. Consequently, all Echo Request packets reached the destination without impairment, whereas only the corresponding Echo Reply packets experienced the emulated channel fading. This configuration ensured that any packet loss was exclusively caused by the imposed optical attenuation rather than by the failure of the request packets to reach the remote host. Packet transmission was performed by means of the nping utility included in the Network mapper (Nmap) suite, configured to generate one Echo Request every 5 ms, while the received traffic was captured and analyzed using Wireshark on the server PC to evaluate both the packet loss ratio and the response time jitter.

Before executing the fading experiments, the receiver sensitivity of the commercial transceiver connected to the server PC was experimentally determined. For this purpose, an increasing constant attenuation was progressively introduced by the VOA while transmitting 10 000 Echo Request packets for each attenuation level. The applied attenuation was increased in 1-dB steps until Echo Reply packets losses were experienced. As shown in Fig. 3.19, packet losses first appeared for attenuation values higher than 15 dB, whereas communication was completely interrupted for attenuations equal to or greater than 18 dB. Therefore, the 15-dB value was assumed as the attenuation corresponding to the receiver sensitivity and subsequently used to convert the normalized received power generated by the fading synthesis algorithm into equivalent attenuation time series. Following the convention adopted during the KIODO experimental campaign, the fading threshold, corresponding to a received power 3 dB below the mean level, was associated with an attenuation of 18 dB.

The generated fading profiles reproduced the atmospheric conditions measured during the KT06-04 trial of the KIODO campaign [177]. This choice allowed the comparison between synthesized profiles and measured ones, thus validating the turbulence-related generation algorithm. Four representative satellite elevation

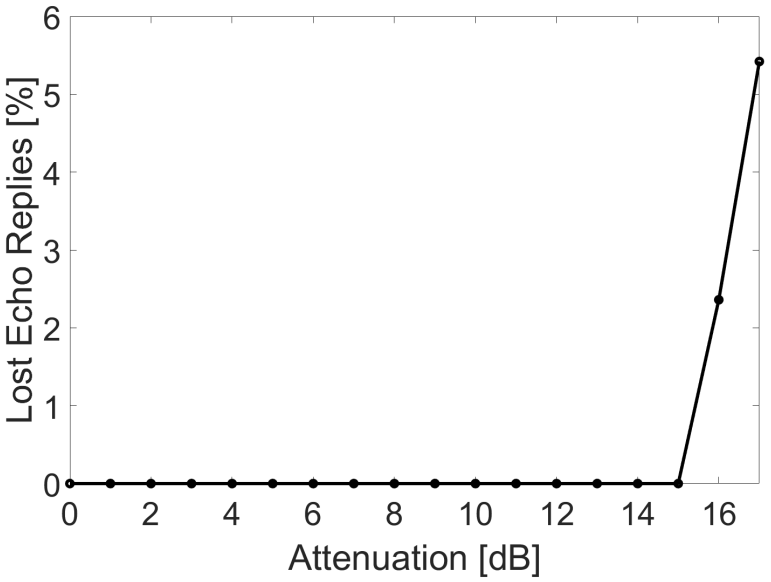


Figure 3.19 – Percentage of Echo Replies lost packets as a function of the attenuation imposed on the link branch connecting the client PC to the server PC

angles have been considered, namely 10°, 15°, 20°, and 25°, corresponding to measured power scintillation indices of 0.22, 0.10, 0.08, and 0.04, respectively, and auto-correlation times of 1.00 ms, 1.02 ms, 0.93 ms, and 0.79 ms [177]. Since the considered link benefited from aperture averaging, the cutoff frequencies and roll-off slopes of the low-pass filters employed for the time series synthesis have been determined according to the methodology described in Section 3.2.1, yielding cutoff frequencies close to 241 Hz, 237.5 Hz, 243 Hz, and 301.4 Hz, for increasing elevations.

Figure 3.20a shows the first 120 seconds of the generated time series of normalized irradiance. As expected, the lower elevation angles are characterized by significantly larger fluctuations. The corresponding histograms, shown in Fig. 3.20b together with the theoretical lognormal distributions, closely follow the theoretical curves and closely match the measured distributions reported for the original KIODO measurements (see Fig. 3.21a). Likewise, the signals' autocorrelation functions reported in Fig. 3.20c accurately reproduce the target coherence times while matching the overall measured trend shown in Fig. 3.21b, demonstrating that the synthesized fading sequences correctly emulate not only the statistical

distribution but also the temporal evolution of atmospheric scintillation.

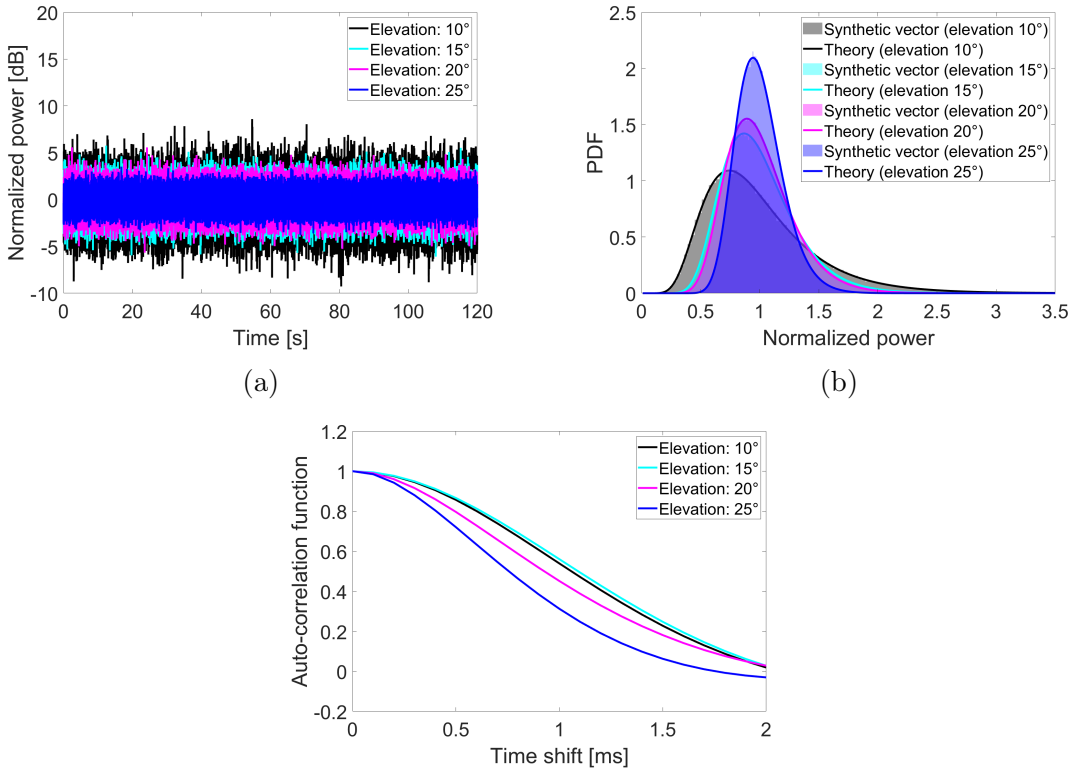
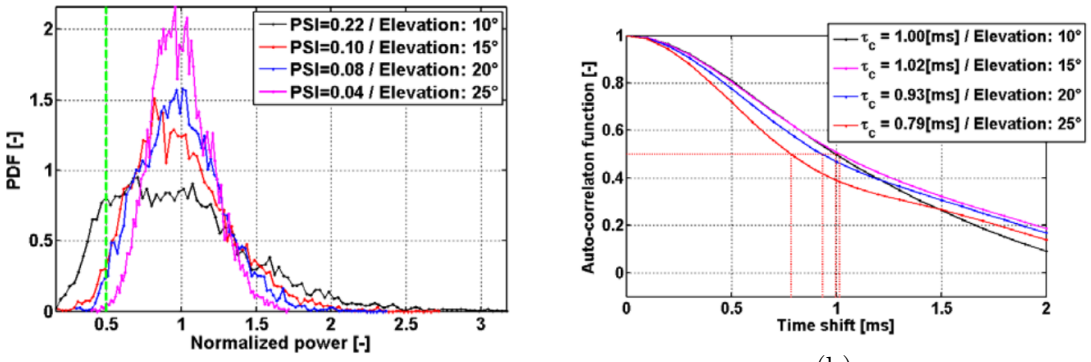


Figure 3.20 – (a) Generated scintillation-affected time series of receiver power for the LEO downlink OFL as a function of time, together with (b) their histograms and theoretical lognormal PDF, and (c) their auto-correlation functions

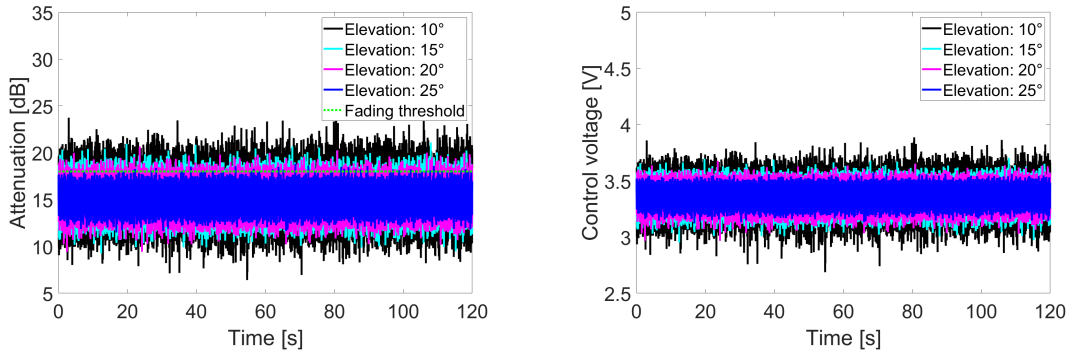
In order to convert the power time series of Fig. 3.20a to attenuation time series, the -3 dB fading threshold experienced during the KIODO trials, and reported in Fig. 3.21a was taken into account. This fading threshold implies that, during the trial, the mean received power was 3 dB above the receiver sensitivity. To reproduce this condition, the power time series were converted into attenuation values by associating a -3 dB value of normalized power to a 18 dB attenuation value, i.e., 3 dB below the previously measured transceiver sensitivity. The obtained attenuation time series are shown in Fig. 3.22a, while the related control voltage time series are plotted in Fig. 3.22b. The latter curves were obtained by exploiting the inverse function of the VOA characteristic reported in Section



(a) (b)

Figure 3.21 – (a) Probability density functions and (b) autocorrelation functions for selected elevations in KT06-04. In (a), the bright green line marks the -3 dB threshold with respect to unity mean. In (b), the dashed red lines denote the 50% roll-offs [177]

3.3.1.1.

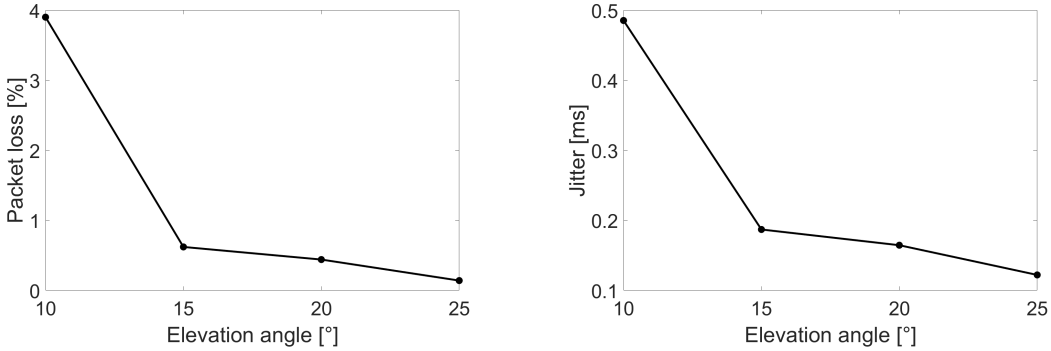


(a) (b)

Figure 3.22 – Generated scintillation-affected time series of (a) attenuation and (b) control voltage for the LEO downlink OFL as a function of time. In (a), the green line marks the fading threshold

Finally, the generated control-voltage profiles were applied to the OTG, and communication tests were performed by transmitting 10 000 ICMP Echo Request packets for each emulated elevation angles. The measured packet loss ratios and response time jitters are shown in Figs. 3.23a and 3.23, respectively. Both metrics clearly improve as the satellite elevation increases. The lower elevation angle pro-

duces deeper and longer fading events, owing to its higher scintillation index and longer correlation time, which substantially increase the probability of fading as well as the fade lengths. Conversely, the weaker turbulence associated with higher elevations results in fewer packet losses and reduced response time fluctuations.



(a) (b)

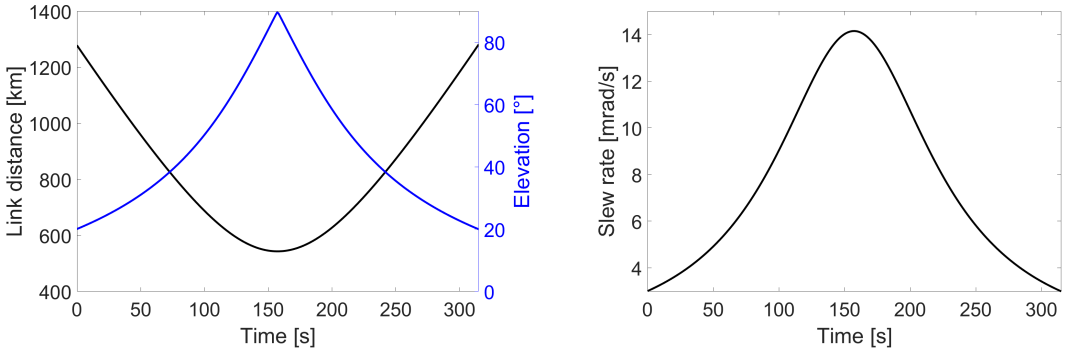
Figure 3.23 – (a) Percentage of Echo Replies packet loss and (b) response time jitter as a function of the elevation angle for the emulated 10 GbE LEO downlink OFL

Although these preliminary experiments involved only simple ICMP traffic, they clearly demonstrate the sensitivity of commercial fiber-optic transceivers to turbulence-induced fading. The obtained results also confirm the capability of the developed laboratory emulator to faithfully reproduce realistic OFL conditions, motivating the more comprehensive performance evaluation presented in the following sections.

3.4.1.2 Experimental emulation of a turbulence-affected downlink LEO OFL

After the preliminary validation, a more comprehensive experimental campaign was carried out to assess the performance of the IM/DD 10GbE transceivers under realistic OFL conditions. Unlike the previous tests, which relied on low-rate ICMP traffic, these experiments employed continuous, 1 Gbit/s UDP traffic generated by the iPerf2 tool, allowing the impact of turbulence-induced fading on commercial 10GbE transceivers to be evaluated under conditions that more closely resemble practical data transmission.

The reference scenario consists of a downlink OFL between a LEO satellite orbiting at an altitude of 550 km and an OGS located 10 m above mean sea level. A circular orbit with an inclination of 99° was considered and propagated in Matlab through a J_2 propagator with a sampling interval of 1 s. The orbital parameters and the ground station location were selected so that the satellite performs a zenith overflight, allowing the communication link to span elevation angles from 20° up to 90°. Lower elevation angles have not been considered because OFLs are generally not operated below this threshold due to the severe propagation conditions. The evolution of the link distance and elevation angle during the satellite pass is reported in Fig. 3.24a. As expected, the propagation distance decreases as the satellite approaches the zenith, reaching its minimum value at the highest elevation angle.



(a) (b)

Figure 3.24 – (a) Link distance (black curve), elevation angle (blue curve) and (b) slew rate as a function of time for the emulated downlink LEO OFL

Besides the link geometry, the apparent wind caused by the satellite slewing relative to the OGS also plays a fundamental role in the temporal evolution of atmospheric turbulence [127]. Under Taylor's frozen turbulence hypothesis, the turbulent eddies are assumed to be transported across the optical beam by the combined action of the natural transverse wind and the apparent wind generated by the tracking motion of the optical terminal. Consequently, the apparent satellite slew rate directly affects the scintillation temporal statistics.

The slew rate can be computed from the satellite azimuth ϕ and elevation ζ angles evaluated at consecutive time instants. Let

$$\vec{p} = \begin{bmatrix} \cos\zeta \sin\phi \\ \cos\zeta \cos\phi \\ \sin\zeta \end{bmatrix} \tag{3.28}$$

be the unit vector pointing from the OGS towards the satellite. Given two pointing vectors $\vec{v}$ and $\vec{w}$, associated with consecutive satellite positions, the angular displacement between the corresponding LoSs, θ [rad], can be evaluated as

$$\theta = 2 \arctan \frac{d}{\sqrt{[1 + (1 + d)][(1 - d) + 1]}} \tag{3.29}$$

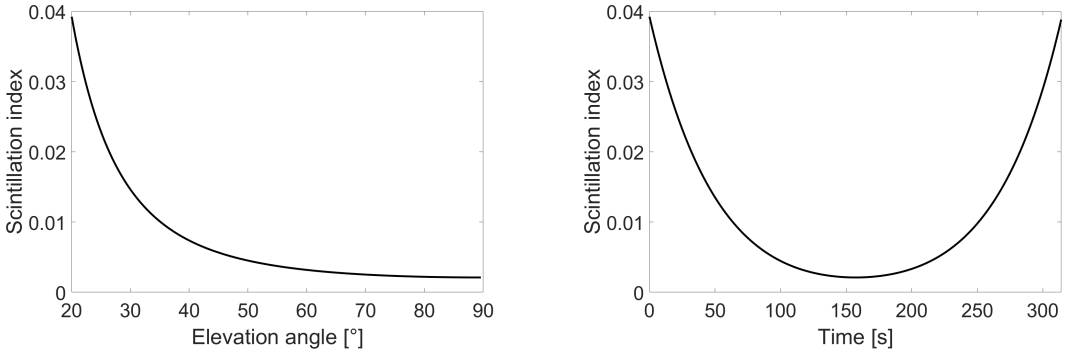
where $d = \|\vec{v} - \vec{w}\| = \sqrt{2 - 2x}$ and $x = \vec{v} \cdot \vec{w}$. Dividing the angular displacement by the corresponding time interval provides the average slew rate between two consecutive satellite positions.

The resulting slew rate profile, for the above scenario, is shown in Fig. 3.24b. It reaches its maximum close to the zenith, where the apparent satellite motion is fastest, and progressively decreases towards lower elevation angles.

The optical link is assumed to operate at a wavelength of 1550 nm, with a transmitting telescope diameter of 15 cm, and a receiving aperture of 50 cm. The atmospheric channel is modeled using the link budget tool presented in Chapter 2. The modified HV turbulence profile is assumed, considering strong turbulence characterized by a ground-level refractive-index structure parameter $A = 1.7 \cdot 10^{-13}$ $\mathrm{m}^{-2/3}$ and a ground wind speed of 8 m/s.

The corresponding power scintillation index as a function of both elevation angle and transmission time is reported in Figs. 3.25a and 3.25b, respectively. Throughout the entire satellite pass, the Rytov variance remains below unity. Consequently, the Rytov theory is adopted. Moreover, the receiver aperture is sufficiently large to provide significant aperture averaging, thus justifying the adoption of the lognormal model for the received power statistics.

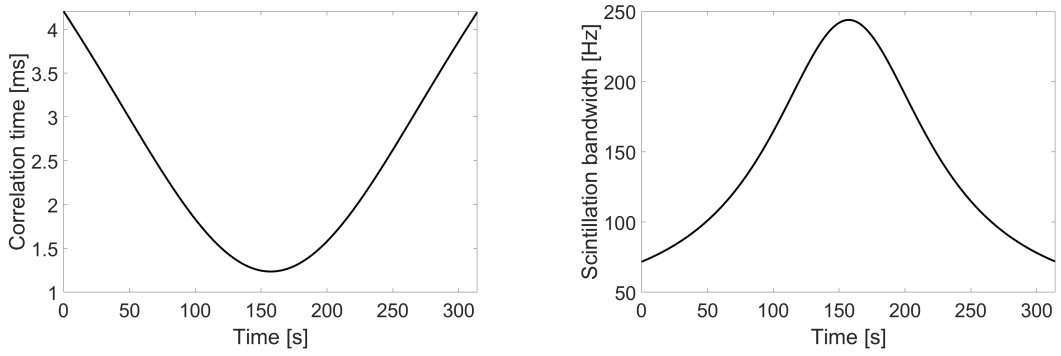
The temporal characteristics of scintillation was obtained from the analytical models presented in Section 3.2.1. Figures 3.26a and 3.26b show the resulting scintillation correlation time and bandwidth, respectively, throughout the satellite pass. As expected, longer correlation times are observed at low elevations, where



(a) (b)

Figure 3.25 – Scintillation index as a function of (a) elevation angle and (b) time for the emulated downlink LEO OFL

the apparent satellite motion is slower. Conversely, near the zenith the higher slew rate increases the apparent transverse wind, leading to shorter coherence times and larger scintillation bandwidths.



(a) (b)

Figure 3.26 – (a) Scintillation correlation time and (b) bandwidth as a function of time for the emulated downlink LEO OFL

The computed statistical parameters were then used to synthesize turbulence -induced fading time series. First, independent fading sequences representative of fixed satellite elevations ranging between 20° and 90°, with a 10° spacing, were generated. Each realization has a duration of 300 s to ensure statistically significant measurements. Figure 3.27a shows the generated normalized received-power

time series. As expected, lower elevation angles produce significantly larger irradiance fluctuations owing to the stronger turbulence encountered along the longer atmospheric path.

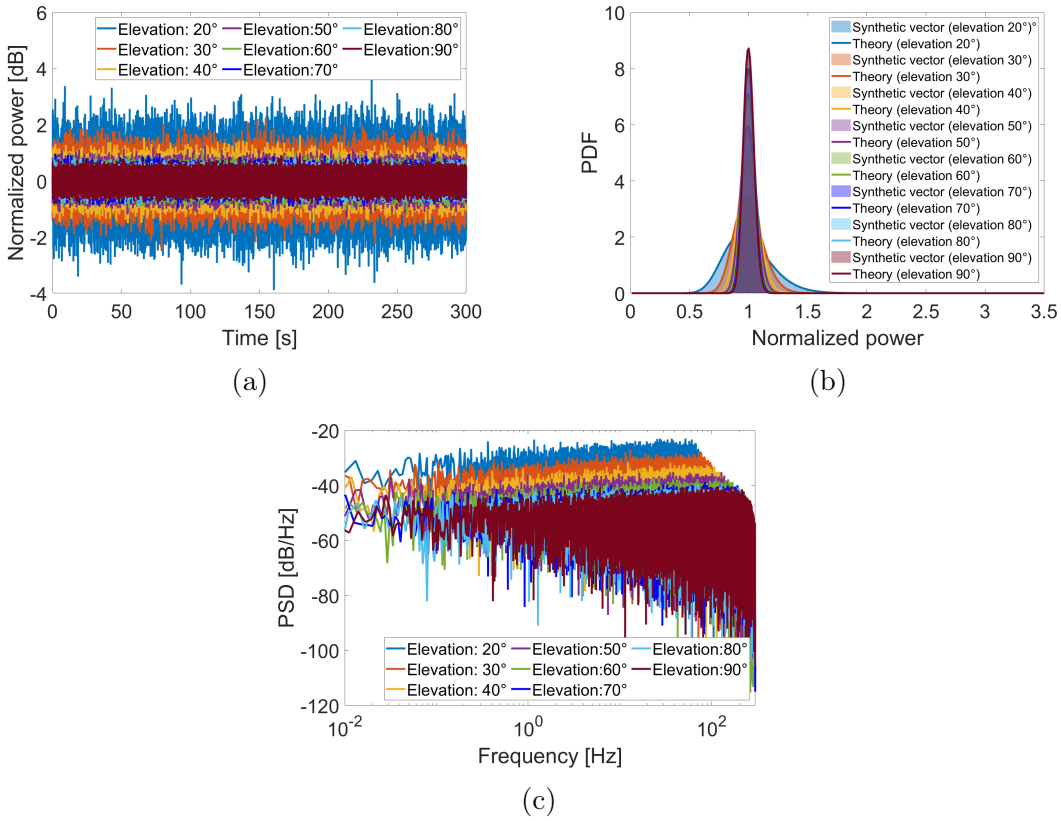


Figure 3.27 – (a) Generated scintillation-affected time series of normalized received power as a function of time for the emulated LEO downlink OFL, together with (b) their histograms and theoretical lognormal PDFs, and (c) their PSDs

The corresponding histograms, reported in Fig. 3.27b, accurately reproduce the theoretical lognormal PDFs associated with the computed scintillation indices. Likewise, the estimated PSDs, shown in Fig. 3.27c, exhibit the expected low-pass behavior, with cutoff frequencies matching the analytically predicted scintillation bandwidths. These results further confirm the capability of the adopted synthesis algorithm to reproduce both the statistical distribution and the temporal evolution of turbulence-induced fading.

In addition to the fixed-elevation scenarios, a dynamic fading sequence reproducing the entire satellite pass was generated. To this end, the atmospheric parameters have been updated every second according to the instantaneous satellite position, and the corresponding fading segments have been concatenated to produce a continuous attenuation profile covering the whole communication duration of approximately 315 s. The resulting time series is shown in Fig. 3.28. In this representation, the mean received power was intentionally kept constant by assuming ideal automatic gain control at the transmitter so that only the temporal variation of scintillation strength is reflected in the synthesized fading profile.

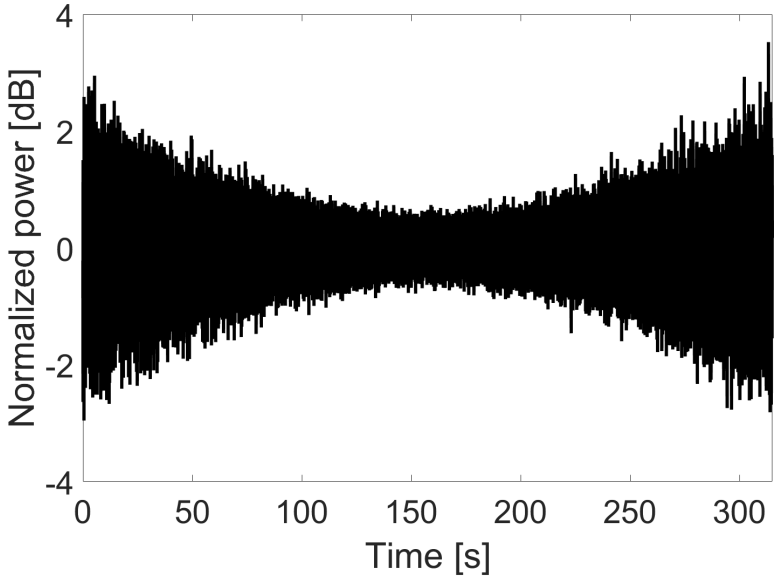
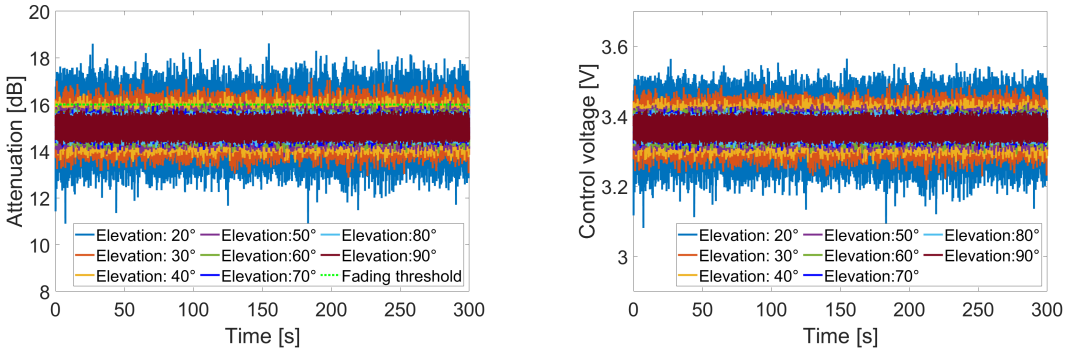


Figure 3.28 – Generated time series of normalized received power as a function of time for the entire pass of the emulated LEO downlink OFL

With respect to the tests of Section 3.4.1.1, the sensitivity was re-measured due to some changes in the testbed connections and was found to correspond to a VOA-induced attenuation of 16 dB.

The synthesized normalized power sequences were been converted into attenuation time series by considering the experimentally determined receiver sensitivity. Specifically, the normalized mean received power has been associated with an attenuation equal to the receiver sensitivity reduced by the selected link margin. The corresponding attenuation profiles were finally translated into VOA control

voltages through the calibrated inverse transfer function. For instance, Fig. 3.29a shows the attenuation time series corresponding to different elevations as a function of time, assuming a link margin of 1 dB. Instead, Fig. 3.29b depicts the corresponding VOA control voltages. The same approach was used for the time series of Fig. 3.28.



(a) (b)

Figure 3.29 – Generated time series of (a) attenuation and (b) control voltage as a function of time for the emulated LEO downlink OFL. In (a), the green line marks the fading threshold

Measurements were first performed for the fixed-elevation scenarios considering three different link margins, namely 0 dB, 0.5 dB, and 1 dB. The resulting FERs are reported in Fig. 3.30. As expected, the transmission performance progressively deteriorates as the satellite elevation decreases owing to the stronger scintillation experienced at lower elevations. Furthermore, increasing the link margin significantly reduces the frame loss probability, demonstrating the importance of adequate power margins in maintaining reliable OFLs.

Finally, the experiments were repeated using the fading profile representative of the complete satellite pass. Figure 3.31a shows the measured FER as a function of the link margin, while Fig. 3.31b plots the corresponding outage probability predicted by the synthesized fading sequence. The latter is computed as the fraction of time in which the received power is below the receiver sensitivity. Both quantities decrease monotonically as the available link margin increases, confirming the direct relationship between channel outages and frame losses.

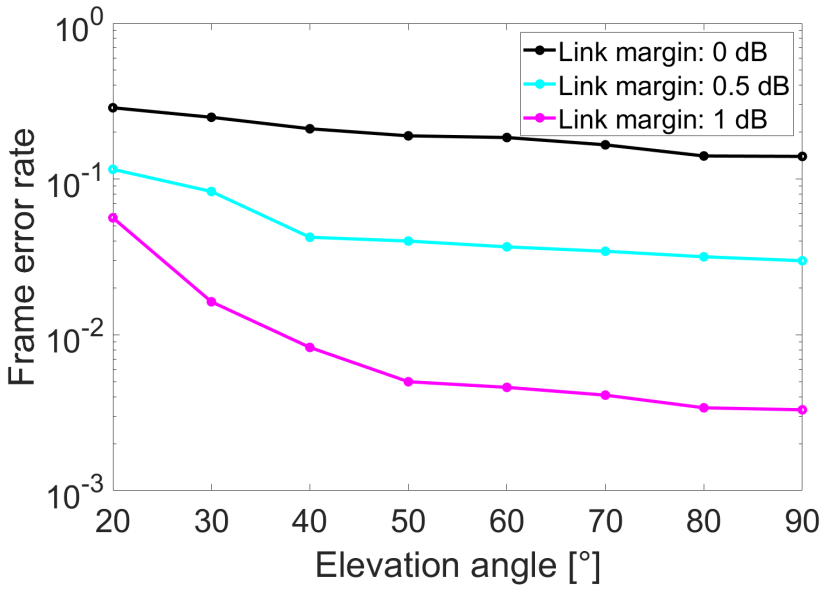
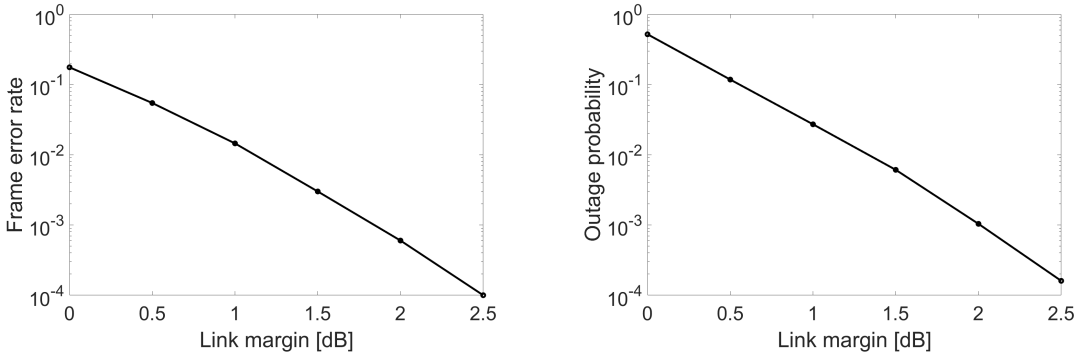


Figure 3.30 – Frame error rate as a function of the elevation angle for the emulated 10GbE LEO downlink OFL

It is worth observing that, even for the largest investigated link margin, the transmission remains affected by non-negligible frame losses. These results clearly indicate that commercial fiber-optic transceivers are unable to cope with the millisecond-scale fading induced by atmospheric turbulence. Consequently, additional mitigation techniques would be required to achieve higher reliability levels where necessary.

3.4.1.3 Experimental emulation of a turbulence- and pointing jitter-affected downlink LEO OFL

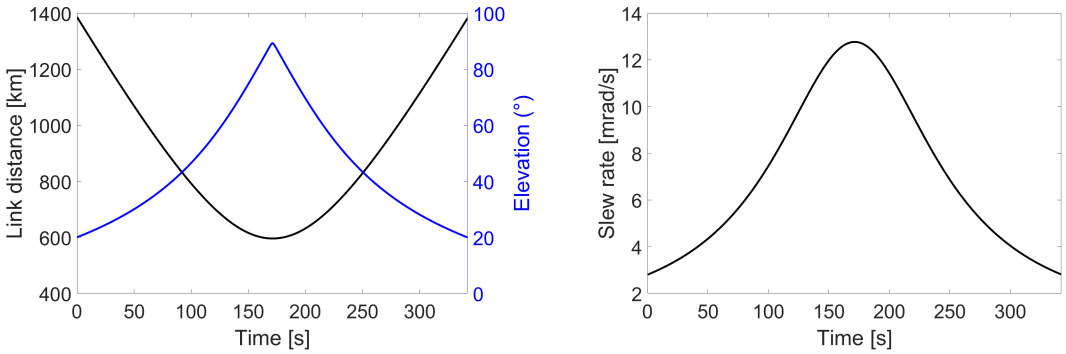
The final experimental campaign extends the previous investigation by considering the simultaneous effects of atmospheric turbulence and satellite's microvibrations, thereby providing a more comprehensive representation of an OFL. The emulated scenario consists of a downlink transmission from a LEO satellite at an altitude of 600 km to an OGS located at an altitude of 10 m. The satellite orbit was propagated in Matlab using the Simplified General Perturbations 4 (SGP4) model, while the orbital parameters and OGS location were selected to obtain a zenith overpass with elevation angles ranging from 20° to 90°, as for the previous scenario. Figure



(a) (b)

Figure 3.31 – (a) Frame error rate and (b) outage probability as a function of the link margin for the emulated 10GbE LEO downlink OFL

3.32a reports the corresponding evolution of the link elevation and propagation distance throughout the satellite pass, whereas Fig. 3.32b shows the associated angular slew rate.

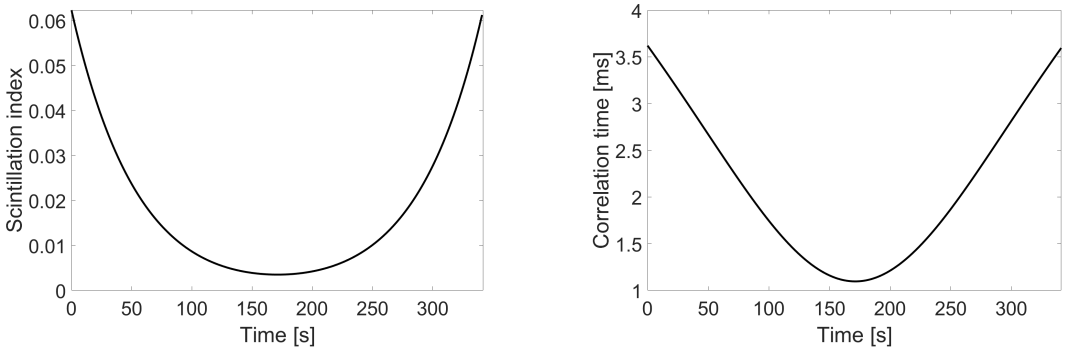


(a) (b)

Figure 3.32 – (a) Link distance (black curve), elevation angle (blue curve) and (b) slew rate as a function of time for the emulated downlink LEO OFL

As for the previous scenario, atmospheric turbulence was modeled at the reference wavelength of 1550 nm by using the modified HV model, with $A = 1.7 \cdot 10^{-13}$ $\mathrm{m}^{-2/3}$ and $w = 8$ m/s. A receiving telescope diameter of 40 cm was considered, so that aperture averaging significantly mitigates irradiance fluctuations. The resulting scintillation index, shown in Fig. 3.33a, remains relatively low throughout the satellite pass and reaches its maximum values at low elevation angles.

Figure 3.33b illustrates the scintillation correlation time, which decreases as the satellite approaches the zenith. This behavior directly follows the increase in angular slew rate, whose contribution to the apparent transverse wind accelerates the evolution of atmospheric turbulence along the propagation path.



(a) (b)

Figure 3.33 – (a) Scintillation index and (b) correlation time as a function of time for the emulated downlink LEO OFL

The computed scintillation index and correlation time were employed as inputs to the time series generation algorithm. The synthesized normalized received-power time series is shown in Fig. 3.34 for the entire satellite pass, where larger fluctuations can be observed at the beginning and end of the pass, consistently with the higher scintillation levels experienced at lower elevations.

Transmitter pointing jitter was been included in the channel model. Nine independent jitter conditions were considered by varying the rms pointing error from 1 μrad to 3 μrad in steps of 0.25 μrad, a range representative of residual tracking errors reported for optical satellite terminals [227]. A transmitter aperture diameter of 15 cm is assumed and, for each pointing-error value, a fading time series has been generated according to the methodology described in Section 3.2.2. Figure 3.35a presents the resulting normalized received-power time series, while Fig. 3.35b compares their histograms with the corresponding theoretical beta distributions. The agreement between simulated and theoretical PDFs confirms the validity of the implemented model. The corresponding PSDs, reported in Fig. 3.35c, exhibit the expected low-pass behavior. As anticipated, increasing

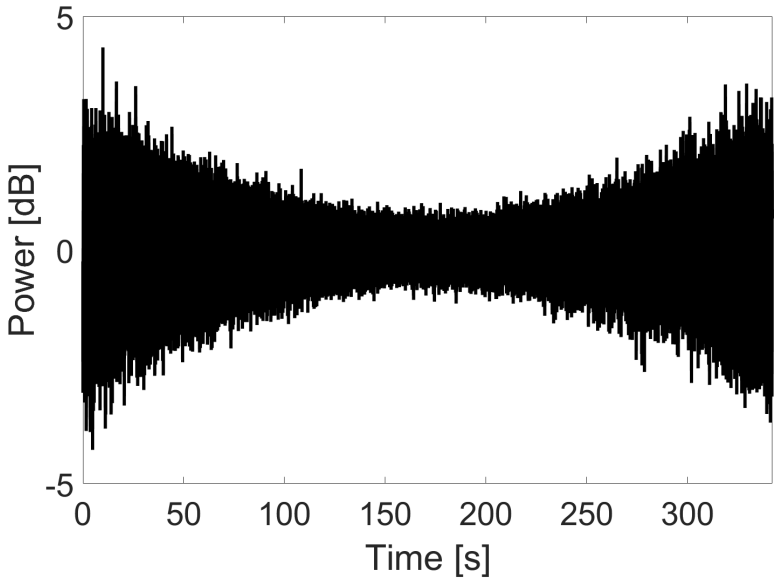


Figure 3.34 – Generated time series of normalized received power as a function of time for the entire pass of the emulated LEO downlink OFL

pointing jitter produces progressively deeper fades together with a higher average attenuation.

The overall channel was finally obtained by combining the turbulence- and jitter-induced fading processes. The resulting fading profiles, reported in Fig. 3.36, reproduce the combined temporal dynamics expected in realistic OFLs, where turbulence-induced irradiance fluctuations are further aggravated by random beam misalignments.

Experimental communication tests were carried out for each combined fading realization using the Poliba testbed. Each experiment reproduced the entire satellite pass, resulting in a transmission duration of approximately 342 s. UDP traffic was generated at 1 Gbit/s by means of iPerf2, corresponding to the transmission of approximately $2.9 \cdot 10^7$ Ethernet frames during each measurement.

Before applying the synthesized fading sequences, the normalized received-power traces were converted into attenuation profiles. As in the previous campaign, the receiver sensitivity of the commercial transceivers corresponds to 16 dB of attenuation. Assuming a link margin of 1 dB, the attenuation time series have been obtained by associating the normalized received power of 0 dB with an attenuation

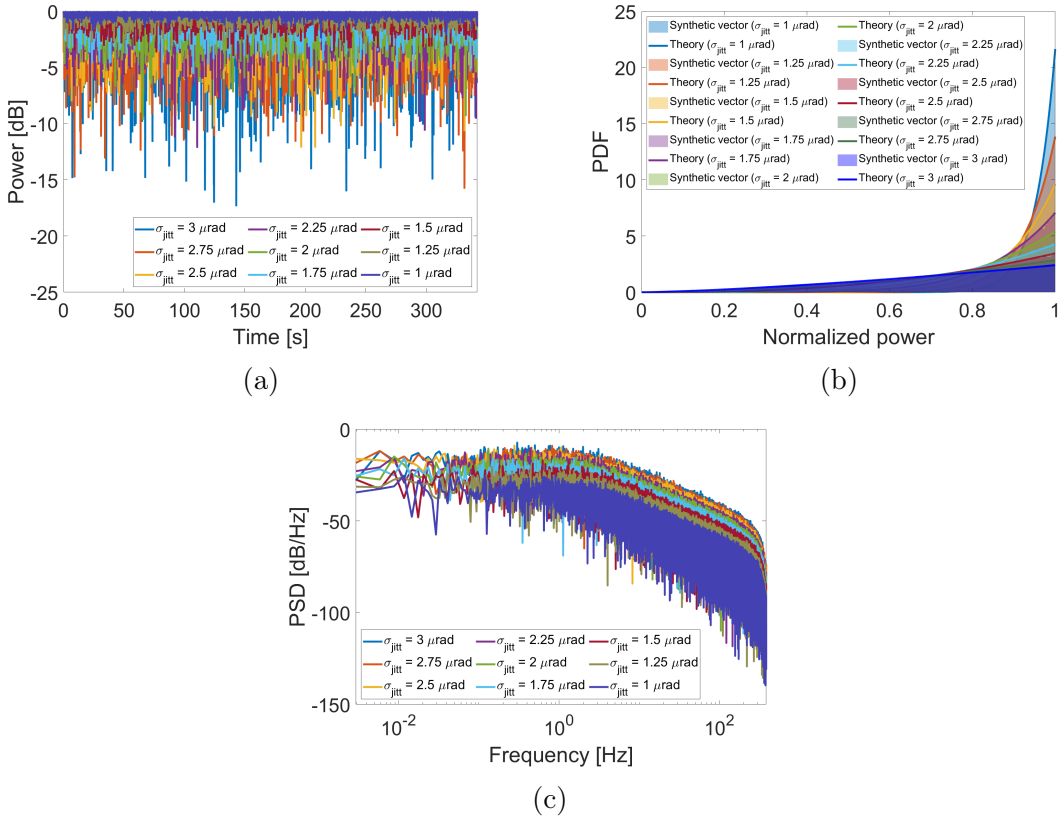


Figure 3.35 – (a) Generated jitter-affected time series of normalized received power as a function of time for the emulated LEO downlink OFL, together with (b) their histograms and theoretical beta PDFs, and (c) their PSDs

of 15 dB. The corresponding control-voltage waveforms were then computed using the calibrated VOA inverse transfer function.

Figure 3.37 reports the measured FER as a function of the rms pointing jitter. Even in the absence of pointing errors, turbulence alone produces a non-negligible frame error rate of $2.3 \cdot 10^{-2}$, confirming that atmospheric scintillation alone can significantly impair commercial fiber-optic transceivers. As the pointing jitter increases, the FER rapidly deteriorates, reaching approximately $6.6{\cdot}10^{-1}$ for $\sigma_{jitt} = 3$ μrad. This trend reflects both the increase in the average pointing loss and the greater occurrence of deep fading events caused by random beam misalignment.

These results clearly demonstrate that residual pointing errors substantially amplify the performance degradation already introduced by atmospheric turbu-

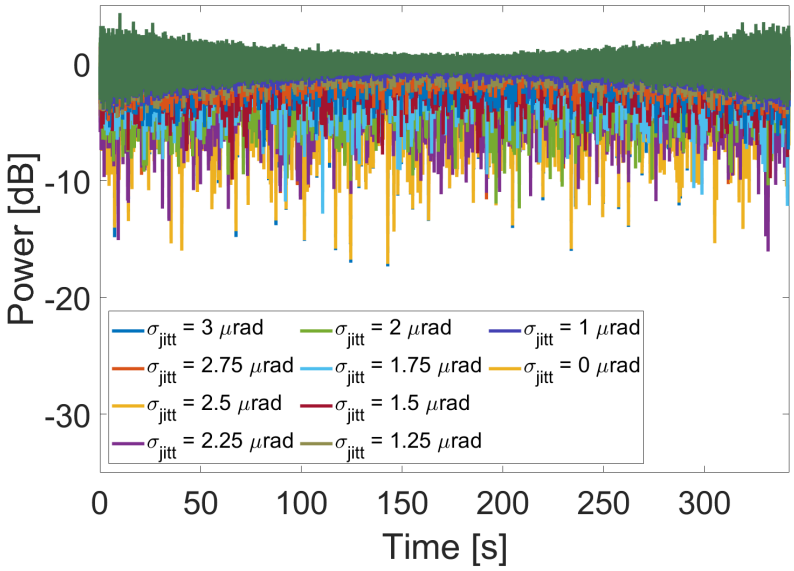


Figure 3.36 – Generated time series of normalized received power as a function of time for the entire pass of the emulated LEO downlink OFL

lence. Although increasing the link margin could partially mitigate this effect, practical limitations on transmitter optical power prevent arbitrarily large margins from being adopted. Consequently, achieving the reliability required by future high-capacity OFLs will likely require the introduction of dedicated countermeasures.

3.4.2 TeCIP experimental campaign

The experimental campaign carried out at the TeCIP facilities aimed at comparing the resilience of commercial transceivers employing IM/DD and coherent transmission techniques when operating over OFLs affected by atmospheric scintillation. Unlike the experiments presented for the Poliba testbed, which focused on Ethernet optical transceivers, these measurements investigated OTN systems capable of operating at 10 Gb/s and 100 Gb/s.

As a preliminary step, the sensitivity of both links (denoted as 10G and 100G, respectively) was experimentally characterized in order to determine the minimum optical power required for error-free operation after FEC. Specifically, the

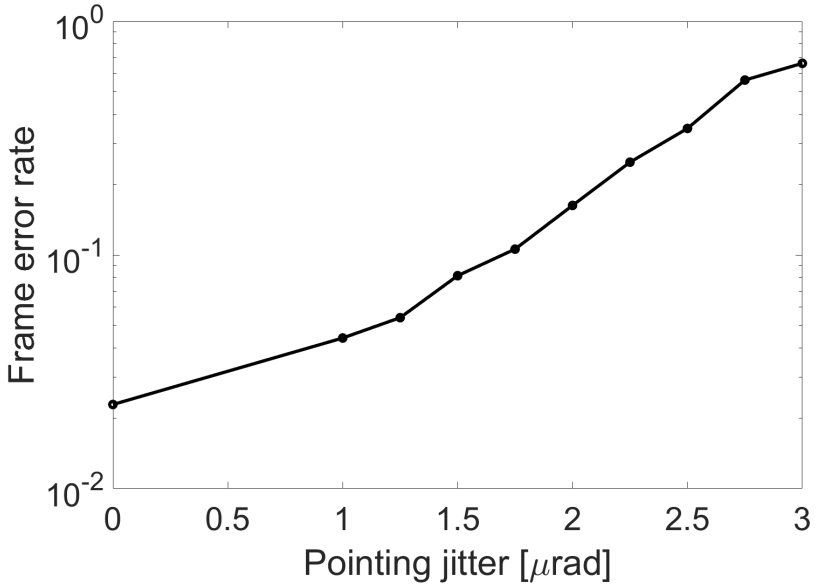


Figure 3.37 – Frame error rate as a function of the rms pointing jitter for the emulated 10GbE LEO downlink OFL

10G transceiver employs an IM/DD architecture based on OOK modulation together with RS coding, whereas the 100G coherent transceiver adopts DP-QPSK modulation and LDPC coding. Owing to the different transmission formats and FEC schemes, the two receivers exhibit different sensitivity thresholds, i.e., 10^{-3} for the 10G receiver and 10^{-2} for the 100G one.

For each link, the optical power at the input of the pre-amplifier was progressively reduced by setting increasing attenuations through the VOA. For each attenuation value, the pre-FEC BER was monitored through the Spirent traffic analyzer. Figure 3.38 reports the measured BER as a function of the optical power at the EDFA input. The experimental results indicate receiver sensitivities of -43.5 dBm for the 10G transceiver and -40.7 dBm for the 100G one. The corresponding OSNRs, measured at the EDFA output by means of the OSA, are 11.4 dB and 14.2 dB, respectively. Consequently, the coherent receiver requires about 2.8 dB more received optical power than the IM/DD one to achieve error-free communication.

To perform the OSNR measurement, the method described in the IEC 61280-2-9 standard was adopted [228]. Specifically, the OSNR was measured over a reference optical bandwidth of 0.1 nm.

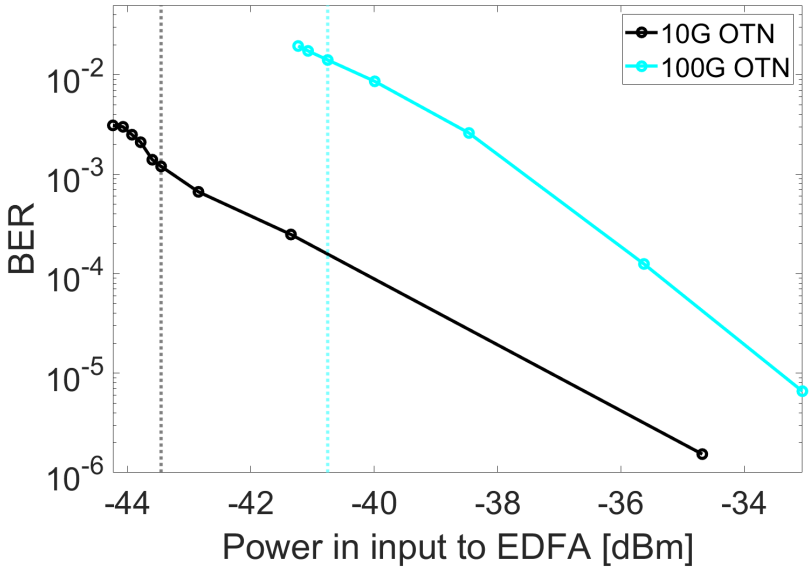
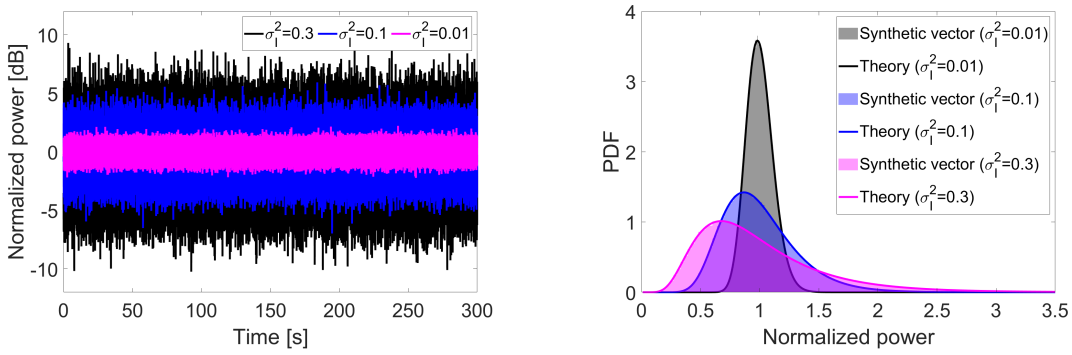


Figure 3.38 – Pre-FEC BER as a function of the EDFA input power for the 10G (black curve) and 100G (cyan curve) links. The dashed lines mark the transceivers' sensitivity thresholds

The communication experiments employed synthetic attenuation time series representative of atmospheric scintillation affecting downlink OFLs from LEO satellites. Three turbulence conditions have been considered, corresponding to scintillation indices of 0.01, 0.10, and 0.30, spanning weak, moderate, and relatively strong aperture-averaged turbulence conditions. For example, the value $\sigma_I^2 = 0.01$ could be derived by assuming a LEO satellite at 800 km transmitting at 1550 nm through a 15-cm telescope towards an OGS located at an altitude of 540 m and deploying an aperture of 50 cm.

During this campaign, a simplified methodology was used to generate fading time series. Specifically, each received-power sequence was randomly generated by assuming a lognormal PDF, and consisted of approximately $3 \cdot 10^5$ samples. The fading sequences have been sampled at a 1-ms time interval, representative of typical Greenwood time constant values, resulting in a total time series duration of approximately five minutes. The three generated time series of normalized receiver power are shown in Fig. 3.39a, while their histograms together with the theoretical lognormal curves are plotted in Fig. 3.39b.



(a) (b)

Figure 3.39 – (a) Generated scintillation-affected time series of normalized received power as a function of time, together with (b) their histograms and theoretical lognormal PDFs

The generated normalized received-power time series have been converted into attenuation sequences based on the receiver sensitivities and analyzed link margin values. Subsequently, the corresponding control-voltage waveforms have been computed by exploiting the calibrated inverse VOA characteristic derived in Section 3.3.2.1 and uploaded to the AWG.

As anticipated in Section 3.3.2.1, because of the finite bandwidth of the VOA, the generated optical power initially differed from the desired statistical distribution. Consequently, the control-voltage waveforms have been empirically predistorted by adjusting their offset and amplitude until the histogram of the measured optical power at the VOA output matched the target lognormal distribution. To this end, the optical signal at the VOA output was monitored by means of a high-speed photodiode connected to a digital oscilloscope, allowing direct comparison between the synthesized and measured fading statistics. As an example, Fig. 3.40 show the achieved match between the histograms of the measured and generated time series for $\sigma_I^2 = 0.01$.

The communication measurements were performed separately for the 10G and 100G links using the experimental configurations described in Section 3.3.2. During each experiment, the Spirent traffic generator continuously transmitted Ethernet frames at a constant bit rate of 800 Mb/s for a total duration of seven minutes, corresponding to approximately $4 \cdot 10^8$ transmitted frames.

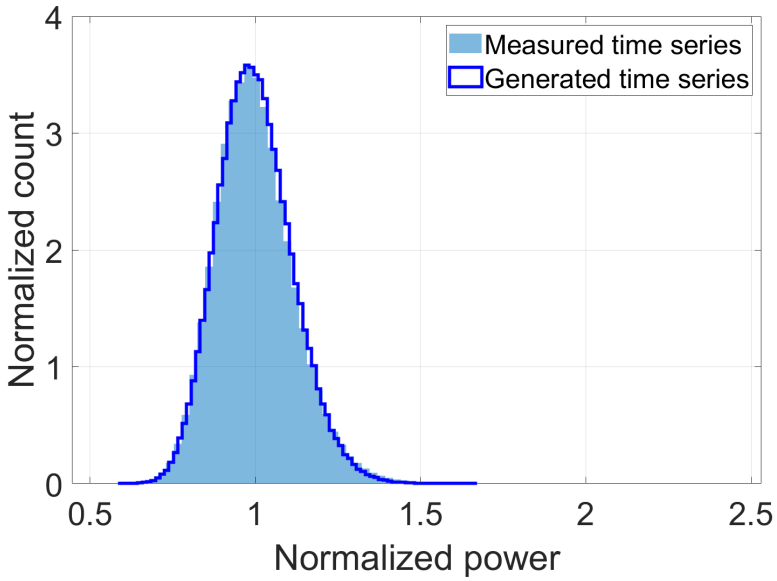


Figure 3.40 – Histograms of the generated and measured time series at $\sigma_I^2 = 0.01$

During the first five minutes of each measurement, one of the three synthesized fading time series was applied through the OGS. During the remaining two minutes, the fading-induced attenuation was removed in order to let the link recover after prolonged fading events.

For each scintillation index, several measurements were performed by varying the link margin, defined as the difference between the average received optical power and the receiver sensitivity. To this end, the average received power was adjusted through the variable attenuator located at the EDFA input so that the desired margin was obtained for each experiment.

For each scintillation index and link margin, the percentage of dropped Ethernet frames was computed from the difference between the transmitted and correctly received frame counters reported by the Spirent platform.

Figure 3.41 shows the measured FER as a function of the link margin for both transceiver technologies under the three considered scintillation conditions.

As expected, the link margin required to achieve a given FER increases with the scintillation index, reflecting the larger irradiance fluctuations experienced under stronger turbulence. For all investigated scenarios, the coherent 100G transceiver exhibits greater sensitivity to fading than the 10G IM/DD one, even though the

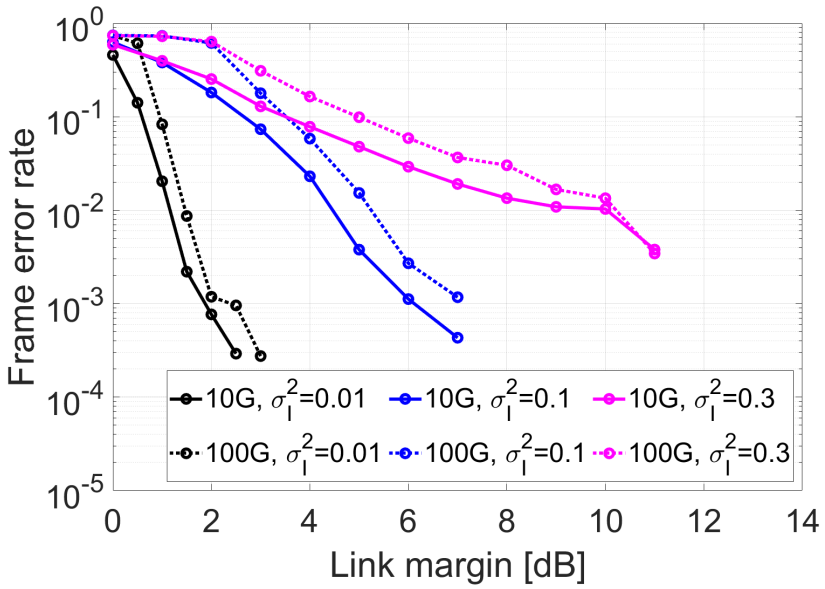


Figure 3.41 – Frame error rate as a function of the link margin for the emulated 10G IM/DD (solid lines) and 100G coherent (dashed lines) OFLss

maximum difference is limited to a few decibels. This results can be attributed to the Digital Signal Processing (DSP). At zero link margin, it was observed that the coherent receiver frequently entered outage conditions with longer recovery times than the 10G link, producing frame loss ratios close to 75% irrespective of the turbulence strength. Conversely, although the 10G transceiver also experienced performance degradation, communication was never completely interrupted, leading to frame loss ratios between approximately 46% and 63%, depending on the scintillation index.

The performance gap progressively decreases as the turbulence strength increases. On average, the 100G link exhibits approximately 2.6, 2.3, and 1.7 times more dropped frames than the 10G system, for scintillation indices of 0.01, 0.10, and 0.30, respectively.

To achieve a frame loss ratio of approximately 1%, the 10G link requires margins of 1.1 dB, 4.5 dB, and 9 dB for scintillation indices of 0.01, 0.10, and 0.30, respectively. The corresponding margins for the coherent 100G system increase to 1.5 dB, 5.2 dB, and 10.2 dB. Therefore, achieving the same communication reliability with the coherent solution requires not only a larger operating margin

but also additional optical power to compensate for its intrinsically lower receiver sensitivity.

Overall, the experimental campaign demonstrates that, under identical atmospheric fading conditions, coherent OTN transceivers are more vulnerable than conventional IM/DD systems to turbulence-induced outages. Although DSP enables the transmission of significantly higher data rates, the associated synchronization and recovery procedures considerably increase recovery times once the received power falls below the decoding threshold. These results highlight the importance of properly accounting for fading dynamics when dimensioning future high-capacity OFLs and further motivate the adoption of suitable mitigation techniques to guarantee the required service availability.

Chapter 4

End-to-end modeling of OFLs exploiting digital mitigation techniques

The link budget and channel models developed in Chapter 2, together with the experimental fading emulation framework presented in Chapter 3, have shown that atmospheric turbulence and pointing impairments induce random fluctuations of the received optical power, eventually resulting in error bursts and temporary link outages. These impairments become particularly critical in high-data-rate OFLs, where even short fading events may severely degrade the end-to-end communication performance. Consequently, the adoption of suitable mitigation strategies is essential to improve link availability and guarantee reliable data delivery.

Fading mitigation techniques can be broadly classified according to the protocol layer at which they operate. Optical techniques act directly on the propagating optical field before photodetection, aiming at reducing the physical mechanisms responsible for signal degradation. Examples include aperture averaging, diversity techniques, image stabilization, and AO. Conversely, digital mitigation techniques operate after detection by exploiting coding and redundancy to recover the information despite channel impairments. Since they do not attempt to restore the optical wavefront, they are complementary to optical mitigation methods rather than alternative solutions.

Among passive optical techniques, aperture averaging reduces scintillation by increasing the receiver aperture, thereby averaging irradiance fluctuations over the

telescope pupil. As discussed in Chapter 2, this approach is particularly effective for downlink OFLs, whereas its benefits are considerably more limited in uplink scenarios. Diversity techniques represent another class of passive mitigation methods and may be implemented in the spatial, temporal, or wavelength domains. Spatial diversity exploits either multiple receiving apertures/transmitting beams or geographically separated OGSs, enabling the communication system to select the link experiencing the most favorable propagation conditions. Time diversity mitigates fading by transmitting redundant information over intervals longer than the channel coherence time, while wavelength diversity provides additional robustness in specific operating conditions, although turbulence statistics generally exhibit only a weak dependence on the optical wavelength [127].

Active optical mitigation techniques compensate wavefront distortions before detection. The simplest implementation consists of image stabilization through tip-tilt correction, which compensates beam wander and improves the stability of the received optical power. More sophisticated systems rely on AO to estimate and correct higher-order wavefront aberrations by means of Wavefront Sensors (WFSs) and DMs. These techniques can significantly improve receiver sensitivity and fiber-coupling efficiency, particularly in coherent optical communication systems. Nonetheless, loop delay, DM actutator density, low-SNR sensing on faint beacons, and anisoplanatism reduce the effectiveness of AO, especially in uplink OFLs. Although AO represents one of the most effective approaches for mitigating atmospheric turbulence, its modeling is already well-documented in the literature and lies outside the scope of this thesis.

The primary focus of this chapter is instead on digital mitigation techniques. At the PHY layer, FEC codes increase communication reliability by introducing controlled redundancy that enables the receiver to detect and correct transmission errors. Since atmospheric turbulence typically generates bursts of errors rather than isolated bit errors, interleaving is commonly used to distribute consecutive erroneous bits over multiple FEC codewords, thereby improving the effectiveness of channel decoding. At HLs of the communication protocol stack, packet-level ECs provide an additional level of protection by recovering lost packets without requiring modifications to the underlying PHY layer, thus offering a flexible solution for mitigating residual errors that remain after PHY-layer decoding.

The effectiveness of these techniques strongly depends on the statistical characteristics of the optical channel. In particular, the coding rates and interleaving depth should be properly dimensioned according to the expected fade depth, duration, and temporal correlation. By exploiting the statistical channel models and fading time series developed in the previous chapters, it is therefore possible to evaluate the end-to-end performance of OFLs under realistic atmospheric conditions and quantify the improvements provided by different digital mitigation strategies.

Accordingly, this chapter develops an end-to-end model for OFLs based on a PHY-layer abstraction, incorporating digital mitigation techniques at multiple layers of the communication stack. Section 4.1 reviews the considered mitigation techniques, including FEC schemes, packet-level ECs, and interleavers. Section 4.2 combines these techniques into a comprehensive end-to-end simulation framework, enabling the assessment of cross-layer mitigation strategies under realistic atmospheric conditions. Results of end-to-end performance analyses are reported. Finally, Section 4.3 presents the last tool developed during this research, i.e., a comprehensive EC simulator able to support the accurate design of this promising mitigation strategy.

4.1 Digital mitigation techniques

In this section, digital mitigation techniques are reviewed. Specifically, PHY-layer FEC codes are surveyed in Section 4.1.1, HL ECs are treated in Section 4.1.2, and interleavers are examined in Section 4.1.3.

4.1.1 Forward error correction codes

Channel coding is one of the most effective technique for improving the reliability of digital communication systems operating over noisy channels. In OFLs, atmospheric turbulence and pointing impairments generate random fluctuations of the received optical power that may result in bursts of bit errors. Rather than relying on retransmissions, which may be impractical or introduce excessive latency, FEC enables the receiver to recover the transmitted information by exploiting redundancy intentionally introduced at the transmitter.

The theoretical foundations of channel coding were established by Shannon in his seminal work on information theory [229]. Shannon demonstrated that, for a communication channel with capacity C, reliable transmission with an arbitrarily small probability of error is theoretically achievable provided that the information transmission rate R_b does not exceed the channel capacity, i.e.,

$$R_b \leq C \tag{4.1}$$

Although Shannon's theorem does not provide explicit coding schemes, it establishes the existence of codes capable of approaching the channel capacity, motivating the development of practical error-correcting codes.

The basic principle of FEC consists in adding redundant symbols to the information sequence before transmission [230]. This redundancy allows the receiver to detect and correct transmission errors without requiring retransmission of the corrupted data. Figure 4.1 illustrates the basic architecture of a communication system employing channel coding. At the transmitter, the encoder maps an input sequence of information bits into a longer codeword containing both information and parity symbols. After propagation through the communication channel, the decoder exploits the redundancy introduced by the encoder to estimate the original information sequence.

Let k denote the number of information symbols and n the total number of transmitted symbols. The code rate is defined as

$$R = \frac{k}{n} \tag{4.2}$$

where $r = n - k$ represents the number of redundant symbols added to each information block. Since redundancy increases the amount of transmitted data, the coded bit rate is

$$R_c = \frac{R_b}{R} \tag{4.3}$$

where R_b is the uncoded information bit rate and R_c is the transmission rate after channel encoding.

From a structural viewpoint, channel codes can be broadly classified into two categories, namely block codes and convolutional codes. Block codes operate on fixed-length data blocks. For every block of k information symbols, the encoder

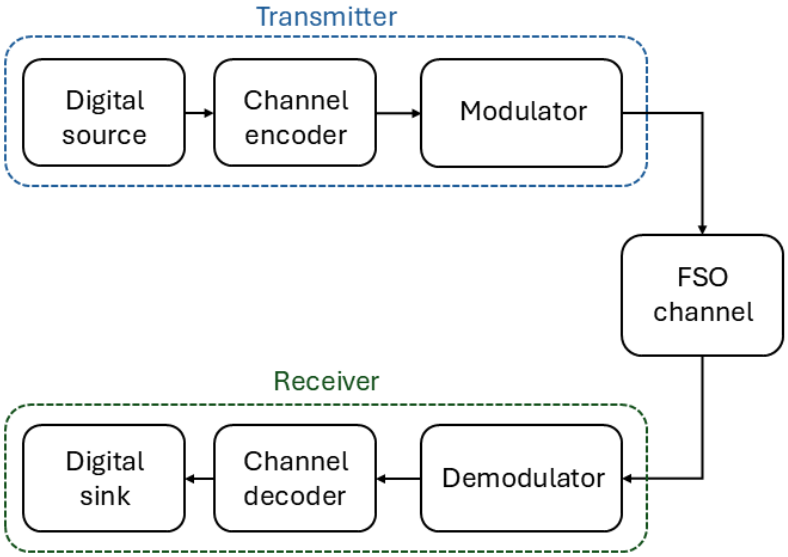


Figure 4.1 – Block diagram of a FSO data transmission system employing channel coding

generates a codeword of length n by appending $r = n-k$ parity symbols computed as linear combinations of the input symbols. Since each codeword is generated independently of previous blocks, block encoders are memoryless systems. Among the most widely adopted block codes are cyclic codes, including Bose, Chaudhari, and Hocquenghe (BCH) and RS codes, which have historically found widespread application in satellite communications due to their excellent burst-error correction capabilities [231].

Conversely, convolutional codes introduce memory into the encoding process. The encoded symbols depend not only on the current input sequence but also on a number of previously transmitted symbols stored within the encoder memory. Such encoders are typically implemented using shift registers and modulo-two adders. If the encoder memory contains $m-1$ previous input blocks, the quantity $(m-1)k$ defines the constraint length of the code, representing the number of information bits that influence the generation of the current output symbols.

Many practical communication systems combine both approaches through concatenated coding schemes, where an outer block code is cascaded with an inner

convolutional code. In this architecture, the inner decoder first corrects most channel errors, while the outer decoder removes the residual error bursts that exceed the correction capability of the inner decoder, resulting in significantly improved reliability [231].

The performance of a FEC scheme is commonly evaluated by comparing the BER before and after decoding. Let $\mathrm{BER}_{\mathrm{in}}$ denote the BER at the decoder input and $\mathrm{BER}_{\mathrm{out}}$ the BER after decoding. For a given decoding algorithm, the decoding performance is typically expressed as a function of the ratio between the energy per information bit E_b and the noise PSD N_0. The coding gain is defined as the reduction in the required E_b/N_0 necessary to achieve a target BER with respect to an uncoded transmission. Since channel coding increases the transmitted bandwidth through the addition of redundancy, the more representative metric is often the net coding gain, which also accounts for the associated increase in receiver noise bandwidth [232].

Finally, decoding algorithms can be classified according to the type of information exploited during the decision process. Hard Decision (HD) decoders operate on binary decisions obtained by comparing the received signal with a single threshold so that each received symbol is interpreted directly as either a logical zero or one. In contrast, Soft Decision (SD) decoders exploit multiple quantization levels to estimate the reliability of each received symbol. By preserving this reliability information, SD decoding generally achieves a significantly larger coding gain than HD decoding, at the expense of increased computational complexity [232]. Modern capacity-approaching codes, including LDPC and Turbo codes, rely almost exclusively on Iterative (IT) SD decoding algorithms.

The choice of the coding scheme depends on the statistical characteristics of the propagation channel, the target communication latency, and the available computational resources. In particular, the bursty nature of turbulence-induced fading often requires combining FEC with interleaving techniques, which distribute consecutive channel errors over multiple codewords and substantially improve the effectiveness of the decoder. For this reason, interleaving is commonly employed together with channel coding in modern optical communication systems.

4.1.1.1 Binary linear block codes: basic concepts

Binary linear block codes constitute one of the most important families of FEC schemes and provide the mathematical foundation for several practical coding techniques, including BCH, RS, and LDPC codes. They can be conveniently described using concepts from linear algebra over the binary Galois field

$$\mathbb{F}_2 = \{0, 1\} \tag{4.4}$$

where both addition and multiplication are performed modulo two [230].

A $\mathbf{C}(n, k)$ binary linear block code is defined as a k-dimensional subspace of the vector space $\mathbb{F}_2^n$. Each element of the subspace is referred to as a codeword and consists of n binary symbols, of which k carry information while the remaining $n - k$ correspond to redundancy introduced by the encoder.

The encoding operation is completely characterized by the generator matrix $\mathbf{G} \in \mathbb{F}_2^{k \times n}$, whose rows form a basis of the code subspace. Given an information vector

$$\mathbf{d} = [d_1 \; d_2 \; \ldots \; d_k] \tag{4.5}$$

the corresponding codeword is obtained through the linear transformation

$$\mathbf{c} = \mathbf{dG} \tag{4.6}$$

where all operations are performed over $\mathbb{F}_2$. Therefore, each transmitted codeword is a linear combination of the rows of the generator matrix.

An important metric for evaluating the performance of a linear block code is the Hamming weight, defined as the number of non-zero symbols in a codeword. Similarly, the Hamming distance between two codewords corresponds to the number of positions in which they differ. The minimum Hamming distance of the code is

$$d_{\min} = \min \{d_H(\mathbf{c}_i, \mathbf{c}_j) \; i, j = 1, \ldots, k\} \quad i \neq j \tag{4.7}$$

where $d_H(\cdot, \cdot)$ denotes the Hamming distance. Since the sum of two codewords of a linear code is itself a valid codeword, the minimum distance is equal to the minimum Hamming weight among all non-zero codewords. The parameter $d_{\min}$ plays a fundamental role because it directly determines the error detection and correction capabilities of the code [230].

Associated with every linear block code is the parity-check matrix $\mathbf{H} \in \mathbb{F}_2^{(n-k)\times n}$, which spans the dual code and satisfies the orthogonality condition

$$\mathbf{G}\mathbf{H}^T = \mathbf{0} \tag{4.8}$$

Consequently, every valid codeword fulfills

$$\mathbf{c}\mathbf{H}^T = \mathbf{0} \tag{4.9}$$

which represents the set of parity constraints defining the code.

For practical implementations, the generator matrix is often converted into its systematic form

$$\mathbf{G} = [\mathbf{I}_k \ \mathbf{P}] \tag{4.10}$$

where $\mathbf{I}_k$ denotes the $k \times k$ identity matrix and $\mathbf{P}$ is a $k \times (n-k)$ binary matrix. In this case, the generated codeword becomes

$$\mathbf{c} = [\mathbf{d} \ \mathbf{d}_p] \tag{4.11}$$

where the first k bits coincide with the information sequence, while the remaining $n-k$ bits are parity symbols computed from the information bits. The corresponding parity-check matrix is

$$\mathbf{H} = \left[\mathbf{P}^T \ \mathbf{I}_{n-k}\right] \tag{4.12}$$

At the receiver, decoding aims at identifying the transmitted codeword that best matches the received sequence. The capability of a code to detect and correct errors depends exclusively on its minimum distance. Specifically, a $\mathbf{C}(n,k)$ linear block code with minimum distance $d_{\min}$ can detect up to

$$t_d = d_{\min} - 1 \tag{4.13}$$

bit errors and can correct up to

$$t_c = \left\lfloor \frac{d_{\min} - 1}{2} \right\rfloor \tag{4.14}$$

random bit errors, where $\lfloor \cdot \rfloor$ denotes the floor operator [230]. Maximum-Likelihood (ML) decoding consists of selecting the codeword having the minimum Hamming distance from the received vector.

The minimum distance is itself bounded by the Singleton bound, i.e.,

$$d_{\min} \leq n - k + 1 \tag{4.15}$$

and codes achieving equality are referred to as Maximum Distance Separable (MDS) codes.

A particularly important subclass of linear block codes is represented by cyclic codes. A code $\mathbf{C}(n, k)$ is said to be cyclic if every cyclic shift of a valid codeword is itself another valid codeword. This property allows the encoding process to be described through a generator polynomial

$$g(x) = a_{n-k}x^{n-k} + a_{n-k-1}x^{n-k-1} + \cdots + a_1 x + a_0 \tag{4.16}$$

where the coefficients belong to $\mathbb{F}_2$ and $a_{n-k} = a_0 = 1$. Every codeword of a cyclic code can be generated as the product of the information word polynomial and the generator polynomial, enabling highly efficient hardware implementations. Many practical coding schemes, including BCH and RS codes, belong to this family and exploit the algebraic structure of cyclic codes to achieve efficient encoding and decoding algorithms.

4.1.1.2 Nonbinary linear block codes: basic concepts

While binary linear block codes operate over the binary Galois field $\mathbb{F}_2$, several powerful coding schemes are constructed over extended finite fields, commonly referred to as Galois fields. These nonbinary codes are particularly attractive for communication systems affected by burst errors, since they operate on multi-bit symbols rather than individual bits.

An extended finite field $\mathrm{GF}(2^m)$ is generated starting from a primitive polynomial via a recursive operation. Let $p(x)$ denote such a primitive polynomial and let α be one of its roots, i.e., $p(\alpha) = 0$. Since α satisfies the primitive polynomial, every power of α greater than or equal to m can be recursively expressed as a linear combination of lower-order powers,

$$\alpha^m = c_1\alpha^{m-1} + c_2\alpha^{m-2} + \cdots + c_m \qquad c_i \in \mathbb{F}_2, i = 1, \ldots, m \tag{4.17}$$

thus enabling the construction of all the elements of the extended field. The resulting field contains 2^m elements,

$$\mathrm{GF}(2^m) = \left\{0, 1, \alpha, \alpha^2, \ldots, \alpha^{2^m-2}\right\} \tag{4.18}$$

where every non-zero element can be represented as a power of the primitive element α.

A fundamental concept in the construction of nonbinary codes is that of conjugate classes. If β is an element of $\mathrm{GF}(2^m)$, all of its conjugates are generated through successive squaring as

$$\left\{\beta,\, \beta^2,\, \beta^4,\, \beta^8,\, \ldots,\, \beta^{2^r}\right\} \tag{4.19}$$

where r depends on the size of the conjugate class. Associated with each conjugate class is a unique minimal polynomial, defined as

$$m(x) = \prod_{i=1}^{L}(x + \beta_i) \tag{4.20}$$

where $\{\beta_1, \beta_2, \ldots, \beta_L\}$ denotes the corresponding conjugate class [230]. Although the polynomial is constructed using elements of $\mathrm{GF}(2^m)$, its coefficients belong to the binary field $\mathbb{F}_2$. Minimal polynomials constitute the basic building blocks for the construction of several families of cyclic codes.

These concepts have been used in the literature to define some classes of linear block codes, including BCH codes. A t-error-correcting BCH code is obtained by defining the generator polynomial as the least common multiple of the minimal polynomials associated with a prescribed set of consecutive roots, i.e.,

$$g(x) = \mathrm{LCM}\left\{m_1(x), m_3(x), m_5(x), \ldots, m_{2t-1}(x)\right\} \tag{4.21}$$

where $\mathrm{LCM}(\cdot)$ denotes the least common multiple operation. For a BCH code constructed over $\mathrm{GF}(2^m)$, the code length is

$$n = 2^m - 1 \tag{4.22}$$

while the dimension is

$$k = n - r \tag{4.23}$$

with r representing the degree of the generator polynomial.

A closely related family is represented by RS codes. Unlike BCH codes, which operate on binary symbols, RS codes directly manipulate symbols belonging to GF(2^m), making them particularly effective in the presence of burst errors. The generator polynomial of a t-error-correcting RS code is given by

$$g(x) = (x + \beta)(x + \beta^2) \cdots (x + \beta^{2t}) \tag{4.24}$$

where β is an extended field element. If the generator polynomial has degree r, the corresponding code parameters are

$$n = 2^m - 1 \qquad k = n - r \tag{4.25}$$

and the error-correction capability is

$$t_c = \left\lfloor \frac{n-k}{2} \right\rfloor \tag{4.26}$$

An important property of RS codes is that their minimum Hamming distance satisfies

$$d_{\min} = n - k + 1 \tag{4.27}$$

which corresponds to the Singleton bound. Consequently, RS codes belong to the class of MDS codes and achieve the largest possible minimum distance for a given code length and dimension.

Since decoding is performed on symbols rather than individual bits, an erroneous symbol can be corrected regardless of the number of corrupted bits it contains. This characteristic makes RS codes particularly well suited for channels affected by burst errors, where consecutive bit errors are concentrated within a limited number of symbols. For this reason, RS codes have been extensively adopted in storage systems, deep-space communications, and optical communication links, where burst-error events frequently arise due to channel impairments such as atmospheric turbulence.

Several efficient decoding algorithms have been proposed for BCH and RS codes. Classical approaches include the Peterson-Gorenstein-Zierler (PGZ) algorithm, whereas the Berlekamp algorithm provides a computationally more efficient solution for codes with large error-correction capability and is therefore widely adopted in practical implementations [230].

4.1.1.3 Convolutional codes: basic concepts

Unlike block codes, which encode independent blocks of information bits, convolutional codes introduce memory into the encoding process. Consequently, each encoded symbol depends not only on the current input symbols but also on a number of previously transmitted symbols stored within the encoder. This memory enables convolutional codes to exploit temporal redundancy, making them particularly effective against random transmission errors.

A convolutional encoder is typically implemented as a logic circuit composed of shift registers, modulo-two adders, and a common clock signal. At every clock cycle, the contents of the memory registers are shifted, a new information symbol enters the encoder, and a set of encoded symbols is generated according to the connections between the shift registers and the modulo-two adders.

The behavior of a convolutional encoder can be completely described by its impulse response, defined as the encoder output generated by a single 1 input symbol. For non-recursive convolutional encoders, the impulse response has finite duration and is determined by the encoder memory m. Conversely, recursive convolutional encoders incorporate one or more feedback paths, resulting in impulse responses of theoretically infinite length.

Similarly to linear block codes, the encoding operation can be represented through generator functions. However, since convolutional codes operate on continuous data streams rather than finite information blocks, the corresponding generator matrix depends on the length of the transmitted sequence [230].

The operation of convolutional codes is commonly represented by graphical models that describe the evolution of the encoder states. The three most frequently adopted representations are the tree diagram, the state diagram, and the trellis diagram. Among them, the trellis representation is of particular importance because it forms the basis of ML decoding through the Viterbi algorithm. In this approach, each branch of the trellis corresponds to a possible state transition of the encoder, while decoding consists of identifying the path whose encoded sequence most closely matches the received observations. By efficiently discarding unlikely paths, the Viterbi algorithm achieves ML performance with computational complexity that increases linearly with the length of the received sequence, making it

the standard decoding algorithm for convolutional codes [230].

Although convolutional codes have historically been employed in numerous wireless and satellite communication systems, they are nowadays often used as components of concatenated coding schemes or have been superseded by more powerful capacity-approaching codes, such as Turbo and LDPC codes.

4.1.1.4 Iterative decoding: basic concepts

The objective of any channel decoder is to identify the transmitted codeword from the noisy observations available at the receiver. Let $X \in \mathbf{C}(n,k)$ denote the transmitted codeword and let Y represent the corresponding channel observation. The optimum decoding rule minimizing the probability of decoding error is the Maximum A Posteriori (MAP) criterion, which selects the codeword maximizing the a posteriori probability, i.e.,

$$\hat{x}^{\mathrm{MAP}}(y) = \arg\max_{\mathbf{x}\in\mathbf{C}} p_{X|Y}(x|y) \tag{4.28}$$

By applying Bayes theorem, the MAP decoder can be rewritten as

$$\hat{x}^{\mathrm{MAP}}(y) = \arg\max_{\mathbf{x}\in\mathbf{C}} p_{Y|X}(y|x)p_X(x) \tag{4.29}$$

where the constant term $p_Y(y)$ that should appear at the denominator has been omitted since it does not depend on the transmitted codeword [230].

If all codewords are equally likely, i.e., the a priori probability $p_X(x)$ is uniform, then the MAP criterion simplifies to the ML decoding rule, i.e.,

$$\hat{x}^{\mathrm{MAP}}(y) = \arg\max_{\mathbf{x}\in\mathbf{C}} p_{Y|X}(y|x)p_X(x) = \arg\max_{\mathbf{x}\in\mathbf{C}} p_{Y|X}(y|x) = \hat{x}^{\mathrm{ML}}(y) \tag{4.30}$$

which searches for the codeword that is most likely to have generated the received observation. Therefore, for equiprobable codewords, MAP and ML decoding are equivalent [233].

Classical coding theory has focused on designing codes with large minimum Hamming distance and strong algebraic properties, allowing efficient decoding while maintaining satisfactory error-correction capability. Nevertheless, such algebraic decoding techniques still exhibit a non-negligible performance gap with respect to the Shannon limit [233].

A major breakthrough in coding theory was achieved through the introduction of IT decoding, which approaches the optimum decoding solution by repeatedly exchanging probabilistic information among simpler decoding units. Rather than solving the decoding problem globally, IT algorithms decompose it into a sequence of local estimation problems that progressively refine the reliability associated with each transmitted bit or symbol. As a result, IT decoders can achieve performance remarkably close to the Shannon capacity while maintaining computational complexity that grows approximately linearly with the code length [233].

The concept of IT decoding was first introduced by Berrou and Glavieux in the early 1990s with the invention of Turbo codes [234]. Turbo codes are obtained through the parallel concatenation of two or more constituent convolutional encoders separated by an interleaver. At the receiver, each constituent decoder performs Soft-Input Soft-Output (SISO) decoding and exchanges reliability information, commonly referred to as extrinsic information, with the other decoders. This exchange is repeated iteratively until convergence or until a maximum number of iterations is reached, resulting in decoding performance significantly closer to the Shannon limit at reduced complexity [131].

The success of Turbo codes stimulated the development of several other coding families relying on IT decoding principles, including repeat–accumulate codes, polar codes, and, most notably, LDPC codes. Specifically, LDPC codes are binary linear block codes characterized by a sparse parity-check matrix, in which the number of non-zero entries is much smaller than the total number of matrix elements. This sparse structure enables efficient message-passing algorithms, such as the belief-propagation algorithm [233]. Depending on the distribution of non-zero elements within the parity-check matrix, LDPC codes are classified as regular, when each row and column contains the same number of non-zero entries, or irregular, when these weights are allowed to vary. Irregular constructions generally provide improved decoding performance and constitute the basis of most modern capacity-approaching LDPC codes adopted in practical communication standards [128, 233].

4.1.1.5 FEC schemes for laser SatComs: CCSDS specifications

The CCSDS has developed a series of experimental specifications defining the PHY layer, synchronization procedures, and channel coding techniques for high-data-rate optical space communications. These standards target a broad range of optical communication scenarios, including space-to-space, space-to-ground, ground-to-space, and airborne optical links, and provide interoperable solutions for future optical satellite communication systems [226, 235, 236].

Although the proposed waveforms and transmission formats differ according to the considered application, all CCSDS optical communication standards rely on powerful FEC schemes to guarantee reliable data transmission over channels affected by atmospheric turbulence, pointing errors, and receiver noise.

The main features of the three specifications are summarized in Table 4.1, and detailed in the following.

One of the first CCSDS experimental specifications for optical communications is presented in [226], which addresses high-data-rate laser communication systems operating at wavelengths around 1550 nm. As shown in Fig. 4.2, the recommendation supports a variety of communication scenarios, including relay links through GEO satellites, inter-satellite crosslinks, DTE downlinks, and OFLs. Depending on the application, user data rates ranging from approximately 15 Mbit/s to 100 Gbit/s are supported through different modulation formats and WDM techniques.

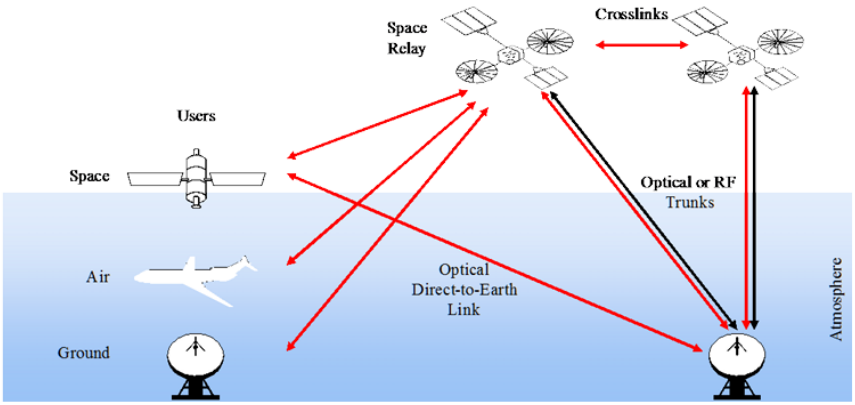


Figure 4.2 – Link scenarios showing possible optical)red) and RF (black) links [226]

Table 4.1 – Summary of the main CCSDS recommendations for high-data-rate optical satellite communications

CCSDS Standard	**Wavelength**	**Modulation**	**FEC Scheme**	**Data Rate**	**Target Applications**
[226]	1550 nm	BPSK, QPSK, DPSK, DQPSK	BCH + DVB-S2 LDPC (multiple code rates) or RS(255,239)	15 Mbit/s - 100 Gbit/s	Relay links, OFLs, OISLs, DTE links
[235]	1064 nm	BPSK	RS(255,239)	∼2.9 Gbit/s	LEO-GEO and GEO-GEO optical links (also applicable to OFLs with additional mitigation techniques)
[236]	1550 nm	OOK	RS-PC	100 Mbit/s - 10 Gbit/s	LEO-LEO, LEO-Ground, Ground-LEO

Two alternative channel coding solutions are considered. The first employs a concatenated coding scheme composed of an outer BCH code followed by an inner LDPC code based on the DVB-S2 standard [237], allowing several selectable code rates according to the required communication reliability. The second option relies on a RS code defined over 8-bit symbols with parameters $n = 255$ and $k = 239$, capable of correcting up to eight erroneous symbols per codeword [238]. Both coding schemes generate codewords of 64 800 bits, while several modulation formats, including BPSK, QPSK, DPSK, and Differential Quadrature Phase-Shift Keying (DQPSK), are supported to accommodate different spectral efficiencies and implementation requirements.

A second experimental specification, reported in [235], targets high-data-rate optical communication systems operating at 1064 nm using BPSK modulation. Although primarily intended for LEO-GEO and GEO-GEO OISLs, the proposed transmission architecture can potentially be applied to OFLs provided that additional mitigation techniques, such as AO, interleaving, or erasure coding, are employed to compensate for atmospheric impairments.

In this recommendation, the incoming information stream is partitioned into blocks of 1904 bytes, to which an 8-byte synchronization header is appended. The resulting payload is then encoded using RS(255,239), thus producing eight codewords, achieving a total frame length of 2040 bytes after parity generation. The encoded data are finally mapped onto a BPSK symbols and superimposed on an optical carrier with a nominal transmission rate of approximately 2912.5 Mbit/s.

More recently, in [236], CCSDS specified synchronization and channel coding procedures for optical communication systems employing OOK modulation at 1550 nm. The specification targets short-range optical communication links, including LEO-to-LEO and LEO-to-ground scenarios, supporting user data rates ranging from 100 Mbit/s up to 10 Gbit/s.

Differently from the previous recommendations, channel coding is performed through a RS Product Code (RS-PC), originally proposed by Yamazoe et al. [239]. Product codes are constructed by serially applying two linear block codes along orthogonal dimensions of a data array. More specifically, if two component codes have parameters $(n_1, k_1, d_{\min,1})$ and $(n_2, k_2, d_{\min,2})$, the information symbols are

first arranged into a $k_1 \times k_2$ matrix. As shown in Fig. 4.3, one component code is then applied to each row, whereas the second component code is subsequently applied to each column. The resulting product code is characterized by $n = n_1 n_2$, $k = k_1 k_2$, and $d_{\min} = d_{\min,1} d_{\min,2}$, while the overall code rate is simply the product of the component code rates, i.e., $R = R_1 R_2$.

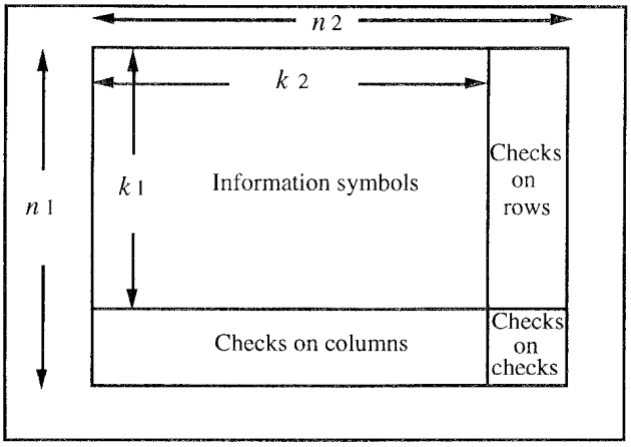


Figure 4.3 – Construction of a generic product code [240]

The CCSDS RS-PC employs an outer RS(255,223) code operating on the columns of the information array, followed by a shortened inner RS(221,205) code acting on the rows. After the parity symbols have been generated, a synchronization marker is appended to form the final FEC block. Multiple FEC blocks may be concatenated to improve robustness against burst errors. At the receiver, decoding is performed iteratively by alternately decoding the row and column component codes until convergence or until a predefined maximum number of iterations is reached.

Compared with conventional single RS codes, the adopted product code provides significantly improved error-correction capability while maintaining relatively low implementation complexity. In particular, it represents an attractive compromise between decoding performance and hardware complexity, requiring substantially lower computational resources than SD iterative decoders based on LDPC or serially concatenated convolutional codes, while still providing excellent burst-error correction capability [239].

The evolution of the CCSDS recommendations clearly reflects the increasing adoption of powerful IT decoding techniques for optical satellite communications. While early experimental standards mainly relied on conventional RS and BCH codes, more recent recommendations progressively introduced concatenated and product-code architectures capable of approaching the performance of modern SD schemes with moderate implementation complexity.

4.1.1.6 FEC schemes for laser SatComs: ESTOL specification

In parallel with the CCSDS standardization activities, ESA has developed the ESTOL specification, which defines a flexible air interface for bidirectional high-capacity optical satellite communications [187]. ESTOL targets both OISLs and optical ground-to-space links involving LEO, MEO, and GEO satellites. By exploiting coherent optical transmission together with WDM, the specification aims at enabling aggregate data rates exceeding 1 Tbit/s per link and communication direction.

Unlike traditional optical communication standards specifically developed for space applications, ESTOL builds upon mature terrestrial coherent optical networking technologies. In particular, it relies upon existing Digital Coherent Optics (DCO) fiber transceivers and OTN framing, thereby extending the terrestrial optical backbone towards space-based optical networks. This approach is fully aligned with ESA's HydRON vision, whose objective is the seamless integration of TN and NTN optical communication infrastructures [21].

To accommodate a wide variety of mission profiles, ESTOL defines several PHY-layer configurations covering both coherent and IM/DD architectures. Three modulation formats are supported, i.e., DP-QPSK, DP-16QAM, and OOK.

The coherent interfaces support data rates of 100, 200 and 400 Gbit/s per wavelength, whereas the IM/DD interfaces target lower-rate applications at 2.5 and 10 Gbit/s. Such flexibility enables the standard to address both resource-constrained missions and future ultra-high-throughput optical communication systems.

The adopted FEC scheme depends on the selected air interface. The 2.5 Gbit/s OOK interface employs the Quasi-Cyclic LDPC (QC-LDPC) code adopted in the 5G NR standard, with selectable coding rates equal to 1, 0.8462, 0.6667, and 0.5. Instead, the 10 Gbit/s OOK interface relies on the RS code defined for the SDA

optical transport architecture [241]. Finally, all coherent interfaces operating at data rates of 100 Gbit/s and above rely on the open FEC (oFEC) scheme adopted by the OpenROADM Multi-Source Agreement (MSA) [242], which constitutes the reference FEC solution for coherent, terretsrial optical transport networks.

The oFEC architecture is based on a block-oriented product-code structure employing an extended BCH(256,239) component code with minimum Hamming distance equal to six. The resulting code has a rate

$$R = \frac{111}{128} \approx 0.867 \tag{4.31}$$

corresponding to a coding overhead of approximately 15.3%. The encoding process is performed on the FlexO frame structure defined in [243], which represents the basic transport container for coherent optical signals. Depending on the selected transmission rate, multiple FlexO frames are combined to form FlexO-2 or FlexO-4 structures before FEC encoding.

Prior to parity generation, the payload bits are scrambled and reorganized into a set of fixed-length coding blocks. Two parallel BCH encoders independently process the resulting block matrices, generating the parity symbols that are subsequently combined with the information bits to form the encoded FEC (i.e., the FlexO-x-DO frame). Unlike conventional BCH coding schemes, the parity computation is tightly integrated with a two-stage interleaving process specifically designed to improve burst-error resilience.

The first stage consists of an intra-block interleaver, which redistributes the coded bits within each encoded block in order to maximize the spatial separation between adjacent transmitted bits. A second inter-block interleaver subsequently spreads neighboring coded symbols. As a consequence, localized channel impairments affecting consecutive transmitted bits are converted into sparse error patterns before decoding, substantially improving the effectiveness of the BCH component decoders.

At the receiver, decoding is performed through an IT SD algorithm. Rather than independently decoding each BCH codeword, the product-code structure allows information to be exchanged iteratively between decoders.

The IT decoder belongs to the family of SISO algorithms commonly employed for Turbo product codes. Among the available solutions, the Pyndiah-Chase-II

decoding represents one of the most widely adopted algorithms owing to its excellent compromise between decoding performance and computational complexity [240]. Experimental implementations have demonstrated that this approach enables throughputs of several hundreds of gigabits per second [244].

4.1.2 Erasure codes

As discussed in the previous section, FEC represents one of the key enabling technologies for high-data-rate OFLs, allowing the receiver to detect and correct bit errors introduced by noise and fading. Nevertheless, bit-level channel coding alone may not always guarantee the reliability required by future optical satellite communication systems. In particular, atmospheric turbulence and pointing impairments may generate deep fading events lasting several milliseconds or even tens of milliseconds. At the data rates envisioned for next-generation OFLs, such outages may affect hundreds or even thousands of consecutive frames. Furthermore, severe fades may cause the receiver to lose frame or symbol synchronization, resulting in the loss of additional packets before synchronization is re-established. Under these conditions, the residual packet loss rate after FEC decoding may still be unacceptable for many applications.

A straightforward solution consists in recovering the missing packets through ARQ protocols operating at HLs of the communication stack. ARQ schemes rely on retransmission requests generated by the receiver whenever a packet is not correctly received. Although this approach can achieve virtually error-free communications, it inevitably introduces additional latency associated with the retransmission process. Such delay becomes particularly detrimental in satellite communication systems characterized by long Round-Trip Times (RTTs), during which the transmitter may remain idle while awaiting acknowledgements. Moreover, in several practical scenarios, such as simplex communication systems or multicast transmissions, a reliable return channel may not be available, making ARQ impractical.

Packet-level ECs provide an attractive alternative for recovering packet losses without requiring retransmissions. Similarly to channel coding, erasure coding introduces redundancy into the transmitted information. However, unlike FEC

codes, which operate on individual bits or symbols, ECs work on complete data packets. Starting from a block of information packets, the encoder generates a set of redundant packets according to a predefined coding algorithm. The original and redundant packets are then transmitted, allowing the receiver to reconstruct the missing information provided that a sufficient number of packets are successfully received.

This operating principle assumes that the underlying communication layers are capable of determining whether each received packet is correct or corrupted. Typically, this functionality is provided by lower-layer error-detection mechanisms, such as Cyclic Redundancy Checks (CRCs). Packets failing the integrity check are discarded before delivery to higher protocol layers, which therefore observe only erasures, i.e., missing packets, rather than packets containing erroneous bits. Since the positions of the missing packets are known, erasure decoding is generally simpler than error correction, enabling highly efficient packet recovery algorithms [245, 246].

Erasure coding should therefore be regarded as complementary to conventional channel coding rather than as an alternative. While FEC codes mitigate bit errors caused by receiver noise and short-duration fading events, ECs operate at packet level to recover losses associated with longer channel outages or synchronization failures. The two approaches naturally complement each other in optical satellite communication systems, where both random errors and burst packet losses may coexist. When a feedback channel is available, erasure coding can also be combined with retransmission protocols, giving rise to hybrid ARQ/EC strategies that further improve communication reliability [246].

In principle, erasure coding can be implemented at any protocol layer where information is organized into packets. Application- and transport-layer implementations operate on an end-to-end basis and do not require modifications to the underlying communication protocols. This approach offers considerable flexibility, since the coding parameters can be tailored to the specific requirements of each application independently of the underlying network infrastructure. However, the coding configuration must generally be selected according to the characteristics of the most challenging communication link along the end-to-end path.

Alternatively, erasure coding may be implemented at the network or data-link layer. In these cases, coding is performed on a hop-by-hop basis, allowing the code parameters to be adapted to the channel conditions of each individual link. Such an approach is particularly attractive in heterogeneous multi-hop networks, where different links may exhibit significantly different packet loss characteristics. On the other hand, link-layer and network-layer implementations require modifications to the communication protocols adopted by the network nodes, thereby reducing interoperability and increasing implementation complexity [247].

Overall, erasure coding has attracted considerable interest for optical satellite communications, where it can be deployed on top of existing communication protocols without requiring modifications to the PHY layer. The following sections review the main concepts and families of packet-level ECs and discuss their suitability for mitigating packet losses in OFLs.

4.1.2.1 Packet-level ECs: basic concepts

Packet-oriented ECs operate according to the same fundamental principle as conventional FEC schemes, but they treat packets rather than bits or symbols as the elementary coding units. More specifically, a block composed of k source packets is encoded into a larger set of n packets, each having the same length T. As for channel coding, such a code is commonly denoted by $\mathbf{C}(n, k)$, where $n - k$ represents the number of redundant packets generated by the encoder.

In most practical applications, systematic ECs are employed. In this case, the first k encoded packets coincide with the original source packets, whereas the remaining $n - k$ packets contain redundancy information generated by the encoder. At the receiver, the source packets can be immediately delivered to the upper protocol layers whenever they are correctly received, while the redundant packets are only exploited to recover missing packets. Figure 4.4 illustrates the general encoding and decoding process of a packet-oriented erasure coding system. The source packets correspond to Protocol Data Units (PDUs) generated at the protocol layer where the EC is implemented. During encoding, these packets are arranged into an encoding matrix, also referred to as a source block, composed of n rows of T bytes each. The first k rows are filled with the source packets, whereas

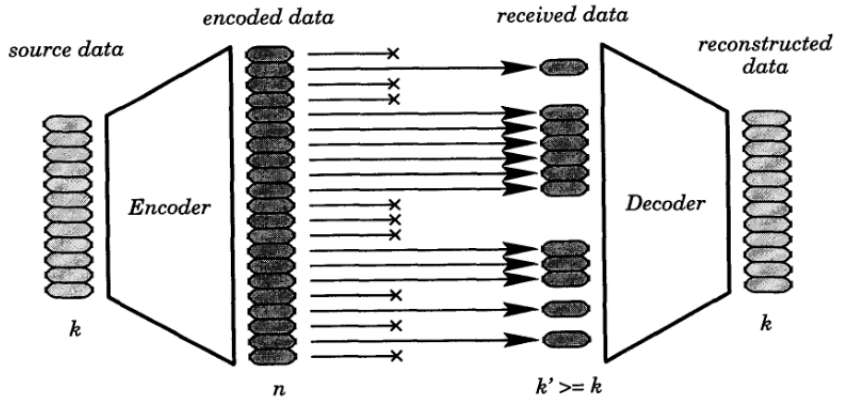


Figure 4.4 – Graphical representation of erasure coding and decoding processes [245]

the remaining rows are reserved for the repair packets generated by the coding algorithm. Depending on the adopted protocol, additional metadata, such as packet length or source-block identifiers, may also be included. Once the source block has been completed, the repair packets are computed as linear combinations of the source packets according to the selected coding scheme. Finally, both source and repair packets are encapsulated into lower-layer PDUs together with the signaling information required by the decoder.

At the receiver, a decoding matrix is associated with each transmitted source block. Correctly received source and repair packets are inserted into the appropriate rows of the matrix using the information carried in the packet headers, whereas erased packets simply leave empty positions within the decoding table. Decoding is typically initiated either when all the expected packets have been received or when a predefined timeout expires. The decoding process is considered successful if all the missing source packets can be reconstructed. Otherwise, decoding failure is declared.

From the perspective of the erasure decoder, the communication channel is conveniently modeled as a Packet Erasure Channel (PEC) [246, 248]. In this model, each transmitted packet is either received correctly or completely lost, without considering the presence of partially corrupted packets. This assumption is justified by the fact that lower protocol layers usually employ error-detection mechanisms,

such as CRCs, to discard corrupted packets before delivery to HLs. Consequently, the erasure decoder only observes the positions of the missing packets rather than erroneous packet contents.

The PEC was originally introduced by Elias [249], who showed that its capacity is simply given by

$$C = 1 - p \tag{4.32}$$

where p denotes the packet erasure probability. Moreover, it can be shown that random codes with rates approaching the channel capacity can be decoded with an exponentially small decoding error probability under ML decoding.

For linear block codes, ML decoding over the PEC can be formulated as the solution of a system of linear equations. Let $\mathbf{H}$ denote the parity-check matrix of a systematic linear code. Any valid codeword $\mathbf{x}$ satisfies the parity constraints

$$\mathbf{x}\mathbf{H}^T = \mathbf{0} \tag{4.33}$$

where $\mathbf{0}$ is a vector made by all-zero packets. By partitioning the received codeword into known and erased packets, denoted by $\mathbf{x}_K$ and $\mathbf{x}_{\bar{K}}$, respectively, the decoding problem can be expressed as

$$\mathbf{x}_{\bar{K}}\mathbf{H}_{\bar{K}}^T = \mathbf{x}_K\mathbf{H}_K^T \tag{4.34}$$

where $\mathbf{H}_K$ and $\mathbf{H}_{\bar{K}}$ are obtained by selecting the columns of the parity-check matrix corresponding to the received and erased packets, respectively. Solving the above linear system yields the unknown packets whenever a unique solution exists. Although Gaussian elimination provides optimal ML decoding performance, its computational complexity scales as $\mathcal{O}(n^3)$, making it impractical for long codewords [248, 250].

The erasure correction capability of a linear block code is directly related to its minimum Hamming distance. A code with minimum distance $d_{\min}$ can recover any pattern of up to $d_{\min} - 1$ erasures. Consequently, MDS codes, such as RS codes, represent the optimal solution from a coding-theoretic perspective, allowing the recovery of the original information from any subset of k correctly received packets. However, this optimal correction capability comes at the expense of relatively high

encoding and decoding complexity. Furthermore, RS codes defined over the Galois field GF(2^m) are limited to maximum codeword lengths equal to $2^m - 1$ [246, 247].

To overcome these limitations, considerable research has focused on sparse-graph ECs, whose parity-check matrices contain only a small fraction of non-zero elements. These codes can be decoded through IT algorithms with computational complexity that scales approximately linearly with the codeword length [246–248,250,251]. Typical examples include LDPC codes and their numerous variants, such as Irregular Repeat-Accumulate (IRA), protograph, generalized LDPC, and generalized IRA codes [246, 251]. Although these codes are not MDS, and therefore generally require more than k received packets to guarantee successful decoding, their ability to employ extremely long codewords often compensates for this limitation, providing excellent performance against long burst erasures while maintaining low implementation complexity [251].

In detail, Eq. (4.34) can be solved for LDPC codes by recursively processing one equation at time through the bitwise XOR of the known packets [251]. Moreover, effective LDPC code design techniques based on Extrinsic Information Transfer (EXIT) charts exist that enable to design low-complexity, long codes with near-optimum performance [248]. IRA codes are characterized by a further reduction in encoding complexity [252]. Despite these advantages, the suboptimality of IT decoding leads to a coding gain loss with respect to ML decoding, especially for reduced n. In addition, the presence of small size stopping sets leads to high error floors at low error rates [251]. To overcome these issues, efficient ML decoding algorithms have been devised for LDPC codes by relying on the parity check matrix sparseness [248, 252].

In general, packet-oriented ECs intended for communication networks should satisfy several practical requirements. First, they should preferably be systematic, allowing correctly received source packets to be immediately forwarded without waiting for the decoding process to terminate. Second, both encoding and decoding algorithms should exhibit low computational complexity in order to support high-throughput implementations. Third, the coding overhead should be kept as small as possible, corresponding to code rates close to unity. Finally, the adopted coding scheme should provide good robustness against burst packet losses while allowing the redundancy level to be adapted to the channel conditions whenever

required. Rateless coding techniques, such as Fountain codes, represent a particularly attractive solution in this respect, as they can generate an arbitrary number of repair packets on demand, enabling flexible adaptation of the coding overhead to the observed channel conditions [250]. Nonetheless, this technique implies variable waiting times to recover the source packets, other than requiring feedback from the receiver to the transmitter.

4.1.2.2 Erasure codes for laser SatComs: CCSDS specification

To improve the reliability of future space communication systems operating under stringent latency and availability requirements, the CCSDS has standardized packet-oriented erasure coding mechanisms intended to complement conventional PHY-layer FEC schemes [253].

The proposed techniques are applicable to both RF and optical communication systems, significantly improving end-to-end reliability without requiring retransmissions.

The CCSDS recommendation adopts systematic LDPC codes as the reference family for packet-level erasure correction because they provide performance close to the PEC capacity while maintaining affordable implementation complexity.

Instead of employing a dedicated encoder based on a generator matrix, CCSDS exploits the parity-check matrix directly during encoding. More specifically, the $n-k$ repair symbols are initially treated as unknown symbols, whereas the k information symbols are assumed to be known. The repair symbols are then obtained by solving the parity-check equations through the Maximum-Likelihood Pivoting (ML-P) decoding algorithm [254]. Consequently, the encoding procedure is transformed into a decoding problem based solely on the parity-check matrix.

To further reduce the encoding complexity, CCSDS recommends the adoption of IRA LDPC codes [255]. In this case, the parity-check matrix assumes the form

$$\mathbf{H} = [\mathbf{H}_u \mid \mathbf{H}_p] \tag{4.35}$$

where $\mathbf{H}_u$ is a sparse matrix associated with the information symbols, while $\mathbf{H}_p$ is a double-diagonal matrix corresponding to the repair symbols. The double-diagonal structure of $\mathbf{H}_p$ enables the repair symbols to be generated recursively.

Specifically, each repair symbol depends only on a subset of information symbols and on the previously computed repair symbol, allowing the encoding complexity to scale linearly with the block length.

At the receiver, decoding is performed through the ML-P algorithm, which combines IT decoding with selective ML decoding, if necessary [254]. The main objective is to retain the low computational complexity of IT decoding while approaching the performance of full Gaussian-elimination decoding.

Initially, IT decoding is applied to recover as many erased symbols as possible by exploiting the sparse parity-check equations. If decoding cannot be completed, only a limited subset of unresolved symbols, referred to as pivots, is recovered through ML decoding.

The complexity and performance of the algorithm are controlled by the parameter $\alpha_{\max}$, representing the maximum number of pivots that may be processed by the ML decoder. Two limiting cases can be identified, i.e.,

- $\alpha_{\max} = 0$, only IT decoding is performed
- $\alpha_{\max} = n - k$, the algorithm reduces to ML decoding.

Intermediate values provide a trade-off between decoding complexity and erasure recovery performance.

CCSDS recommends implementing packet-level erasure coding immediately above the data-link layer, within a dedicated EC shim layer. Positioning the EC functions close to the PHY layer minimizes the propagation of packet losses toward higher protocol layers, particularly when lower-layer packet aggregation mechanisms are employed.

The EC shim layer encapsulates the application data received from the upper layer into dedicated PDUs while transparently interacting with the lower communication protocols. This architecture allows erasure coding to remain independent of the underlying physical transmission technology.

Depending on the availability of a return channel, CCSDS defines four possible operating modes, i.e.,

- Pure EC, in which only packet-level redundancy is exploited without retransmissions mechanisms

- Type-I Hybrid ARQ, where unrecovered source packets are retransmitted after unsuccessful erasure decoding
- Type-II Hybrid ARQ, in which additional repair packets are transmitted instead of retransmitting the original information packets
- Weather Genie, which dynamically adapts the coding strategy according to channel state information obtained through a feedback channel.

Among these alternatives, pure EC represents the simplest implementation since it does not require a feedback channel. The two hybrid ARQ solutions provide greater adaptability to time-varying propagation conditions, whereas the Weather Genie approach requires continuous interaction between transmitter and receiver and therefore introduces the highest implementation complexity. In addition, CCSDS recommends keeping retransmission functionalities outside the EC engine and delegating ARQ operations to upper protocol layers whenever required.

The CCSDS specification supports two different code design methodologies depending on the desired level of flexibility. The first approach, referred to as online code design, allows the coding parameters (n, k) to be dynamically selected according to the current channel conditions or application requirements. This solution employs Flexible IRA (F-IRA) codes, obtained by concatenating a short random outer code with an inner IRA LDPC code generated through random-permutation construction techniques [252].

When adaptive code generation is unnecessary, CCSDS proposes an ad-hoc approach based on a finite set of pre-designed IRA codes constructed from circulant permutation matrices. These structured parity-check matrices generally provide improved decoding performance while simplifying hardware implementation [256]. The standard defines nine code configurations characterized by different codeword lengths and code rates which, for convenience, are reported in Table 4.2.

Within the proposed protocol architecture, the Service Data Unit (SDU) of the EC shim layer corresponds to the Application Data Unit (ADU) received from the upper layer. The encoding process transforms these ADUs into Erasure Coding Data Units (ECDUs), which constitute the PDUs exchanged with the lower

Table 4.2 – CCSDS ad-hoc IRA codes parameters [253]

Code number	n	k	R
1	768	512	2/3
2	3072	2048	2/3
3	24 576	16 384	2/3
4	640	512	4/5
5	2560	2048	4/5
6	20 480	16 384	4/5
7	576	512	8/9
8	2304	2048	8/9
9	18 432	16 384	8/9

communication layers. The EC shim layer interactions with adjacent layers are schematized in Fig. 4.5.

Each EC protocol entity consists of three functional blocks, i.e,

- the encoding (or decoding) matrix
- the encoding (or decoding) engine implementing the LDPC algorithm
- the protocol engine responsible for packetization and protocol management.

At the transmitter, the encoding procedure can be summarized as follows:

1. configure the encoder according to the selected coding parameters
2. copy the k ADUs into the rows of the encoding matrix
3. insert padding bytes whenever there are incomplete rows
4. assign a row index to every source symbol
5. generate the $n - k$ repair symbols, also known as Data Redundancy Units (DRUs)

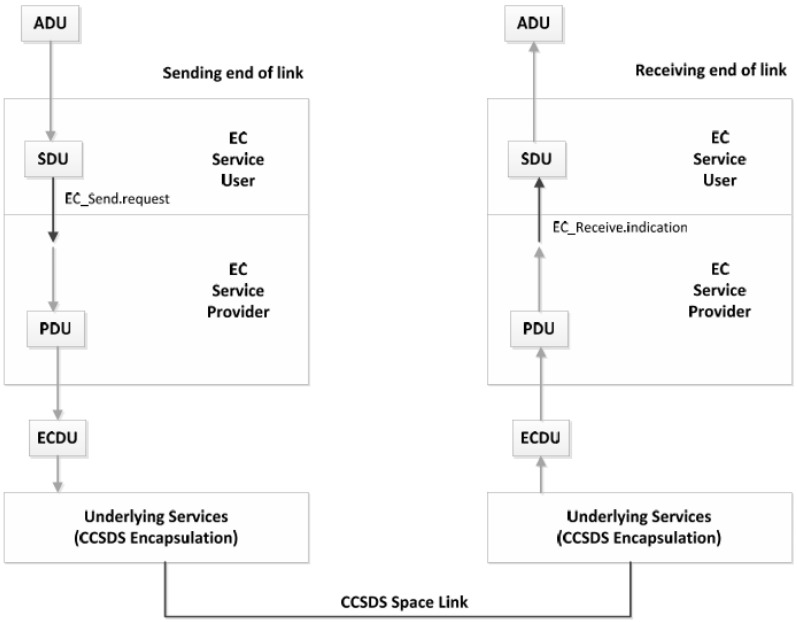


Figure 4.5 – Interaction of the EC shim layer with adjacent layers [253]

6. associate all source and repair symbols with a common codeword identifier
7. encapsulate each symbol into an ECDU by appending an EC header
8. compute and append a CRC trailer
9. forward the resulting ECDUs to the lower communication layer.

The enumerated protocol procedures at the sending side are illustrated in Fig. 4.6. At the receiver, incoming ECDUs are processed according to the information contained in the EC header. Symbols belonging to the same codeword are stored within a temporary decoding matrix. Source symbols received correctly and consecutively can be immediately forwarded to the upper layer, whereas missing symbols trigger the decoding procedure once sufficient redundancy becomes available. If decoding succeeds, the reconstructed ADUs are delivered to the upper layer and the temporary buffer is released.

A practical implementation of the CCSDS erasure coding architecture has been developed by the University of Bologna and the DLR within the Interplanetary

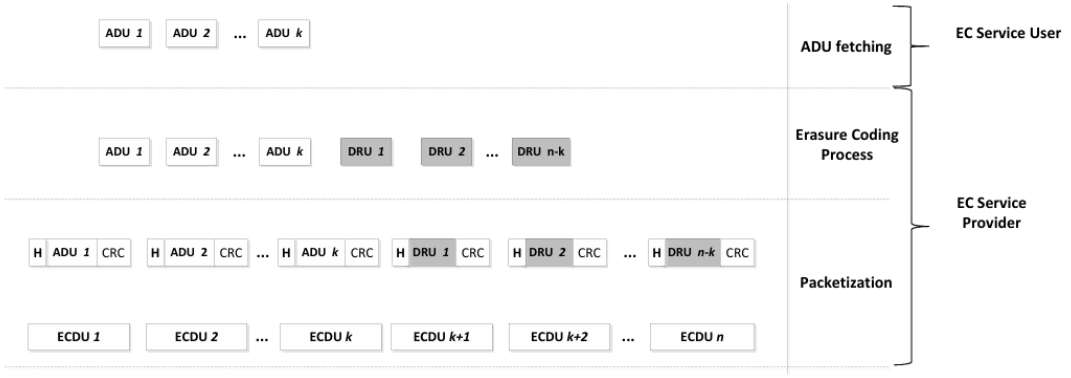


Figure 4.6 – EC processing [253]

Overlay Network (ION) software package [257]. Specifically, ION is NASA-JPL's implementation of the DTN suite, based on the Bundle Protocol (BP) and the Licklider Transmission Protocol (LTP). LTP segments are eventually encapsulated into UDP datagrams through Link Service Adapters (LSAs). Since the standard ION implementation does not include the CCSDS Encapsulation Service, Alessi et al. introduces a new component called Erasure Coding Link Service Adapter (ECLSA), positioned immediately below the LTP layer [257].

In this architecture, LTP segments are treated as source symbols of the EC shim layer. ECLSA supports multiple coding families, including CCSDS-compliant IRA LDPC codes and LDPC staircase codes [258], while also allowing dynamic adaptation of both the codeword length and the code rate [257]. Two external coding libraries may be employed in ECLSA. The proprietary LibecDLR library implements the CCSDS IRA codes, whereas the open-source OpenFEC library supports LDPC Staircase codes [259]. Although based on different code constructions, both libraries implement IT decoding complemented by ML decoding and support the coding parameters defined by CCSDS.

ECLSA is divided into two complementary protocol entities, i.e., (i) the Erasure Coding Link Service Outduct (ECLSO), responsible for encoding and packet transmission, and (ii) the Erasure Coding Link Service Induct (ECLSI), responsible for reception and decoding. Within ECLSO, k incoming LTP segments are interpreted as the source symbols of the EC. The encoder generates $n - k$ repair symbols, and the resulting n encoded symbols are individually encapsulated into

UDP datagrams. To simplify the coding process, all symbols are assumed to have the same length T [bytes]. The corresponding coding matrix therefore consists of n rows and T columns, as shown in Fig. 4.7. Since LTP segments may exhibit variable lengths, the first two bytes of each symbol store the actual segment size, whereas any remaining unused bytes are padded with zeros. If fewer than k source segments are available before the aggregation timer expires, the remaining matrix rows are also padded with zeros before encoding.

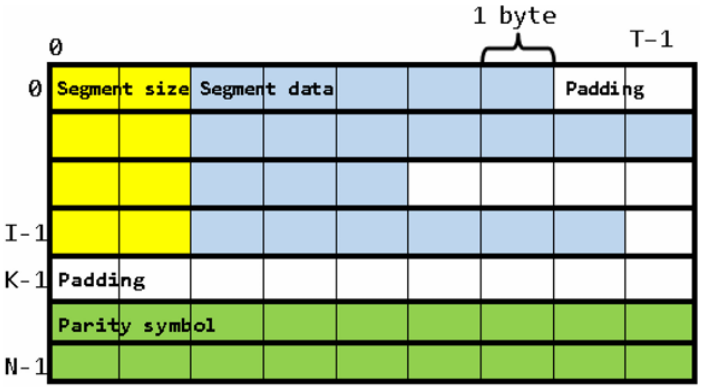


Figure 4.7 – Example of an ECLSA coding matrix [257]

The coding parameters may be selected either statically or dynamically. In particular, the value of k can be adapted to the number of available source segments, while the code rate may be modified according to feedback received from the destination node.

After encoding, each symbol is encapsulated into an individual UDP datagram together with an ECLSA header containing all information required for decoding. The encapsulation process is schematized in Fig. 4.8. The proposed header structure, consisting of 17 bytes, includes the protocol version, extension count, control flags, engine identifier, coding matrix identifier, symbol identifier, and the coding parameters (I, k, n, T). Specifically, I is the number of actual LTP information segments.

At the receiving side, ECLSI reconstructs the decoding matrix by processing the ECLSA headers. Matrix filling terminates when one of the following conditions is satisfied

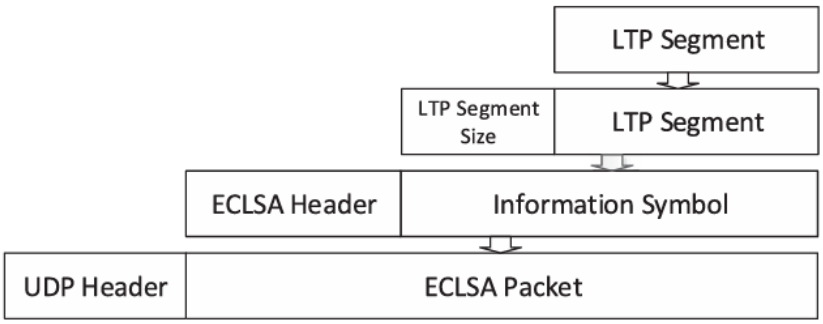


Figure 4.8 – LTP segment incapsulation into a UDP datagram via ECLSA [257]

1. all source symbols have been correctly received
2. one or more source symbols are missing but the last repair symbol has arrived
3. a symbol belonging to the next coding matrix is received
4. a timeout expires.

Once the matrix is complete, LDPC decoding is performed whenever necessary. Successfully recovered source symbols are depacketized by removing the size field and padding bytes before being delivered to the LTP layer. If decoding is unsuccessful, the reliable transmission mechanisms already implemented by LTP transparently recover the missing segments through retransmissions.

Performance evaluations reported in the literature demonstrate that the LDPC-based implementations supported by ECLSA operate very close to the theoretical performance limits over uncorrelated PECs while maintaining practical computational complexity [257].

4.1.3 Interleaving

Interleaving is a well-established technique that can be employed together with both bit-level FEC codes and packet-level ECs to improve the robustness of communication systems against burst errors.

The main objective of an interleaver is to introduce temporal diversity by distributing the symbols of the same codeword over a sufficiently long transmission

interval, so that they experience statistically independent channel realizations. At the receiver, a corresponding deinterleaver restores the original ordering before decoding. As a result, consecutive errors introduced by the propagation channel are dispersed among multiple codewords, making the residual errors appear nearly independent from the decoder perspective.

Interleavers are generally classified into two main categories, namely block interleavers and convolutional interleavers. A block interleaver stores the encoded symbols into a rectangular memory array composed of m rows and n columns, where n typically corresponds to the codeword length. As illustrated in Fig. 4.9, the symbols are written into the memory row by row and subsequently transmitted by reading the matrix column by column. At the receiver, the deinterleaver performs the inverse operation, writing the received symbols column-wise and reading them row-wise. This rearrangement transforms a burst of channel errors into mul-

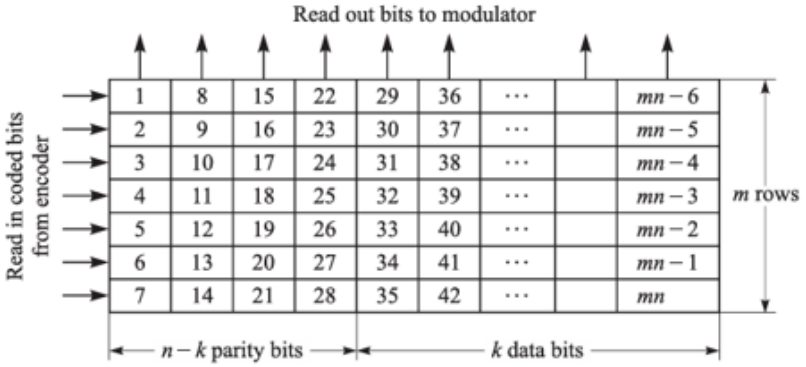


Figure 4.9 – Block interleaver [231]

tiple shorter bursts distributed over different codewords. In particular, a burst affecting $l = mb$ consecutive transmitted symbols is converted into m independent bursts of length b. Consequently, if a block code $\mathbf{C}(n, k)$ is capable of correcting bursts shorter than

$$b < \left\lfloor \frac{n-k}{2} \right\rfloor \tag{4.36}$$

its combination with a block interleaver of degree m results in an interleaved code $\mathbf{C}(mn, mk)$ capable of correcting burst errors of length mb symbols [260].

The improved burst-error resilience comes at the expense of additional latency. Since an entire interleaving matrix must be filled before transmission and completely received before deinterleaving, the overall delay introduced by a block interleaver is approximately $2mn$ symbols [251].

Convolutional interleavers provide an alternative approach that significantly reduces the delay introduced by block interleaving while maintaining comparable burst-error mitigation capabilities. Instead of storing symbols in a two-dimensional memory array, a convolutional interleaver consists of n parallel shift registers having progressively increasing lengths. The incoming encoded symbols are grouped into blocks of n symbols. The i-th symbol of each block, with $i = 1, \ldots, n$, is delayed by $(i-1)nj$ time units through a shift register containing $(i-1)j$ stages, where

$$j = \frac{b}{n} \tag{4.37}$$

and b denotes the target burst length. This concept is shown in Fig. 4.10.

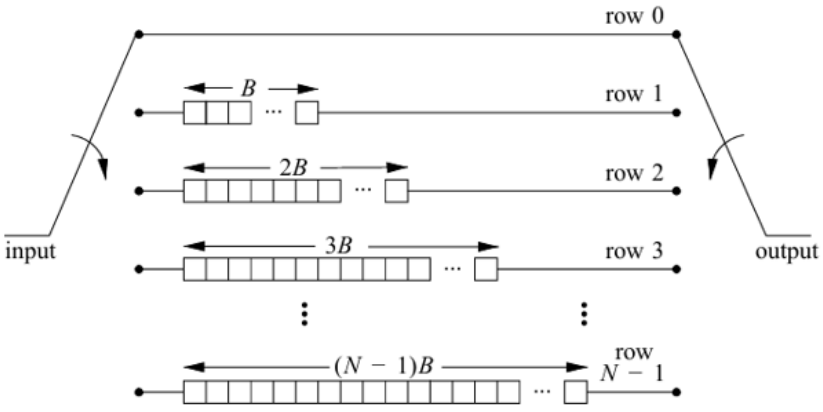


Figure 4.10 – Convolutional interleaver [226]

At the receiver, the deinterleaver applies the complementary delays by means of another bank of shift registers. Specifically, the i-th symbol of each received block is delayed by $(n-i)nj$ time units before being delivered to the decoder, thereby restoring the original ordering of the transmitted sequence.

Unlike block interleavers, convolutional interleavers operate continuously on the incoming data stream and do not require storing an entire interleaving matrix before transmission. Consequently, they introduce a constant latency equal to $(n-$

1)b symbols, which is approximately half the delay required by an equivalent (n, b) block interleaver while providing similar burst-error spreading capability [231]. For applications where latency is a critical design constraint, convolutional interleavers therefore represent an attractive compromise between burst-error protection and transmission delay.

4.1.3.1 Channel interleavers for laser SatComs: CCSDS specifications

The use of channel interleaving in combination with FEC coding is considered in all three CCSDS recommendations for high-data-rate optical communications presented in Section 4.1.1.5 [226, 235, 236].

The first CCSDS recommendation [226], which supports both the concatenated BCH-LDPC coding scheme and the standalone RS code, adopts a convolutional interleaver. Its configuration is determined by three managed parameters, i.e., (i) the number m of binary digits composing each interleaver symbol, (ii) the number N of delay branches (tap delay lines), and (iii) the relative delay B between consecutive delay branches. The parameter m may assume values between 1 and 8, whereas N and B shall satisfy the constraint that the product NB shall be an integer multiple of $64800/m$, which, in turn, is a multuple of N. These conditions ensure compatibility between the interleaver structure and the fixed codeword length adopted by the CCSDS FEC schemes.

The possibility of selecting the interleaver symbol size through the parameter m is particularly advantageous when nonbinary channel codes are employed. In particular, for the RS code defined over the Galois field GF(2^8), choosing $m = 8$ causes each interleaver symbol to coincide with one RS symbol. Consequently, after deinterleaving, burst errors remain confined to the smallest possible number of RS symbols, thereby maximizing the error correction capability of the decoder.

Unlike the previous recommendation, the CCSDS specifications presented in [235,236] adopt block interleavers. Specifically, in [235], the interleaver operates on the output frames generated by the RS encoder, whereas the specification in [236], based on RS product codes, defines the block interleaver through three parameters, i.e., (i) the number K of binary digits composing each interleaver symbol, (ii) the number N of columns of the interleaving matrix, and (iii) the number L of rows. The parameter L is fixed to 2040, corresponding to the number of binary digits

contained in each FEC output frame, while K is set equal to 8 so that each interleaver symbol corresponds to one RS symbol. The number of columns is instead given by

$$N = (k_I + 1)M \tag{4.38}$$

where $k_I = 204$ is a fixed parameter of the interleaver structure and M is a managed parameter representing the number of consecutive FEC blocks concatenated before transmission.

By varying M, the interleaving depth can be adapted to the expected burst-error duration. Larger values of M provide greater protection against long fading events by increasing the temporal separation between adjacent symbols of the same codeword, at the expense of proportionally larger memory requirements and transmission latency.

4.1.3.2 Interleavers for laser SatComs: literature overview

Several studies have investigated the design and dimensioning of interleavers for FSO SatComs systems, providing practical guidelines for mitigating burst errors caused by atmospheric fading [26, 261, 262]. In particular, the impact of channel interleaving has been extensively analyzed for both direct-detection and coherent optical links.

One of the earliest investigations is presented by Mazzali et al. [261], who carried out numerical simulations to optimize the design of channel interleavers for OOK downlink OFLs. The assumed communication chain employs a Serially Concatenated Convolutional Code (SCCC) combined with a convolutional channel interleaver. The SCCC encoder is composed of two four-state rate-1/2 convolutional encoders. The output of the outer encoder is first punctured to obtain an intermediate coding rate of 2/3, then passed through an internal bit interleaver before entering the inner encoder. A second puncturing stage determines the overall code rate, with values of 0.46, 0.69, and 0.87 considered in the performance evaluation. Following channel coding, the encoded bit stream is distributed among the branches of a convolutional interleaver consisting of N delay lines and an interleaving unit of length B. The resulting temporal diversity is given by

$$M = \frac{BN(N-1)}{2R_s}, \tag{4.39}$$

where R_s denotes the transmitted symbol rate. For interleaving to effectively decorrelate consecutive fading events, the memory span M should exceed the coherence time of the optical channel. The reported simulation results show that increasing the interleaver memory significantly improves temporal diversity and enhances the robustness of the communication link against atmospheric fading. Furthermore, the authors provide practical criteria for selecting suitable values of N and B for a desired interleaver memory.

The same design methodology is subsequently extended in [262] to investigate Variable Data Rate (VDR) LEO downlink OFLs. In this work, physical-layer simulations again assume OOK modulation together with SCCC channel coding and convolutional interleaving, while evaluating the influence of adaptive transmission rates on system performance under varying atmospheric conditions.

A comprehensive end-to-end analysis is presented in [26], where channel coding, packet-level erasure coding, PHY-layer interleaving, and HL interleaving are jointly considered. Unlike the previous studies, this work focuses on coherent optical uplinks operating at a data rate of 100 Gbit/s. Two alternative PHY-layer FEC schemes are evaluated, namely oFEC and LDPC codes, while packet-level erasure coding is modeled through an ideal MDS code. The performance assessment investigates several PHY-layer configurations, including different FEC code rates and channel interleaving spans, by estimating the average unfaded received optical power required to maintain an outage probability below 10^{-3}. In addition, the combined effect of channel coding, packet-level erasure coding, and HL interleaving is evaluated in terms of the resulting Packet Error Rate (PER), highlighting the benefits of jointly optimizing protection mechanisms across multiple layers of the communication protocol stack.

4.2 End-to-end OFL simulation framework

The design and assessment of effective mitigation techniques for OFLs require accurate models capable of reproducing the impact of atmospheric scintillation and other channel impairments on communication performance. Building upon the channel modeling background presented in Chapters 2 and 3, this chapter describes the numerical framework developed to model and evaluate the digital

mitigation techniques considered throughout this research, namely channel coding, interleaving, and packet-oriented erasure coding.

The proposed framework has been implemented in Matlab as an extension of the previously-developed numerical tool. While the link budget tool focused on estimating the average received optical power, the present extension enables the evaluation of the complete end-to-end communication performance by introducing the estimation of the PER. The newly developed PER evaluation module exploits the outputs already generated by the link budget tool and SNR models presented in Chapter 2, together with the fading generation framework of Chapter 3.

A direct simulation of the complete PHY layer would result in prohibitive computational complexity, especially when system-level analyses involving long observation times and numerous channel realizations are required. For this reason, the proposed simulator adopts PHY layer abstraction techniques, which provide an efficient approximation of the PHY layer performance while accurately accounting for the effects of channel impairments such as atmospheric fading. Indeed, PHY layer abstraction has become a widely adopted methodology for system-level performance evaluation, as it enables the assessment of advanced communication techniques with significantly reduced computational cost compared to detailed bit-level simulations. Nevertheless, the reliability of the obtained results strongly depends on the accuracy of the adopted abstraction model.

In the following, existing PHY layer abstraction techniques are reviewed, motivating the selection of the methodology adopted for FSO communications. The corresponding abstraction model is then derived and integrated into the simulation framework. Subsequently, the overall simulation algorithm employed to evaluate the performance of both PHY and HL mitigation techniques over OFLs is presented. Finally, the numerical results obtained with the developed simulator are discussed and compared with results available in the literature, thereby validating the proposed implementation. Particular attention is devoted to communication architectures based on commercially available coherent optical transceivers, consistently with the ESTOL specification.

4.2.1 Physical layer abstraction

The SNR is one of the fundamental performance metrics in information theory, as it provides the basis for deriving theoretical limits on channel capacity and transmission reliability. For several conventional modulation formats, analytical expressions relating the SNR to the Symbol Error Rate (SER) and the channel capacity have been established in the literature [260]. However, modern communication systems typically employ sophisticated modulation and FEC schemes, for which closed-form expressions describing the decoding performance are generally unavailable. In these cases, the relationship between the SNR and relevant performance metrics is usually obtained through detailed PHY-layer simulations or experimental implementations under Additive White Gaussian Noise (AWGN). For instance, the performance curves of the oFEC scheme adopted in OTN have been obtained through extensive simulations and hardware implementations in [244].

To avoid the computational burden associated with full bit-level PHY layer simulations, system-level simulators commonly rely on PHY layer abstraction techniques. These methods map the instantaneous channel conditions onto an equivalent scalar metric, which is subsequently used to estimate the decoding performance [263]. Different abstraction methods employ different mapping functions, resulting in varying levels of accuracy depending on the considered communication system and channel conditions.

Among the available approaches, Mutual Information (MI)-based abstraction has attracted significant attention. A link quality model relying on MI was proposed in [263], motivated by the observation that the MI constitutes a reliable predictor of the post-FEC BER in Coded Modulation (CM) systems [264]. In particular, when expressed as normalized MI, the decoding performance becomes independent of the adopted modulation format [263]. This abstraction methodology has also been applied to FSO communications in [265], where it has been exploited to jointly optimize channel interleaving and FEC based on finite-geometry LDPC and Turbo product codes.

Nevertheless, the oFEC scheme adopted in the ESTOL specification belong to the class of Bit-Interleaved Coded Modulation (BICM) systems. For this family of communication schemes, the Generalized Mutual Information (GMI) has been

shown to provide a significantly more accurate prediction of the post-FEC BER [264]. Consequently, GMI has been selected in the present work as the PHY layer abstraction metric for coherent OFLs.

The following sections recall the principles of CM and BICM, highlighting their main differences. Subsequently, the concepts of MI and GMI are discussed together with the corresponding computation methods adopted within the developed simulation framework.

4.2.1.1 CM and BICM: basic concepts

Consider a digital communication system in which a sequence of N_b independent and uniformly distributed (i.u.d.) information bits $\mathbf{i} = [i[1], i[2], \ldots, i[N_b]]$ is encoded and mapped into a sequence of N_s modulation symbols

$$\mathbf{x} = [\mathbf{x}[1], \mathbf{x}[2], \ldots, \mathbf{x}[N_s]] \tag{4.40}$$

which are used to modulate a finite-energy real-valued waveform $v(t)$ for transmission over the communication channel. The transmitted signal can be expressed as

$$s(t) = \sum_{n=0}^{N_s-1} x[n]\, v(t - nT_s) \tag{4.41}$$

where T_s denotes the symbol interval and $R_s = 1/T_s$ is the signaling rate, proportional to the occupied bandwidth. The resulting information rate is

$$\mathrm{R} = \frac{N_b}{N_s T_s} = R_s R \qquad [\text{bit/s}] \tag{4.42}$$

where

$$R = \frac{N_b}{N_s} \qquad [\text{bit/symbol}] \tag{4.43}$$

represents the spectral efficiency of the transmission.

After propagation through the communication channel, the received samples are affected by both channel gain $h(t)$ and additive noise $z(t)$. Assuming a discrete-time equivalent channel model, the received sampled signal can be written as

$$\mathbf{y}[n] = h[n]\mathbf{x}[n] + z[n] \tag{4.44}$$

where $\mathbf{h}[n]$ is the channel gain, $\mathbf{z}[n]$ denotes the additive noise contribution, $\mathbf{x}[n]$, $\mathbf{y}[n]$, $\mathbf{z}[n] \in \mathbb{R}^N$, and $\mathbf{h}[n] \in \mathbb{R}$.

The objective of the encoder is to map the information sequence $\mathbf{i}$ into a sequence of symbols $\mathbf{x}$ in a way that enables reliable communication while maintaining a manageable decoding complexity. In practical systems, each transmitted symbol belongs to a discrete constellation $\mathcal{S}$ of size $M = |\mathcal{S}| = 2^m$. As shown in Fig. 4.11, the encoding process can be separated into two consecutive operations. First, a binary encoder generates a sequence of N_c code bits

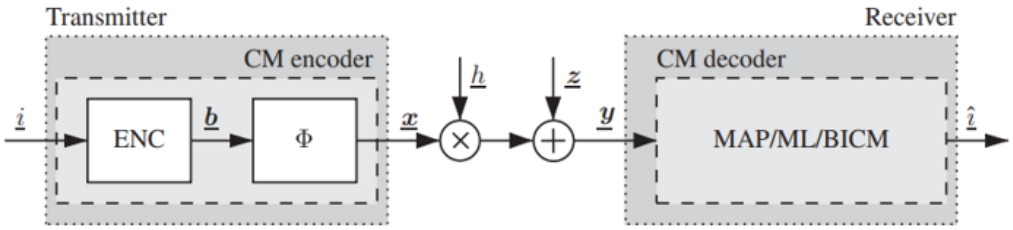


Figure 4.11 – Block diagram of a CM communication system [266]

$$\mathbf{b} = [\mathbf{b}[1], \mathbf{b}[2], \ldots, \mathbf{b}[N_c]] \tag{4.45}$$

which are subsequently grouped into m-bit tuples and mapped onto constellation symbols. This joint design of channel coding and modulation is generally referred to as CM [266].

The binary encoder is characterized by the code rate

$$R_c = \frac{N_b}{N_c} \qquad \text{[bit/code bit]} \tag{4.46}$$

where $N_c = mN_s$. Consequently, the overall spectral efficiency becomes

$$R = mR_c \tag{4.47}$$

The encoder maps each possible information message into a unique sequence of transmitted symbols, thereby defining a code $\mathcal{X} \subset \mathcal{S}^{N_s}$ composed of 2^{N_b} codewords. At the receiver, the decoder exploits the received observation vector $\mathbf{y}$ to estimate the transmitted information sequence.

Several practical implementations of CM have been proposed in the literature. Among the most representative are Trellis-coded modulation, which combines convolutional coding with M-ary modulation, multilevel coding, which relies on the use of a demultiplexer that separates the information bits into m independent messages which are then encoded by m parallel binary encoders, and BICM, which has become the de facto solution adopted by modern communication standards owing to its flexibility and implementation simplicity [266].

In a BICM system, illustrated in Fig. 4.12, the binary encoder is followed by a bit-level interleaver Π before symbol mapping. The interleaver permutes the encoded bit sequence $\mathbf{c}$, producing a new binary sequence

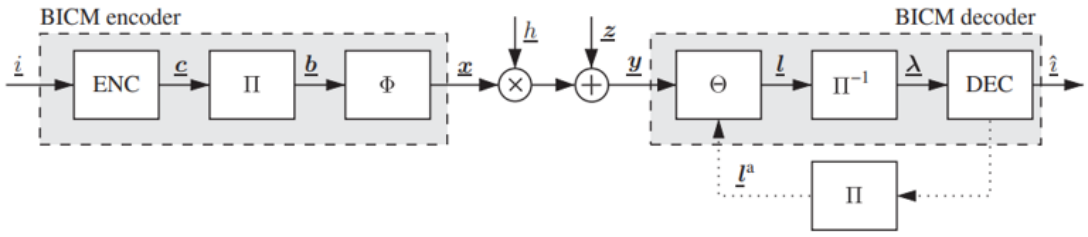


Figure 4.12 – Block diagram of a BICM communication system [266]

$$\mathbf{b} = \Pi(\mathbf{c}) \tag{4.48}$$

which is then mapped by the mapper Φ onto constellation symbols according to a predefined binary labeling.

The corresponding receiver is composed of three functional blocks, i.e., (i) a demapper, Θ, (ii) a deinterleaver, Π^{-1}, and (iii) a binary decoder. The demapper computes, for every transmitted bit, a Log-Likelihood Ratio (LLR), also referred to as an L-value, which measures the reliability associated with the received bit. After deinterleaving, the resulting LLRs are forwarded to the channel decoder, which estimates the transmitted information bits.

The BICM architecture naturally enables IT receiver structures, commonly referred to as Bit-Interleaved Coded Modulation with Iterative Decoding/Demapping (BICM-ID). In this configuration, the demapper and the channel decoder iteratively exchange reliability information about the code bits, known as extrinsic

L-values, progressively refining the LLR estimates and improving the decoding performance. Compared with conventional CM schemes, BICM offers a high degree of modularity because modulation and channel coding can be designed independently. This characteristic facilitates the implementation of adaptive modulation and coding strategies. The modest performance degradation introduced by the bit-wise receiver is generally compensated by the substantial reduction in implementation complexity [266].

The performance of a BICM system strongly depends on the adopted signal constellation and on its binary labeling. Let

$$\mathcal{S} = \{\mathbf{x}_1, \mathbf{x}_2, \ldots, \mathbf{x}_M\} \tag{4.49}$$

be an M-ary constellation. The difference between two constellation points is defined as

$$\mathbf{d}_{i,j} = \mathbf{x}_i - \mathbf{x}_j \tag{4.50}$$

while the minimum Euclidean distance of the constellation is

$$d_{\mathcal{S}}^{\min} = \min_{i,j \in \mathcal{J} i \neq j} \|\mathbf{d}_{i,j}\| \tag{4.51}$$

where $\mathcal{J} = 1, \ldots, M$ enumerates all the constellation points. Assuming equiprobable transmission, each constellation symbol is selected with probability

$$P_{\mathbf{X}}(\mathbf{x}_i) = \frac{1}{M} \tag{4.52}$$

The ESTOL specification considers both PSK and QAM modulation formats. An MPSK constellation is defined as

$$\mathcal{S}_{\text{MPSK}} = \left\{ \left[\cos\left(\frac{(2i-1)\pi}{M}\right), \sin\left(\frac{(2i-1)\pi}{M}\right) \right] : i \in \mathcal{J} \right\} \tag{4.53}$$

whereas rectangular MQAM constellations are obtained as the Cartesian product of two MPAM constellations, i.e.,

$$\mathcal{S}_{\text{MQAM}} = \mathcal{S}_{M_1\text{PAM}} \times \mathcal{S}_{M_2\text{PAM}}. \tag{4.54}$$

with $M_1 = 2^{m_1}$, $M_2 = 2^{m_2}$, and $|\mathcal{S}_{MQAM}| = M = 2^{m_1+m_2}$. In detail,

$$\mathcal{S}_{MPAM} = \{\pm(M-1)\Delta, \pm(M-3)\Delta, \ldots, \pm\Delta\} \tag{4.55}$$

in which, for uniform symbols distributions

$$\Delta = \sqrt{\frac{3}{M^2 - 1}} \tag{4.56}$$

A square MQAM constellation is obtained as a particular case of a rectangular MQAM when $M_1 = M_2 = \sqrt{M}$. In this case,

$$\Delta_{QAM} = \sqrt{\frac{3}{2(M-1)}} \tag{4.57}$$

A constellation can be represented in an ordered manner by means of the $N \times M$ matrix $\mathbf{X} = [\mathbf{x}_1, \ldots, \mathbf{x}_M]$ where, for MPSK

$$\mathbf{x}_i = [\cos((2i-1)\pi/M), \sin((2i-1)\pi/M)]^T \tag{4.58}$$

while for MPAM

$$\mathbf{x}_i = -(M - 2i + 1)\Delta \tag{4.59}$$

Finally, $\mathbf{X}_{MQAM}$ can be obtained as the ordered product of two MPAM constellations [266]. It is important to note that this definition implies that, even though 4PSK and 4QAM are equivalent, the ordering is different.

For a $N \times M$ constellation, it is possible to define a binary labeling as an $m \times M$ binary matrix $\mathbf{Q} = [\mathbf{q}_1, \ldots, \mathbf{q}_M]$, where $\mathbf{q}_i = [q_{i,1}, \ldots, q_{i,m}]^T \in \mathbb{B}^m$ is the binary label of the constellation symbol $\mathbf{x}_i$. Among the various possibilities, Gray labeling is such that constellation points at minimum Euclidean distance have labels that differ only in one bit. The most widely adopted Gray labeling is the Binary Reflected Gray Code (BRGC), which is also employed by the OpenROADM specification referenced in ESTOL [242]. BRGC owes its popularity to two main properties, i.e., (i) it minimizes the bit-error probability when the SNR tends to infinity, and (ii) it leads to high achievable rates in BICM transmissions for medium-to-high SNRs.

From a decoding perspective, the BICM receiver performs bit-wise ML estimation by exploiting the LLRs generated by the demapper. This approach approximates the joint symbol likelihood as the product of the individual bit likelihoods, namely

$$p_{\mathbf{Y}|\mathbf{B}}(\mathbf{y}[n]|\mathbf{b}[n]) \approx \prod_{k=1}^{m} p_{\mathbf{Y}|B_k}(\mathbf{y}[n]|b_k[n]) \tag{4.60}$$

Therefore, the BICM decoder can be interpreted as a mismatched implementation of the optimal ML receiver [266, 267]. The approximation in Eq. (4.60) becomes an identity when bits are independently mapped into each of the dimensions of the constellation $\mathcal{S}$.

Despite the suboptimality of the mismatched decoder, the simplicity of its bit-level operations most often outweighs the related decoding loss.

4.2.1.2 MI and GMI: basic concepts

The fundamental limits on the transmission rates achievable by CM and BICM systems can be established through information-theoretic principles. By modeling the transmitted symbols $\mathbf{x}[n]$ as N-dimensional independent random variables with probability mass function $P_{\mathbf{X}}(\mathbf{x}[n])$, and omitting the discrete-time index n for simplicity, the channel model of Eq. (4.44) can be rewritten in terms of random vectors as

$$\mathbf{Y} = H\mathbf{X} + \mathbf{Z} \tag{4.61}$$

where $\mathbf{Z} \in \mathbb{R}^N$ is an N-dimensional Gaussian noise vector with independent and identically distributed (i.i.d.) zero-mean components and PSD equal to $N_0/2$, while H denotes the channel gain.

Assuming continuous, i.i.d. input symbols with PDF $p_{\mathbf{X}}(\mathbf{x})$, $\mathcal{S} = \mathbb{R}^N$, and perfect channel state information at the receiver, the MI between the transmitted and received random vectors, conditioned on the channel realization $H = h$, is defined as

$$\begin{aligned} I(\mathbf{X};\mathbf{Y}) = \mathbb{E}_{\mathbf{X},\mathbf{Y}|H=h}\left[\log_2 \frac{p_{\mathbf{X},\mathbf{Y}|H}(\mathbf{X},\mathbf{Y}|h)}{p_{\mathbf{Y}|H}(\mathbf{Y}|h)p_{\mathbf{X}}(\mathbf{X})}\right] \\ \int_{\mathbb{R}^N} p_{\mathbf{x}}(\mathbf{x}) \int_{\mathbb{R}^N} p_{\mathbf{Y}|\mathbf{X},H}(\mathbf{y}|\mathbf{x},h) \log_2 \frac{p_{\mathbf{Y}|\mathbf{X},H}(\mathbf{y}|\mathbf{x},h)}{p_{\mathbf{Y}|H}(\mathbf{y}|h)} d\mathbf{y} d\mathbf{x} \end{aligned} \tag{4.62}$$

Equation (4.62) outlines that the MI depends on both the instantaneous SNR and the input distribution. Measured in bit/symbol or, equivalently, bit/channel use, it represents the maximum transmission rate that allows reliable communication, provided that sufficiently long randomly generated codewords are employed. Therefore,

$$R \leq I(\mathbf{X};\mathbf{Y}) \tag{4.63}$$

The channel capacity is obtained by maximizing the MI over all possible input distributions, i.e.,

$$C(\mathbf{X};\mathbf{Y}) = \max_{p_X} I(\mathbf{X};\mathbf{Y}) \tag{4.64}$$

In practical communication systems, finite constellations are employed. Consequently, PDFs are replaced by Probability Mass Functions (PMFs) $P_{\mathbf{X}}$ with M non-zero mass points.

For a CM system with uniformly distributed input symbols over AWGN channel, the MI can be expressed as

$$\begin{aligned} I^{\mathrm{cm}}\left(\mathrm{snr},\mathbf{X},\mathbf{p}_{s,u}\right) = m - \frac{1}{M}\int_{\mathbb{R}^N}\left(\frac{\mathrm{snr}}{\pi}\right)^{N/2}\sum_{i\in\mathcal{I}} e^{-\mathrm{snr}\|\mathbf{y}-\mathbf{x}_i\|^2} \\ \cdot\log_2\left(\frac{\sum_{j\in\mathcal{I}} e^{-\mathrm{snr}\|\mathbf{y}-\mathbf{x}_j\|^2}}{e^{-\mathrm{snr}\|\mathbf{y}-\mathbf{x}_i\|^2}}\right) d\mathbf{y} \end{aligned} \tag{4.65}$$

where $\mathbf{p}_{s,u}$ denotes the uniform symbol distribution. More generally, the achievable rate can be increased by optimizing both the constellation geometry and the input probabilities, giving rise to the CM capacity

$$C^{\mathrm{cm}}(\mathrm{snr}) = \max_{\mathbf{X},\mathbf{p}_s} I^{\mathrm{cm}}(\mathrm{snr},\mathbf{X},\mathbf{p}_s) \tag{4.66}$$

where the joint optimization of the constellation and symbol probabilities is commonly referred to as signal shaping.

Unlike CM receivers, BICM receivers employ a mismatched decoding metric based on bitwise probabilities. The decoding rule can be written as

$$\hat{\mathbf{b}}^{\mathrm{bi}} = \arg\max_{\mathbf{b}\in\mathcal{B}} \prod_{n=1}^{N_s} \text{ı}(\mathbf{b}[n],\mathbf{y}[n]) \tag{4.67}$$

where the symbol-decoding metric is factorized as

$$\text{ı}(\mathbf{b},\mathbf{y}) = \prod_{k=1}^{m} \text{ı}_k(b_k,\mathbf{y}) \tag{4.68}$$

with

$$\text{ı}_k(b,\mathbf{y}) = p_{\mathbf{Y}|B_k}(\mathbf{y}|b) \tag{4.69}$$

Since the metric in Eq. (4.68) differs from the optimal ML metric, the relevant achievable information rate is no longer the MI but the GMI, defined as

$$I_{\shortparallel}^{\mathrm{gmi}}(\mathbf{B};\mathbf{Y}) = \max_{s\geq 0} I_{\shortparallel,s}^{\mathrm{gmi}}(\mathbf{B};\mathbf{Y}) \tag{4.70}$$

where

$$I_{\mathbf{q},s}^{\mathrm{gmi}}(\mathbf{B};\mathbf{Y}) = \mathbb{E}_{\mathbf{B};\mathbf{Y}}\left[\log_2 \frac{\shortparallel(\mathbf{B};\mathbf{Y})^s}{\sum_{\mathbf{b}\in\mathbb{B}^m} P_{\mathbf{B}}(\mathbf{b})\,\shortparallel(\mathbf{b},\mathbf{Y})^s}\right] \tag{4.71}$$

It is worth observing that when the decoding metric is matched to the channel statistics, i.e., $\shortparallel(\mathbf{b},\mathbf{y}) \propto p_{\mathbf{Y}|\mathbf{B}}(\mathbf{y}|\mathbf{b})$, and $s = 1$, the GMI reduces to the MI [266]. Furthermore, it has been shown that the symbol metric of Eq. (4.68) is optimal among all bitwise decoding metrics for BICM systems [266]. Under these conditions, the achievable rate of a BICM receiver becomes

$$I^{\mathrm{bi}}(\mathrm{snr},\mathbf{X},\mathbf{p}_b,\mathbf{Q}) = \sum_{k=1}^{m} I(B_k;\mathbf{Y}) \tag{4.72}$$

where $\mathbf{Q}$ denotes the binary labeling of the constellation and $\mathbf{p}_b$ is the bits PMF. The bitwise MIs in Eq. (4.72) is given by

$$I(B_k;\mathbf{Y}) = \mathbb{E}_{B_k,\mathbf{Y}|H=h}\left[\log_2 \frac{p_{\mathbf{Y}|H,B_k}(mathbfY|h,B_k)}{p_{\mathbf{Y}|H}(\mathbf{Y}|h)}\right] \tag{4.73}$$

Therefore, the MI represents an achievable rate for any CM systems employing optimal ML decoding, whereas the GMI is an achievable rate for the usboptimal BICM receivers relying on mismatched bitwise decoding. Although the GMI is not theoretically guaranteed to be the largest achievable rate for mismatched decoders, practical coding schemes most often operate very close to this limit [266].

For AWGN channels and uniformly distributed input bits, i.e., $P_{B_k}(0) = 1/2$ for $k = 1,\ldots,m$, the GMI becomes

$$\begin{aligned} I^{\mathrm{bi}}(\mathrm{snr},\mathbf{X},\mathbf{p}_{b,u},\mathbf{Q}) = m - \int_{\mathbb{R}^N} \frac{1}{M}\left(\frac{\mathrm{snr}}{\pi}\right)^{N/2} \sum_{k=1}^{m}\sum_{b\in\mathcal{B}}\sum_{i\in\mathcal{I}_{k,b}} e^{-\mathrm{snr}\|\mathbf{y}-\mathbf{x}_i\|^2} \\ \cdot \log_2\left(\frac{\sum_{j\in\mathcal{I}_{k,b}} e^{-\mathrm{snr}\|\mathbf{y}-\mathbf{x}_j\|^2}}{\sum_{j'\in\mathcal{I}} e^{-\mathrm{snr}\|\mathbf{y}-\mathbf{x}_{j'}\|^2}}\right) d\mathbf{y} \end{aligned} \tag{4.74}$$

where $\mathbf{p}_{b,u} = [0.5,\ldots,0.5]^T$ denotes the uniform bit distribution, and $\mathcal{I}_{k,b} \subset 1,\ldots,M$, with $|\mathcal{I}_{k,b}| = M/2$, identifies the subset of constellation points whose k-th labeling bit equals b.

Similarly to CM, a BICM pseudo-capacity can be defined as

$$C^{\mathrm{bi}}(\mathrm{snr}) = \max_{\mathbf{X},\mathbf{p}_b,\mathbf{Q}} I^{\mathrm{bi}}(\mathrm{snr}, \mathbf{X}, \mathbf{p}_b, \mathbf{Q}) \tag{4.75}$$

where the optimization is carried out over the constellation and its binary labeling, other than over the vector of bitwise probabilities. The term pseudo-capacity is adopted because the GMI does not necessarily coincide with the maximum achievable rate for given $\mathbf{X}, \mathbf{p}_b, \mathbf{Q}$.

For systems employing M-ary modulation with uniformly distributed symbols, it is convenient to normalize the GMI by the number of bits per symbol, obtaining the Normalized Generalized Mutual Information (NGMI)

$$\mathrm{NGMI} = \frac{\mathrm{GMI}}{m} \tag{4.76}$$

whose values lie in the interval $0 \leq \mathrm{NGMI} \leq 1$.

The NGMI has the same information-theoretic interpretation as the rate of a binary channel code, since it represents the fraction of information bits conveyed per transmitted coded bit. Consequently, an ideal binary FEC code with rate R_c can achieve error-free decoding whenever

$$\mathrm{NGMI} > R_c \tag{4.77}$$

In practice, however, real FEC implementations exhibit a finite performance gap with respect to the theoretical limit. Therefore, successful decoding requires

$$\mathrm{NGMI} > \mathrm{NGMI}^{\star} = R_c + \Delta \qquad \Delta \geq 0 \tag{4.78}$$

where Δ accounts for the implementation loss of the adopted coding scheme [268]. The effectiveness of NGMI as a post-FEC predictor, particularly for SD decoders and MQAM constellations, has been extensively proved in the literature [244, 264, 268].

4.2.1.3 Numerical computation of MI and GMI

The MI and GMI can be evaluated numerically through different techniques, including Monte-Carlo integration and Gauss-Hermite (GH) quadrature [266, 269]. Owing to its high accuracy and computational efficiency, the latter approach has

been adopted for the PHY layer abstraction implementation and is therefore described in the following.

For a generic function $g(t)$ possessing bounded $2J$-th derivative, the J-point GH quadrature is given as

$$\int_{-\infty}^{+\infty} \exp\left[-|t|^2\right] g(t)\, dt \approx \sum_{k=1}^{J} \alpha_k g(\xi_k) \tag{4.79}$$

where ξ_k and α_k denote the quadrature nodes and weights, respectively, and can be numerically derived for different values of J. The approximation becomes exact as $J \to \infty$ [269]. The quadrature nodes correspond to the roots of the Hermite polynomial

$$H_J(x) = J! \sum_{r=0}^{\lfloor J/2 \rfloor} \frac{(-1)^r}{r!(J-2r)!} (2x)^{J-2r} \tag{4.80}$$

whereas the associated weights are defined as

$$\alpha_k = \frac{2^{J-1} J! \sqrt{\pi}}{\left[J H_{J-1}(\xi_k)\right]^2} \tag{4.81}$$

The GH quadrature naturally extends to N-dimensional spaces according to

$$\int_{\mathbb{R}^N} \exp\left[-\|\mathbf{t}\|^2\right] g(\mathbf{t})\, d\mathbf{t} \approx \sum_{k_1=1}^{J} \cdots \sum_{k_N=1}^{J} g(\boldsymbol{\xi}) \prod_{n=1}^{N} \alpha_{k_n} \tag{4.82}$$

where $\mathbf{t} = [t_1, \ldots, t_N]^T \in \mathbb{R}^N$ and $\boldsymbol{\xi} = [\xi_{k_1}, \ldots, \xi_{k_N}]^T \in \mathbb{R}^N$.

Using this formulation, the CM MI of Eq. (4.65) can be rewritten as

$$I^{\mathrm{cm}}(\mathrm{snr}, \mathbf{X}, \mathbf{p}_{s,u}) = m + \int_{\mathbb{R}^N} \exp\left[-\|\mathbf{t}\|^2\right] g_u^{\mathrm{cm}}(\mathbf{t})\, d\mathbf{t} \tag{4.83}$$

where

$$g_u^{\mathrm{cm}}(\mathbf{t}) = -\pi^{-N/2} \sum_{i \in \mathcal{I}} p_{s,i} \log_2 \left(\sum_{j \in \mathcal{I}} p_{s,j} \exp\left(-2\sqrt{\mathrm{snr}} \langle \mathbf{t}, \mathbf{d}_{i,j} \rangle - \mathrm{snr} \|\mathbf{d}_{i,j}\|^2\right) \right) \tag{4.84}$$

Similarly, the BICM GMI of Eq. (4.74) can be expressed as

$$I^{\mathrm{bi}}(\mathrm{snr}, \mathbf{X}, \mathbf{p}_{b,u}, \mathbf{Q}) = m + \int_{\mathbb{R}^N} \exp\left(-\|\mathbf{t}\|^2\right) g_u^{\mathrm{bi}}(\mathbf{t})\, d\mathbf{t} \tag{4.85}$$

where

$$g_u^{\mathrm{bi}}(\mathbf{t}) = m\, g_u^{\mathrm{cm}}(\mathbf{t}) + \frac{\pi^{-N/2}}{M} \sum_{k=1}^{m} \sum_{b\in\mathbb{B}} \sum_{i\in\mathcal{I}_{k,b}} \log_2 \left(\sum_{j\in\mathcal{I}_{k,b}} \exp\left(-2\sqrt{\mathrm{snr}}\langle \mathbf{t}, \mathbf{d}_{i,j}\rangle - \mathrm{snr}\|\mathbf{d}_{i,j}\|^2\right) \right) \tag{4.86}$$

By replacing the multidimensional integrals with the GH approximation of Eq. (4.82), the MI and GMI become

$$I^{\mathrm{cm}}(\mathrm{snr}, \mathbf{X}, \mathbf{p}_{s,u}) \approx m + \sum_{k_1=1}^{J} \cdots \sum_{k_N=1}^{J} g_u^{\mathrm{cm}}(\boldsymbol{\xi}) \prod_{n=1}^{N} \alpha_{k_n} \tag{4.87}$$

and

$$I^{\mathrm{bi}}(\mathrm{snr}, \mathbf{X}, \mathbf{p}_{b,u}, \mathbf{Q}) \approx m + \sum_{k_1=1}^{J} \cdots \sum_{k_N=1}^{J} g_u^{\mathrm{bi}}(\boldsymbol{\xi}) \prod_{n=1}^{N} \alpha_{k_n} \tag{4.88}$$

Equations (4.87) and (4.88) have been implemented in Matlab as a basis to develop the OFL PHY layer abstraction for the coherent modulation formats adopted by ESTOL, namely DP-QPSK and DP-16QAM [187]. Following the OpenROADM specification [242], BRGC labeling has been employed for all constellations. A GH quadrature order of $J = 20$ has been selected as a suitable compromise between computational accuracy and execution time.

Figures 4.13a, 4.13b, and 4.13c report the numerically-evaluated MI and GMI curves as functions of the SNR for QPSK, 8PSK, and 16-ary Quadrature Amplitude Modulation (16QAM), respectively.

As expected, the MI generally exceeds the GMI because the former assumes optimum symbol-wise decoding, whereas the latter accounts for the suboptimal bit-wise decoding. Nevertheless, Gray-labeled QPSK constitutes a special case in which the two metrics coincide. This property arises because the independent in-phase and quadrature components allow Gray-coded QPSK to be interpreted as two independent BPSK constellations, making the bit-wise and symbol-wise decoding rules equivalent [269].

The obtained curves further show that higher-order modulation formats achieve larger MI and GMI values at a given SNR, thus enabling higher spectral efficiencies. However, the performance gap between MI and GMI becomes increasingly

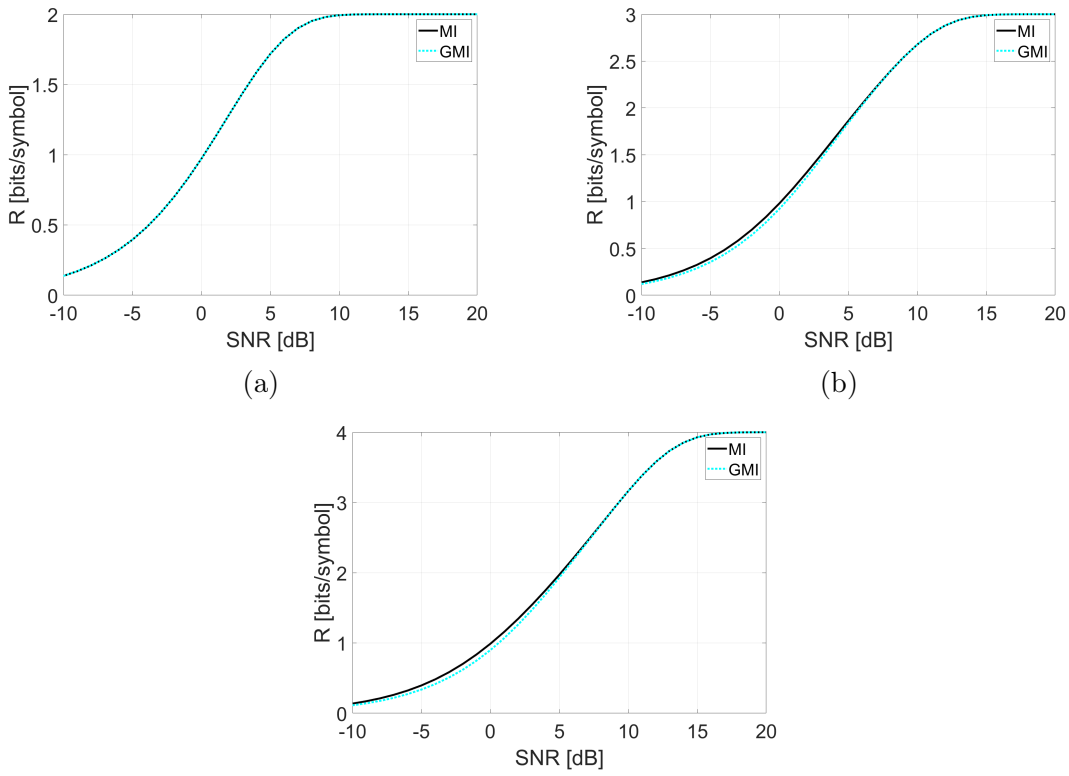


Figure 4.13 – CM MI and BICM GMI for (a) QPSK, (b) 8PSK, and (c) 16QAM modulation over the AWGN channel

pronounced as the modulation order grows, reflecting the loss associated with mismatched BICM decoding. Moreover, higher-order constellations are inherently more sensitive to synchronization impairments and therefore require larger SNR values for reliable operation [269].

The numerical results presented in Figs. 4.13a, 4.13b, and 4.13c have been compared with the reference curves reported in [269], confirming the correctness of the developed implementation.

Finally, Fig. 4.14 illustrates the NGMI obtained for the considered modulation formats. As expected, lower-order constellations provide larger NGMI values for a given SNR, indicating greater robustness and lower coding redundancy requirements to reach a target PER.

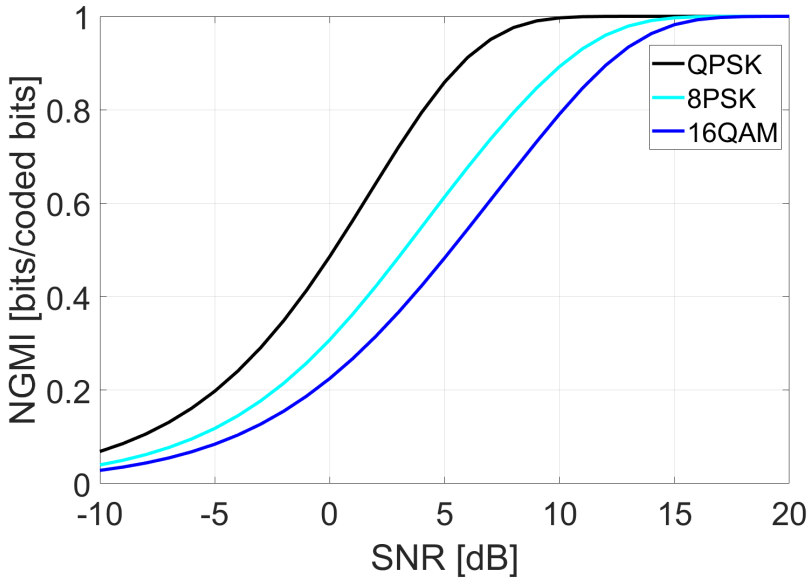


Figure 4.14 – NGMI as a function of the SNR for QPSK (black curve), 8PSK (cyan curve), and 16QAM (blue curve) modulation schemes over the AWGN channel

4.2.2 End-to-end OFL simulation framework: algorithm definition

The end-to-end numerical framework developed to evaluate the effectiveness of the PHY and HL mitigation techniques follows the methodology proposed in [26, 270]. Specifically, the implemented algorithm provides an efficient link-level abstraction of the complete optical communication chain while preserving the accurate modeling of channel impairments.

The algorithm takes as input time series of the received optical power at either the satellite terminal or the OGS. These time series account for both the deterministic attenuation mechanisms determining the average received power and the stochastic fluctuations introduced by atmospheric turbulence and, eventually, pointing jitter. They are generated by means of the numerical tools presented in Chapters 1 and 2. In detail, the link budget tool is used to determine the average received power, while the fading generation algorithms are used to synthesize turbulence- and/or jitter-induced power fluctuations over time.

The complete processing chain implemented in the proposed numerical frame-

work is summarized in Fig. 4.15, which schematically illustrates the successive stages of received-power processing, PHY layer abstraction, channel interleaving, packet erasures generation, HL interleaving, erasure decoding, and final PER estimation, detailed hereafter.

Starting from the received-power time series, the corresponding sequence of instantaneous SNRs is evaluated by exploiting the noise models presented in Section 2.3. The resulting SNR samples are subsequently converted into instantaneous NGMI values by means of the numerical procedure described in Section 4.2.1.3. This operation constitutes the PHY layer abstraction step. In particular, assuming that the communication system employs a FEC with code rate R_c, reliable decoding is considered feasible whenever the instantaneous NGMI exceeds the decoding threshold $R_c + \Delta$, where Δ represents the implementation gap of the adopted FEC code, as discussed in Section 4.2.1.2. Owing to the random nature of the FSO channel, however, an outage may occur with probability

$$P_{\text{outage}} = P(\text{NGMI} < R_c + \Delta) \tag{4.89}$$

The effect of channel interleaving is reproduced by applying a moving average to the instantaneous NGMI sequence through a uniform sliding window whose duration is chosen equal to the latency introduced by the considered channel interleaver. This aproach tacitly assumes that (i) the transmitted bits are uniformly distributed over the interleaver span and (ii) a convolutional interleaver is adopted [26,270]. Nonetheless, it is worth noting that implementing channel interleavers with durations compatible with hundreds-of-Gbit/s optical links requires extremely large, high-speed, space-qualified memory resources, which currently represent a significant technological challenge [26].

Whenever the instantaneous NGMI falls below the decoding threshold, the PHY layer FEC will not permit error-free decoding, leading to the loss of the corresponding packet at higher protocol layers. Consequently, the NGMI sequence is converted into an instantaneous PER time series by means of a binary threshold operation. More specifically,

$$\text{PER}(t) = \begin{cases} 1 & \text{NGMI}(t) < R_c + \Delta \\ 0 & \text{NGMI}(t) \geq R_c + \Delta \end{cases} \tag{4.90}$$

where a value of one denotes complete packet erasure, whereas a value of zero indicates successful decoding.

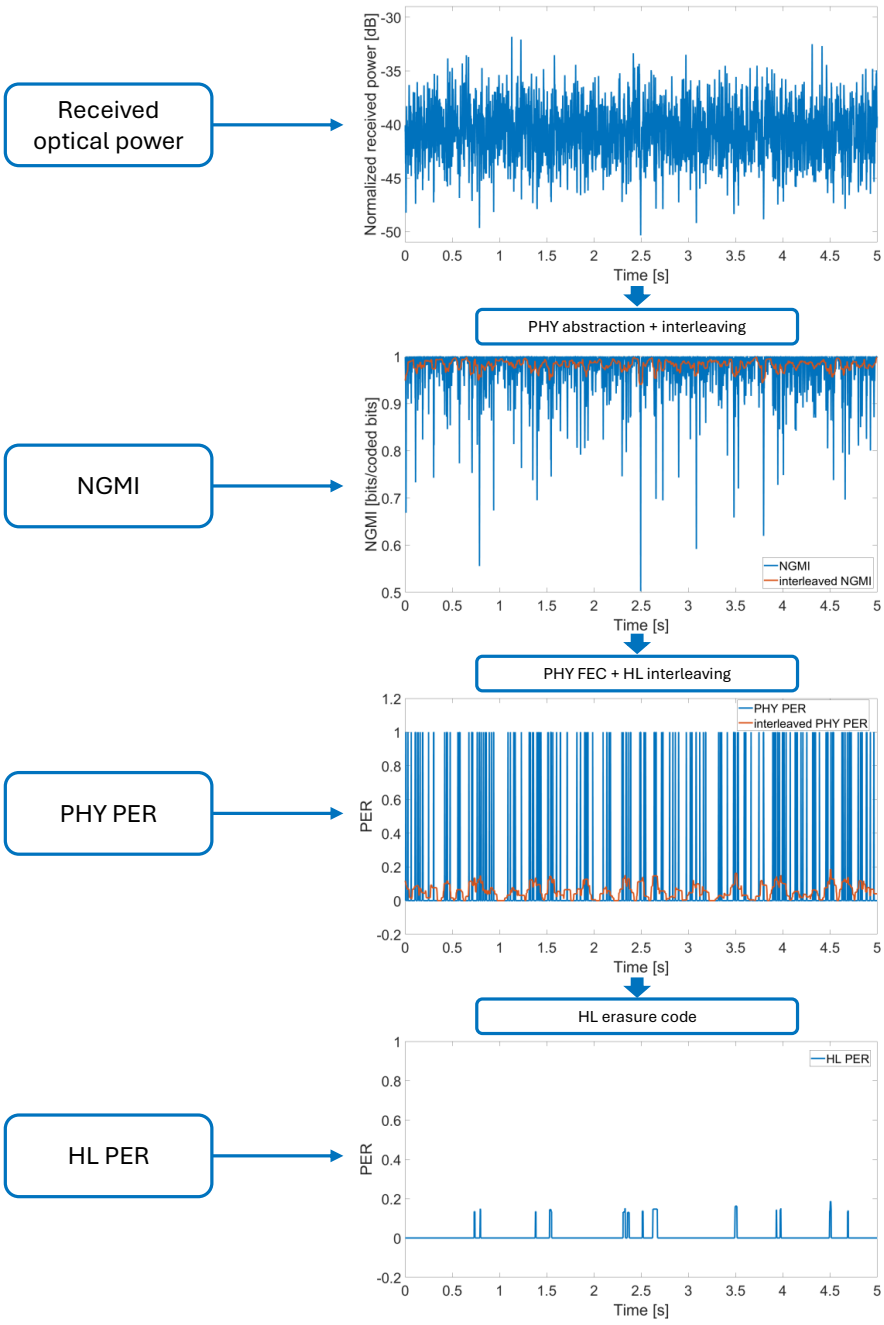


Figure 4.15 – Schematic representation of the algorithm implemented in the end-to-end OFL simulation tool

Similarly to the PHY layer case, packet-level interleaving is modeled by averaging the PER sequence through a uniform sliding window. This abstraction again assumes a convolutional packet interleaver with packets uniformly distributed over the interleaver duration.

The packet-oriented EC is modeled as an ideal MDS code. Under this assumption, successful decoding is achieved whenever the fraction of correctly received packets exceeds the EC rate R_{EC}. Denoting by $\mathrm{PER}_{\mathrm{HL}}^{\mathrm{int}}(t)$ the PER after HL deinterleaving, the output PER after erasure decoding is given by

$$\mathrm{PER}_{\mathrm{HL}}^{\mathrm{dec}}(t) = \begin{cases} 0 & 1 - \mathrm{PER}_{\mathrm{HL}}^{\mathrm{int}}(t) > R_{\mathrm{EC}} \\ \mathrm{PER}_{\mathrm{HL}}^{\mathrm{int}}(t) & \text{otherwise} \end{cases} \tag{4.91}$$

Therefore, whenever a sufficient number of packets is available, the erasure decoder completely reconstructs the missing information. Otherwise, decoding fails and the residual packet losses remain unchanged.

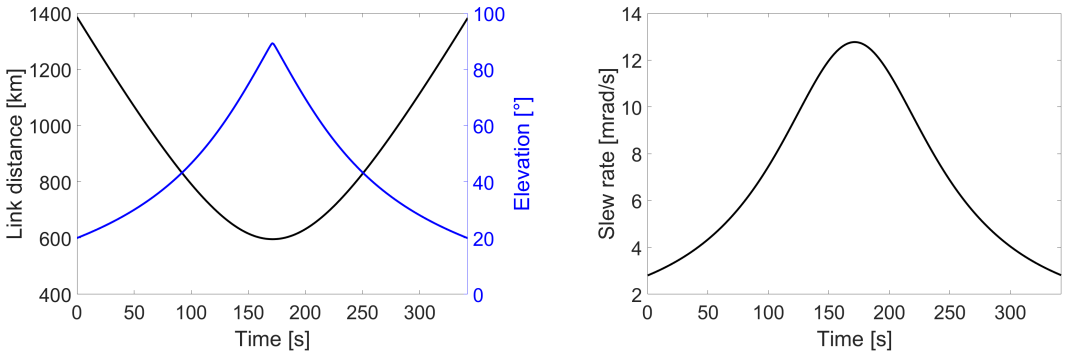
Finally, the overall communication performance is quantified by computing the time-average value of the decoded HL PER, $\left\langle \mathrm{PER}_{\mathrm{HL}}^{\mathrm{dec}}(t) \right\rangle$, which represents the final performance metric employed to assess the effectiveness of the considered mitigation techniques.

4.2.3 Performance assessment of 100 Gbit/s coherent OFLs

To validate the developed end-to-end simulation framework and assess the effectiveness of the considered digital mitigation techniques, a 100 Gbit/s coherent downlink OFL has been simulated.

The same approach is adopted by Canuet to assess the performance of AO pre-compensated coherent OFLs [26]. Specifically, the author employs received optical power time series obtained from the ESA's Alpha-Up experimental campaign, eventually complemented by laboratory-generated fading traces. On the contrary, the analysis reported hereafter relies upon fading time series entirely generated through the numerical models presented in Sections 3.2 and 2.2. Consequently, both the deterministic propagation losses and the temporal statistics of atmospheric turbulence are consistently reproduced within a unified simulation framework.

The analyzed scenario considers the downlink transmission from a LEO satellite orbiting at an altitude of 600 km toward an OGS located at an altitude of 10 m. The satellite trajectory has been generated using a SGP4 propagator. Figure 4.16a reports the evolution of the propagation distance (black curve) and elevation angle (blue curve) during the satellite pass, where the initial time, $t = 0$, corresponds to the instant at which the satellite becomes visible above an elevation angle of 20°.



(a) (b)

Figure 4.16 – (a) Link distance (black curve), elevation angle (blue curve) and (b) slew rate as a function of time for the simulated downlink LEO OFL

The corresponding satellite slew rate, shown in Fig. 4.16b, has been numerically derived from the satellite azimuth and elevation coordinates as observed from the OGS, and subsequently employed as an input to the fading synthesis algorithm. In this way, the influence of the apparent wind induced by satellite motion on the temporal characteristics of atmospheric scintillation is explicitly included in the model. The resulting scintillation coherence time is illustrated in Fig. 4.17a. As expected, the coherence time decreases as the satellite approaches higher elevation angles because the increasing apparent wind accelerates the evolution of atmospheric turbulence, thereby reducing the temporal correlation of irradiance fluctuations.

Another key parameter required by the fading generator is the scintillation index. This quantity has been computed at a wavelength of $\lambda = 1550$ nm using the optical link budget tool. The corresponding results are presented in Fig. 4.17b. Atmospheric turbulence has been modeled through the modified HV profile assuming a refractive-index structure parameter at ground level equal to 1.7×10^{-13} m$^{-2/3}$

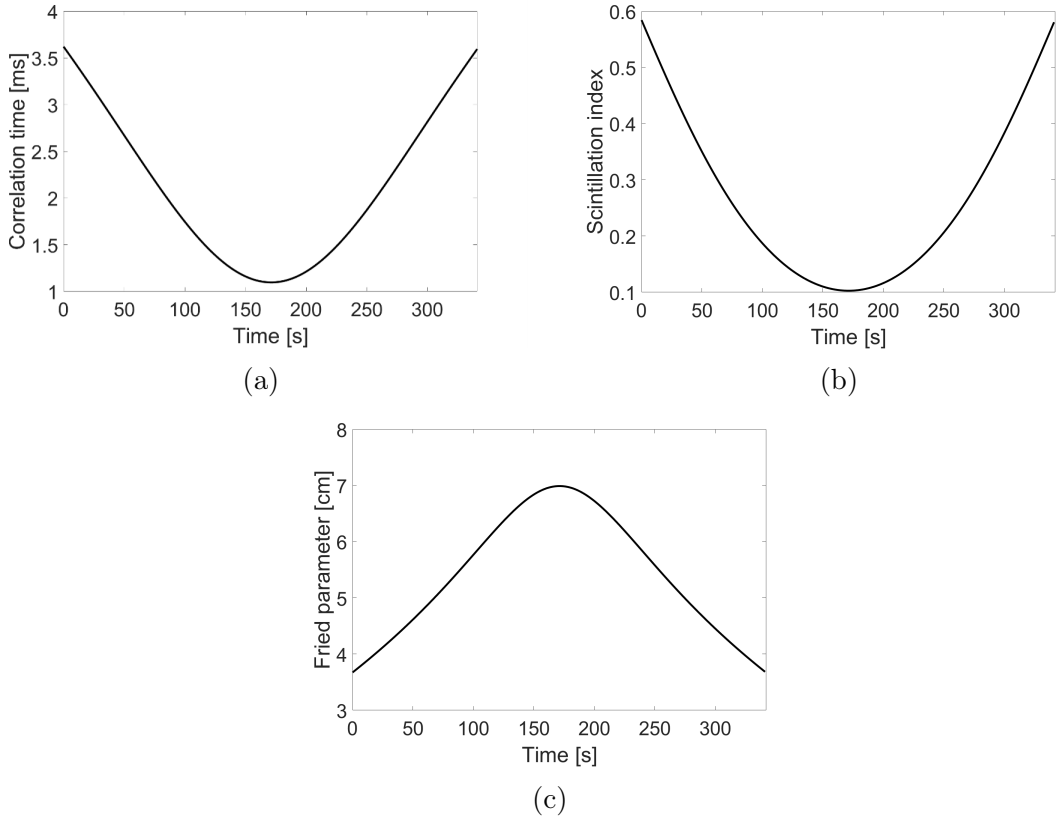


Figure 4.17 – (a) Scintillation correlation time, (b) scintillation index, and (c) Fried's parameter as a function of time for the simulated downlink LEO OFL

and a ground wind speed of 8 m/s, representative of strong turbulence conditions. Nevertheless, the adoption of a receiving telescope with a diameter of 40 cm significantly mitigates irradiance fluctuations through aperture averaging. Extended Rytov theory has been used to perform this analysis.

As expected, stronger scintillation occurs at lower elevation angles, where the optical path through the turbulent atmosphere is longer. This behavior is reflected by the larger scintillation index and the corresponding reduction of the Fried's parameter reported in Fig. 4.17c.

To assess the link performance under the worst-case scenario, the received power time series has been generated at an elevation angle of 30°. Under these conditions, the computed Fried's parameter is $r_0 = 4.62$ cm. Figure 4.18 illustrates the resulting one-minute received optical power time series, normalized with re-

spect to the unfaded mean received optical power.

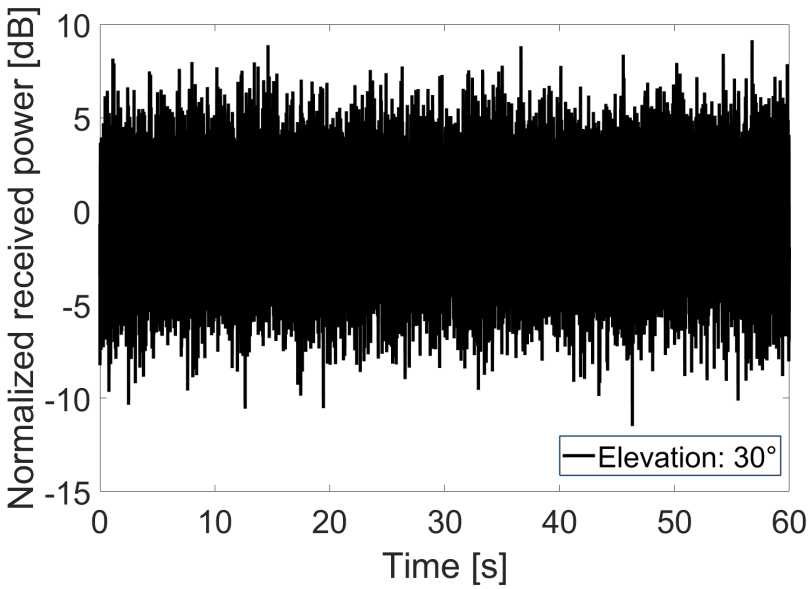


Figure 4.18 – Time series of normalized received optical power as a function of time for the simulated LEO downlink OFL at 30° elevation

The first step of the end-to-end algorithm consists of abstracting the PHY layer by converting the received optical power into NGMI values. To this end, the instantaneous SNR is first evaluated using the coherent noise models of Section 2.3.4.

The considered system is a pre-amplified 100 Gbit/s coherent receiver employing DP-QPSK modulation [187]. Following the recommendations of ESTOL and OpenROADM [187, 242], a symbol rate of 32 Gbaud is assumed, already accounting for the overhead introduced by the PHY layer framing and oFEC coding scheme. The remaining receiver parameters are representative of typical coherent pre-amplified receivers and are summarized in Table 4.3.

To evaluate the SNR, the electrical receiver bandwidth is derived from the symbol rate assuming a roll-off factor of 0.35 [271].

Figure 4.19 reports the computed NGMI as a function of both the instantaneous received optical power per polarization at the EDFA input and the OSNR. The obtained curves closely reproduce those reported in [26], confirming the consistency of the implemented relationships among received power, OSNR, SNR, and NGMI.

Table 4.3 – Receiver parameters for the simulated LEO downlink OFL

Parameter	**Value**
Modulation format	DP-QPSK
Symbol rate	32 Gbaud
LO laser power	15 dBm
EDFA noise figure	5 dB
EDFA gain	30 dB
Photodiode responsivity	0.9 A/W
Photodiode dark current	10 nA
Trans-impedance amplifier thermal one-sided PSD	$9{\cdot}10^{-22}$ W/Hz

The subsequent analyses target an outage probability below 10^{-3}, corresponding to an availability of 99.9% against turbulence-induced fading.

Regarding the PHY-layer coding performance, the target post-FEC BER is fixed to 10^{-10}. For a DVB-S2 system employing a digital OFL, this value was proven to ensure error-free operation for both regenerative and transparent optical communication architectures [272]. According to the performance curves presented in [244], this BER target corresponds to an NGMI threshold of approximately 0.92 for the considered oFEC over an AWGN channel.

The PHY layer performance is first evaluated by determining the minimum unfaded received optical power per polarization required to satisfy the outage probability target as a function of the channel interleaving duration. The corresponding results are shown in Fig. 4.20, where the unfaded received power denotes the average received power in the absence of turbulence. As expected, increasing the interleaving span provides greater temporal diversity and consequently reduces the required average received power.

Interleaver spans of up to 70 ms have been analyzed, which already produce a significant reduction in the required unfaded power. Note that, for broadband GEO connectivity, longer interleavers may not support the Quality of Serive (QoS)

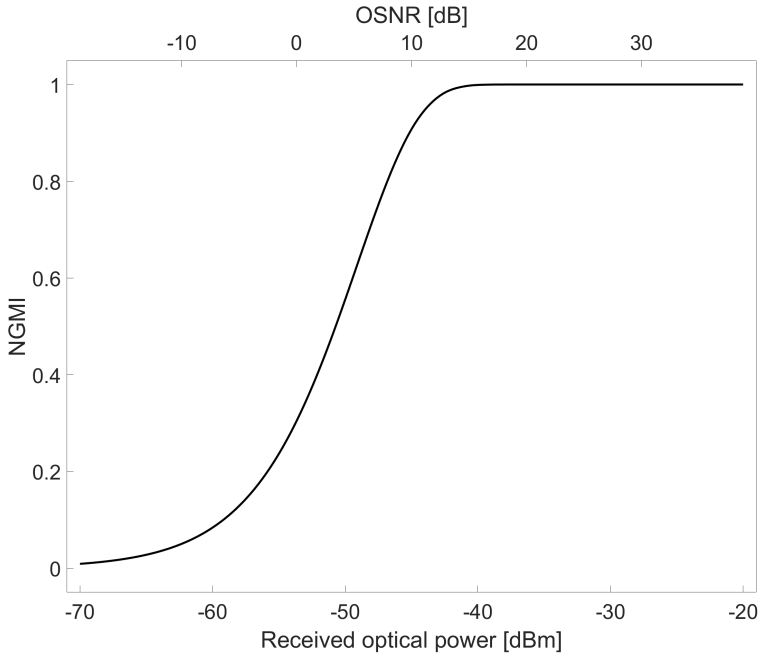


Figure 4.19 – TNGMI as a function of the per-polarization received optical power at the EDFA input and OSNR

requirements set by ITU for Internet Protocol (IP)-based services [273]. In this case, the maximum admissible IP packet transfer delay is set to 400 ms [273]. Considering that propagation and processing delays account for roughly 330 ms at low elevations [273, 274], approximately 70 ms remain available for channel interleaving. Nevertheless, LEO systems exhibit significantly shorter end-to-end propagation delays, typically between 20 and 60 ms [273,275], potentially enabling even longer interleavers.

It should be noted that the analysis of Fig. 4.20 assumes ideal receiver synchronization, meaning that coherent carrier recovery is maintained even during deep fading events. In practice, sufficiently severe fades may cause synchronization loss, resulting in the complete loss of transmitted frames until carrier recovery is re-established. To model this behavior, the NGMI values following a deep fade event (i.e., corresponding to an NGMI value in the sequence below the loss of synchronization threshold) are forced to zero for a time duration corresponding to the re-synchronization time [26]. The concepts is illustrated in Fig. 4.21.

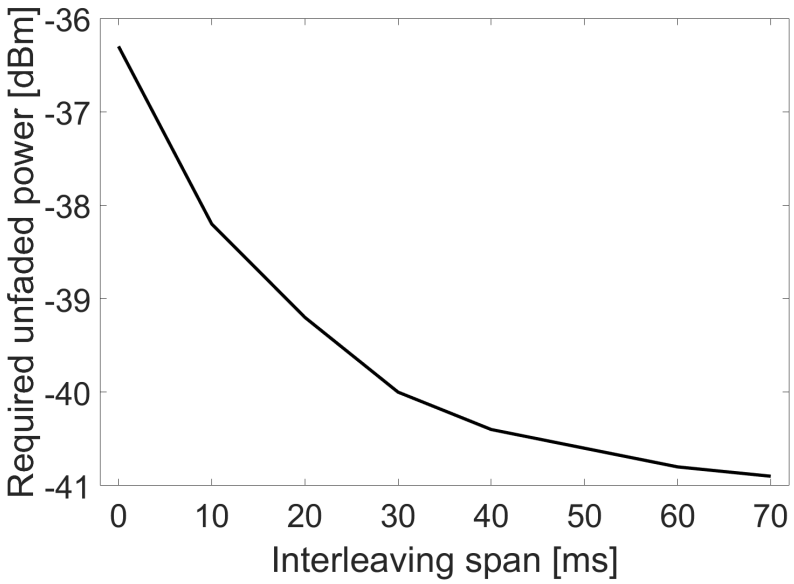


Figure 4.20 – Unfaded optical power per polarization at the pre-amplifier input, as a function of the PHY-layer interleaver span, required to guarantee an outage probability below 10^{-3} for the simulated LEO downlink OFL at $\zeta = 30°$

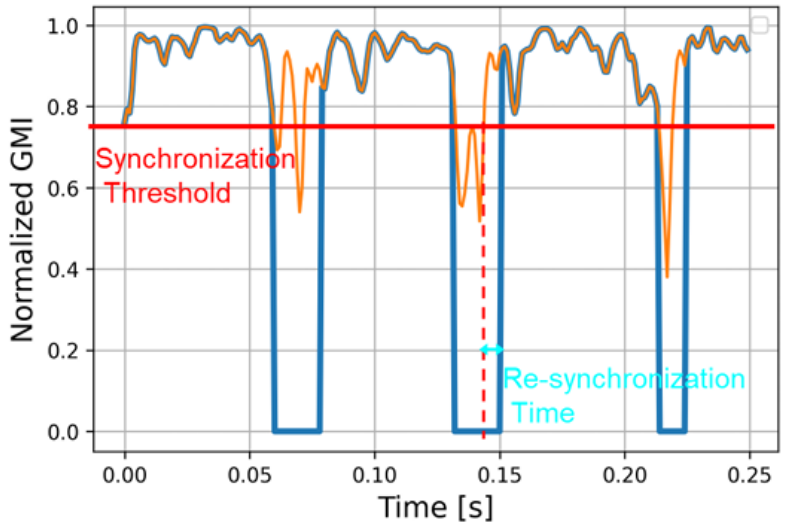


Figure 4.21 – Illustration of the approach to model the impact of synchronization loss and re-synchronization time in the presence of deep fading events [26]

Based on this approach, Fig. 4.22 quantifies the additional received-power

penalty introduced by synchronization loss as a function of both the synchronization threshold and the receiver re-synchronization time, assuming a 70 ms PHY-layer interleaver. The results indicate that even moderate increases in re-

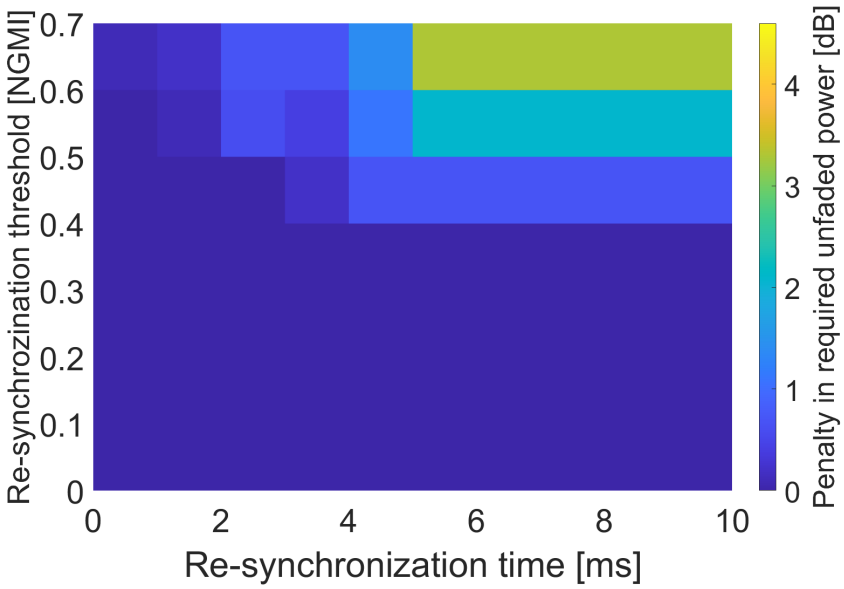


Figure 4.22 – Penalty in required unfaded optical power per polarization at the pre-amplifier input as a function of the re-synchronization time and synchronization loss threshold for the simulated LEO downlink OFL at $\zeta = 30°$. The analysis assumes a PHY-layer interleaver span of 70 ms

synchronization time can significantly increase the required unfaded received power if the loss of synchronization threshold is high.

After assessing the PHY-layer performance, the combined exploitation of PHY and HL mitigation techniques has been investigated. In the following analyses, synchronization losses are neglected to isolate the benefits of coding and interleaving.

The first considered architecture relies on the use of commercial coherent transceivers implementing oFEC coding without additional channel interleaving. Under these conditions, residual turbulence mitigation is entirely entrusted to HL packet-level erasure coding combined with packet interleaving. Figure 4.23 presents the average decoded HL packet error rate, $\langle \mathrm{PER}_{\mathrm{HL}}^{\mathrm{dec}}(t) \rangle$, as a function of

the unfaded received optical power for three EC rates equal to 0.87, 0.76, and 0.65, assuming a 70-ms-long packet interleaver.

As expected, lower EC rates, corresponding to larger redundancy, require lower received powers to satisfy the target packet error rate. For example, when the EC rate is 0.65, an unfaded received power of approximately -41 dBm is sufficient to achieve an average packet error rate of 10^{-3}. Considering the oFEC rate of 0.867, this configuration corresponds to an overall coding rate of 0.56.

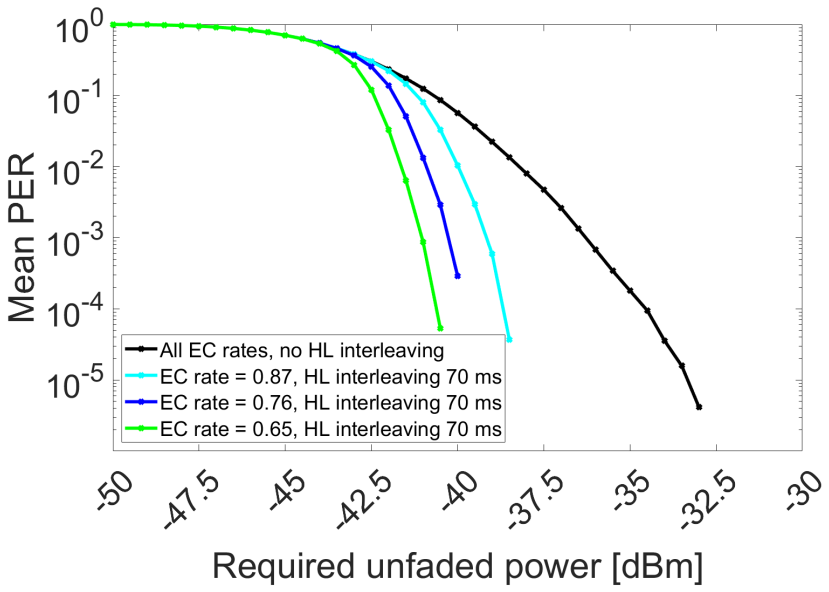


Figure 4.23 – Average HL decoded PER as a function of the per-polarization unfaded received power at the EDFA input for the simulated LEO downlink OFL at $\zeta = 30°$. The analysis assumes oFEC channel coding without additional channel interleaver

A second mitigation strategy investigates the joint optimization of PHY-layer FEC and HL erasure coding. Specifically, PHY-layer coding rates of 0.55, 0.77, and 0.97 are combined with HL EC rates of 0.91, 0.64, and 0.51, respectively, resulting in an identical overall code rate of 0.5 information bits per channel use. No PHY-layer interleaving is assumed, whereas packet interleaving spans 70 ms. Figure 4.24 compares these configurations with a reference solution employing a PHY-layer FEC rate of 0.5 together with a 70-ms channel interleaver. For this

analysis, practical implementation losses of the FEC with respect to the theoretical decoding threshold are neglected.

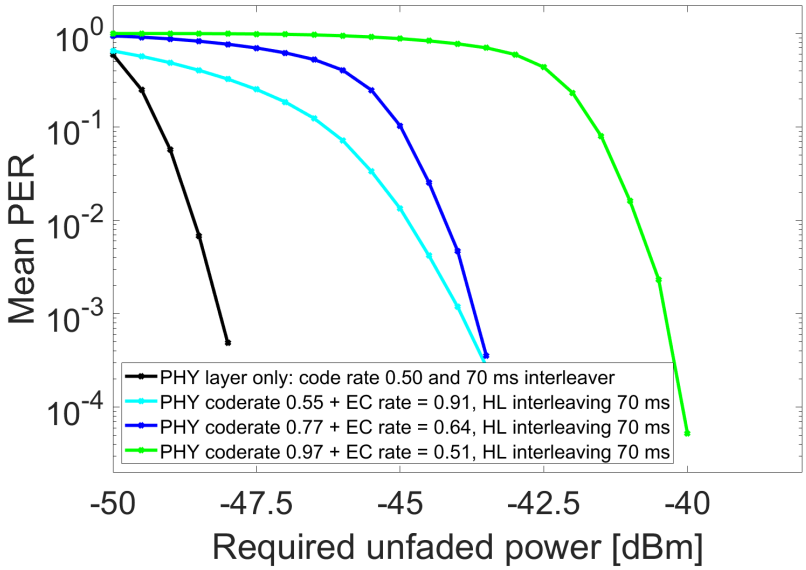


Figure 4.24 – Average HL decoded PER as a function of the per-polarization unfaded received power at the EDFA input for the simulated LEO downlink OFL at $\zeta = 30°$. The analysis assumes channel coding rates of 0.55, 0.77, and 0.79, respectively combined with HL EC rates of 0.91 (cyan curve), 0.64 (blue curve), and 0.51 (green curve) with a HL 70-ms interleaver

The cyan and blue performance curves corresponding to 0.77 and 0.64 EC rates, respectively, intersect. This trend indicates that the optimal distribution of redundancy between the PHY and HL depends on the operating channel conditions.

Despite the reference solution (black curve) can potentially provide the same average PER at lower unfaded powers, it entails some challenges, such as the need for long, space-grade PHY-layer interleavers operating at more than 100 Gbit/s, other than the need to develop ad-hoc transceivers.

These outcomes suggests that neither concentrating all redundancy at the PHY layer nor exclusively relying on HL protection is generally optimal. Instead, an appropriate combination of channel coding and packet-level erasure coding can maximize system performance at reasonable complexity while maintaining the desired overall coding rate.

4.3 Enhanced end-to-end OFL simulation framework with comprehensive packet-level EC modeling

The end-to-end simulation framework presented in the previous section enables an efficient assessment of the combined impact of PHY and HL mitigation techniques against turbulence-induced fading. By relying on PHY-layer abstraction through the NGMI and by modeling the packet-level EC as an ideal MDS code, the developed Matlab tool provides a computationally efficient methodology for evaluating the performance of different coding and interleaving strategies over OFLs.

Although suitable for system-level analyses, the adopted abstraction of the packet-level EC does not account for the finite-length behavior of practical coding schemes nor for the characteristics of their decoding algorithms. In particular, practical ECs exhibit non-ideal decoding performance, whose effectiveness depends on several factors, including the selected code parameters, the codeword length, and the temporal distribution of packet losses. Therefore, a more detailed simulation framework is required to accurately assess the performance of packet-level erasure coding strategies for potential use in OFLs.

To address this need, a second end-to-end simulation framework has been developed by coupling Matlab and C environments. Similarly to the previously described tool, the PHY layer is abstracted through the NGMI-based methodology presented in Section 4.2.1, thus avoiding the computational burden associated with bit-level PHY-layer simulations. However, instead of relying on an ideal MDS EC abstraction, the new framework performs explicit packet-level encoding and decoding by employing a practical, open-source implementation of LDPC erasure coding schemes. Consequently, the effects of finite codeword length, practical decoding algorithms, and realistic packet loss patterns can be directly evaluated.

Another key feature of the developed framework is the realistic modeling of the encapsulation process from Ethernet traffic to the OTN hierarchy adopted by fiber-based coherent optical transceivers [187, 242]. This enables packet erasures generated at the PHY layer to be correctly propagated to the HLs, allowing

the erasure coding process to operate on data units representative of an actual communication system.

The remainder of this section is organized as follows. Section 4.3.1 describes the proposed protocol stack, including the EC shim layer, as well as the encapsulation process of 100GbE traffic into the OTN transmission hierarchy. Subsequently, Section 4.3.2 presents the overall simulation algorithm and discusses the interaction between the PHY-layer abstraction and the packet-level erasure coding process. Finally, Section 4.3.3 presents numerical results obtained with the developed framework and analyzes the performance of the erasure coding schemes discussed in Section 4.1.2.2 under different code rates and payload sizes.

4.3.1 EC-enabled protocol stack for OFLs

The developed simulation framework reproduces the encapsulation process followed by a 100GbE client before transmission over the OFL, as envisioned in [187]. This functionality is required because the HL EC operates on PDUs whose correspondence with PHY-layer FEC codewords determines the receiver erasure pattern. Consequently, a realistic representation of the encapsulation process is essential to correctly evaluate the effectiveness of packet-level erasure coding and to quantify the impact of packet losses generated by turbulence-induced fading.

The implemented encapsulation procedure follows the recommendation defined by OpenROADM [242], which is based on the FlexO-x-DO information structure defined by ITU [276]. Moreover, despite the analysis focuses on 100 Gbit/s coherent links, similar considerations would apply to the higher speeds supported by ESTOL, making the simulation framework extension straightforward.

Figure 4.25 schematically illustrates the proposed protocol hierarchy. The mapping procedure starts from Ethernet Media Access Control (MAC) frames generated by the client, which are denoted as MAC info frames. As discussed in Section 4.1.2, it is desirable to implement the EC as close as possible to the PHY layer. Consequently, the proposed HL EC accepts client MAC frames as the EC shim layer SDUs.

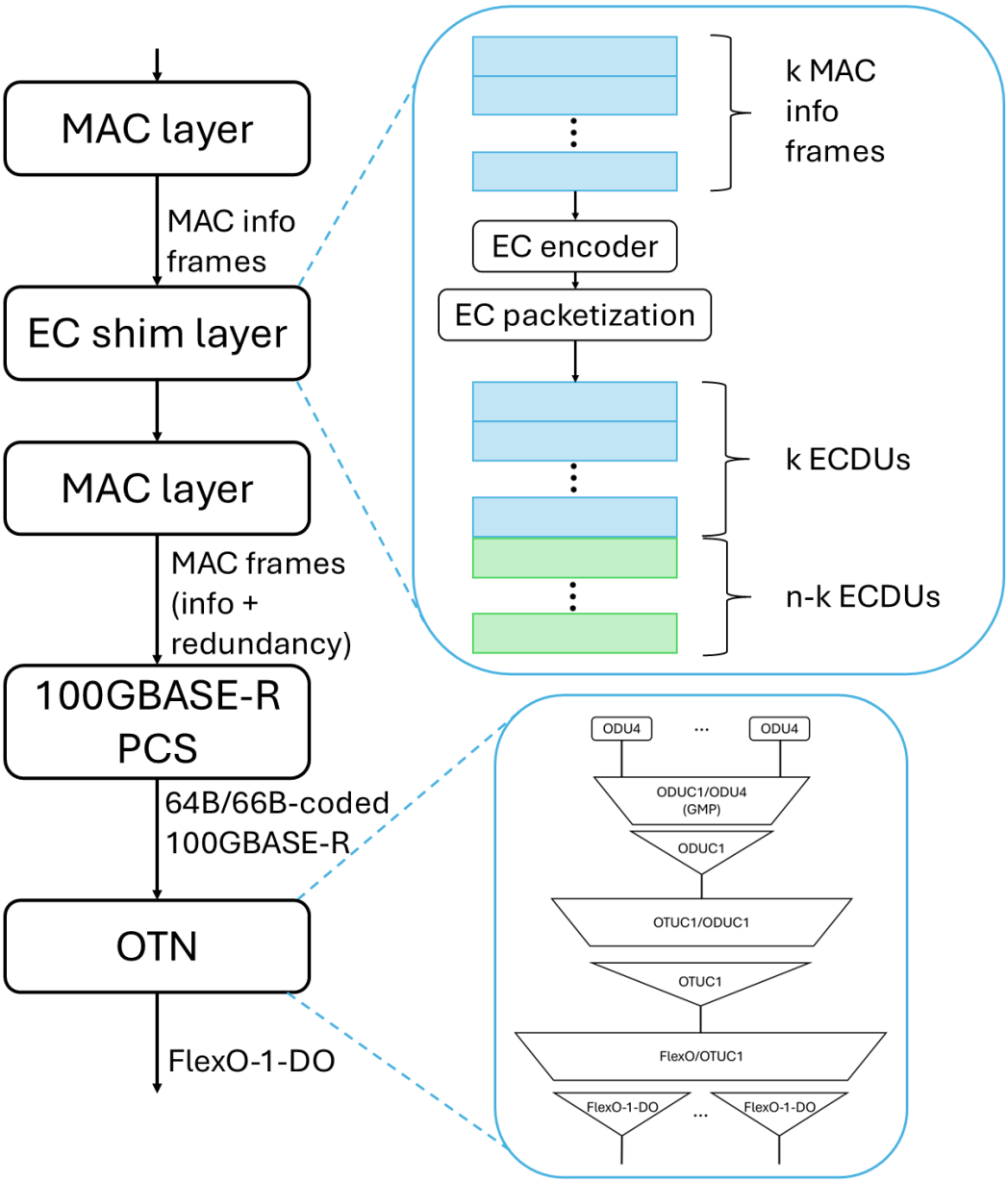


Figure 4.25 – Transmitter protocol stack showing the EC shim layer operation and OTN encapsulation process for a 100 Gbit/s OFL

The Ethernet MAC frame structure is shown in Fig. 4.26.

An Ethernet frame is composed of destination address, source address, length/

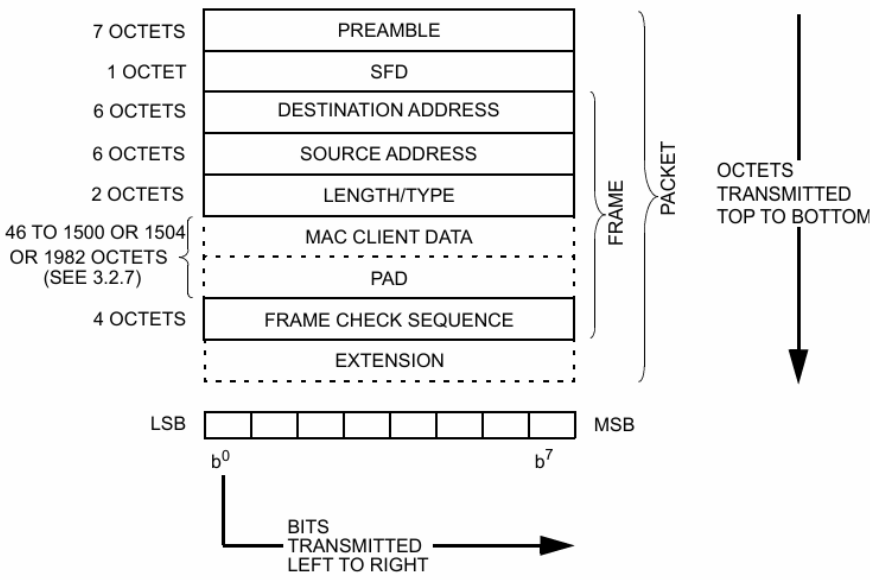


Figure 4.26 – Ethernet packet format [277]

type, MAC client data, Frame Check Sequence (FCS), and, if required, padding fields. Of these fields, all except the MAC client data (and, consequently, the padding) are of fixed size. Specifically, for a basic frame, the MAC client data can contain an integer number of octets ranging from 46 to 1500 bytes. If client data smaller than 46 bytes are available from the upper layer, padding is used to achieve the minimum required size of 46 bytes.

As shown in Fig. 4.27, each MAC info frame constitutes an EC SDU. Since EC symbols must all be equally long (i.e., T bytes), each MAC info frame is eventually padded with zero bytes, as suggested in [257]. To deal with this process, the first 2 bytes of each EC symbol are reserved for indicating the MAC info frame size. Thus, the maximum MAC info frame size must be limited to $T - 2$ bytes. The obtained EC symbols are prepended by the EC header, which contains the information needed by the receiver to correctly perform EC decoding. Considering the implementation of [257], a header of 17 bytes is assumed. The EC symbol prepended by the header forms an ECDU (i.e., EC PDU), which is again encapsulated in a MAC frame.

The FCS field of the resulting MAC frame consists of a CRC computed as a function of the content of the destination address, source address, length/type,

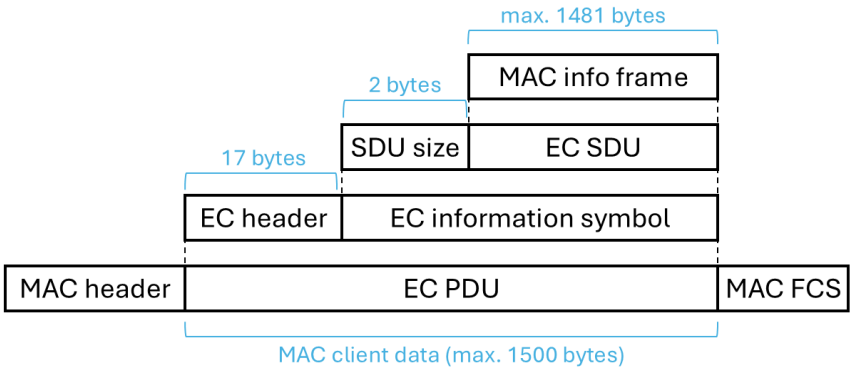


Figure 4.27 – Ethernet info frames encapsulation process via the EC shim layer

MAC client data (i.e. the ECDU), and pad fields. Thus, it is inherently exploited in the proposed architecture to determine which EC PDUs are received in error and, thus, treated as erasures.

The encapsulation process of Fig. 4.27 holds for the EC information symbols. Instead, parity symbols are generated by the EC shim layer and then encapsulated into MAC frames, thus skipping the first two layers.

Overall, it is possible to consider the EC shim layer as an intermediate layer between an "upper" and a "lower" MAC layer, the latter running at 100 Gbit/s. Consequently, the speed and maximum client data size of the "upper" MAC layer must be limited to accommodate the EC process. Specifically, if the maximum MAC client size at the "lower" MAC is 1500 bytes, the maximum "upper" MAC frame length (including the header) shall be limited to 1481 bytes (i.e., $1500 - 17 - 2$).

Despite introducing some additional redundancy, the proposed stack enables the EC to be implemented without requiring modifications to the underlying OTN devices while asking for limited changes to the client side.

Each resulting MAC frame is encapsulated in a packet at the "lower" MAC layer by prepending the preamble and Start Frame Delimiter (SFD) fields [277] and passed to lower layers.

According to the Ethernet standard, the 100GbE uses the IEEE 802.3 MAC sublayer operating at a data rate of 100 Gbit/s, coupled with any IEEE 802.3

100GBASE PHY implementation [277]. The Media Independent Interface (MII) defined in [277] provides a logical interconnection between the MAC sublayer and the PHY-layer device, and is also essential to define the OTN mapping. Indeed, in compliance with [278], 100GBASE-R is assumed as the OTN client signal in the following. Specifically, for 100GbE signals, the CGMII is instantiated in [277], supporting 100 Gbit/s operation through its 64-bit-wide transmit and receive data paths.

Below the MAC layer, the Reconciliation Sublayer (RS) adapts the serial bit stream coming from the MAC layer to the parallel format of the CGMII. To this end, the RS generates continuous data or control characters on the transmit side, which are then transported by the CGMII.

The CGMII is composed of independent transmit and receive paths, each of them using 64 data signals, 8 control signals, and a clock. Thus, every 64-bit times, the RS generates 64 data bits and 8 control bits, where the value of the data bits depends on the data received from the MAC layer.

RS data are transferred within the CGMII data stream, i.e., a sequence of bytes, where each byte conveys either a data octet or a control character. As shown in Fig. 4.28, the CGMII data stream is made up of different parts.

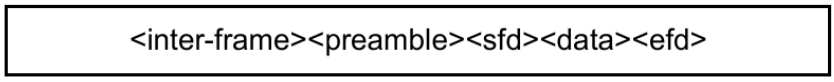


Figure 4.28 – CGMII data stream [277]

The inter-frame period is an interval during which no frame data activity occurs. Indeed, according to [277], a minimum 96-bit inter-packet gap shall be considered at the transmitter side, during which idle control characters are generated. Instead, as the name says, the end-of-frame delimiter (efd in Fig. 4.28) enable the CGMII to signal the end of a frame. Further details on the RS and CGMII procedures can be found in [277].

After the CGMII mapping, 64B/66B encoding is applied to the bit stream according at the 100GBASE-R Physical Coding Sublayer (PCS), resulting in a nominal 100GBASE-R bit rate of 103.125 Gbit/s in input to the OTN mapping procedure.

100GBASE-R clients are mapped into OPU4 payloads by means of the Generic Mapping Procedure (GMP), which performs asynchronous adaptation between the client bit stream and the OPU payload while preserving the client information [278].

As shown in Fig. 4.29, the OPU4 frame consists of four rows and 3810 columns. The first two columns of the OPU area contain overhead information, whereas the remaining payload area carries the client data. Specifically, the payload is organized into 190 groups of 80 bytes, each of which can either transport client information or stuffing bits under the control of the GMP justification mechanism. For a 100GBASE-R client, the payload contains 4×3800 bytes available for client data and 4×8 bytes permanently reserved for fixed stuffing.

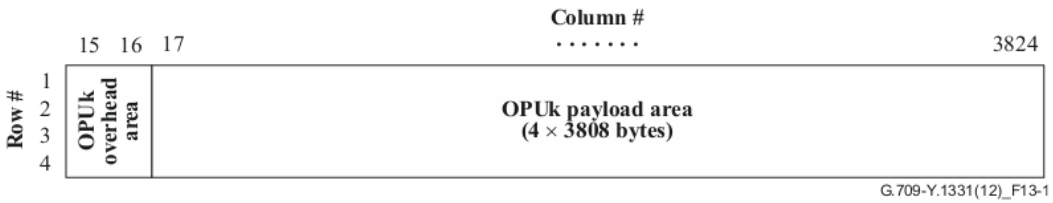


Figure 4.29 – OPU frame structure [278]

After the Ethernet client has been mapped into the OPU4 payload, the OPU4 is encapsulated into an ODU4 frame through the addition of the ODU overhead. The ODU4 frame is organized as a structure of four rows and 3824 columns, where the first 14 columns are dedicated to ODU overhead information and the remaining columns carry the complete OPU4 frame.

The adaptation of ODU4 frames to the FlexO frame structure adopted by ESTOL can be achieved by mapping them to ODUC1 signals and, subsequently, OTUC1 signal structures [242, 276]. This can be achieved again by means of the GMP procedure [276]. Then the Bit-suynchronous Mapping Procedure (BMP) can be used to map OTUC1 signals to FlexO-1 multiframes [279].

Finally, the FlexO is transported over the physical interface by means of FlexO-1-DO frames, which include oFEC coding [242, 276]. Thus, FlexO provides an adaptation layer between OTUC signals and the physical transmission interface.

In particular, a stream of FlexO-1 frames is partitioned into oFEC Block Groups (OFBGs) which are then protected by oFEC coding that consists of an

extended BCH(256, 239) product-like code combined with two interleaving stages, namely an intra-block and an inter-block interleaver. The overall PHY-layer processing, starting from the FlexO signals, is shown in Fig. 4.30.

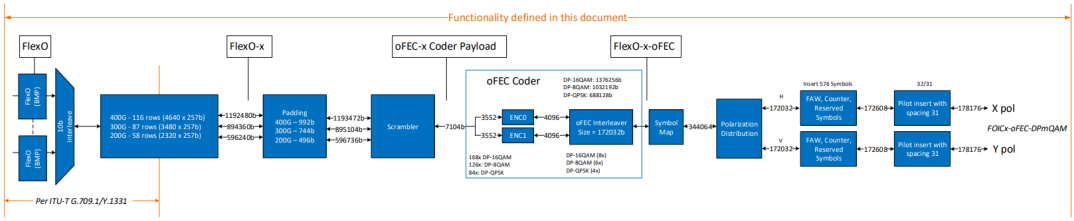


Figure 4.30 – PHY-layer processing [242]

The output of the encapsulation procedure is therefore a continuous sequence of FlexO-1-DO multiframes, each of them transporting an oFEC codeword. The FlexO-1-DO bits are then mapped to constellation symbols and sent over the OFL by exploiting orthogonal polarizations.

These operations are entirely handled by the PHY layer and are therefore abstracted in the proposed simulator through the NGMI-based methodology presented in the previous sections. Nonetheless, to achieve a proper matching between MAC info frames and oFEC codewords, the simulation framework must account for the 64/66B coding of the 100GBASE-R signal and for the overhead added by the OTN encapsulation process. Specifically, by knowing the MAC frame size, PCS rate, FlexO-1-DO rate (i.e., $2936832/2314805 \cdot 99532800$ kbit/s [242, 276]), and FlexO-1-DO multiframe size (i.e., 712 704 bits [242,276]), it is possible to evaluate for each EC symbol (i.e., MAC frame) if the related codeword(s) has been correctly decoded. If not, the EC symbol will be erased.

4.3.2 Enhanced end-to-end OFL simulation framework: algorithm definition

Figure 4.31 summarizes the workflow adopted by the developed Matlab/C simulation framework.

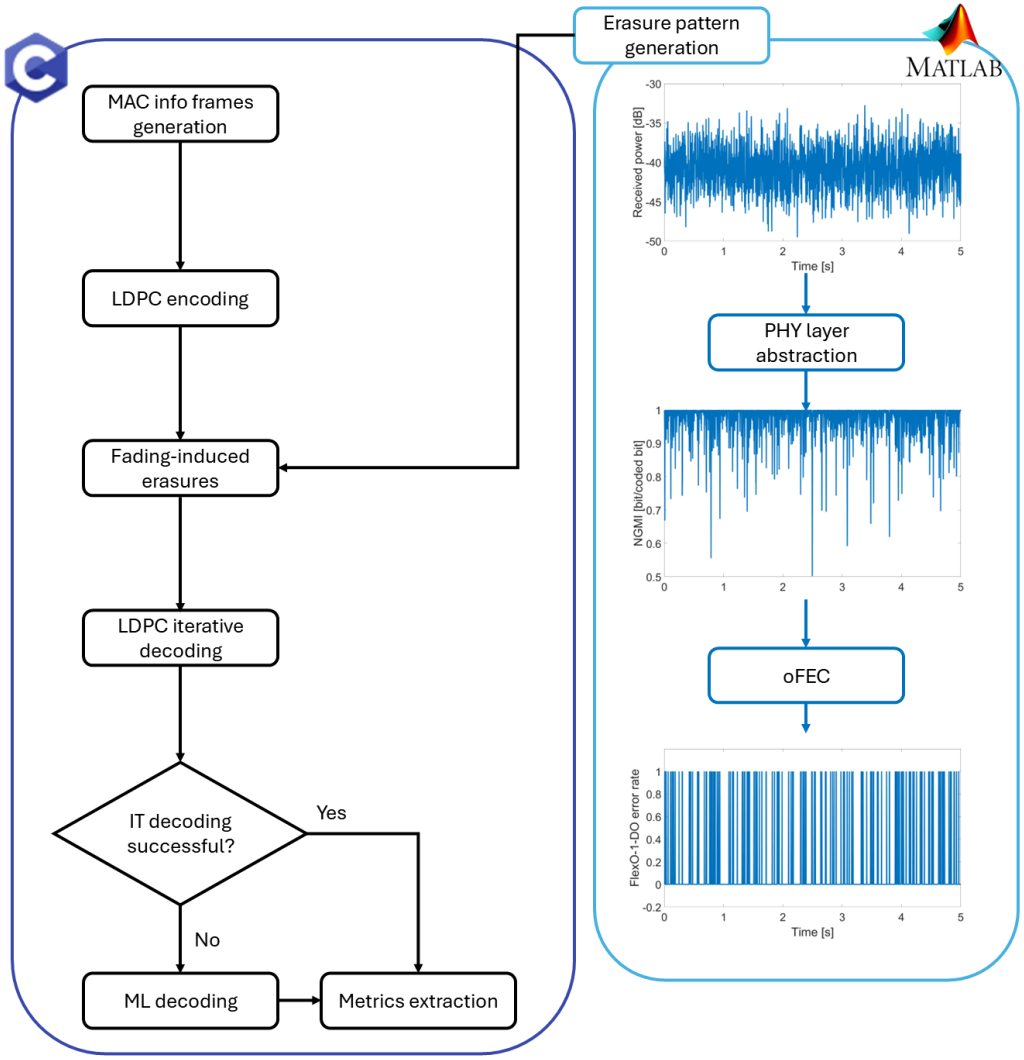


Figure 4.31 – High-level representation of the workflow implemented in the enhanced end-to-end OFL simulation tool

Unlike the simulator presented in Section 4.2.2, where both the PHY-layer FEC and the HL EC were abstracted, the new framework combines PHY layer abstraction with an explicit packet-level simulation of the erasure coding process. This approach preserves the computational efficiency associated with the NGMI-based abstraction of the PHY layer while enabling an accurate evaluation of practical

LDPC erasure codes, including the effects of finite codeword length, iterative decoding, and realistic packet loss patterns.

The simulation starts from the time series of received optical power generated by the propagation modules presented in Chapters 2 and 3. These time series include both the deterministic propagation losses and the turbulence-induced scintillation. Similarly to the previous framework, the received optical power is converted into a time series of instantaneous SNR values by means of the receiver noise model. Subsequently, the SNR values are mapped into instantaneous NGMI values through the numerical implementation described in Section 4.2.1.3. Finally, the NGMI values are compared with the decoding threshold of the adopted oFEC code, generating a binary time series that indicates whether each transmitted FlexO-1-DO multiframe is correctly decoded or not.

Note that the effect of additional PHY layer interleaving is intentionally not investigated so as to avoid any deviation from the commercially available optical transceivers. Nonetheless, it could be easily included in the framework by following the same procedure of Section 4.2.2.

Differently from the previous end-to-end simulation framework, the PHY layer PER sequence is not converted into an average HL PER. Instead, the binary PHY-layer decoding outcomes are associated with the actual sequence of transmitted FlexO-1-DO multiframes generated by the encapsulation process. Since each multiframe transports a different number of MAC frames, the decoding failures are propagated to the higher layers in the form of "lower" MAC frame erasures by identifying which MAC frames are contained within each discarded multiframe. Whenever a multiframe cannot be decoded by the PHY layer, all the MAC frames contained in its payload are marked as erased, whereas correctly decoded multiframes deliver all the corresponding MAC frames without errors. Thus, the simulator generates a realistic sequence of "lower" MAC frame erasures whose temporal correlation naturally derives from the PHY-layer fading process and from the OTN encapsulation structure.

The one-to-one correspondence between "lower"MAC frames, EC symbols, and "upper" MAC frames easily allows the simulator to establish which MAC info frames are correctly received or reconstructed after EC decoding.

Specifically, the generated sequence of PHY-layer error rates, with one sample per each FlexO-1-DO multiframe period, constitutes an input of the C-based EC simulator. The latter has been developed around the open-source OpenFEC library, which implements the LDPC Staircase ECs described in Section 4.1.2.2, with hybrid IT and ML decoding [259]. The simulator groups the incoming "upper" MAC frames into source blocks composed of k information packets, according to the selected coding parameters. Once a complete source block has been collected, the OpenFEC encoder generates the corresponding $n - k$ repair symbols, producing a systematic codeword composed of n symbols.

The transmission of the encoded packets over the emulated OFL channel is performed via the PHY layer abstraction. During this step, every ECDU inherits the reception status associated with the corresponding "lower" MAC frame determined by the encapsulation process. Consequently, each ECDU is either correctly delivered or completely erased, consistently with the PEC model.

The ECDUs belonging to the same EC codeword are then passed to the OpenFEC decoder together with the retrieved erasure pattern. The EC decoder first attempts IT decoding and, whenever necessary, activates the ML decoding procedure implemented by the library. If decoding succeeds, all missing information symbols are reconstructed and delivered to the upper layer. Otherwise, the unrecovered frames are declared lost.

Besides reproducing the complete encoding and decoding procedure, the simulator records several statistics for each transmitted codeword. In particular, it stores

- the number of transmitted "lower" MAC frames
- the number of transmitted "upper" MAC info frames
- the number of transmitted EC codewords
- the number of IT decoded, ML decoded, and undecoded codewords
- the number of successfully received "lower" and "upper" MAC frames.

These statistics allow not only the evaluation of the final FER, but also the characterization of the decoding behavior for the different code rates and channel conditions.

A more detailed description of the C algorithm composing to overall framework is reported in Algorithm 1.

Algorithm 1 Enhanced end-to-end OFL simulation framework: C algorithm

Require: Time series of FlexO-1-DO decoding outcome, EC parameters (n, k, T), simulation time t_{end}

Initialize OpenFEC encoder and decoder
Initialize simulation statistics
Compute number of EC codewords N_{EC} transmitted in t_{end} seconds
$N = 0$
while $N < N_{EC}$ **do**
    Randomly generate k EC information symbols
    Generate $n - k$ parity symbols via encoder
    for $i = 1$ to n **do**
        Establish if EC symbol i is correctly received or erased
        if symbol i is erased **then**
            Mark EC symbol i as lost
        else
            Store received symbol i
        end if
    end for
    Invoke OpenFEC decoder
    if iterative decoding successful **then**
        Recover missing source symbols
        Update successful decoding statistics
    else if ML decoding successful **then**
        Recover missing source symbols
        Update successful decoding statistics
    else
        Mark unrecovered source symbols as lost
        Update decoding failure statistics
    end if
    Update EC codeword counter N
end while
Compute metrics

With respect to the high-level scheme of Fig. 4.31, it better highlights how the encoding/decoding and erasure generation process are repeatedly carried out along the entire simulation time, t_{end} [s].

Finally, the simulation outputs are post-processed to compute the performance metrics considered throughout this work. In particular, the average FER at the "upper" MAC layer is evaluated as the ratio between the number of unrecovered MAC info frames and the total number of transmitted MAC info frames. Additional statistics, including the percentage of codewords successfully decoded through IT decoding only, the percentage requiring ML decoding, and the overall decoding success probability, are also derived. These quantities are employed in the following section to assess the effectiveness of the LDPC EC schemes under different code rates and Ethernet payload sizes.

4.3.3 Performance assessment of 100 Gbit/s coherent OFLs

The enhanced end-to-end OFL simulation framework has been used to properly assess the effectiveness of HL ECs for potential use in a 100 Gbit/s coherent OFL.

Specifically, the same scenario of Section 4.2.3 has been analyzed, i.e., a downlink transmission from a LEO satellite orbiting at 600 km toward an OGS located at 10 m of altitude. Also in this case, the worst-case analysis has been performed for a link elevation angle of 30°, which is characterized by a scintillation correlation time of 2.67 ms.

Despite the developed tool relies on Staircase LDPC codes, the same CCSDS-standardized EC rates have been adopted in the following analysis. Indeed, it has been proved that the two families of LDPC codes (i.e., Staircase and IRA codes) both provides effective performance, very close to the ideal MDS bound [257]. Thus, analogous results are expected by switching between the two code families.

For the sake of clarity, the analyzed (n, k) EC configurations are reported in Table 4.4, together with an ID used to identify them in the subsequent plots.

In the analyses, the "lower" MAC client data size has been set to the maximum possible value, i.e., 1500 bytes. This value corresponds to an EC symbol size $T = 1500 - 17 = 1483$ bytes.

Table 4.4 – Analyzed EC configurations

ID	n	k	R
1	512	576	8/9
2	512	640	4/5
3	512	768	2/3
4	2048	2304	8/9
5	2048	2560	4/5
6	2048	3072	2/3
7	16384	18432	8/9
8	16384	20480	4/5
9	16384	24576	2/3

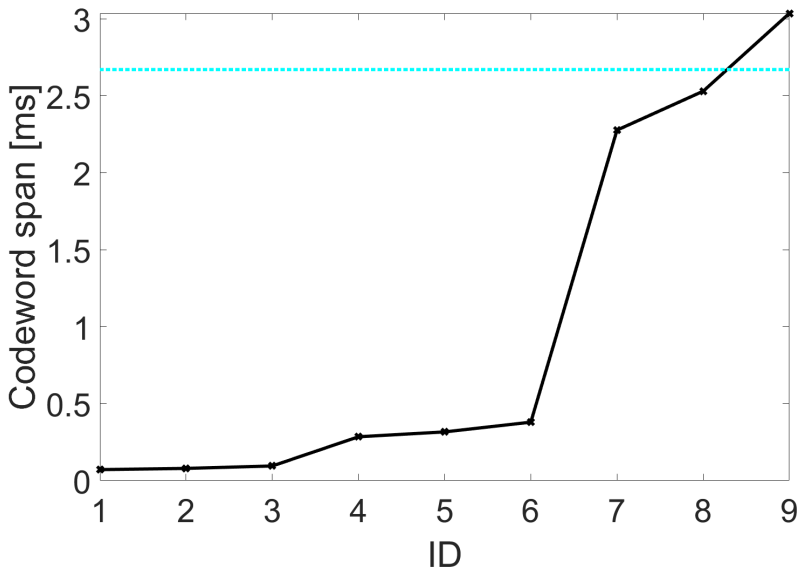


Figure 4.32 – EC codeword transmission time as a function of the EC configuration ID. The plot assumes a "lower" MAC client data length equal to 1500 bytes. The dashed-cyan curve corresponds to the LEO downlink OFL channel correlation time at $\zeta = 30°$

As shown in Fig. 4.32, even by selecting the longest possible symbol size, the

corresponding EC codewords span a time longer than the channel correlation time only for the ninth configuration (i.e., ID = 9, $k = 16384$,$n = 24576$, $R = 2/3$).

This result is reflected in the average power required at the receiver to guarantee an error-free transmission, which is shown in Fig. 4.33. In this case, the term "error-free" refers to the condition when all erased MAC info frames are recovered thanks to EC decoding.

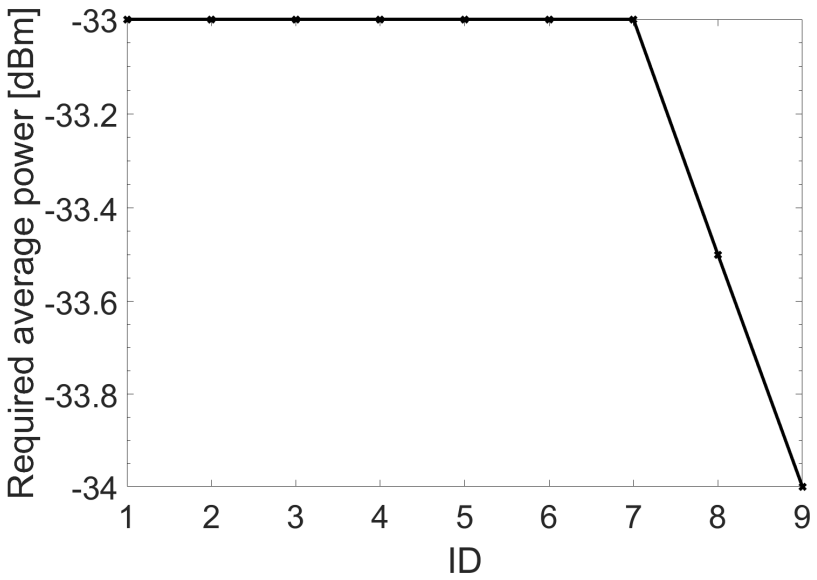
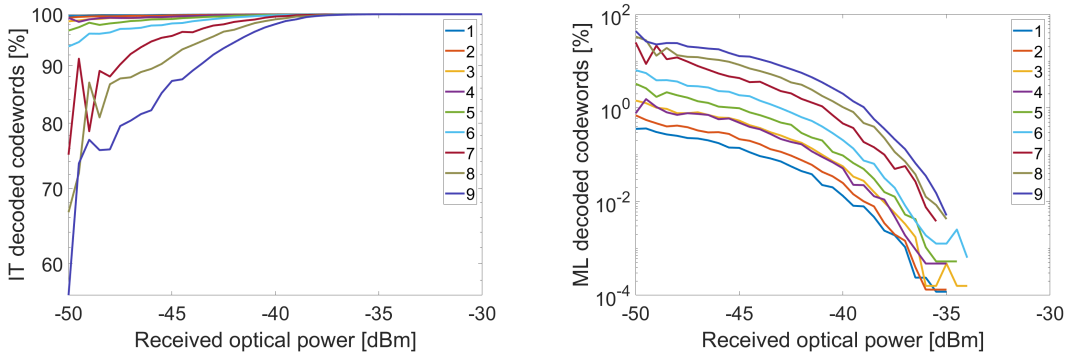


Figure 4.33 – Required average power at the receiver to guarantee an error-free OFL as a function of the EC configuration ID, for the LEO downlink OFL at $\zeta = 30°$. The plot assumes a "lower" MAC client data length equal to 1500 bytes

Compared with the results obtained in Section 4.2.3 and, specifically, the black curve of Fig. 4.23, which assumed oFEC channel coding without additional channel and HL interleavers, it is now evident that the EC rate, as well as the symbol size T, affect the decoding performance.

Figures 4.34a and 4.34b show the percentage of IT and ML decoded EC codewords, respectively, as a function of the unfaded received optical power. As the average received power increases, the amount of IT decoded codewords increases until reaching a power level after which all the decoded codewords are reconstructed by means of IT decoding only. Nonetheless, this condition not necessarily correspond to the error-free power level. For instance, for configuration ID = 8,



(a) (b)

Figure 4.34 – Percentage of (a) IT and (b) ML decoded EC codewords as a function of the unfaded received optical power for the LEO downlink OFL at $\zeta = 30°$. The plot assumes a "lower" MAC client data length equal to 1500 bytes

error-free transmission is achieved at $P_R = -33.5dBm$, while a 100% IT decoding strategy is employed already from $P_R = -34.5dBm$, despite not corresponding to an error-free link, as shown in Fig. 4.35.

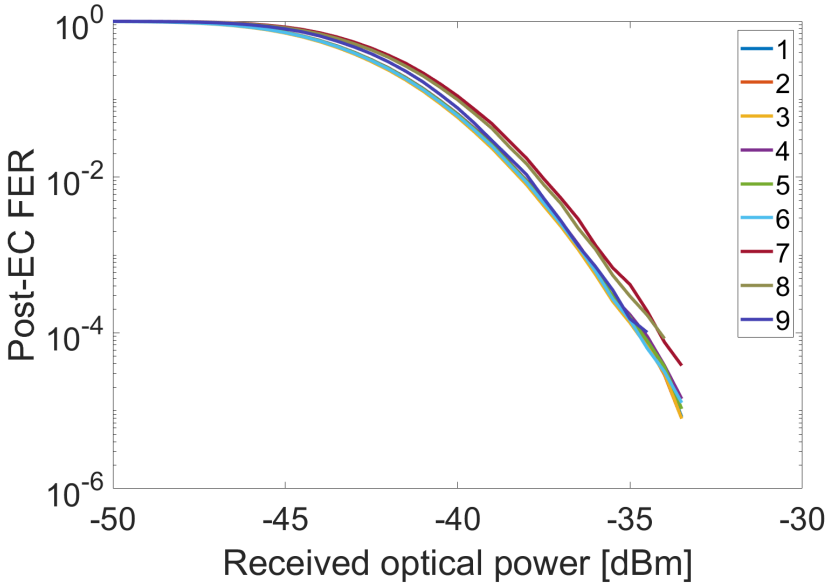


Figure 4.35 – Post-EC FER as a function of the unfaded received optical power for the LEO downlink OFL at $\zeta = 30°$. The plot assumes a "lower" MAC client data length equal to 1500 bytes

When comparing the above results with link budget analyses, such as the one of Section 2.2.1, it is clear that even by selecting the longest possible codeword length and code rate among the analyzed ones, the required power (i.e., -34 dBm) may not be achievable. To relax the power requirement, longer EC symbols may be employed. For example, if the transmission of Jumbo frames is supported by the client, maximum "lower" MAC client data size of up to 9000 bytes can be used.

To evaluate the impact of longer symbol sizes, the last configuration (ID = 9) as been analyzed with "lower" MAC MTU sizes of 2500 and 9000 bytes, which correspond to symbols sizes of 2483 and 8983 bytes, respectively. The related codeword transmission times are reported in Fig. 4.36.

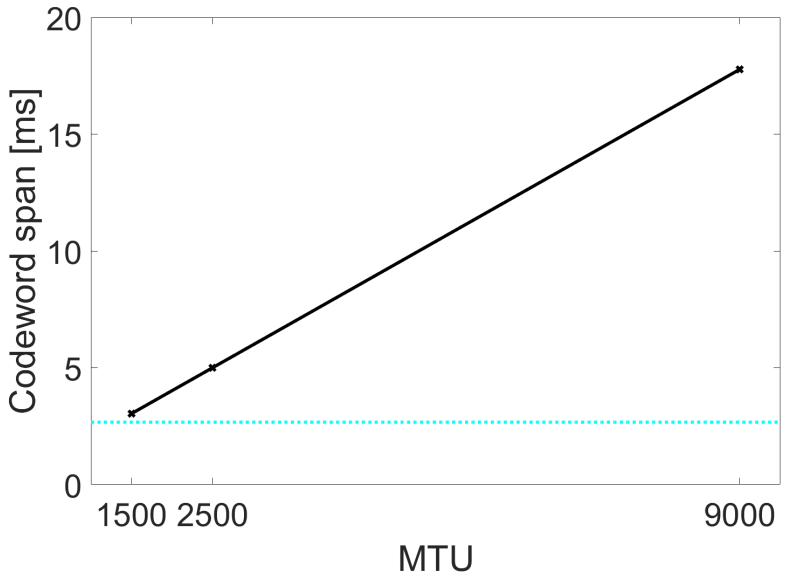


Figure 4.36 – EC codeword transmission time as a function of "lower" MAC client data length. The plot assumes EC ID = 9. The dashed-cyan curve corresponds to the LEO downlink OFL channel correlation time at $\zeta = 30°$

Instead, the simulation outcomes in terms of received unfaded power required to achieve an error-free OFL are shown in Fig. 4.37.

While the power requirement does not decrease while moving from 1500 to 2500 MAC client data sizes, it dramatically reduces when increasing the EC symbol size to 8983 bytes.

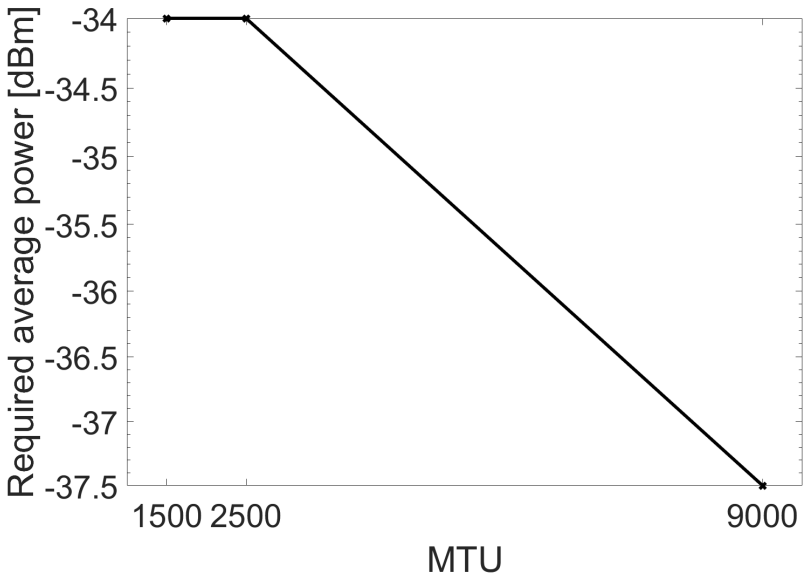


Figure 4.37 – Required average power at the receiver to guarantee an error-free OFL as a function of the "lower" MAC client data length, for the LEO downlink OFL at $\zeta = 30°$. The plot assumes EC ID = 9

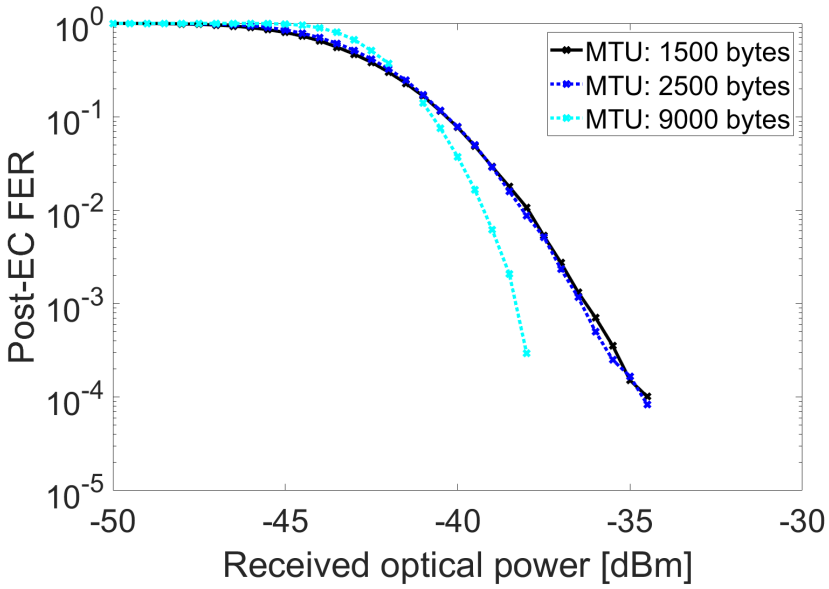


Figure 4.38 – Post-EC FER as a function of the unfaded received optical power for the LEO downlink OFL at $\zeta = 30°$. The plot assumes "lower" MAC client data lengths equal to 1500 bytes (black curve), 2500 bytes (blue curve), and 9000 bytes (cyan curve)

Indeed, moving from a 1500- to a 9000-bytes MAC client data size, the required average received power goes from -34 to -37.5 dBm. This result is achieved at the expense of increased delay. Indeed, from Fig. 4.36, the EC codeword transmission time increases from about 3 ms to approximately 17.8 ms.

Moreover, in Fig. 4.38, starting from -41 dBm of unfaded received power, it is possible to appreciate a decrease in post-EC FER thanks to the increased symbol size.

The obtained results highlight that, despite being a promising technique potentially capable of achieving error-free OFLs, the optimal erasure coding strategy requires to make a compromise between available power and end-to-end delay.

Conclusions

This thesis has tackled the design and performance assessment of space-based optical links, a promising technology for the integration of TN and NTN segments in next-generation networks. To enable high-speed OFLs, a thorough understanding of the atmospheric propagation channel, design methodologies, and the development of suitable reliability techniques become essential and, thus, have been addressed throughout this work.

A distinctive aspect of this research is the adoption of a unified perspective on OFLs, addressing the problem across multiple levels rather than focusing on a single component of the communication chain. The research has progressed from the accurate electromagnetic modeling of FSO propagation, through the experimental emulation of realistic atmospheric impairments and the assessment of commercial optical transceivers, to the development of end-to-end OFL simulation frameworks incorporating digital fading mitigation techniques. Although each of these contributions addresses a specific research problem, together they constitute a coherent design methodology that enables OFL to be analyzed from the PHY layer up to the overall link level.

Within this framework, several original contributions have been presented. These include:

- the development of a flexible and comprehensive link budget tool integrating the main propagation impairments affecting OFLs
- the identification and correction of inaccuracies associated with the conventional beam wander formulation through a more accurate treatment of the propagation geometry

- the realization of compact, computationally-efficient laboratory testbeds capable of reproducing both turbulence- and pointing-induced fading under realistic LEO operating conditions

- the experimental characterization of commercial IM/DD and coherent fiber-optic transceivers in the presence of atmospheric impairments, and

- the development of end-to-end simulation frameworks capable of jointly evaluating PHY and HL performance as well as to support the design of digital mitigation strategies.

For what concerns the first contributions, the proposed link budget model integrates the main electromagnetic phenomena affecting optical propagation through the atmosphere, including atmospheric attenuation, turbulence-induced effects, pointing impairments, weather conditions, and receiver and transmitter characteristics, while allowing different models available in the literature to be selected according to the specific application scenario. This flexibility makes the framework suitable not only for the analysis of existing optical links but also for supporting the design of future systems characterized by different orbital configurations and propagation conditions.

The developed tool has been validated against experimental campaigns reported in the literature, demonstrating its capability to accurately reproduce realistic system performances. Moreover, the framework has enabled the investigation of aspects that are often overlooked in conventional link budget analyses. In particular, the impact of the commonly adopted link-distance approximation on beam wander estimation has been thoroughly analyzed for the first time. The obtained results have shown that the conventional approximation leads to a systematic overestimation of beam wander variance and of the corresponding optical losses, especially at low elevation angles, where accurate system dimensioning becomes particularly critical. By introducing a more precise geometrical description of the propagation path, the proposed methodology provides more reliable estimates of the required link margins, thus improving the accuracy of OFL design.

The second major contribution regards the experimental investigation of turbulence impaired OFLs. To this end, compact and cost-effective OTGs based on

VOAs have been developed together with computationally efficient algorithms capable of reproducing the statistical and temporal properties of turbulence- and jitter-induced fading experienced by OFLs. Particular attention has been devoted to the calibration procedure of the experimental setup, allowing the developed OTG to accurately reproduce the desired attenuation profiles over a wide dynamic range. Furthermore, the proposed fading generation algorithms have been designed to efficiently emulate both fixed satellite positions and the time-varying atmospheric conditions experienced during complete LEO satellite passes.

The two developed experimental testbeds have enabled the performance assessment of commercial fiber-optic transceivers operating under realistic atmospheric impairments. Experimental results have demonstrated that atmospheric turbulence significantly affects communication performance even under relatively weak turbulence conditions, producing packet losses, increased jitter, frame errors, and communication outages. The obtained results further emphasize the stringent pointing requirements imposed by OFLs, confirming that even moderate pointing errors may considerably degrade communication performance when combined with atmospheric fading.

A comparison between IM/DD and coherent commercial technologies under emulated turbulence has been performed for the first time, highlighting that higher-capacity coherent systems, despite their remarkable spectral efficiency, exhibit a greater sensitivity to fading-induced power fluctuations, requiring larger system margins to achieve comparable reliability. These observations provide valuable indications for the adoption of commercial optical networking technologies in future satellite optical communications and underline the importance of considering atmospheric dynamics already during system design.

Overall, the developed laboratory testbeds constitutes versatile experimental platforms that can support the validation of future optical communication equipment.

Building upon the numerical and experimental analyses, the final part of this work has addressed the development of end-to-end simulation frameworks capable of evaluating communication performance beyond the PHY layer. To this end, two comprehensive end-to-end simulation frameworks have been developed by integrating an accurate PHY-layer abstraction with the modeling of HL digital

mitigation techniques. The proposed frameworks account for the temporal evolution of turbulence-induced fading, receiver characteristics, and synchronization losses, while considering the adoption of FEC scheme, packet-level ECs, and interleaving mechanisms, allowing the interaction among different protocol layers to be realistically represented. Moreover, the enhanced end-to-end OFL simulation framework allowed, for the first time, faithful analysis of HL ECs for potential use in OFLs, thus supporting the design of this emerging fading mitigation strategy.

The obtained results demonstrate that the joint optimization of PHY and HL mitigation techniques plays a fundamental role in improving OFL performance. In particular, the analyses show that packet-level ECs can effectively compensate for residual frame losses without requiring modifications to commercial PHY-layer transceivers. While properly selecting EC rate and codeword duration with respect to the channel coherence time significantly enhances communication reliability, it requires a trade-off between achievable FER and end-to-end latency. These findings provide practical design guidelines for future FSO systems exploiting commercial OTN technologies in space communications.

Rather than representing independent developments, the proposed models, experimental platforms, and simulation tools form a consistent framework that bridges theoretical analysis, laboratory validation, and system-level performance evaluation. In this sense, the main contribution of this PhD is not only the advancement of individual methodologies, but also the establishment of an integrated approach for the design and assessment of OFLs, which can support both future research activities and the development of next-generation integrated terrestrial and non-terrestrial networks.

Several research directions naturally emerge from the present work. On the modeling side, the developed numerical frameworks could be further extended to include additional aspects and scenarios, such as AO correction, optical diversity techniques, and optical links involving HAPs or UAVs.

From the experimental viewpoint, the developed fading emulators may be enhanced to reproduce moderate-to-strong turbulence regimes by generating gamma-gamma-distributed fading processes and to include the effect of time-varying SMF coupling efficiency. Moreover, the experimental testbed could also be employed

to experimentally assess digital mitigation strategies under realistic atmospheric conditions.

Finally, future developments of the end-to-end simulation framework may include the integration of adaptive communication strategies capable of dynamically adjusting coding rates, modulation formats, or transmission parameters according to channel conditions. Likewise, extending the framework to system-level analyses involving multiple OGSs, satellites, or hybrid RF/optical architectures would provide useful insights into the design of resilient 3D networks.

In conclusion, this thesis demonstrates that the successful deployment of OFLs requires the combination of accurate modeling, realistic experimental validation, and comprehensive link-level optimization. The methodologies and tools developed throughout this work represent a step toward this objective, providing flexible instruments for the design, analysis, and optimization of future high-capacity optical satellite communication systems.

References

[1] A. Jahid, M. H. Alsharif, and T. J. Hall, "A contemporary survey on free space optical communication: Potentials, technical challenges, recent advances and research direction," *Journal of Network and Computer Applications*, vol. 200, p. 103311, 2022.

[2] "Ericsson Mobility Report," Ericsson, Tech. Rep., November 2025. [Online]. Available: https://www.ericsson.com/4aca6f/assets/local/reports-papers/mobility-report/documents/2025/ericsson-mobility-report-november-2025.pdf

[3] A. Guidotti *et al.*, "Architectures, standardisation, and procedures for 5G Satellite Communications: A survey," *Computer Networks*, vol. 183, p. 107588, 2020.

[4] M. M. Azari *et al.*, "Evolution of Non-Terrestrial Networks From 5G to 6G: A Survey," *IEEE Communications Surveys & Tutorials*, vol. 24, no. 4, pp. 2633–2672, 2022.

[5] C.-X. Wang *et al.*, "On the Road to 6G: Visions, Requirements, Key Technologies, and Testbeds," *IEEE Communications Surveys & Tutorials*, vol. 25, no. 2, pp. 905–974, 2023.

[6] "5G NTN takes flight: technical overview of 5G Non-Terrestrial Networks," Rohde & Schwarz, White Paper, 2022. [Online]. Available: https://www.rohde-schwarz.com/us/solutions/wireless-communications-testing/wireless-standards/5g-nr/non-terrestrial-networks-ntn/non-terrestrial-networks-ntn_256719.html

[7] V. K. Quy, A. Chehri, N. M. Quy, N. D. Han, and N. T. Ban, "Innovative Trends in the 6G Era: A Comprehensive Survey of Architecture, Applications, Technologies, and Challenges," *IEEE Access*, vol. 11, pp. 39 824–39 844, 2023.

[8] M. Toyoshima, "Recent Trends in Space Laser Communications for Small Satellites and Constellations," *Journal of Lightwave Technology*, vol. 39, no. 3, pp. 693–699, 2021.

[9] W. Jiang, B. Han, M. A. Habibi, and H. D. Schotten, "The Road Towards 6G: A Comprehensive Survey," *IEEE Open Journal of the Communications Society*, vol. 2, pp. 334–366, 2021.

[10] O. I. Younus *et al.*, "Overview of Space-Based Laser Communication Missions and Payloads: Insights from the Autonomous Laser Inter-Satellite Gigabit Network (ALIGN)," *Aerospace*, vol. 11, no. 11, 2024.

[11] R. Li, B. Lin, Y. Liu, M. Dong, and S. Zhao, "A Survey on Laser Space Network: Terminals, Links, and Architectures," *IEEE Access*, vol. 10, pp. 34 815–34 834, 2022.

[12] G. Park, V. Mai, H. Lee, S. Lee, and H. Kim, "Free-Space Optical Communication Technologies for Next-Generation Cellular Wireless Communications," *IEEE Communications Magazine*, vol. 62, no. 3, pp. 24–30, 2024.

[13] M. A. Fernandes *et al.*, "Unraveling "Fiber in the Sky": Terabit Capacity Enabled by Coherent Optical Wireless," *IEEE Communications Magazine*, vol. 62, no. 3, pp. 40–46, 2024.

[14] E. Agrell *et al.*, "Roadmap on optical communications," *Journal of Optics*, vol. 26, no. 9, p. 093001, 2024.

[15] D. M. Boroson *et al.*, *A New Optical Communication Architecture for Delivering Extremely Large Volumes of Data from Space to Ground.*

[16] S. A. Al-Gailani *et al.*, "A Survey of Free Space Optics (FSO) Communication Systems, Links, and Networks," *IEEE Access*, vol. 9, pp. 7353–7373, 2021.

[17] A. Ahmad, S. Majeed, and Y. Dawood, "A Survey of 6G Mobile Systems, Enabling Technologies, and Challenges," *International Journal of Electrical and Electronic Engineering & Telecommunications*, vol. 12, p. 21, 01 2023.

[18] A. Mansour, R. Mesleh, and M. Abaza, "New challenges in wireless and free space optical communications," *Optics and Lasers in Engineering*, vol. 89, pp. 95–108, 2017.

[19] F. P. Guiomar, M. A. Fernandes, J. L. Nascimento, V. Rodrigues, and P. P. Monteiro, "Coherent Free-Space Optical Communications: Opportunities and Challenges," *Journal of Lightwave Technology*, vol. 40, no. 10, pp. 3173–3186, 2022.

[20] A. S. Hamza, J. S. Deogun, and D. R. Alexander, "Classification Framework for Free Space Optical Communication Links and Systems," *IEEE Communications Surveys & Tutorials*, vol. 21, no. 2, pp. 1346–1382, 2019.

[21] H. Hauschildt *et al.*, "HydRON: High thRoughput Optical Network," in *2019 IEEE International Conference on Space Optical Systems and Applications (ICSOS)*, 2019, pp. 1–6.

[22] M. Toyoshima, "Trends in satellite communications and the role of optical free-spacecommunications," *Journal of Optical Networking*, vol. 4, no. 6, pp. 300–311, Jun 2005.

[23] A. U. Chaudhry and H. Yanikomeroglu, "Free Space Optics for Next-Generation Satellite Networks," *IEEE Consumer Electronics Magazine*, vol. 10, no. 6, pp. 21–31, 2021.

[24] "Optical Communications: The Next Satellite Frontier," Keysight Technologies, White Paper, 2023. [Online]. Available: https://www.keysight.com/us/en/assets/7123-1055/white-papers/Optical-Communications-The-Next-Satellite-Frontier.pdf

[25] H. Kaushal and G. Kaddoum, "Optical Communication in Space: Challenges and Mitigation Techniques," *IEEE Communications Surveys & Tutorials*, vol. 19, no. 1, pp. 57–96, 2017.

[26] L. Canuet, "Coherent optical feeder links for very high throughput satellite systems," in *Free-Space Laser Communications XXXVI*, vol. 12877. SPIE, 2024, p. 128770E.

[27] K. E. Wilson and J. R. Lesh, "An overview of the Galileo optical experiment (GOPEX)," *The Telecommunications and Data Acquisition Report*, 1993.

[28] Y. Arimoto, M. Toyoshima, M. Toyoda, T. Takahashi, M. Shikatani, and K. Araki, "Preliminary result on laser communication experiment using Engineering Test Satellite-VI (ETS-VI)," in *Free-Space Laser Communication Technologies VII*, vol. 2381. SPIE, 1995, pp. 151 – 158.

[29] K. Araki *et al.*, "Performance evaluation of laser communication equipment onboard the ETS-VI satellite," in *Free-Space Laser Communication Technologies VIII*, vol. 2699. SPIE, 1996, pp. 52 – 59.

[30] M. Shikatani *et al.*, "Ground system development for the ETS-VI/LCE laser communications experiment," in *Free-Space Laser Communication Technologies V*, vol. 1866. SPIE, 1993, pp. 21 – 29.

[31] K. E. Wilson, "An overview of the GOLD experiment between the ETS-6 satellite and the table mountain facility," *The Telecommunications and Data Acquisition Report*, 1996.

[32] M. Jeganathan, K. Wilson, and J. Lesh, "Preliminary analysis of fluctuations in the received uplink-beacon-power data obtained from the GOLD experiments," *The Telecommunications and Data Acquisition Report*, 1996.

[33] G. Fletcher, T. Hicks, and B. Laurent, "The SILEX optical interorbit link experiment," *Electronics & Communication Engineering Journal*, vol. 3, pp. 273–279, 1991.

[34] B. Laurent and O. Duchmann, "SILEX project: the first European optical intersatellite link experiment," in *Free-Space Laser Communication Technologies III*, vol. 1417. SPIE, 1991, pp. 2 – 12.

[35] T. Tolker-Nielsen and J. Guillen, "SILEX: The first European optical communication terminal in orbit," *ESA bulletin*, vol. 96, no. 1, p. 998, 1998.

[36] T. Tolker-Nielsen and G. Oppenhauser, "In-orbit test result of an operational optical intersatellite link between ARTEMIS and SPOT4, SILEX," in *Free-Space Laser Communication Technologies XIV*, vol. 4635. SPIE, 2002, pp. 1 – 15.

[37] M. R. Garcia-Talavera, Z. Sodnik, P. Lopez, A. Alonso, T. Viera, and G. Oppenhauser, "Preliminary results of the in-orbit test of ARTEMIS with the Optical Ground Station," in *Free-Space Laser Communication Technologies XIV*, vol. 4635. SPIE, 2002, pp. 38 – 49.

[38] A. Alonso, M. Reyes, and Z. Sodnik, "Performance of satellite-to-ground communications link between ARTEMIS and the Optical Ground Station," in *Optics in Atmospheric Propagation and Adaptive Systems VII*, vol. 5572. SPIE, 2004, pp. 372 – 383.

[39] Z. Sodnik, B. Furch, and H. Lutz, "Optical Intersatellite Communication," *IEEE Journal of Selected Topics in Quantum Electronics*, vol. 16, no. 5, pp. 1051–1057, 2010.

[40] V. Kuzkov, D. Volovyk, S. Kuzkov, Z. Sodnik, S. Pukha, and V. Caramia, "Laser ground system for communication experiments with ARTEMIS," in *Proc. International Conference on Space Optical Systems and Applications (ICSOS)*, vol. 2012, 2012.

[41] Y. Fujiwara *et al.*, "Optical inter-orbit communications engineering test satellite (OICETS)," *Acta Astronautica*, vol. 61, no. 1, pp. 163–175, 2007.

[42] T. JONO *et al.*, "In-orbit Experiment Result of Inter-satellite Laser Communication by OICETS ("Kirari")," *The Journal of Space Technology and Science*, vol. 23, no. 2, pp. 2_21–2_29, 2007.

[43] T. Jono, "Optical Inter-orbit Communication Experiment between OICETS and ARTEMIS," *Journal of the National Institute of Information and Communications Technology*, vol. 59, no. 1.2, pp. 023–033, 2012.

[44] M. TOYOSHIMA *et al.*, "Laser Beam Propagation in Ground-to-OICETS Laser Communication Links," *The Journal of Space Technology and Science*, vol. 23, no. 2, pp. 2_30–2_45, 2007.

[45] E. Okamoto, Y. Shoji, M. Toyoshima, and Y. Takayama, "Transmission Experiments on OICETS Repeater Mode for Verification of Channel Coding Effect," *Journal of the National Institute of Information and Communications Technology*, vol. 59, no. 1.2, pp. 083–093, 2012.

[46] N. Perlot, M. Knapek, D. Giggenbach, J. Horwath, M. Brechtelsbauer, Y. Takayama, and T. Jono, "Results of the optical downlink experiment KIODO from OICETS satellite to optical ground station Oberpfaffenhofen (OGS-OP)," in *Free-Space Laser Communication Technologies XIX and Atmospheric Propagation of Electromagnetic Waves*, vol. 6457. SPIE, 2007, p. 645704.

[47] Y. Takayama *et al.*, "Expanded laser communications demonstrations with OICETS and ground stations," in *Free-Space Laser Communication Technologies XXII*, vol. 7587. SPIE, 2010, p. 75870D.

[48] K. Böhmer, M. Gregory, F. Heine, H. Kämpfner, R. Lange, M. Lutzer, and R. Meyer, "Laser communication terminals for the European Data Relay System," in *Free-Space Laser Communication Technologies XXIV*, vol. 8246. SPIE, 2012, p. 82460D.

[49] M. Gregory, F. Heine, H. Kämpfner, R. Meyer, R. Fields, and C. Lunde, "TESAT laser communication terminal performance results on 5.6Gbit coherent inter satellite and satellite to ground links," in *International Conference on Space Optics — ICSO 2010*, vol. 10565. SPIE, 2017, p. 105651F.

[50] R. Lange and B. Smutny, "BPSK laser communication terminals to be verified in space," in *IEEE MILCOM 2004. Military Communications Conference, 2004.*, vol. 1, 2004, pp. 441–444 Vol. 1.

[51] R. Fields *et al.*, "NFIRE-to-TerraSAR-X laser communication results: satellite pointing, disturbances, and other attributes consistent with successful performance," in *Sensors and Systems for Space Applications III*, vol. 7330. SPIE, 2009, p. 73300Q.

[52] W. Pitz and D. Miller, "The TerraSAR-X Satellite," *IEEE Transactions on Geoscience and Remote Sensing*, vol. 48, no. 2, pp. 615–622, 2010.

[53] R. Fields *et al.*, "5.625 Gbps bidirectional laser communications measurements between the NFIRE satellite and an Optical Ground Station," in *2011 International Conference on Space Optical Systems and Applications (ICSOS)*, 2011, pp. 44–53.

[54] Q.-j. Zhang and G.-y. Wang, "Influence of hy-2 satellite platform vibration on laser communication equipment: Analysis and on-orbit experiment," in *3rd International Symposium of Space Optical Instruments and Applications*, H. P. Urbach and G. Zhang, Eds. Cham: Springer International Publishing, 2017, pp. 95–111.

[55] V. Grigoryev, V. Kovalev, V. Shargorodskiy, and V. Sumerin, "High-bit-rate laser space communication technology and results of on-board experiment," in *Proceedings of the International Conference on Space Optics, Tenerife, Spain*, 2014, pp. 6–10.

[56] S. Seel, D. Troendle, F. Heine, H. Zech, M. Motzigemba, and U. Sterr, "Alphasat laser terminal commissioning status aiming to demonstrate GeoRelay for Sentinel SAR and optical sensor data," in *2014 IEEE Geoscience and Remote Sensing Symposium*, 2014, pp. 100–101.

[57] B. Schlepp, R. Kahle, J. Saleppico, S. Kuhlmann, and U. Sterr, "Laser Communication with Alphasat - FD Challenges and First Flight Results," in *24th International Symposium on Space Flight Dynamics (ISSFD)*, May 2014.

[58] D. Tröndle *et al.*, "Alphasat-Sentinel-1A optical inter-satellite links: run-up for the European data relay satellite system," in *Free-Space Laser Communication and Atmospheric Propagation XXVIII*, vol. 9739. SPIE, 2016, p. 973902.

[59] G. Losquadro, G. Losquadro, and P. Conforto, *Architecture and Link Design for a 2nd Generation Data Relay System.*

[60] F. Heine *et al.*, "LCT for the European data relay system: in orbit commissioning of the Alphasat and Sentinel 1A LCTs," in *Free-Space Laser Communication and Atmospheric Propagation XXVII*, vol. 9354. SPIE, 2015, p. 93540G.

[61] G. J. Rossmanith, S. Kuhlmann, and T. Beck, "The different roles of the DLR German Space Operations Center in recent Laser Communication Projects," in *68th International Astronautical Congress (IAC)*, September 2017.

[62] M. Gregory *et al.*, "Status on laser communication activities at Tesat-Spacecom," in *Free-Space Laser Communications XXXVI*, vol. 12877. SPIE, 2024, p. 1287704.

[63] F. Heine *et al.*, "The European data relay system and Alphasat to T-AOGS space to ground links, status, and achievements in 2017," in *Free-Space Laser Communication and Atmospheric Propagation XXX*, vol. 10524. SPIE, 2018, p. 105240T.

[64] K. Saucke *et al.*, "Characterisation of the optical channel GEO to ground: using five years of data from Alphasat TDP1 and T-AOGS for investigation of different conditions," in *International Conference on Space Optics — ICSO 2020*, vol. 11852. SPIE, 2021, p. 118525W.

[65] ——, "The Tesat transportable adaptive optical ground station," in *Free-Space Laser Communication and Atmospheric Propagation XXVIII*, vol. 9739. SPIE, 2016, p. 973906.

[66] F. Heine *et al.*, "Laser based bi-directional Gbit ground links with the Tesat transportable adaptive optical ground station," in *Free-Space Laser Communication and Atmospheric Propagation XXIX*, vol. 10096. SPIE, 2017, p. 100960Y.

[67] K. Kudielka, E. Fischer, T. Berkefeld, and C. Fischer, "Optical feeder link demonstrations between the ESA Optical Ground Station and Alphasat," in *2023 IEEE International Conference on Space Optical Systems and Applications (ICSOS)*, 2023, pp. 64–68.

[68] K. Kudielka *et al.*, "Successful first optical feeder link demonstration between a ground station and a GEO satellite applying adaptive optics precompensation ("Alpha-Up")," in *COAT2023*, Durham, United Kingdom, Mar. 2023.

[69] A. Buckner *et al.*, "Up- and down- link atmospheric compensation experiment with Alphasat: design and initial results," in *Free-Space Laser Communications XXXVII*, vol. 13355. SPIE, 2025, p. 1335516.

[70] I. R. Hristovski *et al.*, "Pre-distortion adaptive optics: experimental results from bi-directional tracking links between DLR's optical ground station and Alphasat's TDP-1 terminal," in *Free-Space Laser Communications XXXVI*, vol. 12877. SPIE, 2024, p. 1287718.

[71] M. J. Abrahamson, O. Sindiy, B. Oaida, M. Wilkerson, and M. Kokorowski, "OPALS: mission system operations architecture for an optical communications demonstration on the ISS," in *SpaceOps 2014 Conference*, 2014, p. 1627.

[72] B. V. Oaida *et al.*, "Optical link design and validation testing of the Optical Payload for Lasercomm Science (OPALS) system," in *Free-Space Laser Communication and Atmospheric Propagation XXVI*, vol. 8971. SPIE, 2014, p. 89710U.

[73] M. J. Abrahamson, B. V. Oaida, O. Sindiy, and A. Biswas, "Achieving operational two-way laser acquisition for OPALS payload on the International Space Station," in *Free-Space Laser Communication and Atmospheric Propagation XXVII*, vol. 9354. SPIE, 2015, p. 935408.

[74] A. Biswas, B. Oaida, K. S. Andrews, J. M. Kovalik, M. Abrahamson, and M. W. Wright, "Optical payload for lasercomm science (OPALS) link validation during operations from the ISS," in *Free-Space Laser Communication and Atmospheric Propagation XXVII*, vol. 9354. SPIE, 2015, p. 93540F.

[75] B. V. Oaida, D. S. Bayard, and M. J. Abrahamson, "On-orbit measurement of ISS vibrations during OPALS extended mission operations," in *2017 IEEE Aerospace Conference*, 2017, pp. 1–10.

[76] O. Sindiy, M. Abrahamson, A. Biswas, M. W. Wright, J. H. Padams, and A. Konyha, *Lessons Learned from Optical Payload for Lasercomm Science (OPALS) Mission Operations*.

[77] M. W. Wright, J. Kovalik, J. Morris, M. Abrahamson, and A. Biswas, "LEO-to-ground optical communications link using adaptive optics correction on the OPALS downlink," in *Free-Space Laser Communication and Atmospheric Propagation XXVIII*, vol. 9739. SPIE, 2016, p. 973904.

[78] Y. Takayama *et al.*, "Current development status of Small Optical TrAnsponder (SOTA) for satellite-ground laser communications," in *Free-Space Laser Communication Technologies XXIV*, H. Hemmati and D. M. Boroson, Eds., vol. 8246, International Society for Optics and Photonics. SPIE, 2012, p. 824607.

[79] M. Akioka, H. Takenaka, M. Toyoshima, Y. Koyama, Y. Takayama, and T. Seki, "The NICT's New Optical Ground Station for Satellite Laser Communication and SOTA-SOCRATES Experiment," in *14th International Conference on Space Operations*, 2016, p. 2376.

[80] A. G *et al.*, "Laser communication experiments between Sota and Meo optical ground station," in *International Conference on Space Optics — ICSO 2016*, B. Cugny, N. Karafolas, and Z. Sodnik, Eds., vol. 10562, International Society for Optics and Photonics. SPIE, 2017, p. 105624B.

[81] C. Fuchs *et al.*, "Sota optical downlinks to DLR's optical ground stations," in *International Conference on Space Optics — ICSO 2016*, vol. 10562, International Society for Optics and Photonics. SPIE, 2017, p. 1056247.

[82] F. Moll, D. Kolev, M. Abrahamson, C. Schmidt, R. M. Calvo, and C. Fuchs, "LEO-ground scintillation measurements with the optical ground station Oberpfaffenhofen and SOTA/OPALS space terminals," in *Advanced Free-Space Optical Communication Techniques and Applications II*, vol. 9991, International Society for Optics and Photonics. SPIE, 2016, p. 999102.

[83] H. Takenaka *et al.*, "In-orbit verification of small optical transponder (SOTA): evaluation of satellite-to-ground laser communication links," in *Free-Space Laser Communication and Atmospheric Propagation XXVIII*, H. Hemmati and D. M. Boroson, Eds., vol. 9739, International Society for Optics and Photonics. SPIE, 2016, p. 973903.

[84] A. Carrasco-Casado *et al.*, "LEO-to-ground optical communications using SOTA (Small Optical TrAnsponder) – Payload verification results and experiments on space quantum communications," *Acta Astronautica*, vol. 139, pp. 377–384, 2017.

[85] W. Chen *et al.*, "5.12gbps optical communication link between leo satellite and ground station," in *2017 IEEE International Conference on Space Optical Systems and Applications (ICSOS)*, 2017, pp. 260–263.

[86] C. Schmidt and C. Fuchs, "The OSIRIS program — First results and Outlook," in *2017 IEEE International Conference on Space Optical Systems and Applications (ICSOS)*, 2017, pp. 19–22.

[87] D. Giggenbach *et al.*, "Optical Data Downlinks from OSIRIS on Flying Laptop Satellite," in *online Proceedings of TT&C 2019*, September 2019.

[88] P. Martín Pimentel *et al.*, "Cube laser communication terminal (CubeLCT) state of the art," *Acta Astronautica*, vol. 211, pp. 326–332, 2023.

[89] S. Ishtiaq, C. Schmidt, and F. Moll, "Modular FSO optical system design for classical and quantum optical communication systems," in *International Conference on Space Optics — ICSO 2020*, vol. 11852, International Society for Optics and Photonics. SPIE, 2021, p. 118520G.

[90] S. Janson and R. Welle, "The NASA optical communication and sensor demonstration program," 2013.

[91] S. W. Janson *et al.*, "The NASA optical communication and sensors demonstration program: preflight up-date," 2015.

[92] S. Janson *et al.*, "The NASA optical communications and sensor demonstration program: initial flight results," 2016.

[93] T. S. Rose *et al.*, "Optical communications downlink from a 1.5U Cubesat: OCSD program," in *International Conference on Space Optics — ICSO 2018*, vol. 11180, International Society for Optics and Photonics. SPIE, 2019, p. 111800J.

[94] T. Rose *et al.*, "Optical communications downlink from a low-earth orbiting 1.5 U CubeSat," *Optics express*, vol. 27, no. 17, pp. 24 382–24 392, 2019.

[95] R. P. Welle, C. M. Coffman, D. W. Pack, and J. R. Santiago, "Cubesat laser communication crosslink pointing demonstration," 2019.

[96] T. Kuwahara *et al.*, "Laser data downlink system of micro-satellite RISESAT," 2013.

[97] ——, "Satellite-to-ground optical communication system on Low Earth Orbit micro-satellite RISESAT," in *2012 IEEE/SICE International Symposium on System Integration (SII)*, 2012, pp. 939–944.

[98] H. Tomio *et al.*, "Assembly and integration of optical downlink terminal VSOTA on microsatellite RISESAT," in *International Conference on Space Optics — ICSO 2018*, vol. 11180, International Society for Optics and Photonics. SPIE, 2019, p. 111805Z.

[99] E. Luzhanskiy *et al.*, "Overview and status of the laser communication relay demonstration," in *Free-Space Laser Communication and Atmospheric Propagation XXVIII*, vol. 9739, International Society for Optics and Photonics. SPIE, 2016, p. 97390C.

[100] D. J. Israel *et al.*, "NASA's laser communications relay demonstration (LCRD) experiment program: characterization and initial operations," in *Free-Space Laser Communications XXXVI*, vol. 12877, International Society for Optics and Photonics. SPIE, 2024, p. 1287705.

[101] ——, "Early results from NASA's laser communications relay demonstration (LCRD) experiment program," in *Free-Space Laser Communications XXXV*, vol. 12413, International Society for Optics and Photonics. SPIE, 2023, p. 1241303.

[102] J. Woodward *et al.*, "Insights and Observations from Operating a Geostationary Laser Communication Relay Mission: Operational Lessons from NASA's Laser Communications Relay Demonstration (LCRD) and Associated Optical Ground Stations (OGSs)," in *29th Ka and Broadband Space Communications and Navigation Conference*, 2024.

[103] F. I. Khatri *et al.*, "Experimental results from integrated LCRD low-earth orbit user modem and amplifier terminal (ILLUMA-T) program," in *Free-Space Laser Communications XXXVII*, vol. 13355, International Society for Optics and Photonics. SPIE, 2025, p. 1335506.

[104] S. Yamakawa *et al.*, "LUCAS: The second-generation GEO satellite-based space data-relay system using optical link," in *2022 IEEE International Conference on Space Optical Systems and Applications (ICSOS)*, 2022, pp. 14–16.

[105] Y. Satoh, T. Itahashi, Y. Takano, and S. Yamakawa, "Operational Results of JAXA's Optical Data Relay System LUCAS as of Oct. 2025," *IEEE Journal of Selected Topics in Quantum Electronics*, vol. 32, no. 1: Advances in Free Space Laser Communications, pp. 1–6, 2026.

[106] H. Kotake *et al.*, "Experimental analysis of atmospheric channel model with misalignment fading for GEO satellite-to-ground optical link using “LUCAS” onboard optical data relay satellite," *Opt. Express*, vol. 31, no. 13, pp. 21 351–21 366, Jun 2023.

[107] ——, "Seasonal analysis of atmospheric channel model for GEO satellite-to-ground laser links using LUCAS," *Opt. Express*, vol. 34, no. 7, pp. 12 191–12 210, Apr 2026.

[108] ——, "Experimental Demonstration of Next-Generation FEC-Coded Data Transmission for GEO Satellite-to-Ground Laser Link Using LUCAS Onboard the Optical Data Relay Satellite," in *2025 IEEE International Conference on Space Optical Systems and Applications (ICSOS)*, 2025, pp. 1–6.

[109] Y. Munemasa *et al.*, "Development Status of NICT's High-Speed Laser Communications Mission, "HICALI" on Engineering Test Satellite 9 (ETS-9)," in *2025 IEEE International Conference on Space Optical Systems and Applications (ICSOS)*, 2025, pp. 1–4.

[110] Y. Saito, T. Usami, T. Okura, J. Nakazono, S. Hosono, and H. Tsuji, "HICALI-GATE: Testbeds of The Optical Ground Station in Japan," in *2025 IEEE International Conference on Space Optical Systems and Applications (ICSOS)*, 2025, pp. 1–4.

[111] L. Blarre, A. Aresta, D. Parrain, S. Poulenard, and J.-C. Richard, "Airbus Defence and Space high speed cross atmospheric optical comms program," in *2023 IEEE International Conference on Space Optical Systems and Applications (ICSOS)*, 2023, pp. 19–25.

[112] S. Poulenard *et al.*, "Ground-to-GEO Bidirectional Optical Links between TELEO and various OGS: In Orbit Test Result, Experimental Comparison with Numerical Models for power budget and telecom link margins," in *2025 IEEE International Conference on Space Optical Systems and Applications (ICSOS)*, 2025, pp. 1–7.

[113] N. Védrenne *et al.*, "Received Optical Power Statistics analysis for bidirectional optical feeder links measurements with FEELINGS and TELEO," in *2025 IEEE International Conference on Space Optical Systems and Applications (ICSOS)*, 2025, pp. 1–4.

[114] G. Artaud *et al.*, "French Optical Ground Station (FrOGS) Results of GEO Optical Bidirectional Links With TELEO," *IEEE Journal of Selected Topics in Quantum Electronics*, vol. 32, no. 1: Advances in Free Space Laser Communications, pp. 1–16, 2026.

[115] B. Rödiger *et al.*, "OSIRIS4CubeSat—The World's Smallest Commercially Available Laser Communication Terminal," *Aerospace*, vol. 12, no. 8, 2025.

[116] C. Fuchs, D. Laidlaw, F. Moll, J. Poliak, C. Schmidt, and A. Shrestha, "Recent results in optical satellite link research at DLR," in *Free-Space Laser Communications XXXVII*, vol. 13355, International Society for Optics and Photonics. SPIE, 2025, p. 1335503.

[117] N. Doelman *et al.*, "Design and In-Orbit Performance of a 1U 1 Gbit/s Optical Communication Terminal," *IEEE Journal of Selected Topics in Quantum Electronics*, vol. 32, no. 1: Advances in Free Space Laser Communications, pp. 1–16, 2026.

[118] K. Cahoy *et al.*, "The CubeSat Laser Infrared CrosslinK Mission (CLICK)," in *International Conference on Space Optics — ICSO 2018*, vol. 11180, International Society for Optics and Photonics. SPIE, 2019, p. 111800Y.

[119] W. Kammerer *et al.*, "CLICK-A: Optical communication experiments from a cubesat downlink terminal," 2023.

[120] A. Carrasco-Casado, K. Shiratama, D. R. Kolev, H. Tsuji, A. Miura, and M. Toyoshima, "Overview of the CubeSOTA mission: A miniaturized lasercom terminal onboard a 6U CubeSat," in *2025 IEEE International Conference on Space Optical Systems and Applications (ICSOS)*, 2025, pp. 1–5.

[121] C. M. Schieler *et al.*, "200 Gbps TBIRD CubeSat downlink: pre-flight test results," in *Free-Space Laser Communications XXXIV*, vol. 11993, International Society for Optics and Photonics. SPIE, 2022, p. 119930P.

[122] C. Schieler *et al.*, "NASA's terabyte infrared delivery (TBIRD) program: Large-volume data transfer from LEO," 2019.

[123] C. M. Schieler *et al.*, "On-orbit demonstration of 200-Gbps laser communication downlink from the TBIRD CubeSat," in *Free-Space Laser Communications XXXV*, vol. 12413, International Society for Optics and Photonics. SPIE, 2023, p. 1241302.

[124] ——, "Recent On-Orbit Results and ARQ Performance Analysis for the TBIRD 200-Gbps Mission," in *2023 IEEE International Conference on Space Optical Systems and Applications (ICSOS)*, 2023, pp. 49–55.

[125] S. Mansilla *et al.*, "Development of a Compact Optical Communications Terminal for the PULSE-A CubeSat," 2025.

[126] C. M. Schieler *et al.*, "200 Gbps TBIRD CubeSat downlink: pre-flight test results," in *Free-Space Laser Communications XXXIV*, vol. 11993. SPIE, 2022, p. 119930P.

[127] L. C. Andrews and L. R. Phillips, *Laser beam propagation through random media: Second edition*. SPIE Press, 2005.

[128] H. Kaushal, V. Jain, and S. Kar, *Free space optical communication*. Springer, 2017, vol. 60.

[129] S. Cakaj, B. Kamo, V. Koliçi, and O. Shurdi, "The range and horizon plane simulation for ground stations of low earth orbiting (LEO) satellites," *Int. J. Commun. Netw. Syst. Sci.*, vol. 4, no. 9, pp. 585–589, 2011.

[130] H. Kaushal and G. Kaddoum, "Optical Communication in Space: Challenges and Mitigation Techniques," *IEEE Communications Surveys & Tutorials*, vol. 19, no. 1, pp. 57–96, 2017.

[131] H. Hemmati, "Near-earth laser communications," in *Near-Earth Laser Communications, Second Edition*. CRC press, 2020, pp. 1–40.

[132] L. C. Andrews, *Field guide to atmospheric optics*. DC, USA: SPIE Press, 2019.

[133] *Propagation data required for the design of earth-space systems operating between 20 THz and 375 THz*, Rec. ITU-R P.1621-2, International Telecommunication Union Std., 2015.

[134] R. Barrios, S. Dimitrov, R. Mata-Calvo, and D. Giggenbach, "Link budget assessment for GEO feeder links based on optical technology," *International Journal of Satellite Communications and Networking*, vol. 39, no. 2, pp. 160–177, 2021.

[135] R. R. Beland, "Propagation through atmospheric optical turbulence," in *The Infrared and Electro-Optical Systems Handbook*. The Environmental Research Institute of Michigan and SPIE Press, Bellingham, Washington, 1996, vol. 2.

[136] A. Carrasco Casado and R. Mata Calvo, "Free-space optical links for space communication networks," in *Springer Handbook of Optical Networks*. Berlin, Germany: Springer, 2020, pp. 1057–1103.

[137] H. Henniger and O. Wilfert, "An introduction to free-space optical communications," *Radioengineering*, vol. 19, no. 2, pp. 203–212, 2010.

[138] D. Giggenbach and H. Henniger, "Fading-loss assessment in atmospheric free-space optical communication links with on-off keying," *Optical Engineering*, vol. 47, no. 4, p. 046001, 2008.

[139] L. C. Andrews and R. L. Phillips, "Recent results on optical scintillation in the presence of beam wander," in *Atmospheric Propagation of Electromagnetic Waves II*, O. Korotkova, Ed., vol. 6878, International Society for Optics and Photonics. SPIE, 2008, p. 687802.

[140] L. C. Andrews, R. L. Phillips, R. J. Sasiela, and R. R. Parenti, "Strehl ratio and scintillation theory for uplink Gaussian-beam waves: beam wander effects," *Optical Engineering*, vol. 45, no. 7, p. 076001, 2006.

[141] Z. Zhao and R. Liao, "Effects of beam wander on free-space optical communications through turbulent atmosphere," in *Atmospheric Propagation VII*,

L. M. W. Thomas and E. J. Spillar, Eds., vol. 7685, International Society for Optics and Photonics. SPIE, 2010, p. 76850K.

[142] S. Dimitrov, R. Barrios, B. Matuz, G. Liva, R. Mata-Calvo, and D. Giggenbach, "Digital modulation and coding for satellite optical feeder links with pre-distortion adaptive optics," *International Journal of Satellite Communications and Networking*, vol. 34, no. 5, pp. 625–644, 2016.

[143] Z. Sodnik, J. P. Armengol, R. H. Czichy, and R. Meyer, "Adaptive optics and ESA's optical ground station," in *Free-Space Laser Communications IX*, A. K. Majumdar and C. C. Davis, Eds., vol. 7464, International Society for Optics and Photonics. SPIE, 2009, p. 746406.

[144] G. A. Tyler, "Bandwidth considerations for tracking through turbulence," *J. Opt. Soc. Am. A*, vol. 11, no. 1, pp. 358–367, Jan 1994.

[145] M. Toyoshima, "Trends in satellite communications and the role of optical free-spacecommunications," *J. Opt. Netw.*, vol. 4, no. 6, pp. 300–311, Jun 2005.

[146] S. Arnon, "Power versus stabilization for laser satellite communication," *Appl. Opt.*, vol. 38, no. 15, pp. 3229–3233, May 1999.

[147] A. Carrillo-Flores, D. Giggenbach, M. Knopp, D. Orsucci, and A. Shrestha, "Effects of pointing errors on intensity losses in the optical LEO uplink," in *International Conference on Space Optics — ICSO 2022*, vol. 12777, International Society for Optics and Photonics. SPIE, 2023, p. 127775U.

[148] G. M. Pettersson, J. Perdigues, and Z. Sodnik, "Unmodified Portable Telescope for Space-to-Ground Optical Links," in *2019 IEEE International Conference on Space Optical Systems and Applications (ICSOS)*, 2019, pp. 1–7.

[149] M. Toyoshima and K. Araki, "Far-field pattern measurement of an onboard laser transmitter by use of a space-to-ground optical link," *Appl. Opt.*, vol. 37, no. 10, pp. 1720–1730, Apr 1998.

[150] J. Ma, X. Li, S. Yu, L. Tan, and Q. Han, "Influence of satellite vibration on optical communication performance for intersatellite laser links," *Optical review*, vol. 19, no. 1, pp. 25–28, 2012.

[151] M. Toyoshima, Y. Takayama, H. Kunimori, T. Jono, and S. Yamakawa, "In-orbit measurements of spacecraft microvibrations for satellite laser communication links," *Optical Engineering*, vol. 49, no. 8, p. 083604, 2010.

[152] M. A. Esmail, H. Fathallah, and M.-S. Alouini, "Analysis of fog effects on terrestrial free space optical communication links," in *2016 IEEE International Conference on Communications Workshops (ICC)*, 2016, pp. 151–156.

[153] R. Nebuloni, "Empirical relationships between extinction coefficient and visibility in fog," *Appl. Opt.*, vol. 44, no. 18, pp. 3795–3804, Jun 2005.

[154] H. Vasseur and C. J. Gibbins, "Prediction of apparent extinction for optical transmission through rain," *Appl. Opt.*, vol. 35, no. 36, pp. 7144–7150, Dec 1996.

[155] J. S. Marshall and W. M. K. Palmer, "The distribution of raindrops with size," *J. Meteor.*, vol. 5, no. 4, pp. 165–166, 1948.

[156] S. Muhammad, P. Kohldorfer, and E. Leitgeb, "Channel modeling for terrestrial free space optical links," in *Proceedings of 2005 7th International Conference Transparent Optical Networks, 2005.*, vol. 1, 2005, pp. 407–410 Vol. 1.

[157] U. A. Korai, L. Luini, and R. Nebuloni, "Model for the Prediction of Rain Attenuation Affecting Free Space Optical Links," *Electronics*, vol. 7, no. 12, 2018.

[158] V. Sharma, "Degradation measures in Free Space Optical communication (FSO) and its mitigation techniques-a review," *International Journal of Computer Applications*, vol. 55, no. 1, pp. 23–27, 2012.

[159] Z. Ghassemlooy, W. Popoola, and S. Rajbhandari, *Optical wireless communications: system and channel modelling with MATLAB*. Boca Raton, FL, USA: CRC press, 2019.

[160] T. Plank, M. Czaputa, E. Leitgeb, S. S. Muhammad, N. Djaja, B. Hillbrand, P. Mandl, and M. Schönhuber, "Wavelength selection on fso-links," in *Proceedings of the 5th European Conference on Antennas and Propagation (EUCAP)*, 2011, pp. 2508–2512.

[161] M. Yousuf and S. S. Muhammad, "Cloud attenuation predictive model using solution of radiative transfer equation for optical feeder links from satellite to ground," ser. FIT '10, 2010.

[162] R. Wilson, E. Milton, and J. Nield, "Are visibility-derived AOT estimates suitable for parameterizing satellite data atmospheric correction algorithms?" *International Journal of Remote Sensing*, vol. 36, no. 6, pp. 1675–1688, 2015.

[163] Y. Dikmelik and F. M. Davidson, "Fiber-coupling efficiency for free-space optical communication through atmospheric turbulence," *Appl. Opt.*, vol. 44, no. 23, pp. 4946–4952, Aug 2005.

[164] D. Giggenbach, M. T. Knopp, and C. Fuchs, "Link budget calculation in optical LEO satellite downlinks with on/off-keying and large signal divergence: A simplified methodology," *International Journal of Satellite Communications and Networking*, vol. 41, no. 5, pp. 460–476, 2023.

[165] H. Kotake, Y. Abe, M. Sekiguchi, T. Fuse, H. Tsuji, and M. Toyoshima, "Link Budget Design of Adaptive Optical Satellite Network for Integrated Non-Terrestrial Network," in *2022 IEEE International Conference on Space Optical Systems and Applications (ICSOS)*, 2022, pp. 240–247.

[166] T. Plank, E. Leitgeb, and M. Loeschnigg, "Recent developments on free space optical links and wavelength analysis," in *2011 International Conference on Space Optical Systems and Applications (ICSOS)*, 2011, pp. 14–20.

[167] J. Liang, A. U. Chaudhry, E. Erdogan, and H. Yanikomeroglu, "Link Budget Analysis for Free-Space Optical Satellite Networks," in *2022 IEEE 23rd International Symposium on a World of Wireless, Mobile and Multimedia Networks (WoWMoM)*, 2022, pp. 471–476.

[168] M. Toyoshima, K. Takizawa, T. Kuri, W. Klaus, M. Toyoda, H. Kunimori, T. Jono, Y. Takayama, and K. Arai, *Development of the Optical Ground Station for the OICETS Satellite and Experimental Results.*

[169] M. Toyoshima *et al.*, "Overview of the Laser Communication System for the NICT Optical Ground Station and Laser Communication Experiments on Ground-to-Satellite Links," *NICT Journal*, vol. 59, no. 1.2, pp. 053–075, 2012.

[170] H. Takenaka, M. Toyoshima, and Y. Takayama, "Experiment of the Fiber Coupling Efficiency for Satellite Downlinks," *NICT Journal*, vol. 59, no. 1.2, pp. 077–082, 2012.

[171] "Space-track." [Online]. Available: https://www.space-track.org/

[172] K. Saucke *et al.*, "The TESAT transportable adaptive optical ground station and the operational experiences," in *International Conference on Space Optics—ICSO 2016*, vol. 10562. SPIE, 2017, pp. 1033–1056.

[173] ——, "Three years of optical satellite to ground links with the T-AOGS: data transmission and characterization of atmospheric conditions," in *International Conference on Space Optics — ICSO 2018*, vol. 11180. SPIE, 2019, p. 111801D.

[174] M. Toyoshima *et al.*, "Ground-to-satellite optical link tests between Japanese laser communications terminal and European geostationary satellite ARTEMIS," in *Free-Space Laser Communication Technologies XVI*, vol. 5338. SPIE, 2004, p. 1.

[175] L. W. Bradford, "Maui4: a 24 hour Haleakala turbulence profile," in *Proceedings of the AMOS Technical Conference*, 2010.

[176] N. Perlot *et al.*, "Results of the optical downlink experiment KIODO from OICETS satellite to optical ground station Oberpfaffenhofen (OGS-OP)," in *Free-Space Laser Communication Technologies XIX and Atmospheric Propagation of Electromagnetic Waves*, vol. 6457. SPIE, 2007, p. 645704.

[177] F. Moll and M. Knapel, "Free-space laser communications for satellite downlinks: Measurements of the atmospheric channel," *Proceedings of IAC2011*, 2011.

[178] M. Brechtelsbauer *et al.*, "Report on DLR-JAXA joint experiment: The Kirari optical downlink to Oberpfaffenhofen (KIODO)," Japan Aerospace Exploration Agency (JAXA), Tech. Rep., 2007.

[179] A. Knoedler and F. Moll, "Atmospheric Turbulence Statistics and Profile Modeling. Local to DLR Oberpfaffenhofen," in *COAT-2019 - workshop.* Châtillon, France: ONERA, Dec. 2019.

[180] K. Iizuka, *Elements of Photonics, Volume II: For Fiber and Integrated Optics.* John Wiley & Sons, 2002, vol. 1.

[181] S. Bottacchi, *Noise and signal interference in optical fiber transmission systems: an optimum design approach.* John Wiley & Sons, 2008.

[182] A.-R. Camboulives, M.-T. Velluet, S. Poulenard, L. Saint-Antonin, and V. Michau, "Statistical and temporal irradiance fluctuations modeling for a ground-to-geostationary satellite optical link," *Appl. Opt.*, vol. 57, no. 4, pp. 709–721, Feb 2018.

[183] R.-J. Essiambre, G. Kramer, P. J. Winzer, G. J. Foschini, and B. Goebel, "Capacity Limits of Optical Fiber Networks," *Journal of Lightwave Technology*, vol. 28, no. 4, pp. 662–701, 2010.

[184] P. M. Becker, A. A. Olsson, and J. R. Simpson, *Erbium-doped fiber amplifiers: fundamentals and technology.* Elsevier, 1999.

[185] G. P. Agrawal, *Fiber-optic communication systems.* John Wiley & Sons, 2012.

[186] G. Ellinas, I. Roudas *et al.*, *WDM systems and networks: Modeling, simulation, design and engineering.* Springer Science & Business Media, 2011.

[187] "ESA Specification for Terabit/sec Optical Links (ESTOL)," ESA-CSC-T-SP-0001, Issue 2.2, 2024.

[188] L. Jolissaint, "Optical Turbulence Generators for Testing Astronomical Adaptive Optics Systems: A Review and Designer Guide," *Publications of the Astronomical Society of the Pacific*, vol. 118, no. 847, p. 1205, sep 2006.

[189] T. A. Rhoadarmer and J. R. P. Angel, "Low-cost, broadband static phase plate for generating atmosphericlike turbulence," *Appl. Opt.*, vol. 40, no. 18, pp. 2946–2955, Jun 2001.

[190] C. Nelson, S. Avramov-Zamurovic, R. Malek-Madani, O. Korotkova, R. Sova, and F. Davidson, "Measurements and comparison of the probability density and covariance functions of laser beam intensity fluctuations in a hot-air turbulence emulator with the maritime atmospheric environment," in *Laser Communication and Propagation through the Atmosphere and Oceans*, vol. 8517, International Society for Optics and Photonics. SPIE, 2012, p. 851707.

[191] B. Kebapci, F. Miramirkhani, H. Nouri, and M. Uysal, "A custom-design atmospheric channel emulator for the performance evaluation of free space optical communication systems," in *2017 19th International Conference on Transparent Optical Networks (ICTON)*, 2017, pp. 1–5.

[192] J. Alameri *et al.*, "Atmospheric propagation emulator for free space optical applications: design and performances," in *Laser Communication and Propagation through the Atmosphere and Oceans XII*, vol. 12691. SPIE, 2023, p. 126910Q.

[193] L. Zhang, C. Yanan, X. Zhao, and X. Shao, "Joint mitigation of frequency offset and phase noise for coherent free-space optical communication in atmospheric turbulence," *Optics Communications*, vol. 552, p. 130071, 2024.

[194] X. Liu *et al.*, "128 Gbit/s Free-Space Laser Transmission Performance in a Simulated Atmosphere Channel With Adjusted Turbulence," *IEEE Photonics Journal*, vol. 10, no. 2, pp. 1–10, 2018.

[195] W. Popoola, Z. Ghassemlooy, C. Lee, and A. Boucouvalas, "Scintillation effect on intensity modulated laser communication systems—a laboratory demonstration," *Optics & Laser Technology*, vol. 42, no. 4, pp. 682–692, 2010.

[196] M. Ijaz, Z. Ghassemlooy, S. Ansari, O. Adebanjo, H. Le Minh, S. Rajbhandari, and A. Gholami, "Experimental investigation of the performance of different modulation techniques under controlled FSO turbulence channel," in *2010 5th International Symposium on Telecommunications*, 2010, pp. 59–64.

[197] M. Abtahi, P. Lemieux, W. Mathlouthi, and L. A. Rusch, "Suppression of Turbulence-Induced Scintillation in Free-Space Optical Communication Systems Using Saturated Optical Amplifiers," *J. Lightwave Technol.*, vol. 24, no. 12, pp. 4966–4973, Dec 2006.

[198] S. Trisno, I. I. Smolyaninov, S. D. Milner, and C. C. Davis, "Delayed diversity for fade resistance in optical wireless communications through turbulent media," in *Optical Transmission Systems and Equipment for WDM Networking III*, vol. 5596. SPIE, 2004, pp. 385 – 394.

[199] H. Kaushal, V. Kumar, A. Dutta, H. Aennam, V. K. Jain, S. Kar, and J. Joseph, "Experimental Study on Beam Wander Under Varying Atmospheric Turbulence Conditions," *IEEE Photonics Technology Letters*, vol. 23, no. 22, pp. 1691–1693, 2011.

[200] N. A. M. Nor *et al.*, "Experimental Investigation of All-Optical Relay-Assisted 10 Gb/s FSO Link Over the Atmospheric Turbulence Channel," *Journal of Lightwave Technology*, vol. 35, no. 1, pp. 45–53, 2017.

[201] A. Dixit, V. Porwal, A. Kumar, and S. K. Mishra, "Systematic Characterization of Near-Index-Matched Optics Based Atmospheric Turbulence Simulator," *Mapan*, vol. 35, no. 2, pp. 221–232, 2020.

[202] Y. Ren *et al.*, "Atmospheric turbulence effects on the performance of a free space optical link employing orbital angular momentum multiplexing," *Opt. Lett.*, vol. 38, no. 20, pp. 4062–4065, Oct 2013.

[203] P. Robles *et al.*, "Emulating and characterizing strong turbulence conditions for space-to-ground optical links: the PICOLO bench," *Journal of Astronomical Telescopes, Instruments, and Systems*, vol. 9, no. 4, p. 049002, 2023.

[204] Z. Chen, C. Li, P. Ding, J. Pu, and D. Zhao, "Experimental investigation on the scintillation index of vortex beams propagating in simulated atmospheric turbulence," *Applied Physics B*, vol. 107, no. 2, pp. 469–472, 2012.

[205] Y. Li *et al.*, "Enhanced Atmospheric Turbulence Resiliency With Successive Interference Cancellation DSP in Mode Division Multiplexing Free-Space Optical Links," *Journal of Lightwave Technology*, vol. 40, no. 24, pp. 7769–7778, 2022.

[206] P. Polynkin, A. Peleg, L. Klein, T. Rhoadarmer, and J. Moloney, "Optimized multiemitter beams for free-space optical communications through turbulent atmosphere," *Opt. Lett.*, vol. 32, no. 8, pp. 885–887, Apr 2007.

[207] H. Ivanov, P. Pezzei, T. Plank, C. Pock, and E. Leitgeb, "Design of a hardware channel emulator as lab demonstrator for detailed verification of long-distance FSO systems," in *2016 International Conference on Broadband Communications for Next Generation Networks and Multimedia Applications (CoBCom)*, 2016, pp. 1–5.

[208] H. Ivanov, F. Marzano, E. Leitgeb, and P. Bekhrad, "Testbed Emulator of Satellite-to-Ground FSO Downlink Affected by Atmospheric Seeing Including Scintillations and Clouds," *Electronics*, vol. 11, no. 7, 2022.

[209] D. J. Geisler *et al.*, "Atmospheric Emulation and Testing Methodology for Laboratory Verification of FSO Communications Transceivers," in *2019 IEEE International Conference on Space Optical Systems and Applications (ICSOS)*, 2019, pp. 1–5.

[210] A. Shrestha, D. Giggenbach, A. Mustafa, J. Pacheco-Labrador, J. Ramirez, and F. Rein, "Fading testbed for free-space optical communications," in *Advanced Free-Space Optical Communication Techniques and Applications II*, vol. 9991. SPIE, 2016, p. 999105.

[211] T. Sasaki, M. Toyoshima, and H. Takenaka, "Fading Simulator for Satellite-to-Ground Optical Communication," *NICT Journal*, vol. 59, no. 1.2, pp. 095–102, 2012.

[212] J. M. Roth, S. Rauch, B. Reynolds, C. M. Schieler, and T. G. Ulmer, "Forward error correction and interleaving performance for lasercom terminals in fading channels," in *Free-Space Laser Communications XXXIV*, vol. 11993. SPIE, 2022, p. 1199307.

[213] C. M. Schieler, A. S. Garg, B. C. Bilyeu, J. P. Wang, and B. S. Robinson, "Demonstration of Reliable High-Rate Optical Communication over an Atmospheric Link using ARQ," in *2019 IEEE International Conference on Space Optical Systems and Applications (ICSOS)*, 2019, pp. 1–6.

[214] A. Mustafa, D. Giggenbach, J. Poliak, A. Shrestha, R. Mata-Calvo, and C. Fuchs, "Lab Implementation of 10 Gbps/channel Optical Transmitter Diversity Scheme for Geostationary Satellite Feeder Links," in *Photonic Networks; 16. ITG Symposium*, 2015, pp. 1–3.

[215] H. Ivanov, E. Leitgeb, P. Pezzei, and G. Freiberger, "Experimental characterization of SNSPD receiver technology for deep space FSO under laboratory testbed conditions," *Optik*, vol. 195, p. 163101, 2019.

[216] J. M. Roth, R. J. Murphy, W. E. Wilcox, and R. A. Conrad, "Experimental emulation of air-to-space laser communication links," in *LEOS 2008 - 21st Annual Meeting of the IEEE Lasers and Electro-Optics Society*, 2008, pp. 886–887.

[217] W. S. Rabinovich, R. Mahon, M. S. Ferraro, J. L. Murphy, and C. I. Moore, "Characterization of modems and error correcting protocols using a scintillation playback system," in *Free-Space Laser Communication and Atmospheric Propagation XXVIII*, vol. 9739. SPIE, 2016, p. 97390M.

[218] E. J. Katz, Y. K. Chahine, B. E. Vyhnalek, and S. A. Tedder, "Acousto-optic modulator for emulating atmospheric fade in free-space optical communication systems," in *Free-Space Laser Communications XXXII*, vol. 11272. SPIE, 2020, p. 1127219.

[219] U. Gujar and R. Kavanagh, "Generation of random signals with specified probability density functions and power density spectra," *IEEE Transactions on Automatic Control*, vol. 13, no. 6, pp. 716–719, 1968.

[220] M. M. Sondhi, "Random Processes With Specified Spectral Density and First-Order Probability Density," *Bell System Technical Journal*, vol. 62, no. 3, pp. 679–701, 1983.

[221] B. Epple, "Simplified channel model for simulation of free-space optical communications," *J. Opt. Commun. Netw.*, vol. 2, no. 5, pp. 293–304, May 2010.

[222] D. Giggenbach, S. Parthasarathy, A. Shrestha, F. Moll, and R. Mata-Calvo, "Power vector generation tool for free-space optical links — PVGeT," in *2017 IEEE International Conference on Space Optical Systems and Applications (ICSOS)*, 2017, pp. 160–165.

[223] H. T. Yura, "Optical downlink propagation from space-to-earth: aperture-averaged power fluctuations, temporal covariance and power spectrum," *Optics Express*, vol. 26, no. 21, pp. 26 787–26 809, Oct 2018.

[224] Y. K. Chahine, E. J. Katz, B. E. Vyhnalek, and S. A. Tedder, "Statistical analysis of fading power vectors for real-time atmospheric channel emulation," in *Free-Space Laser Communications XXXV*, vol. 12413. SPIE, 2023, p. 124131L.

[225] *Electronic Variable Optical Attenuator, 1250 to 1650 nm, FC/PC*, Thorlabs, V1550F. [Online]. Available: https://media.thorlabs.com/globalassets/items/v/v6/v60/v600f/ttn126022-s01.pdf?v=0625080550

[226] "Optical High Data Rate (HDR) Communication- 1550 nm," CCSDS 141.10-O-1, Experimental Specification (Orange Book). Issue 2, 2022.

[227] Y. T. others, "Tracking and pointing characteristics of OICETS optical terminal in communication demonstrations with ground stations," in *Free-Space Laser Communication Technologies XIX and Atmospheric Propagation of Electromagnetic Waves*, vol. 6457. SPIE, 2007, p. 645707.

[228] *Fibre optic communication subsystem test procedures - Part 2-9: Digital systems - Optical signal-to-noise ratio measurement for dense wavelength-division multiplexed systems*, IEC 61280-2-9 Std., 2009.

[229] C. E. Shannon, "A mathematical theory of communication," *The Bell System Technical Journal*, vol. 27, no. 3, pp. 379–423, 1948.

[230] O. Gazi, *Forward error correction via channel coding.* Springer, 2020.

[231] G. Maral, M. Bousquet, and Z. Sun, *Satellite communications systems: systems, techniques and technology.* John Wiley & Sons, 2020.

[232] G. Tzimpragos *et al.*, "A Survey on FEC Codes for 100 G and Beyond Optical Networks," *IEEE Communications Surveys & Tutorials*, vol. 18, no. 1, pp. 209–221, 2016.

[233] T. Richardson and R. Urbanke, *Modern coding theory.* Cambridge university press, 2008.

[234] C. Berrou and A. Glavieux, "Near optimum error correcting coding and decoding: turbo-codes," *IEEE Transactions on Communications*, vol. 44, no. 10, pp. 1261–1271, 1996.

[235] "Optical High Data Rate (HDR) Communication - 1064 nm," CCSDS 141.11-O-1, Experimental Specification (Orange Book), 2018.

[236] "Reed-Solomon product code for optical communication," CCSDS 142.10-O-1, Experimental Specification (Orange Book), 2023.

[237] "Second Generation Framing Structure, Channel Coding and Modulation Systems for Broadcasting, Interactive Services, News Gathering and Other Broadband Satellite Applications," Digital Video Broadcasting (DVB), ETSI EN 302 307 V1.2.1 (2009-08). Sophia-Antipolis: ETSI, 2009.

[238] "TM Synchronization and Channel Coding," CCSDS 131.0-B-4, Issue 4. Recommendation for Space Data System Standards (Blue Book), 2022.

[239] H. Yamazoe, S. Ohta, H. Komatsu, K. Suzuki, E. Okamoto, and K. Iwamoto, "Evaluation of the forward error correction format for LEO-ground optical communication using Reed-Solomon product code," in *Free-Space Laser Communications XXXIII*, vol. 11678. SPIE, 2021, p. 1167811.

[240] R. Pyndiah, A. Glavieux, A. Picart, and S. Jacq, "Near optimum decoding of product codes," in *1994 IEEE GLOBECOM. Communications: The Global Bridge*, 1994, pp. 339–343 vol.1.

[241] "Optical Intersatellite Link (OISL)," Space Development Agency (SDA), SDA-9100-0001-03, Standard, Version 2.1.2, 2022.

[242] "Open ROADM MSA 5.0 W-Port Digital Specification (100G-400G)," OpenROADM, Tech. Rep., 2021.

[243] "Flexible OTN common elements," ITU, ITU-T Recommendation G.709.1, 2024.

[244] W. Wang *et al.*, "Real-Time FPGA Investigation of Potential FEC Schemes for 800G-ZR/ZR+ Forward Error Correction," *Journal of Lightwave Technology*, vol. 41, no. 3, pp. 926–933, 2023.

[245] L. Rizzo, "Effective erasure codes for reliable computer communication protocols," *SIGCOMM Comput. Commun. Rev.*, vol. 27, no. 2, p. 24–36, 1997.

[246] G. P. Calzolari, M. Chiani, F. Chiaraluce, R. Garello, and E. Paolini, "Channel Coding for Future Space Missions: New Requirements and Trends," *Proceedings of the IEEE*, vol. 95, no. 11, pp. 2157–2170, 2007.

[247] T. De Cola and M. Marchese, "Reliable data delivery over deep space networks: Benefits of long erasure codes over ARQ strategies," *IEEE Wireless Communications*, vol. 17, no. 2, pp. 57–65, 2010.

[248] T. de Cola, E. Paolini, G. Liva, and G. P. Calzolari, "Reliability Options for Data Communications in the Future Deep-Space Missions," *Proceedings of the IEEE*, vol. 99, no. 11, pp. 2056–2074, 2011.

[249] P. Elias, "Coding for two noisy channels," in *Proc. 3rd London Symp., Information Theory, 1955*, 1955.

[250] A. Shokrollahi, "Raptor codes," *IEEE Transactions on Information Theory*, vol. 52, no. 6, pp. 2551–2567, 2006.

[251] E. Paolini, M. Chiani, and G. P. Calzolari, "Long erasure correcting codes: The new frontier for zero loss in space applications?" in *SpaceOps 2006 Conference*, 2006, p. 5827.

[252] G. Liva, P. Pulini, and M. Chiani, "On-Line Construction of Irregular Repeat Accumulate Codes for Packet Erasure Channels," *IEEE Transactions on Wireless Communications*, vol. 12, no. 2, pp. 680–689, 2013.

[253] "Erasure correcting codes for use in near-Earth and deep-space communications," CCSDS 131.5-O-1, Experimental Specification (Orange Book), 2014.

[254] E. Paolini, G. Liva, B. Matuz, and M. Chiani, "Maximum Likelihood Erasure Decoding of LDPC Codes: Pivoting Algorithms and Code Design," *IEEE Transactions on Communications*, vol. 60, no. 11, pp. 3209–3220, 2012.

[255] H. Jin, A. Khandekar, R. McEliece *et al.*, "Irregular repeat-accumulate codes," in *Proc. 2nd Int. Symp. Turbo codes and related topics*, 2000, pp. 1–8.

[256] "Second Generation Framing Structure, Channel Coding and Modulation Systems for Broadcasting, Interactive Services, News Gathering and Other Broadband Satellite Applications," Digital Video Broadcasting (DVB), ETSI EN 302 307 V1.3.1 (2013 03). Sophia-Antipolis: ETSI, 2013.

[257] N. Alessi, C. Caini, T. de Cola, and M. Raminella, "Packet Layer Erasure Coding in Interplanetary Links: The LTP Erasure Coding Link Service Adapter," *IEEE Transactions on Aerospace and Electronic Systems*, vol. 56, no. 1, pp. 403–414, 2020.

[258] V. Roca, C. Neumann, and D. Furodet, "Low density parity check (LDPC) staircase and triangle forward error correction (FEC) schemes," Internet RFC 5170, 2008.

[259] INRIA, ISAE, OpenFEC. [Online]. Available: https://openfec.inrialpes.fr/accueil.html

[260] J. G. Proakis and M. Salehi, *Digital communications*. McGraw-Hill, 2008.

[261] N. Mazzali and P.-D. Arapoglou, "Channel Interleaver Dimensioning for Optical LEO Direct-to-Earth Systems," in *2020 10th Advanced Satellite Multimedia Systems Conference and the 16th Signal Processing for Space Communications Workshop (ASMS/SPSC)*, 2020, pp. 1–6.

[262] P.-D. Arapoglou and N. Mazzali, "System-level benefit of variable data rate in optical LEO direct-to-earth links," in *International Conference on Space Optics — ICSO 2020*, vol. 11852. SPIE, 2021, p. 118524I.

[263] L. Wan, S. Tsai, and M. Almgren, "A fading-insensitive performance metric for a unified link quality model," in *IEEE Wireless Communications and Networking Conference, 2006. WCNC 2006.*, vol. 4, 2006, pp. 2110–2114.

[264] A. Alvarado, E. Agrell, D. Lavery, R. Maher, and P. Bayvel, "Replacing the Soft-Decision FEC Limit Paradigm in the Design of Optical Communication Systems," *Journal of Lightwave Technology*, vol. 33, no. 20, pp. 4338–4352, 2015.

[265] S. Poulenard *et al.*, "Forward error correcting code for high data rate LEO satellite optical downlinks," in *International Conference on Space Optics — ICSO 2018*, vol. 11180. SPIE, 2019, p. 111805L.

[266] L. Szczecinski and A. Alvarado, *Bit-interleaved coded modulation: fundamentals, analysis and design*. John Wiley & Sons, 2015.

[267] A. Martinez, A. Guillen i Fabregas, G. Caire, and F. M. J. Willems, "Bit-Interleaved Coded Modulation Revisited: A Mismatched Decoding Perspective," *IEEE Transactions on Information Theory*, vol. 55, no. 6, pp. 2756–2765, 2009.

[268] J. Cho, L. Schmalen, and P. J. Winzer, "Normalized Generalized Mutual Information as a Forward Error Correction Threshold for Probabilistically Shaped QAM," in *2017 European Conference on Optical Communication (ECOC)*, 2017, pp. 1–3.

[269] A. Alvarado, T. Fehenberger, B. Chen, and F. M. J. Willems, "Achievable information rates for fiber optics: Applications and computations," *J. Lightwave Technol.*, vol. 36, no. 2, pp. 424–439, Jan 2018.

[270] C. Lucien, L. Jérôme, V. Nicolas, R. Angélique, and G. Artaud, "Performance evaluation of coded transmission for adaptive-optics corrected satellite-to-ground laser links," in *2017 IEEE International Conference on Space Optical Systems and Applications (ICSOS)*, 2017, pp. 71–76.

[271] "Open ROADM Multi-Source Agreement (MSA) Specification)," OpenROADM, Ver 5.1, 2019.

[272] H. Méric and L. Péricart, "Performance evaluation of a DVB-S2 system with a digital optical feeder link," *International Journal of Satellite Communications and Networking*, vol. 38, no. 6, pp. 463–479, 2020.

[273] ITU, "Network performance objectives for IP-based servicess," ITU-T Recommendation Y.1541, 2011.

[274] ETSI, "Satellite Earth Stations and Systems (SES); Broadband Satellite Multimedia; IP Interworking over satellite; Performance, Availability and Quality of Service," ETSI TR 102 157 V1.1.1, 2003.

[275] ITU, "Basic reference models and performance parameters of Internet Protocol packet network transmission in the mobile-satellite service," ITU-R Recommendation M.1636, 2003.

[276] ——, "Flexible OTN B100G long-reach interfaces," Recommendation ITU-T G.709.3, March 2003.

[277] I. computer society, "IEEE Standard for Ethernet," IEEE Standard 802.3, 2022.

[278] ITU, “Interfaces for the optical transport network, Amendement 4,” Recommendation ITU-T G.709/Y.1331 (2020) Amd. 4, July 2025.

[279] ——, “Flexible OTN common elements,” Recommendation ITU-T G.709.1, March 2024.